Instabilities and flow-induced structures in anisotropic systems

by

Qing Zhang

B.S., Mechanical Engineering
Beijing Institute of Technology (2012)
S.M., Mechanical Engineering
Beijing Institute of Technology (2015)

Submitted to the Department of Mechanical Engineering
in partial fulfillment of the requirements for the degree of

Doctor of Philosophy in Mechanical Engineering

at the

MASSACHUSETTS INSTITUTE OF TECHNOLOGY

September 2022

Author .....
Department of Mechanical Engineering
August 5, 2022

Certified by .....
Irmgard Bischofberger
Associate Professor of Mechanical Engineering
Thesis Supervisor

Accepted by .....
Nicolas G. Hadjiconstantinou
Professor of Mechanical Engineering
Graduate Officer, Department Committee on Graduate Students

This page is intentionally left blank.

Instabilities and flow-induced structures in anisotropic systems

by

Qing Zhang

Submitted to the Department of Mechanical Engineering
on August 5, 2022 in partial fulfillment of the
requirements for the degree of
Doctor of Philosophy in Mechanical Engineering

Abstract

The natural world is full of patterns that spontaneously emerge across length scales and material properties. Examples range from microscopic dendritic snowflakes to macroscopic sand ripples and intricate river networks. Central to the formation of patterns is the concept of an instability; complex forms spontaneously develop when a system is driven out of equilibrium. Nature leverages instabilities to 'fabricate' complex structures that maximize performance using minimal resources, exploiting the self-amplification of small perturbations. The potential to use instabilities in practical applications, for example to engineer or assemble structured materials, is barely exploited due to the notorious difficulty and limited available strategies to control the self-amplified and non-linear growth that characterizes instabilities. In this thesis, we focus on fluid instabilities due to the adaptivity of fluids to their environments, and establish novel strategies to tune the growth morphology of interfacial instabilities and flow-induced structures at different length scales.

At the macroscale, we induce a morphology transition from the generic dense-branching growth characterized by repeated tip-splitting of the growing fingers to dendritic growth characterized by stable fingertips in the presence of anisotropy in the viscous-fingering instability. This instability arises when a less viscous fluid displaces a more viscous one in a confined environment. When the growth environment is rendered anisotropic by engraving a lattice of channels on a Hele-Shaw cell, we show that the morphology transition and the global symmetry of the dendrites can be controlled by tuning the viscosity ratio between the two fluids or the degree of anisotropy set by the lattice topography. We further exploit a material with shear-enhanced anisotropy where the anisotropy is intrinsic to the fluid, a lyotropic chromonic liquid crystal (LCLC) in the nematic phase. For high enough flow velocities, the tumbling behavior of LCLC solutions can be suppressed, which results in a flow-alignment of the material. This microscopic change in the director field macroscopically enhances the liquid crystal anisotropy to induce the transition from dense-branching to dendritic growth.

Microscopically, we discover the emergence of flow-induced defects and structures in LCLC solutions. Pure-twist disclination loops form in a range of shear rates as a consequence of the low twist elastic constant of LCLC solutions. We demonstrate that the size of the pure-twist disclination loops is governed by the balance between nucleation and annihilation forces, which can be tuned by controlling the flow velocity. Strikingly, at lower shear rates, chiral periodic double-twist structures spontaneously emerge, even though the LCLC is achiral. We

show that the mirror symmetry breaking is triggered at regions of biaxial-splay deformations that are unstable and evolve into the energetically cheaper double-twist elastic mode. Our results reveal a novel path to structural chirality in an achiral system.

The control gained over the pattern morphology and structure formation from fluid instabilities can open pathways to harnessing unstable growth to design programmable microstructures in materials and to control assembly and flow of biological systems in microfluidic devices.

Thesis Supervisor: Irmgard Bischofberger

Title: Class of 1942 Career Development Professor; Associate Professor of Mechanical Engineering

Acknowledgments

PhDs are expected to reach and explore the boundaries of human knowledge. In this exploring process, I have been inspired, excited and mentored by a number of people.

Great science begins with curiosity, which keeps us excited about our work and drives us to push new bounds. In my PhD journey, my adviser, Prof. Irmgard Bischofberger, is the person who has shown me this path. Her passion in revealing physical principles in pattern formation that is ubiquitous in nature taught me how research can be enjoyable when driven by curiosity and inspired me to always ask what, why and how in terms of apparent phenomena around us. Irmgard provided me with a lot of flexibility in research and motivated me to find my own interests. This allowed me to think independently and keep an open mind to continuously probe new things. At the same time, Irmgard was always available for my questions and always willing to help me out. I would like to express my sincere gratitude to Irmgard for her invaluable mentorship and tremendous support in this journey.

I would like to extend my sincere thanks to Prof. Anette (Peko) Hosoi and Prof. Mathias Kolle, for serving on my PhD committee and helping me complete my PhD journey. I thank Peko for her vision and her profound knowledge in the areas of, amongst many others, fluid dynamics and instabilities. She provided much deep insight in my work, showed me the methodology to resolve complex problems, and expanded my vision in physics. I thank Mathias for his generous help and his advice not only in my research, particularly, in optics, but also in my career development. Mathias's enthusiasm for bridging fundamental science and real-world problems showed me a different perspective in doing research and inspired me to keep exploring fundamental questions and to rethink the connection between fundamental discoveries and technological advances.

I also want to express my gratitude to my collaborators, not only for their brilliant ideas shared with me, but also for their guidance in the areas I had not been involved before. I thank Prof. Martin Bazant and Dr. Amin Amooie for showing me and expanding my vision in mathematics, in particular for modelling the growth morphology and interfacial instabilities. I much appreciate the help in optics provided by Prof. Peter T. C. So and Dr. Baoliang Ge. I thank Prof. Pedro J. Sáenz, Prof. Rama Bansil, Dr. Clover Su, Prof. Shuang Zhou, Prof. Rui Zhang, Prof. Chenhui Peng and Weiqiang Wang for their helpful discussions in my research projects. Particularly in my study of liquid crystals, I would like to offer my sincere thanks to Shuang, who provided generous mentorship at the beginning of my liquid crystal projects, and to Rui who helped me deepen my understanding in liquid crystals in our tremendous discussions. I also truly cherish my friendship and collaboration with them.

I thank my group members, Jae, Sami, Paul, Ippolyti, Samar, Baudouin, Andrew, Maëlle, Ding and all the members and alumni not listed here. I thank Jae, Sami, Paul, Ippolyti, Baudouin and Samar for their help on my research; I thank Baudouin for his precious advice on my career development; I thank all my group members for building such a dynamic, caring and inclusive team. Additionally, it is very fortunate for me to be working in Hatsopoulos Microfluids laboratory (HML). I had a cherished time spent together with my colleagues

and other friends in HML and in the social events. I thank Michela, Bavand, Jan, Philippe, Youzhi, George, Jonathan, Lani, William, Xinyu, Anthony, Ben, Wenhui, Hannah, Crystal, Jake, Joshua, Rishabh, Alice, Divya, Jianyi, Haiqin, Joseph, Caroline and Athanasios. HML is really a warm community, in which I've also received a plenty of help and support. I thank Prof. Gareth McKinley for guiding me into the fields of rheology and complex fluids; I thank Prof. Ming Guo for his expertise on cell mechanics and biophysics and his valuable advice on my career development; I thank Anoop for his instruction on the rheology measurement; I thank José for his help on the experiments of making hairy surfaces; I thank Sean for his service in the lab, making all possible resources available for us in HML.

I would like to express a sincere thank you to my friends near and far. I am honored to have all of them in my network, providing me support, motivation, and inspiration along the way. With my friends, I got the chance to find a good work-life balance. Together with Youzhi, Dixia, Zhongling, Yiliang, and Can, we founded a student association at MIT, MIT Micro-project Society, which provides a platform for students to access the topics of projects on the basis of real-world problems from industry, targeting to enhance the connection between off-campus opportunities and on-campus resources. In addition, during the pandemics of Covid-19 when cities were locked down, together with Qiheng and Qi, we initiated a community, Qiao Mu You Sheng, to serve students who were alone and single at home. We organized a plenty of activities online and offline that allowed students to meet new friends and helped them get rid of loneliness. When cooking, playing board games, and working out with my friends, Qiheng, Shaoyi, Xiaojun, Hao, Qingyi, Kaiyuan, Qi, Jerry, Shenglan, Anqi and Fengdi, I got refreshed and gained plenty of joyful time. I also thank my friends for all their support and care for me. I thank Youzhi, Yanfei, Yue, Samar, Yan, Zhumei, Qian, Lingbo, Jiliang, Xingzhou, Daniela, Fei, Xinye, Jinghui, Tudor, Xu and Xinyun and all the other friends not mentioned here. I value our friendship and hope it will last forever.

Especially, I thank Zeyu for joining me in this academia adventure and for always being there for me. He always stayed with me and encouraged me whenever I got stuck in a difficult time. I am truly grateful for his love and unwavering support.

Finally, I thank my mom, dad, brother, and sister-in-law for their tremendous encouragement, love and support on the other side of the earth. Even though we have not met each other in person for three years due to the COVID-19 pandemic, the kindness and the passion for learning that were originally delivered by my parents are always with me, and my love is always with them.

I acknowledge financial support from the MIT Research Support Committee. I acknowledge permission granted by the Royal Society of Chemistry, the United States National Academy of Sciences, and the American Chemical Society to use their copyrighted contents in this thesis.

Contents

List of Figures

5.3 **Characteristic size of structures in flowing DSCG solutions controlled by average shear rate.** (A) Normalized 2D spatial autocovariance in the x-direction (top) and in the y-direction (bottom), for different flow rates q. The solid lines denote compressed single or double exponential fits. (B) Characteristic domain sizes versus average shear rate $\overline{\dot{\gamma}}$. Along the x-direction for intermediate average flow rates, L_x (■), and for low and high average flow rates, L_{x_1} (▫), L_{x_2} (×); along the y-direction for intermediate flow rates, L_y (▲), and for low and high flow rates, L_{y_1} (△), L_{y_2} (+); and the average characteristic size $L = \sqrt{L_x L_y}$ (●). The black line denotes $L \propto \overline{\dot{\gamma}}^{-0.19}$. ($C$) Aspect ratio L_x/L_y (●) for intermediate average flow rates, L_{x_1}/L_{y_1} (○) and L_{x_2}/L_{y_2} (×) for low and high average flow rates. The black line indicates $L_x/L_y \approx \sqrt{K_3/K_1} = 1.9$. In ($B$) and ($C$), some of the error bars are smaller than the symbols. 104

List of Tables

Chapter 1

Introduction

1.1 Pattern growth in the viscous-fingering instability

Patterns, ubiquitously forming in nature, are found across different material properties and length scales ranging from microscopic snowflakes, to flames, river networks, and lightning [1]. Despite the variety and complexity of patterns, many of them share similar features and can be grouped into two 'essential shapes' or morphologies: dense-branching growth and dendritic growth [2]. Dense-branching growth arises from repeated tip-splitting of the growing finger and leads to a disordered pattern with many branches [2, 3] (Fig. 1.1(a)). Veins of leaves, neural networks, and blood vessels are all examples of dense-branching growth. In contrast, dendritic growth is characterized by stable protrusions where tip-splitting is prevented, and leads to structures with global symmetries [4–9] (Fig. 1.1(b)). Snowflakes or solidified alloys are examples of dendritic structures. Given the astonishing regularities in these structures, particular interest lies in identifying the common principles governing the pattern formation. Indeed, many patterns result from interfacial instabilities that are triggered by perturbations and driving forces [1]. Reaching control over interfacial pattern growth by gradient-driven transport of mass, heat or charge to the interface could not only provide insight into pattern selection in nature, but could also be exploited in engineering to build functional materials and structures [1, 10, 11]. In Chapters 3–4, we establish novel strategies to control interfacial pattern growth, particularly the growth of dense-branching and dendritic patterns.

The viscous-fingering instability has played an important role in elucidating basic prin-

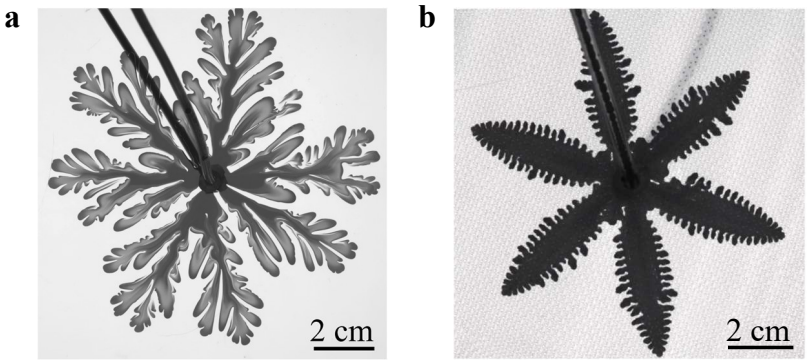

Figure 1.1: **Two common growth morphologies.** (a) Dense-branching growth. (b) Dendritic growth.

ciples of interfacial pattern formation [12–15]. It occurs when a fluid is displaced by a less viscous one in a quasi-two-dimensional geometry [16]. Such a geometry, consisting of two parallel plates placed on top of each other and separated by a small gap, is called a Hele-Shaw cell [17]. The instability has helped reveal the key role of interfacial anisotropy for the selection of the growth morphology; dendritic growth only occurs in anisotropic systems, where the interfacial dynamics becomes directionally dependent [5, 18–20]. In the absence of anisotropy, dense branching is instead the generic mode of growth [5, 18–20].

Experimentally, different strategies have been developed to introduce anisotropy in the interfacial dynamics. The most well-established means is by making geometric changes to the growth environment by engraving a symmetric lattice of channels on one plate of the Hele-Shaw cell or by placing air bubbles at the tips of growing fingers [18, 21–26]. The engraved channels, for example, modulate the local plate spacing and become the preferred growth direction, as the fluid velocity is proportional to the square of the plate spacing [18]. Another strategy is to use nematic thermotropic liquid crystals (TLCs) as one of the fluids, where the anisotropy is an intrinsic property of the medium itself [27]. In particular, the directors can be aligned by flow, which gives rise to a lower viscosity parallel to the flow direction compared to that perpendicular to the flow direction, and the lower viscosity direction becomes the preferred growth direction [28]. These strategies have successfully been applied to study dendritic growth, but only in the limit of very low viscosity ratio between the less-viscous inner fluid and the more-viscous outer one, $\eta_{\text{in}}/\eta_{\text{out}}$, typically with either air or water as

the invading fluid, where the growth is characterized by a single growing length scale, the finger length. However, it has been recently shown that the viscosity ratio, $\eta_{\text{in}}/\eta_{\text{out}}$, acts as a key parameter for pattern growth in the viscous-fingering instability: For larger values of $\eta_{\text{in}}/\eta_{\text{out}}$, unstable growth emerges that is not just characterized by a growing finger, but that exhibits a concomitant growth of an inner circular region within which the outer fluid is completely displaced [29]. This inner circular region becomes increasingly pronounced as the viscosity ratio between the two fluids increases. If and how dendritic growth occurs at higher viscosity ratios where the inner circular region appears is entirely unexplored.

In Chapter 3, we reveal that the previously overlooked control parameter, $\eta_{\text{in}}/\eta_{\text{out}}$, can lead to a rich variety of structures in an anisotropic environment, using a Hele-Shaw cell with engraved ordered channels. Previous experiments using the same anisotropic system in the limit of low $\eta_{\text{in}}/\eta_{\text{out}}$ have identified the degree of anisotropy, defined as the ratio between the channel height h and the plate spacing b, h/b, as a control parameter for the morphology transition from dense-branching to dendritic growth [18]; dendritic structures form beyond a critical value of h/b. For miscible fluids and for immiscible fluids at high capillary number, the dendrites have been shown to directly reflect the underlying symmetry of the lattice [8]. In our study, we show that $\eta_{\text{in}}/\eta_{\text{out}}$ serves a new control parameter in addition to h/b, determining the morphology transition between dense-branching growth and dendritic growth in miscible fluids. Remarkably, upon approaching the morphology transition governed by $\eta_{\text{in}}/\eta_{\text{out}}$ and h/b, the dendrites spontaneously change from six-fold towards twelve-fold symmetric dendrites even though the symmetry of the growth environment is fixed to be six fold. Varying either control parameter provides a new method to tune the symmetry of complex patterns, which may also have relevance for analogous phenomena of gradient-driven interfacial dynamics, such as directional solidification or electrodeposition.

In addition to investigating interfacial pattern formation in anisotropic environments by engraving an ordered lattice on one of the plates of the Hele-Shaw cell where the patterns, to an extent, are slaved to the topology of the lattice, we exploit the intrinsic anisotropy of nematic liquid crystals. Previous studies have employed this strategy using thermotropic liquid crystals (TLCs) as the displaced fluid [27], which, however, allows for dendritic growth in only a narrow range of temperature and pressure. In Chapter 4, we show how we can

controllably induce a transition from dense-branching to dendritic growth over a large range of control parameters in a different class of liquid crystals; aqueous solutions of lyotropic chromonic liquid crystals (LCLCs). We show that the morphology transition to dendritic growth is induced by the suppression of the intrinsic tumbling behavior of nematic LCLC solutions, which leads to flow-alignment of the material that provides a shear-enhanced anisotropy. Using a molecular theory framework to describe the dynamics of flowing LCLC solutions, we reveal the relation between the microscopic alignment and the macroscopic growth morphology selection, which provides a quantitative criterion for controlling the morphology of interfacial fluid instabilities.

1.2 Structure formation in nematic lyotropic chromonic liquid crystals

Liquid crystals (LCs) are materials composed of anisotropic mesogens [30, 31]. Due to their sensitivity to external perturbations, including temperature, electrical, and mechanical perturbations, liquid crystals have been extensively applied in sensors and stimuli-responsive elastomers [32, 33]. In particular, a class of LCs, lyotropic chromonic liquid crystals (LCLCs), have gained increasing attention in both fundamental and applied research in recent decades, as their structural properties are distinct from the more traditional thermotropic liquid crystals (TLCs) [34–42]. In contrast to TLCs formed by small organic molecules, LCLCs are aqueous suspensions of rod-like aggregates composed of disk-shaped molecules, as schematically shown in Fig. 1.2. These molecular stacks are 1 – 2 nm in diameter and tens to hundreds of nm in length; up to hundreds of times longer than TLC molecules, depending on the LCLC concentration and temperature [31, 39, 43–47].

The distinct structural properties of the nematic LCLCs lead to unique material properties, and results in peculiar mechanical behaviors that have so far been mostly studied at rest [48–50]. For example, due to the large aspect ratio and the semi-flexibility of the aggregates, LCLCs have significant elastic anisotropy compared to TLCs; the twist Frank elastic constant, K_2, is much smaller than the splay and bend Frank elastic constants, K_1

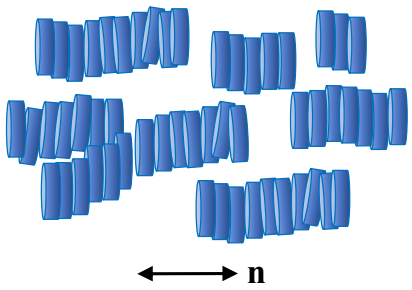

Figure 1.2: **LCLC aggregates.** At certain temperature and concentration, self-assembled LCLC aggregates align in the direction **n** and form a nematic phase.

and K_3 [50, 51]. The resulting relative ease with which twist deformations can occur can lead to a spontaneous symmetry breaking and the emergence of chiral structures in static LCLCs under spatial confinement, despite the achiral nature of the aggregates [39, 49, 52–56]. Additionally, the noncovalent hydrophobic interactions between disc-shaped molecules result in a small 'scission energy', *i.e.*, the energy required to break one aggregate into two, on the order of 10 kT [50]. The low scission energy allows the DSCG aggregates to break under large distortion of the director field, for example at the cores of singular disclinations, and consequently form an isotropic phase with a significant decrease of the order parameter that can extend over large scales, $\sim 10\mu$m [52].

In addition to the special mechanical behaviors at rest, nematic LCLCs in flow exhibit rich phenomena, which are currently poorly understood [57–60]. Different from most nematic TLCs, nematic LCLCs are tumbling liquid crystals characterized by a non-zero viscous torque for any orientation of the director, with $\alpha_2\alpha_3 < 0$, where the director does not adopt a stationary angle and can rotate in the shear plane [61]. The tumbling nature of LCLCs leads to enhanced sensitivity to shear. A recent study has revealed a variety of complex textures that emerge in simple shear flow in a nematic LCLC [61]. At shear rates $\dot{\gamma} < 1$ s^{-1}, the director realigns perpendicular to the flow direction adapting a so-called log-rolling state characteristic of tumbling nematics. For 1 s^{-1} $< \dot{\gamma} <$ 10 s^{-1}, polydomain textures form due to the nucleation of pure-twist disclination loops, for which the rotation vector is parallel to the loop normal, and mixed wedge-twist disclination loops, for which the rotation vector is perpendicular to the loop normal [60, 61]. Above $\dot{\gamma} >$ 10 s^{-1}, the disclination loops gradually transform into periodic stripes, which are parallel to the flow direction and in

which the director aligns predominantly along the flow direction [61].

In Chapter 4, we show that the director field of nematic LCLCs can transition from the tumbling state to the shear aligned state with increasing shear rate in a strong flow. We demonstrate that this transition is a consequence of the large length of the LCLC aggregates, which leads to slow orientational relaxation and which makes high Deborah number regimes experimentally accessible. The Deborah number (De) is the ratio of the rotational relaxation time of the aggregates and the characteristic time of the shear flow [62]. For De of order unity, the director field cannot be considered as a continuum field and the classical Ericksen-Leslie theory does not apply; instead, the transition to shear alignment is described by molecular theories considering the nematic potential resisting the shear flow deforming individual aggregates [62]. Additionally, we show how the low scission energy differentiates the dynamics of nematic LCLCs from nematic TLCs. We reveal that a transition to the isotropic phase can occur in a unaxial externsional flow.

In the intermediate and low shear rate regimes, we explore microstructures emerging in a pressure-driven nematic lyotropic chromonic liquid crystal in a microfluidic channel.

In Chapter 5, we show that pure-twist disclination loops emerge in the bulk flow for a certain range of intermediate shear rates. These loops are elongated in the flow direction and exhibit a constant aspect ratio. We demonstrate that the disclination loops nucleate at the boundary between regions where the director aligns predominantly along the flow direction close to the channel walls and regions where the director aligns predominantly perpendicular to the flow direction in the center of the channel. The large elastic stresses of the director gradient at the boundary are then released by the formation of disclination loops. We show that both the characteristic size and the fluctuations of the pure-twist disclination loops can be tuned by controlling the flow rate.

In Chapter 6, we reveal unexpected chiral structures in the absence of curved or pre-patterned surfaces at lower shear rates than those triggering the defects. We show that the chiral structures are a result of the formation of a complex periodic double-twist structure where the director field twists along both the flow direction and the gap thickness direction. The periodic double-twist structure leads to striking stripe patterns vertical to the flow direction. We reveal that the mirror symmetry breaking is triggered at regions of biaxial-splay

deformation characterized by opposite directions of the splay deformation in two orthogonal planes. We show that the biaxial-splay deformation is unstable and evolves into a lower energy-cost elastic mode, *i.e.*, the periodic double-twist structure, as a consequence of the small twist Frank elastic constant of LCLCs.

This thesis is written based on the following publications and articles that are currently in review or in preparation for submission:

- Q. Zhang, A. Amooie, M. Z. Bazant, I. Bischofberger, Growth morphology and symmetry selection of interfacial instabilities in anisotropic environments. *Soft Matter* 17 (2021): 1202-1209.
- Q. Zhang*, R. Zhang*, B. Ge*, Z. Yaqoob, P. T. C. So, I. Bischofberger, Structures and topological defects in pressure-driven lyotropic chromonic liquid crystals. *Proc. Natl. Acad. Sci. U. S. A.*, 118. 35 (2021): e2108361118.
- B. Ge*, Q. Zhang*, R. Zhang, J. Lin, P. Tseng, C. Chang, C. Dong, R. Zhou, Z. Yaqoob, I. Bischofberger, P. T. C. So, Single-shot quantitative polarization imaging of complex birefringent structure dynamics. *ACS Photonics*, 8.12 (2021): 3440-3449.
- Q. Zhang, S. Zhou, R. Zhang, I. Bischofberger, Dendritic patterns from shear-enhanced anisotropy in nematic liquid crystals. *In review.*
- Q. Zhang, W. Wang, S. Zhou, R. Zhang, I. Bischofberger, Flow-induced periodic chiral structures in an achiral nematic liquid crystal. *In preparation.*

* equal contribution.

Chapter 2

Experimental methods

Parts of this chapter are based on Ref. [63–67].

2.1 Experimental setups

We use Hele-Shaw cells and design microfluidic cells to explore instabilities and flow-induced structures in anisotropic systems.

2.1.1 Hele-Shaw cell

We use radial Hele-Shaw cells consisting of two flat glass plates of thickness 19 mm and diameter L 280 mm or 140 mm, separated by a uniform gap b, as shown in Fig. 2.1(a). The plate spacing b is maintained by spacers (McMASTER-CARR) placed around the plate perimeter. We tune b over a large range from 12 μm to 1350 μm. We inject the fluids into the Hele-Shaw cell through a 2 mm tube at the center of the top plate. The injection rate is controlled by a syringe pump (Harvard PHD 2000). Images are taken from below.

To explore the viscous-fingering instability in an anisotropic environment, we modify the Hele-Shaw cell by engraving six-fold symmetric lattices of channels on acrylic plates with diameter 145 mm using a laser cutter (Universal Laser Systems). The engraved plate is placed on the bottom glass plate of the Hele-Shaw cell, as shown in Fig. 2.1(b). The channels have a width, $w = 800$ μm, and the distance between the edges of two channels is

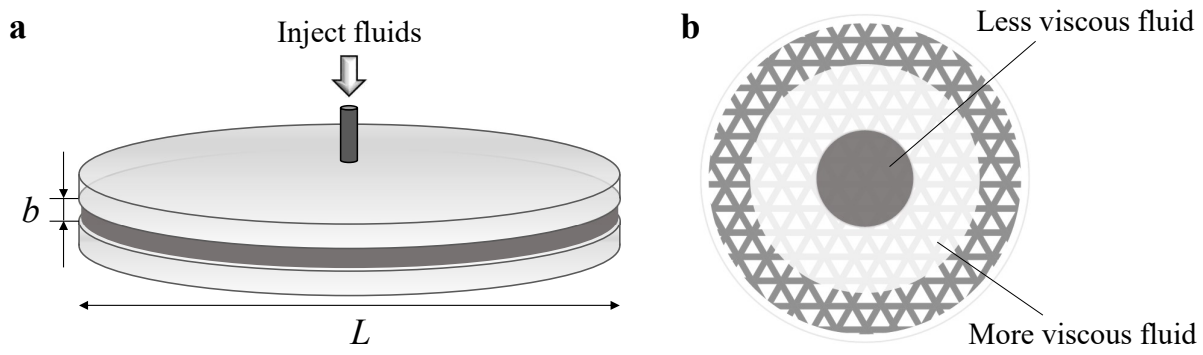

Figure 2.1: **Schematics of the Hele-Shaw cells.** (a) A radial Hele-Shaw cell is a quasi-two-dimensional geometry consisting of two flat plates with diameter, L, separated by a uniform gap, b, where $L >> b$. A 2 mm diameter hole in the center of top plate allows fluids to be injected into the cell. (b) Top view of the modified Hele-Shaw cell where an acrylic plate engraved with six-fold symmetric lattices is placed on the bottom plate of the Hele-Shaw cell. In the experiments, a less viscous fluid displaces a more viscous fluid to induce the viscous-fingering instability.

$d = 850$ μm. We use channel depths h of 10 μm, 28 μm, 50 μm, and 250 μm. The depth of the channels is measured using a profilometer (Dektak).

In the experiments where anisotropy is introduced intrinsically in the outer more fluid by using nematic lyotropic chromonic liquid crystals (LCLCs), we employ a regular Hele-Shaw cell. We control the surface anchoring condition by circularly rubbing the glass plates with a paste of diamond particles of diameter 50 nm (TechDiamondTools, Diamond Polishing Compound Polishing Paste), which yields a circularly planar alignment with anchoring strength $10^{-6} - 10^{-7}$ J/m^2 [68, 69].

2.1.2 Microfluidic channel

To investigate the properties of flowing nematic lyotropic chromonic liquid crystals (LCLCs), we design rectilinear microfluidic channels that are made of two rectangular glass plates. The glass plates are 6 mm in thickness and 51 mm by 76 mm or 25 mm by 76 mm in width and length. We use a paste of diamond particles of diameter $\approx$ 50 nm to rub both glass plates along the channel length direction, which induces a uniform planar alignment [68]. Rectangular spacers (Specac, MY SPR RECT 0.006 mm OMNI, and PRECISION BRAND) are placed between the two glass plates to create a rectangular channel and to maintain a

constant plate spacing. We seal three edges of the channel using 2 Ton Epoxy (DEVCON).

We build two types of channels with different inlet conditions: i) a radial flow at the inlet is induced by a hole drilled at the centerline and close to one end of the channel (Fig. 2.2(a)), and ii) a uniform flow at the inlet achieved by placing a customized reservoir on one end of the channel. The reservoir is glued to the channel using 5 minute Epoxy (DEVCON). The reservoir has a height of 25 mm, a width of 40 mm, and an inner thickness of 2 – 3 mm (Fig. 2.2(b)).

LCLC directors in shear flow tend to align in the direction either perpendicular or parallel to the shear plane [61, 65]. An injection protocol that uses a center hole as an inlet induces a radial flow which leads to bend or splay elastic deformations of the nematic LCLC solutions at the inlet. When we focus exclusively on structures forming far downstream, further than 15 mm away from the inlet where the structures are uniform in space, we use the center hole as inlet to simplify the channel fabrication process (Fig. 2.2(a)). To probe the director field of the flow-induced structures everywhere in the microfluidic channel, we use the reservoir to induce a uniform velocity profile at the inlet (Fig. 2.2(b)). This is particularly important in the small Ericksen number regime, where the elastic deformation at the inlet becomes non-negligible. The Ericksen number evaluates the relative importance of the viscous forces compared to the elastic forces [31, 50].

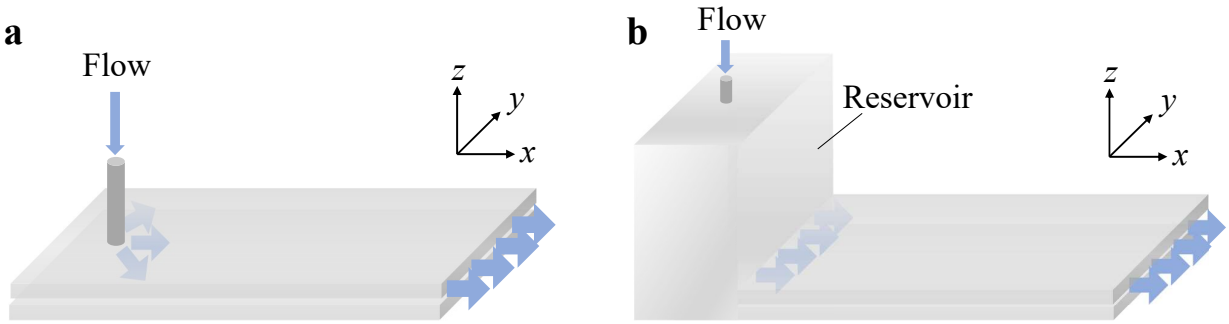

Figure 2.2: **Schematics of microfluidic channels.** (a) The microfluidic channel with an inlet at the centerline of the top glass plate and close to one end of the channel. (b) The microfluidic channel with a uniform flow at the inlet, induced by a reservoir connected to the rectilinear channel. The channel has a thickness of 6.5–26 μm, a length of 50 mm and a width of 15–40 mm.

2.2 Optical techniques

To reveal the director field of nematic liquid crystals, we need to access the out-of-plane polar angle, θ, and the azimuthal angle, φ, of the directors. θ is reflected in the optical retardance, δ, through [70]

$$\delta = |\frac{n_0 n_e}{\sqrt{n_0^2 \cos^2\theta + n_e^2 \sin^2\theta}} - n_0|, \tag{2.1}$$

where n_e and n_o are the extraordinary and ordinary refractive indices.

A crossed polarizer and analyzer are employed to qualitatively identify the director field, as shown in Fig. 2.3. The linear polarized light entering the nematic liquid crystal sample with a thickness b and birefringence $\Delta n = n_\mathrm{e} - n_\mathrm{o}$ is resolved into two rays that propagate at different velocities and recombine at the analyzer. The transmitted intensity of light passing the analyzer is [70]

$$I_{\lambda_w} = \frac{1}{2} {E_0}^2 \sin^2(2\alpha) \sin^2\left(\frac{\pi\delta}{\lambda_w}\right), \tag{2.2}$$

where E_0 is the polarization of the linear polarized light, λ_w is the wavelength of light, and α is the angle between the liquid crystal director and the transmission axis of the polarizer. At fixed α, the transmitted intensity depends only on δ. δ causes destructive interference for certain wavelength of white light, resulting in an interference image [71]. We compare the interference colors with a customized Michel-Lévy color chart (see Chapter 2.3) to determine the optical retardance of the nematic liquid crystals, and therefore the polar angle, θ.

To identify the azimuthal angle, φ, we insert a static full-wave-plate optical compensator (560 nm) between the crossed polarizer and analyzer. The slow axis of the compensator $\vec{\lambda}_\mathrm{g}$ is oriented at 45° to the polarizer. We determine the alignment of the directors in the xy-plane with respect to $\vec{\lambda}_\mathrm{g}$ by comparing the change of retardance before and after insertion of the compensator. An increase in retardance by 560 nm indicates that the director is oriented in the direction perpendicular to $\vec{\lambda}_\mathrm{g}$; a decrease in retardance by 560 nm indicates that the director is oriented in the direction parallel to $\vec{\lambda}_\mathrm{g}$. This can be quantitatively understood by considering the transmitted light intensity of different wavelengths of white light. The

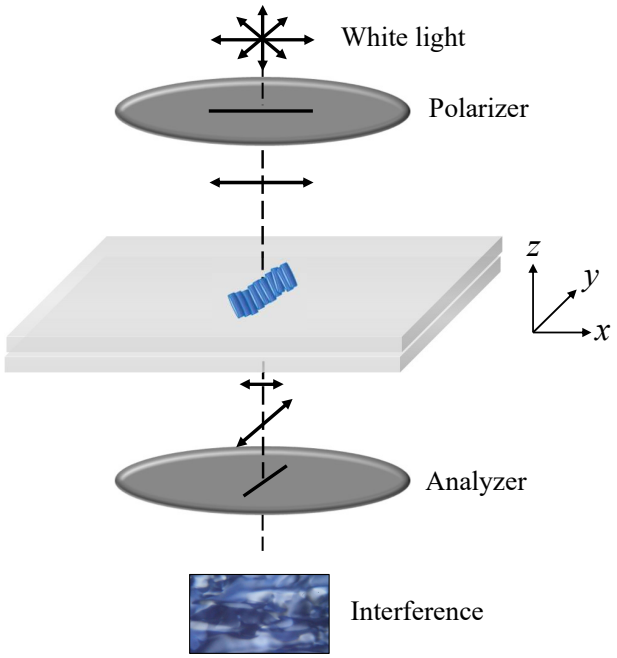

Figure 2.3: **Schematics of the optical setup with crossed polarizer and analyzer**. The arrows represent the polarization of light.

transmitted beam defined by the Stokes vector is calculated as [61]

$$\mathbf{S} = \mathbf{M}_{LP}\left(\pi/2\right) \cdot \mathbf{M}_{\lambda_g}\left(\pi/4\right) \cdot \mathbf{M}_{LC}\left(\varphi\right) \cdot \mathbf{M}_{LP}\left(0\right) \cdot \mathbf{S}_0, \tag{2.3}$$

where $\mathbf{S}_0$ is the Stokes vector of the incident beam with unit intensity and φ is the azimuthal angle between the director and the x-direction. The transformation matrices

$$\mathbf{M}_{LP}\left(0\right) = \frac{1}{2}\begin{pmatrix} 1 & 1 & 0 & 0 \\ 1 & 1 & 0 & 0 \\ 0 & 0 & 0 & 0 \\ 0 & 0 & 0 & 0 \end{pmatrix} \tag{2.4}$$

and

$$\mathbf{M}_{LP}\left(\pi/2\right) = \frac{1}{2}\begin{pmatrix} 1 & -1 & 0 & 0 \\ -1 & 1 & 0 & 0 \\ 0 & 0 & 0 & 0 \\ 0 & 0 & 0 & 0 \end{pmatrix} \tag{2.5}$$

are the Mueller matrices for a linear polarizer with transmission axes that have angles of 0° and 90° with respect to the x-direction.

$$\mathbf{M}_{LC}(\varphi) = \begin{pmatrix} 1 & 0 & 0 & 0 \\ 0 & \cos^2 2\varphi + \sin^2 2\varphi \cos\Gamma & \cos 2\varphi \sin 2\varphi (1 - \cos\Gamma) & \sin 2\varphi \sin\Gamma \\ 0 & \cos 2\varphi \sin 2\varphi (1 - \cos\Gamma) & \cos^2 2\varphi \cos\Gamma + \sin^2 2\varphi & -\cos 2\varphi \sin\Gamma \\ 0 & -\sin 2\varphi \sin\Gamma & \cos 2\varphi \sin\Gamma & \cos\Gamma \end{pmatrix} \tag{2.6}$$

is the Mueller matrix for the nematic liquid crystal sample of thickness b and birefringence Δn, where $\Gamma = 2\pi b \Delta n / \lambda_w$.

$$\mathbf{M}_{\lambda_g}(\pi/4) = \begin{pmatrix} 1 & 0 & 0 & 0 \\ 0 & \cos\left(\frac{2\pi\lambda_g}{\lambda_w}\right) & 0 & \sin\left(\frac{2\pi\lambda_g}{\lambda_w}\right) \\ 0 & 0 & 1 & 0 \\ 0 & -\sin\left(\frac{2\pi\lambda_g}{\lambda_w}\right) & 0 & \cos\left(\frac{2\pi\lambda_g}{\lambda_w}\right) \end{pmatrix} \tag{2.7}$$

is the Mueller matrix for the compensator of wavelength $\lambda_g = 560$ nm, with its optical axis at 45° to the x-direction. The first component of the Stokes vector of the outgoing beam in Eq. 2.3 determines the transmitted light intensity:

$$I(\varphi, \lambda_w) = \frac{1}{2}\left[1 - \left(\cos^2 2\varphi + \cos\Gamma \sin^2 2\varphi\right)\cos\left(\frac{2\pi\lambda_g}{\lambda_w}\right) + \sin 2\varphi \sin\Gamma \sin\left(\frac{2\pi\lambda_g}{\lambda_w}\right)\right]. \tag{2.8}$$

For a given Γ and λ_g, Eq. 2.8 shows that the transmitted light intensity, I, depends on both the azimuthal angle, φ, and the wavelength of light, λ_w. When a beam of white light, where the light spectrum is assumed to be uniform, incidents the system, the wavelength holding the highest transmitted light intensity, $\lambda_{w,max}$, is dominant in the outgoing beam and appears as the corresponding color. $\lambda_{w,max}$ and the corresponding color vary with φ. We can thus identify the azimuthal angle, φ, by assessing the color of the interference image. For example, let us consider a microfluidic channel with $b = 6.5$ μm filled with a liquid crystal solution with $\Delta n = -0.015$ [72]. As a demonstration, we choose three representative wavelengths, 480 nm, 550 nm, 620 nm, in the visible light spectrum (corresponding to blue, green, and orange), and calculate their transmitted intensity at different azimuthal angles

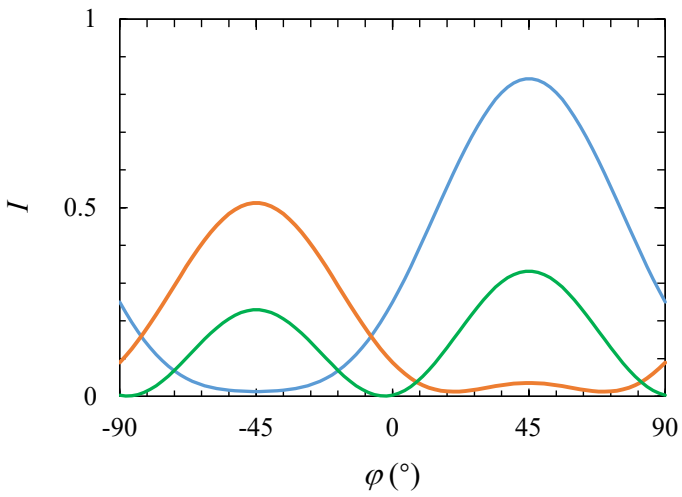

Figure 2.4: **The transmitted light intensity versus the azimuthal angle, φ.** The transmitted light intensity, I, at different wavelengths (λ_w = 480 nm (blue line), λ_w = 550 nm (green line), λ_w = 620 nm (orange line)) transmitted through the setup with crossed polarizer and analyzer compensated with the full-wave-plate optical compensator and the LC sample.

based on Eq. 2.8. The results are shown in Fig. 2.4. The maximum intensity at $\varphi = -45^\circ$ is found for the blue color, whereas the maximum intensity at $\varphi = 45^\circ$ is found for the orange color. This indicates that when the director is oriented parallel to the slow axis of the compensator, the image appears orange. From the Michel-Lévy color chart, we see that orange corresponds to a retardance of $\sim$ 460 nm. We further know that the retardance before the compensator is inserted is approximately 98 nm. The retardance thus decreases by 560 nm, which indicates that the director is oriented parallel to the slow axis of the compensator. In contrast, when the director is oriented perpendicular to the slow axis of the compensator, the image appears blue ($\sim$ 658 nm), which corresponds to an increase of the retardance by 560 nm. As a result, we can estimate the azimuthal angle by assessing the change of retardance upon insertion of the static optical compensator.

We visualize the structures forming in flowing nematic liquid crystals and image their dynamics using a LUMIX GH5 camera at frame rates up to 60 fps, and a high-speed camera (Chronos 1.4) at frame rates of 1069 fps.

2.3 Customized Michel-Lévy color chart

We customize the Michel-Lévy color chart by measuring the transmitted spectrum of a light-emitting diode (LED, Tiktecklab) through the Hele-Shaw cell using a spectroscope (Maya2000 Prob Series, Ocean Insight). The normalized transmitted light intensity D at different wavelengths λ_w is shown in Fig. 2.5(a).

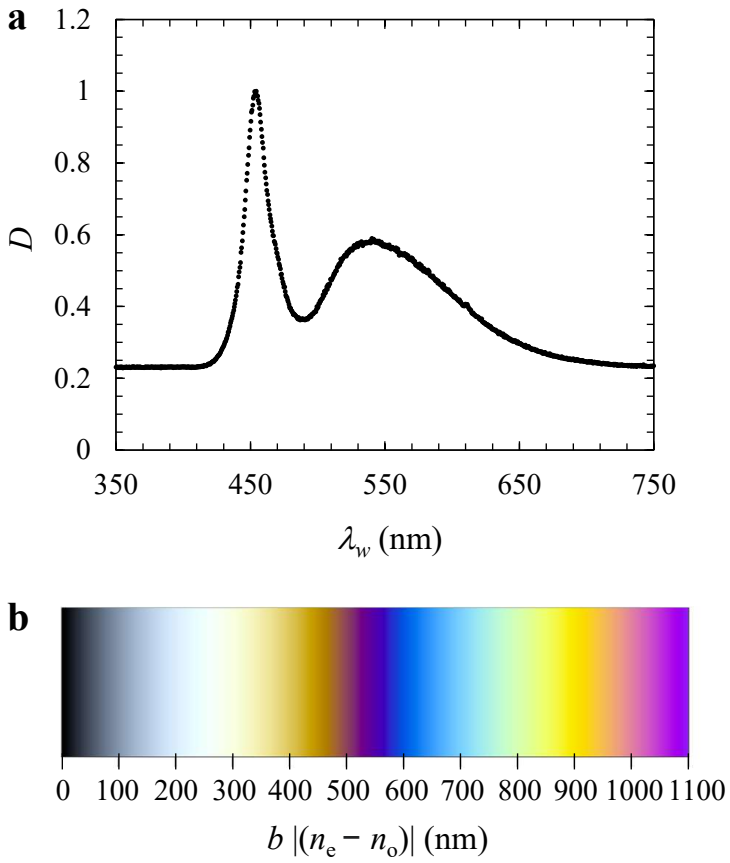

Figure 2.5: **Customized Michel-Lévy color chart.** (a) Transmitted spectrum of a light-emitting diode through the Hele-Shaw cell. (b) Customized Michel-Lévy color chart.

For a given wavelength λ_w of light passing through a liquid crystal sample placed between a crossed polarizer and analyzer, the transmission T is expressed as [73]

$$T = \sin^2(\frac{\pi}{\lambda_w} b|n_\mathrm{e} - n_\mathrm{o}|)\sin^2(2\alpha), \tag{2.9}$$

where n_e and n_o are the extraordinary and ordinary refractive indices of the liquid crystal, b is the plate spacing of the Hele-Shaw cell, and α is the angle between the liquid crystal

director and the transmission axis of the polarizer. By fixing α, Eq. 2.9 gives a spectral transmission matrix, $\mathbf{I}_{\lambda_\mathbf{w}}$, for the visible range. We convert $\mathbf{I}_{\lambda_\mathbf{w}}$ to human vision colors using the CIE 1931 color matching functions ($\vec{r}$, $\vec{g}$, and $\vec{b}$ describe the sensitivity of the human eye to red, green and blue) and considering the spectrum measured in our experimental system:

$$\begin{bmatrix} \vec{X} \\ \vec{Y} \\ \vec{Z} \end{bmatrix} = \begin{bmatrix} \vec{D} \odot \vec{r} \\ \vec{D} \odot \vec{g} \\ \vec{D} \odot \vec{b} \end{bmatrix} \mathbf{I}_{\lambda_\mathbf{w}}, \tag{2.10}$$

where $\vec{X}, \vec{Y}, \vec{Z}$ are the human vision color coordinates. $\odot$ is the Hadamard product. Eq. 2.10 is then transformed to RGB format used by digital devices employing the matrix of Adobe RGB MRGB, following the method reported in [73]. The output is the Michel-Lévy color chart shown in Fig. 2.5(b).

2.4 Single-shot quantitative polarization imaging of complex birefringent structure dynamics

Polarized shearing interference microscopy (PSIM), developed by our collaborators in the So Lab at MIT, is a single-shot quantitative polarization imaging method for extracting the retardance and orientation angle of the laser beam transmitting through optically anisotropic specimens with complex structures. We employ PSIM to quantify the dynamics of a flowing lyotropic chromonic liquid crystal in a microfluidic channel at an imaging speed of 506 frames per second (only limited by the camera frame rate), with a field-of-view of up to $350 \times 350 \mu\text{m}^2$ and a diffraction-limit spatial resolution of $\approx 2\text{m}^2$.

2.4.1 Polarized shearing interference microscopy (PSIM)

A supercontinuum laser (Fianium SC-400) generates a broadband, spatially uniform illumination beam that is coupled to a single-mode optical fiber, as shown in Fig. 2.6. The beam is collimated and transmits through a bandpass filter centered at 633 nm with 10 nm bandwidth. A linear polarizer (LP1) and a quarter wave plate (QWP1) are crossed at an

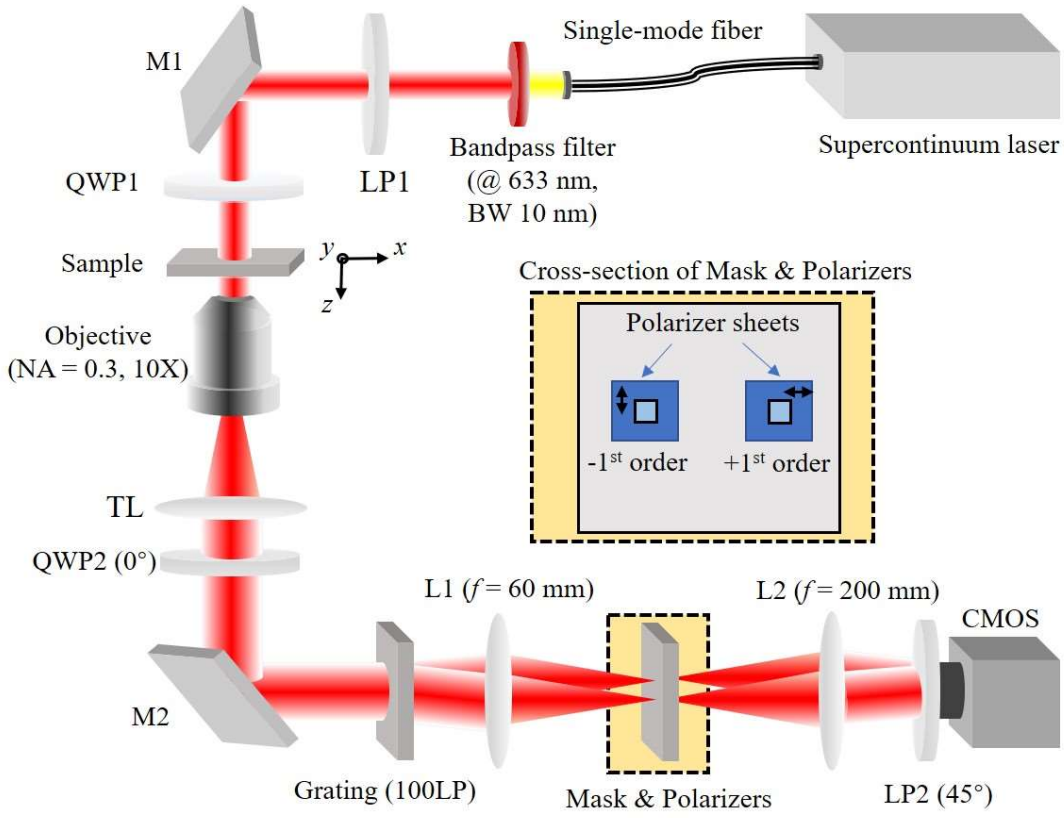

Figure 2.6: **System design of polarized shearing interference microscopy.** LP1, LP2, linear polarizers; M1, M2, mirrors; QWP1, QWP2, quarter wave plates; TL, tube lens; L1, L2, lenses. The z-axis is the direction of the optical axis, and the xy-plane is the sample plane. The zoomed region denotes the location of the masks and polarizer sheets on the Fourier plane.

angle of 45° to generate a circularly polarized illumination. The scattered light is collected by an objective (Olympus UPLFLN10X2, NA = 0.3, 10X) and collimated by a tube lens (TL). The beam, which bears the polarization information of the sample, transmits through another quarter wave plate (QWP2) and then is separated into multiple orders by a 100 line-pair per millimeter (LP) diffraction grating. The grating is positioned at the conjugated plane of the sample plane. A 4f system is positioned after the diffraction grating to relay the beams. On the Fourier plane, a mask is placed that lets only the $+1^{\text{st}}$ order and -1^{st} order beams pass. Two polarizer sheets are placed on the mask: For the $+1^{\text{st}}$ order, the direction of the polarization sheet is 45° to the slow axis of QWP2, for the -1^{st} order, the direction of the polarization sheet is −45° to the slow axis of QWP2. Another linear polarizer (LP2)

with polarization direction 45° to both polarizer sheets is placed in front of the camera to produce interference between the two orders. The interferogram is recorded by a CMOS camera (Optronics CP80-4-M-500, full frame 2304×1720 pixels, pixel size $7 \times 7 \mu m^2$), whose maximum frame rate is 506 frames per second (fps). The imaging speed of PSIM is limited only by the camera frame rate.

2.4.2 Derivation of the Polarization retrieval algorithm

We have developed a new algorithm based on digital holography to quantitatively retrieve the 2D polarization parameters of birefringent samples. In particular, we extract the retardance map from the amplitude of the retrieved complex field, and the orientation angle from the phase. The algorithm for retrieving the retardance and the orientation angle is derived with Jones calculus. The Jones matrix of the sample is:

$$\begin{aligned} J_{sample} &= \begin{pmatrix} \cos\varphi & \sin\varphi \\ -\sin\varphi & \cos\varphi \end{pmatrix} \begin{pmatrix} e^{j\phi_e} & 0 \\ 0 & e^{j\phi_o} \end{pmatrix} \begin{pmatrix} \cos\varphi & -\sin\varphi \\ \sin\varphi & \cos\varphi \end{pmatrix} \\ &= \begin{pmatrix} e^{i\phi_e}\cos^2\varphi + e^{i\phi_o}\sin^2\varphi & -\left(e^{i\phi_e} - e^{i\phi_o}\right)\sin\varphi\cos\varphi \\ -\left(e^{i\phi_e} - e^{i\phi_o}\right)\sin\varphi\cos\varphi & e^{i\phi_e}\sin^2\varphi + e^{i\phi_o}\cos^2\varphi \end{pmatrix}, \end{aligned} \tag{2.11}$$

where ϕ_e is the phase delay in the extraordinary axis of the birefringent sample, ϕ_o is the phase delay in the ordinary axis, and φ is the orientation angle. The retardance Δ is the difference between the phase delay in the extraordinary axis and that in the ordinary axis, $\Delta = \phi_e - \phi_o$. These parameters are mapped in real space, and the notations for Cartesian coordinates (x, y) are omitted for clarity. We utilize a linear polarizer (LP1) and a quarter wave plate (QWP1) to generate a left-handed circular polarization illumination:

$$E_{in} = \frac{1}{\sqrt{2}} \begin{pmatrix} 1 \\ i \end{pmatrix}. \tag{2.12}$$

After the beam is transmitted through the sample, the scattered light is collected by an objective and passes through another quarter wave plate (QWP2). The output field is:

$$\begin{aligned} E_{out} &= e^{i\frac{\pi}{4}} \begin{pmatrix} 1 & 0 \\ 0 & i \end{pmatrix} J_{sample} E_{in} \\ &= \tfrac{1}{\sqrt{2}} e^{i\frac{\pi}{4}} \begin{pmatrix} e^{i\phi_e}\left(\cos^2\varphi - i\sin\varphi\cos\varphi\right) + e^{i\phi_o}\left(\sin^2\varphi + i\sin\varphi\cos\varphi\right) \\ e^{i\phi_e}\left(-\sin^2\varphi - i\sin\varphi\cos\varphi\right) + e^{i\phi_o}\left(-\cos^2\varphi + i\sin\varphi\cos\varphi\right) \end{pmatrix}. \end{aligned} \tag{2.13}$$

Subsequently, the light is separated by a diffraction grating. Only the $+1$ and -1 orders of the light pass through the Fourier plane. After a polarizer with orientation direction of 45° to the slow axis of QWP2, an output field is produced:

$$E_{out,45^\circ} = \frac{1}{2} e^{i\frac{\pi}{4}} \left(e^{i\phi_e} - e^{i\phi_o}\right) \exp\left(-i2\varphi\right) = \sin\frac{\Delta}{2} \exp\left[i\left(\frac{\phi_e + \phi_o}{2} - 2\varphi + \frac{3\pi}{4}\right)\right]. \tag{2.14}$$

Note that the retardance is only contained in the amplitude part and the orientation angle is only contained in the phase part. However, the presence of an average phase delay $\frac{\phi_e+\phi_o}{2}$ prevents the retrieval of the orientation angle. The output electric field for a linear polarizer set to -45° to the slow axis of QWP2 is expressed as:

$$E_{out,-45^\circ} = \frac{1}{2} e^{i\frac{\pi}{4}} \left(e^{i\phi_e} + e^{i\phi_o}\right) = \cos\frac{\Delta}{2} \exp\left[i\left(\frac{\phi_e + \phi_o}{2} + \frac{\pi}{4}\right)\right]. \tag{2.15}$$

The orientation angle contained in the phase part disappears and only the average phase delay remains. This offers a strategy to cancel out the average phase delay. Two perpendicularly oriented polarizers are placed on the Fourier plane to generate these two output fields simultaneously: one is in the $+1^{\text{st}}$, the other is in the -1^{st} order:

$$E_{+1} = \sin\frac{\Delta}{2} \exp\left[i\left(\frac{\phi_e + \phi_o}{2} - 2\varphi + \frac{3\pi}{4} + \frac{kx}{2}\right)\right], \tag{2.16}$$

and

$$E_{-1} = \cos\frac{\Delta}{2} \exp\left[i\left(\frac{\phi_e + \phi_o}{2} + \frac{\pi}{4} - \frac{kx}{2}\right)\right]. \tag{2.17}$$

kx denotes the spatial modulation caused by the separation of the diffraction grating. A second polarizer (LP2) with orientation 45° to both polarizers on the Fourier plane is used to produce interference, and an interferogram is recorded by a CMOS camera:

$$\begin{aligned} I &= \langle (E_{+1} + E_{-1})\,(E_{+1} + E_{-1})\,* \rangle \\ &= |E_{+1}|^2 + |E_{-1}|^2 + \langle E_{+1}E_{-1}^* \rangle + \langle E_{-1}E_{+1}^* \rangle \\ &= \sin^2\tfrac{\Delta}{2} + \cos^2\tfrac{\Delta}{2} + 2\sin\tfrac{\Delta}{2}\cos\tfrac{\Delta}{2}\cos\left[\left(\tfrac{\phi_e+\phi_o}{2} - 2\varphi + \tfrac{3\pi}{4}\right) - \left(\tfrac{\phi_e+\phi_o}{2} + \tfrac{\pi}{4}\right) + kx\right] \\ &= 1 + \sin\Delta\sin\left(2\varphi - kx\right). \end{aligned} \tag{2.18}$$

By recording the interferogram, I, the complex field from the 1st order signal, *i.e.*, the alternating current (AC) term, and the 0 order signal, *i.e.*, the direct current (DC) term, can be retrieved. Recovering the 0 and 1st order signals allows us to calculate the retardance map and orientation angle distribution [74].

As a demonstration of this algorithm, we recover the polarization parameters of a crystallized Orange II fiber from its interferogram, as shown in Fig. 2.7(a). The Orange II (Sigma-Aldrich) aqueous solutions with weight concentration $c = 35.0$ wt% are prepared in the nematic phase. In the interferogram, fringes appear only in regions with high birefringence. We perform a two-dimensional Fourier transform to the interferogram and show the logarithm of the 2D spectrum in decibel (dB), as shown in Fig. 2.7(b), which reveals three orders on the Fourier domain (-1^{st}, 0, $+1^{\text{st}}$ order). By extracting the $+1^{\text{st}}$ order with a circular linear filter and shifting it to the center of the Fourier plane, we can map the amplitude E and the phase ϕ of the light field after an inverse Fourier transform. The 0 order gives access to the amplitude of the DC term A in the Fourier domain. The retardance Δ can be calculated as [74]

$$\Delta = \sin^{-1}\left(\frac{2E}{A}\right), \tag{2.19}$$

and the distribution of the orientation angle φ is calculated as [74]

$$\varphi = \frac{1}{2}\phi. \tag{2.20}$$

The retardance Δ and the orientation angle distribution φ are decoupled into the measured

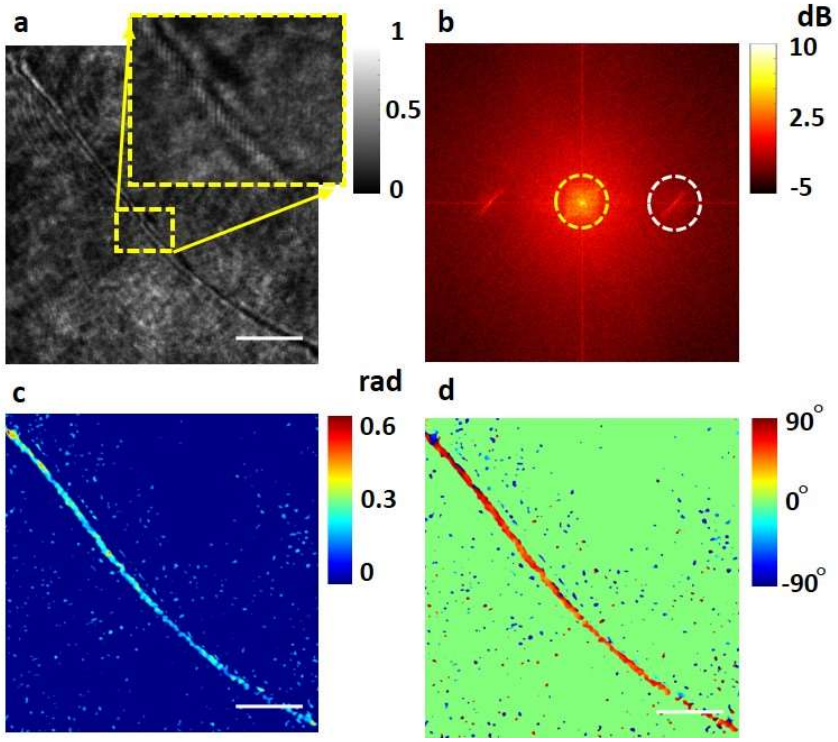

Figure 2.7: **Demonstration of the polarization parameter retrieval algorithm.** (a) Interferogram of a crystal fiber sample. The zoomed region denotes the fiber region with a high birefringence signal. (b) Logarithm map of the Fourier domain of (a), reported in decibel (dB), where the 0 and $+1^{\text{st}}$ orders are labeled with yellow and white circles, respectively. (c) Quantitative map of the retardance distribution. (d) Quantitative map of the orientation angle distribution. The scale bar denotes 20 μm.

amplitude E and the measured phase ϕ, respectively, as shown in Fig. 2.7(c) and (d). Details of the derivations of Eq. 2.19 and Eq. 2.20 can be found in [74].

Chapter 3

Growth morphology and symmetry selection of interfacial instabilities in anisotropic environments

This chapter is based on Ref. [63].

Pattern growth is ubiquitous in nature and leads to the formation of complex structures [1, 75, 76]. Many interfacial patterns can be grouped into two 'essential shapes' or morphologies: isotropic dense-branching growth and anisotropic dendritic growth. Dense-branching growth arises from repeated tip-splitting of the structures and leads to a ramified pattern with many branches [2, 3], controlled by the gradient-driven transport of mass, heat or charge to the interface. In contrast, anisotropic dendritic growth is characterized by protrusions that are stable towards tip-splitting and leads to more regular patterns with global symmetries [4–9]. Here, we show that dendritic patterns – with tunable symmetry – can arise when the growth occurs in anisotropic environments.

The phenomenon of viscous fingering has played an important role in elucidating the basic principles of these two types of growth [12–15], as well as methods to control the resulting patterns [77–88]. Viscous fingers result from the Saffman-Taylor instability, when one fluid is displaced by another less viscous one in the quasi-two dimensional geometry of a

Hele-Shaw cell [16, 17]. It has been shown that dendritic growth requires anisotropy in the interfacial dynamics [5, 18–20]. In its absence, dense branching is instead the generic mode of growth [13]. Anisotropy fixes the tip of an advancing interface into a stable parabolic shape that prevents it from splitting [5, 21, 89, 90] and introduces global symmetries along preferred growth directions, which are also seen in discrete models of diffusion-limited aggregation on crystal lattices [91–93]. Experimentally, anisotropy can be introduced either externally in the growth environment or internally in one of the fluids. External anisotropy can be imposed by engraving ordered channels on one of the plates of a Hele-Shaw cell, by using channels confined with elastic membranes or by placing air bubbles at the tips of growing fingers [18, 21–26]. Internal anisotropy can be induced by replacing one of the fluids with a liquid crystal in the nematic phase [27].

Previous studies have considered a particular limit of the viscous-fingering instability; the limit where the viscosity ratio between the less-viscous inner fluid and the more-viscous outer fluid, $\eta_{\text{in}}/\eta_{\text{out}}$, is very low, which is typically the case when air or water displace a viscous liquid. The patterns are then characterized by one single growing length scale, the finger length. Under these conditions, experiments using a Hele-Shaw cell with engraved ordered channels have identified the degree of anisotropy, defined as the ratio between the channel height h and the plate spacing b, h/b, as a control parameter for the morphology transition from dense-branching to dendritic growth [18]; dendritic structures form beyond a critical value of h/b. When the two fluids are miscible, the degree of anisotropy is the only control parameter for the morphology transition. In the case of two immiscible fluids, the capillary number sets the critical h/b for the transition [19, 94]. For miscible fluids and for immiscible fluids at high capillary number, the dendrites directly reflect the underlying symmetry of the lattice; four-fold symmetric dendrites grow in a four-fold symmetric lattice, six-fold symmetric dendrites grow in a six-fold symmetric lattice [8]. Dendrites grow in the direction of the channels, which are the regions of largest effective plate spacing within which the flow velocity is highest [18, 19].

We here reveal how a previously unexplored control parameter, the ratio of the viscosities of the inner and the outer fluid, $\eta_{\text{in}}/\eta_{\text{out}}$, modifies both the morphology transition and, remarkably, the symmetry of the dendritic structures in miscible fluids in anisotropic envi-

ronments. Recent studies in isotropic environments have identified the viscosity ratio as an important control parameter that governs not only the onset of the instability [29, 95–98], but also the global features of the patterns introducing a second length scale, the radius of a central region of complete outer-fluid displacement that grows concomitantly with the fingers [29, 99–101]. This central region becomes increasingly larger, and therefore the relative length of the fingers increasingly smaller, as the viscosity ratio between the two fluids increases. Here we show that a morphology transition from dense-branching to dendritic growth can occur over a large range of viscosity ratios. We engrave channels creating a six-fold symmetric lattice on one of the plates and show that the critical degree of anisotropy, h/b, required for the transition to dendritic growth depends on the viscosity ratio between the two liquids. Remarkably, the dendrites can adopt a rich variety of emergent structures: they exhibit six-fold symmetric growth far from the morphology boundary and systematically transition towards twelve-fold symmetric structures as the boundary is approached. Our study reveals novel ways to tune both the morphology transition and the symmetry of dendritic patterns by either controlling the viscosity ratio between the two fluids or the geometric features of the growth environment.

3.1 Methods

3.1.1 Experimental methods

Our experiments are performed in a radial Hele-Shaw cell consisting of two 19 mm thick circular glass plates of diameter 280 mm. Six-fold symmetric lattices of diameter 145 mm are engraved on acrylic plates with a laser cutter (Universal Laser Systems) and placed on the bottom glass plate of the Hele-Shaw cell. The width of the lattice channels w and the distance between the edges of two channels d are fixed to $w = 800$ μm and $d = 850$ μm (Fig. 3.1a). Four channel depths h of 10 μm, 28 μm, 50 μm, and 250 μm are used. The plate spacing between the engraved acrylic plate and the top glass plate, b, is maintained by six spacers around the perimeter and varies from 125 μm to 1350 μm. The ratio between the height of the channel and the plate spacing, h/b, defines the degree of anisotropy.

The miscible fluids used in our study are glycerol (PTI Process Chemicals) and water (VWR). We tune the viscosity of the inner fluid by mixing glycerol and water in different proportions and we use pure glycerol as the outer fluid. The composition of the water-glycerol mixtures used in the experiments, and the values of the viscosity ratios $\eta_{\text{in}}/\eta_{\text{out}}$, the viscosities of the inner fluids η_{in} and the viscosities of the outer fluids η_{out} are shown in Table 3.1. The flow rate q, the channel depth h, the plate spacing b and the viscosity ratio $\eta_{\text{in}}/\eta_{\text{out}}$ for each experiment are reported in Table 3.2.

Table 3.1: Composition and viscosities of the water-glycerol mixtures

c_{glycerol} (wt%)	$\eta_{\text{in}}/\eta_{\text{out}}$	η_{in} (Pa s)	η_{out} (Pa s)
0	0.0011	0.0013	1.176
12.3	0.0013	0.0015	1.176
39.1	0.0025	0.0029	1.176
52.9	0.005	0.0059	1.176
59.6	0.0075	0.0088	1.176
63.4	0.0125	0.0147	1.176
72.4	0.0234	0.0275	1.176
76.6	0.03	0.0351	1.176
79	0.04	0.0468	1.176
81.3	0.05	0.0592	1.176
84.4	0.068	0.08	1.176
86.8	0.1	0.118	1.176
89.9	0.157	0.185	1.176

The fluids are injected through a 2 mm diameter hole in the center of one of the plates at a precise volumetric flow rate set by a syringe pump (Harvard PHD 2000). We use flow rates of 1 ml/min and 10 ml/min, which allows us to probe an order of magnitude difference in flow rate while staying in the high Péclet number regime (Pe = Ub/D_{12}, where U is the fingertip velocity and D_{12} is the inter-diffusion coefficient [81]), here ranging between 2100 – 45240. Within this regime, the inter-diffusion of the fluids is negligible so that the fluids remain separated by a well-defined interface [81]. The patterns are recorded with either a Point Grey camera (Grasshopper 3 GS3-U3-91S6M) at frame rates up to 9 fps or a LUMIX GH5 camera at frame rates up to 60 fps.

Table 3.2: Flow rates, channel depths, plate spacings, and viscosity ratios used in the experiments

		q = 1 ml/min						q = 10 ml/min	
h (μm)	η_{in}/η_{out}	b (μm)	b (μm)	b (μm)	b (μm)	b (μm)	b (μm)	b (μm)	b (μm)
10	0.0013	254							
28	0.0013	762	508	254	203	127		762	
	0.0025							762	
	0.03	762	508	254	127				
	0.005							508	
	0.068	762						508	
50	0.0011	508	254						
	0.0013	1000	762	508	127	100	55	762	508
	0.0025	1000	508	254					
	0.005	1000	508	254					
	0.0075	508	254						
	0.0125	1000	508	254				762	
	0.0234	1000	762	508	203				
	0.03	254							
	0.05	1000	762	508	254	203			
	0.068	1350	375	254				508	
250	0.0013	1000	762	508	254	127		508	
	0.0025	508	254						
	0.005	762	508	254					
	0.0075	762							
	0.0125	762	508	254				508	
	0.0234	762	508	203				508	
	0.03	508	254						
	0.04	508	762					508	
	0.05	508	508	254				508	
	0.068	508						508	
	0.1	508	762						
	0.157	508							

3.1.2 Numerical simulations

We complement the experiments with two-dimensional (2D) high-resolution numerical simulations using the finite element software COMSOL Multiphysics (v5.4), which allows us to access the pressure distribution in the fluids. Our model replicates the geometry of the Hele-Shaw cell in terms of the cell diameter and the six-fold symmetric lattice dimensions. The lowest viscosity ratio we can access in our simulations ($\eta_{in}/\eta_{out} = 0.006$) is slightly higher than that probed in experiments ($\eta_{in}/\eta_{out} = 0.0011$), as for very low η_{in}/η_{out} the fingertip velocity becomes too fast compared to the mean flow velocity, which results in numerically

unstable solutions. This is a known issue for a number of numerical approaches [102], but one that could be overcome by designing numerical schemes suited for low viscosity ratios [103]. It, however, does not prevent us from accessing the full range of patterns observed in the experiments.

We employ the finite element method to solve the partial differential equations. We couple the convection-diffusion mass-transport equation from the *Transport of Diluted Species* Module with the continuity equation for the single-phase, incompressible flow velocity from the *Darcy's Law* Module. The governing equations are:

$$\frac{\partial c}{\partial t} + \nabla \cdot (-D\nabla c + c\mathbf{u}) = 0 \tag{3.1}$$

$$\mathbf{u} = -\frac{k}{\eta}\nabla p \tag{3.2}$$

$$\nabla \cdot \mathbf{u} = 0 \tag{3.3}$$

where c is the concentration of the inner fluid and D the molecular diffusion coefficient. The latter is chosen as $D = 10^{-14}$ m^2/s given the high Péclet numbers of the experiments. We note that the pattern morphology remains independent of D for $D < 10^{-8}$ m^2/s, confirming that our simulations are in the high Péclet number regime (see Appendix 3.A.1 for further details). ∇ is the in-plane gradient operator, $\mathbf{u}$ is the Darcy velocity set by the pressure gradient ∇p, and k and η are the permeability and viscosity of the fluids, respectively.

The flow in a Hele-Shaw cell can be approximated as quasi-2D as the plate spacing, b, is much smaller than the radial dimension. The gap-averaged velocity of the fluids is then $\mathbf{u} = -\frac{b_i^2}{12\eta}\nabla p$ with $k = {b_i}^2/12$, where b_i describes the gap thickness at any point of the textured surface. The spatial variability in the plate spacing is incorporated in the numerical model by defining a binary spatial distribution of permeability [L^2], consisting of a permeability value for the obstacles (assigned to the triangles forming the lattice cells), denoted as k_1, and a permeability value for the channels (assigned to the background domain), denoted as k_2. The ratio between the two permeabilities, k_2/k_1, is $(1 + h/b)^2$. We use an exponential

mixing rule for the mixture viscosity η and $\eta = \eta_{\text{out}} e^{-Mc}$, where η_{out} is the viscosity of the outer fluid and $\eta_{\text{in}}/\eta_{\text{out}} = e^{-M}$. For miscible fluids, both the pressure and the normal velocity are continuous at the interface. We define a small circular inlet region around the cell center which provides a smooth boundary, to avoid a point-source injection that could lead to a singularity in the domain. A normal inflow velocity for flow and a Dirichlet boundary condition ($c = 1$) for transport are applied at the perimeter of the circular inlet region, and atmospheric pressure (open-flow) condition for flow and an outflow condition ($\mathbf{n} \cdot D\nabla c = 0$) for transport are imposed on the outer cell boundary. The initial conditions in the entire domain are $c = 0$ and $p = 0$. The absolute values of the injection velocity and the permeability within the computational domain differ from those in experiments. This does not affect the resulting patterns, as only the ratio of the permeabilities ($\sim h/b$) governs the pattern morphology.

We solve for pressure and concentration fields in a fully coupled approach using the Parallel Direct Sparse Solver Interface (PARDISO) and Newton's method with dynamic damping for highly nonlinear systems. The implicit Generalized-α Method is used for the time stepping scheme [104, 105]. We use the default discretization settings that govern the order of discretization in the shape functions for the dependent variables of each module: first-order discretization for the convection-diffusion equation and second-order discretization for Darcy's law, as these settings work efficiently and robustly. The optimal mesh resolution is found with these discretization orders. The annular mesh area used is 0.00606 m^2 discretized by 222,162 triangular elements. We have confirmed the numerical validity and convergence of our simulations (see Appendix 3.A.2). The discretization by a triangular mesh provides a source of perturbation sufficient for the instability to occur; the apparent slight asymmetry of the computed patterns is mesh driven due to the spatial non-uniformity of the perturbation and the triangularization of the domain.

3.2 Results

3.2.1 Morphology transitions in an anisotropic Hele-Shaw cell

We investigate the growth of patterns in anisotropic environments by engraving channels creating a six-fold symmetric lattice on one of the Hele-Shaw plates, as shown in Fig. 3.1a. We use pairs of miscible fluids with different ratios of viscosities between the less-viscous inner fluid and the more-viscous outer fluid, $\eta_{\rm in}/\eta_{\rm out}$. The use of miscible fluids allows us to investigate the role of viscosity ratio without concurrently varying the capillary number.

In agreement with previous studies at very low viscosity ratios and high capillary numbers, we find that the morphology transition from dense-branching growth to dendritic growth

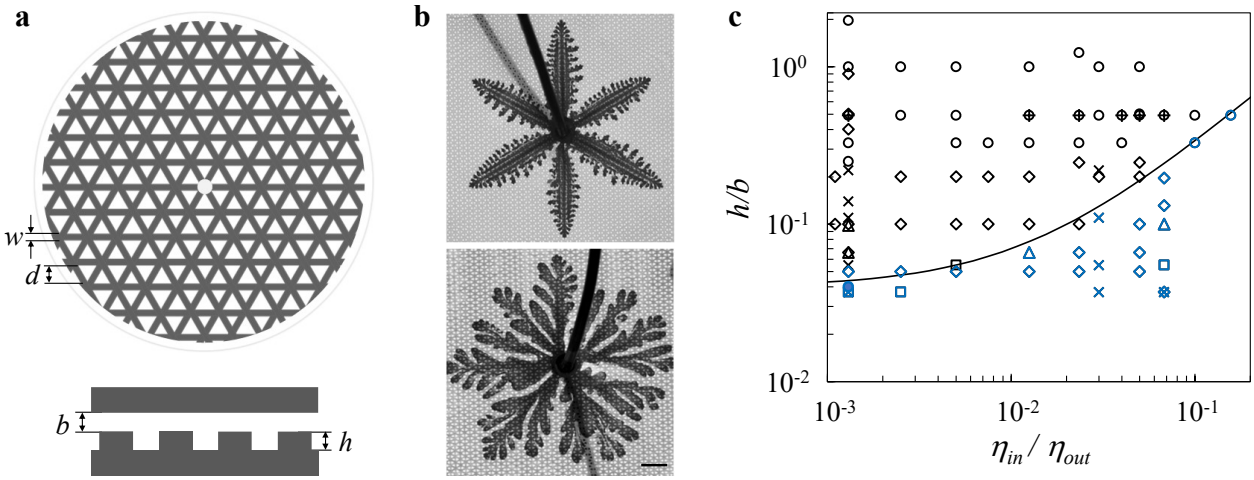

Figure 3.1: (a) Schematic of the modified Hele-Shaw cell. Top image: top view of the bottom plate of the Hele-Shaw cell with an engraved six-fold symmetric lattice, with width of the lattice channels w and distance between the edges of two channels d. Bottom image: side view of the modified Hele-Shaw cell, denoting the plate spacing b and the channel height h. (b) Examples of dendritic growth (top, for $h/b = 0.5$, $h = 50$ μm, $b = 100$ μm) and dense-branching growth (bottom, for $h/b = 0.04$, $h = 10$ μm, $b = 254$ μm) at low viscosity ratio $\eta_{\rm in}/\eta_{\rm out} = 0.0013$. The scale bar is 1 cm. (c) Morphology diagram controlled by the viscosity ratio $\eta_{\rm in}/\eta_{\rm out}$ and the degree of anisotropy h/b. Blue symbols denote dense-branching growth, black symbols denote dendritic growth. Experiments are performed with engraved plates with different channel heights h and plate spacings b and at different volumetric flow rates q. ($\triangledown$) $h = 10$ μm, $q = 1$ml/min; ($\times$) $h = 28$ μm, $q = 1$ml/min; ($\square$) $h = 28$ μm, $q = 10$ ml/min; ($\diamond$) $h = 50$ μm, $q = 1$ ml/min; ($\triangle$) $h = 50$ μm, $q = 10$ ml/min; ($\circ$) $h = 250$ μm, $q = 1$ml/min; ($+$) $h = 250$ μm, $q = 10$ ml/min. The value of b for each experiment is listed in Table 3.2. The solid line denotes a fit to $(h/b - (h/b)^*)$ / $(\eta_{\rm in}/\eta_{\rm out}) = A$ ($A = 3$ and $(h/b)^* = 0.04$ are best-fit parameters).

occurs above a value of $h/b \approx 0.05$ [18, 94] for our lowest η_{in}/η_{out}. Below this value, fingers grow by repeated tip-splitting which results in dense-branching growth, above this value, the fingertip is stabilized which results in dendritic growth, as shown in Fig. 3.1b. Remarkably though, this critical h/b depends strongly on the viscosity ratio: as η_{in}/η_{out} increases, a larger h/b is needed to transition from dense-branching growth to dendritic growth, as shown in Fig. 3.1c. We find that neither the absolute values of the channel height h and the plate spacing b, nor the volumetric flow rate are control parameters for the morphology transition, as shown by the different symbols in Fig. 3.1c, which denote experiments performed with plates of various channel heights h ranging from 10 μm to 250 μm, various plate spacings b ranging from 125 μm to 1350 μm, and at two volumetric flow rates of 1 ml/min and 10 ml/min. For a given viscosity ratio, any combination of h and b yielding a certain value of h/b leads to the same growth morphology.

3.2.2 Dendritic growth adopts different symmetries

The viscosity ratio η_{in}/η_{out} and the degree of anisotropy h/b not only determine the morphology boundary, but have a more dramatic effect on the pattern growth in the dendritic regime. For a fixed h/b, an increase in the viscosity ratio η_{in}/η_{out} leads to a systematic change in the pattern symmetry. Remarkably, the imposed six-fold symmetry of the engraved plate leads to six-fold symmetric growth only at the lowest viscosity ratio. At higher viscosity ratios, the pattern instead transitions towards a twelve-fold symmetry; in addition to the six main dendrites evolving along the straight channels, additional six sub dendrites emerge at a 30° angle to the preferred growth direction, as shown in Fig. 3.2a. The length of the sub dendrites becomes larger with increasing viscosity ratio and eventually comparable to that of the main dendrites. A similar trend is recovered in the simulations, as shown in Fig. 3.2b. A transition from six- towards twelve-fold symmetry also occurs for a fixed η_{in}/η_{out} with a decrease in h/b, as shown in Fig. 3.3 for $\eta_{in}/\eta_{out} = 0.0125$ and a flow rate of 1 ml/min. Previous studies in the limit of low viscosity ratios have seen hints towards the onset of these additional sub dendrites [106–108]. Here we show their systematic growth and that they can become comparable in size to the main dendrites within a certain range of viscosity ratio and h/b.

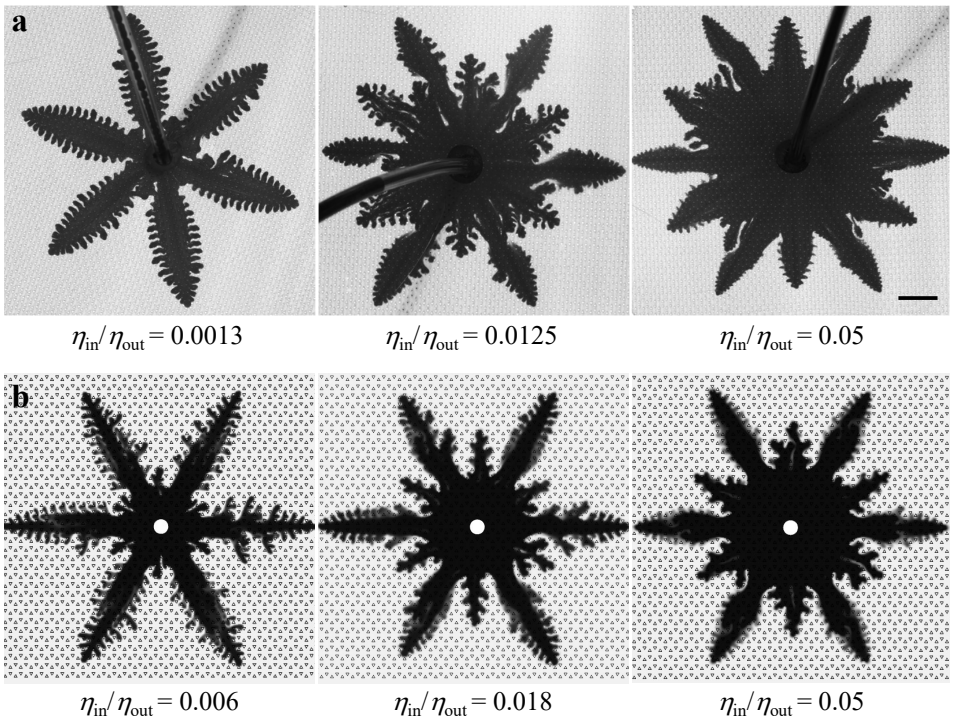

Figure 3.2: Systematic change from six- towards twelve-fold symmetric dendrites. (a) Dendritic patterns for different viscosity ratios obtained at $h/b = 0.49$. As $\eta_{\rm in}/\eta_{\rm out}$ increases, the additional generation of sub dendrites grows progressively larger. The scale bar is 1 cm. (b) Snapshots of the simulations at $h/b = 0.49$.

To quantify the change from six- towards twelve-fold symmetry, we define the length of the main dendrites, $R_{\rm m}$, corresponding to the structures growing in the direction of the six straight channels, and the length of the sub dendrites, $R_{\rm s}$, corresponding to the structures growing at an angle of 30° with respect to the six straight channels, as shown in the inset of Fig. 3.4b. The ratio $R_{\rm s}/R_{\rm m}$ exhibits a transient regime at early times and then remains

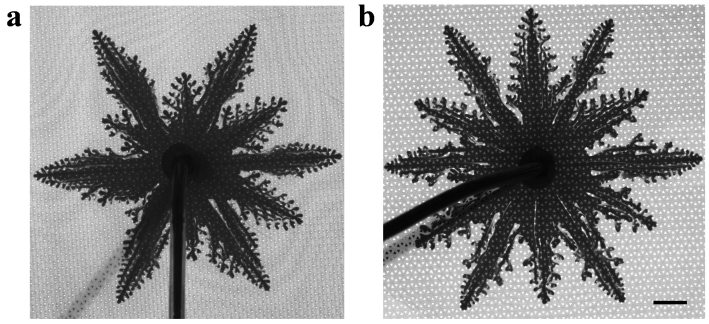

Figure 3.3: Dendritic patterns formed at $\eta_{\rm in}/\eta_{\rm out} = 0.0125$ for (a) $h/b = 1$ and (b) $h/b = 0.2$. The scale bar is 1 cm.

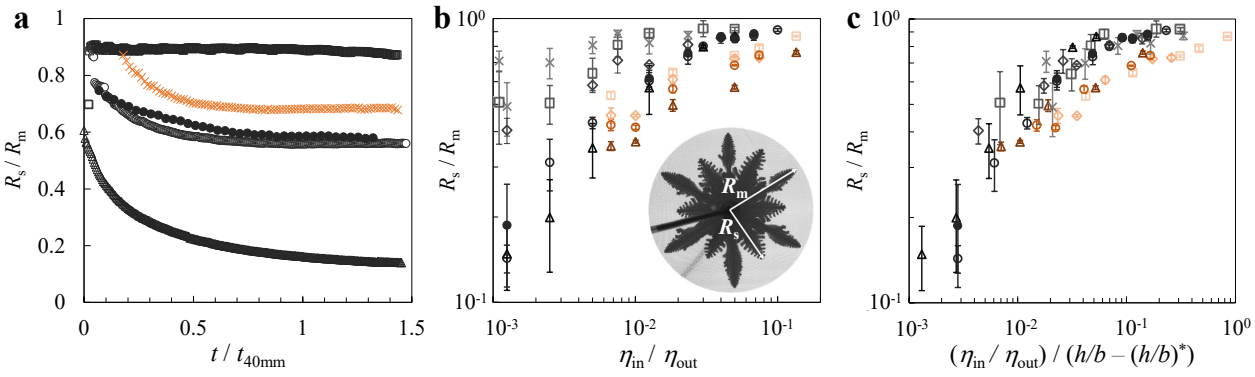

b,c

	×	□	◇	○	△	□	◇	○	△
h/b	0.1	0.2	0.328	0.49	1	0.2	0.328	0.49	1
	Experiments					Simulations			

Figure 3.4: (a) Temporal evolution of R_s/R_m for $\eta_{in}/\eta_{out} = 0.0013$, $h/b = 0.49$ and $q = 1$ ml/min (△), $\eta_{in}/\eta_{out} = 0.0125$, $h/b = 0.49$ and $q = 1$ ml/min (○), $\eta_{in}/\eta_{out} = 0.0125$, $h/b = 0.49$ and $q = 10$ ml/min (●), $\eta_{in}/\eta_{out} = 0.05$, $h/b = 0.49$ and $q = 1$ ml/min (▫) in experiments, and for $\eta_{in}/\eta_{out} = 0.05$, $h/b = 0.49$ (×) in simulations. t_{40mm} is the time when $R_m = 40$ mm. (b) R_s/R_m versus η_{in}/η_{out} for different h/b and q. R_s/R_m is measured when $R_m = 40$ mm. The symbols are defined in the table. Open symbols denote $q = 1$ ml/min, closed symbols denote $q = 10$ ml/min. (c) Scaled master curve of R_s/R_m versus $(\eta_{in}/\eta_{out})/(h/b-(h/b)^*)$. The monotonic increase in R_s/R_m denotes the change from six-fold towards twelve-fold symmetric dendritic patterns. The symbols are the same as in (b).

almost constant in time for fully developed patterns. Moreover, R_s/R_m is independent of the interfacial velocity for the range of flow rates investigated, as shown in Fig. 3.4a, where we normalize the time by t_{40mm} denoting the time when $R_m = 40$ mm. To compare the patterns formed at different viscosity ratios, we measure R_s/R_m when $R_m = 40$ mm, which is well within the fully developed regime. For a fixed h/b, the ratio R_s/R_m monotonically increases with viscosity ratio. In addition, a decrease in h/b leads to an increase in R_s/R_m, as shown in Fig. 3.4b. We can rescale all data by normalizing the viscosity ratio with $(h/b - (h/b)^*)$, as shown in Fig. 3.4c. The factor $(h/b)^*$ will become evident in the discussion of the morphology boundary. The numerical results are in good qualitative agreement with the experiments and exhibit the same scaling with h/b, but yield slightly lower values of R_s/R_m compared to the experimental results. This is likely due to the 2D nature of the simulations (where we average the flow in the third dimension across the gap and assume a parabolic velocity profile in the gap direction [109–111]), which do not capture effects related to the partial

displacement of the outer fluid or to the three-dimensional tongue-like structures that form between miscible fluids in a Hele-Shaw cell [29, 112, 113]. Exploring further improvements to the model, e.g., solving Stokes flow in the full 3D domain, and a deeper investigation into quantitative comparisons with experiments are interesting topics for future work.

3.3 Discussion

The observation that both $\eta_{\mathrm{in}}/\eta_{\mathrm{out}}$ and h/b allow one to systematically tune the symmetry of the patterns reveals a novel aspect of dendritic growth. Remarkably, the change in symmetry is also directly linked to the morphology transition to dense-branching growth: When $R_{\mathrm{s}}/R_{\mathrm{m}}$ reaches ~ 0.85, corresponding to patterns with twelve dendrites of almost equal size, a further decrease in h/b or a further increase in $\eta_{\mathrm{in}}/\eta_{\mathrm{out}}$ induces the transition to dense-branching growth. The morphology transition can therefore be described by the same functional form used to normalize the data in Fig. 3.4c; the morphology boundary denoted by a solid line in Fig. 3.1c corresponds to

$$\frac{h}{b} \;=\; A\frac{\eta_{in}}{\eta_{out}} + \left(\frac{h}{b}\right)^{*} \tag{3.4}$$

where $A = 3$ and $(h/b)^{*} = 0.04$ are best-fit parameters determined by logistic regression. $(h/b)^{*}$ denotes the critical h/b for the morphology transition in the limit of low viscosity ratio.

Why do six-fold dendritic patterns only form far from the morphology boundary, and what leads to the growth of an additional generation of dendrites as we approach the boundary? The importance of the viscosity ratio and the degree of anisotropy for determining $R_{\mathrm{s}}/R_{\mathrm{m}}$ can be seen in a simplified analysis taking into account the effective permeability at different locations corresponding to the growth of sub dendrites or main dendrites, as detailed in the Appendix 3.A.3. Note that the effective permeability in our system is isotropic and lacks a macroscopic preferred direction for single-phase flow. In general, the permeability tensor must be symmetric (by Onsager reciprocity for Stokes flow) and positive definite (by the Second Law of Thermodynamics) and thus represented by an orthogonal matrix [114], so its eigenvectors, corresponding to the fastest and slowest directions, must be mutually perpendicular [115]. This orthogonality is incompatible with triangular symmetry, thus

the permeability eigenvalues in our textured Hele-Shaw cell must be degenerate, implying isotropic single-phase flow.

For two-phase flow, however, the gradient of viscosity at the interface between the two fluids can locally break the symmetry and induce an anisotropic effective permeability near the interface. Using concepts derived for the hydrodynamics of slippage on textured surfaces for two-phase flows over hydrophobic surfaces [116, 117], we consider that the more-viscous outer fluid is partially trapped in the texture as the tip of the less-viscous fluid passes over the texture in the middle of the channel along the "path of least resistance". For small textures, the trapped fluid leads to a local effective slip length tensor [118, 119], $\mathbf{b}_{\text{slip}}$, which causes the effective permeability tensor to become anisotropic and orthogonal in the vicinity of the interface [115], leading to the appearance of sub dendrites that impart this square symmetry to the pattern. In the limit of "weak anisotropy" in the slip tensor, $\text{Tr}(\mathbf{b}_{\text{slip}}) << b$, as is the case for our experiments, we find that the interface velocities of the sub dendrites and the main dendrites, and therefore $R_{\text{s}}/R_{\text{m}}$, are indeed governed by $\eta_{\text{in}}/\eta_{\text{out}}$ and h/b.

To get further insight into the growth of the dendrites, we consider their macroscopic path selection. The main dendrites R_{m} grow along the six straight channels. The sub dendrites R_{s} select a path at a 30° angle from these straight channels. At early stage, two fingers form between each pair of neighboring main dendrites on each side of the 30° direction, due to the anisotropy of the lattice. This is observed at any viscosity ratio, as shown in Fig. 3.5a. Whether these fingers will merge towards each other and grow into a sub dendrite or merge with the main dendrites resulting in a six-fold symmetric pattern depends on the pressure distribution imposed both globally by the main dendrites and locally at the tip of the sub dendrites. At low $\eta_{\text{in}}/\eta_{\text{out}}$ and high h/b, the rapid growth of the main dendrites sets up a large pressure gradient at their tip which in turn induces a small pressure gradient in the 30° direction, as shown in Fig. 3.5a, which prevents the sub dendrites from growing. With increasing $\eta_{\text{in}}/\eta_{\text{out}}$ and decreasing h/b, however, the sub dendrites themselves build locally a high pressure gradient at their tips which amplifies their growth. We provide further details on the growth of the sub dendrites in Appendix 3.A.4.

Once the sub dendrites have emerged, they continue to grow along the 30° direction following a zig-zag path, as illustrated in Fig. 3.5b. As the tip of the sub dendrite reaches

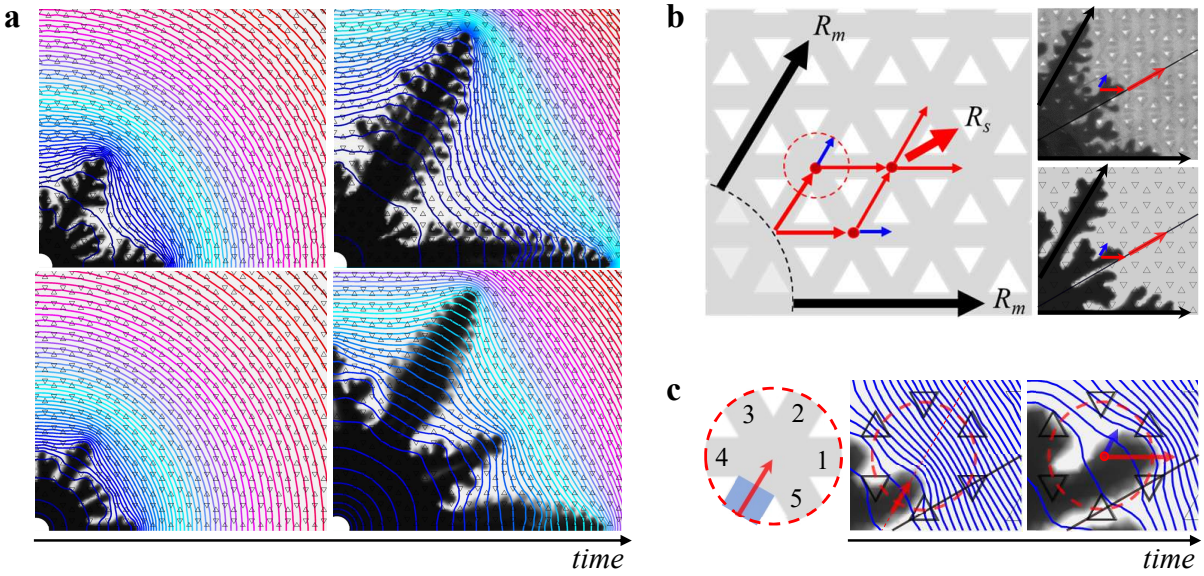

Figure 3.5: Formation and growth of sub dendrites. (a) Pressure field for patterns with $\eta_{in}/\eta_{out} = 0.006$ (top) and $\eta_{in}/\eta_{out} = 0.05$ (bottom) at two different times. The lines indicate pressure contours. The pressure field ranges from atmospheric pressure (denoted by red contours) to a maximum pressure around the inlet (denoted by blue contours), which is different for each panel as it varies with time and viscosity ratio; the colors are guides to the eye. (b) Schematic representation of the path followed by the main dendrites R_m and the sub dendrites R_s. At a lattice junction (indicated by the red dot in the dotted circle), the flow predominantly selects the direction along the red arrow, which leads to the growth of the sub dendrites along the 30° direction, as observed in both experiment (top image) and simulation (bottom image). (c) Zoomed schematics of the lattice junction. The combination of the global pressure distribution from the main dendrites and the local pressure distribution from the tip of the sub dendrites leads to flow into channel 1 along the direction of the red arrow.

a lattice junction, indicated by a red dot, the path towards the 30° direction (red arrow) is selected, rather than the straight path (blue arrow). This selection results from the pressure profile induced in the outer fluid by the main dendrites, which effectively shields the sub dendrites from growing towards the main dendrites and pushes them towards the 30° direction. Indeed, when the tip of a sub dendrite reaches the entrance of a lattice junction, as schematically shown in the zoomed-in region in Fig. 3.5c, it does not grow straight towards channel 2, but is deviated towards the 30° direction as a result of the global pressure distribution built up by the neighboring main dendrites. The local pressure distribution at the tip of the sub dendrite then induces a maximum pressure gradient towards

channel 1, and most of the flow goes into channel 1. It is this combination of the global pressure distribution from the main dendrites and the local pressure distribution from the tip of the sub dendrites that leads to the rich pattern selection in dendritic growth.

These different paths selected by the main dendrites and sub dendrites also reveal the origin of the maximum value of $R_s/R_m \approx 0.85$. It reflects the condition where the velocity of the main and sub dendrites becomes approximately equal. As the path selected by the sub dendrites deviates from the radial direction at each junction, the total path is $2/\sqrt{3}$ times longer than that of the main dendrites in the straight radial channels. The length of the main dendrite, R_m, is therefore $(2/\sqrt{3})R_s$, i.e., $R_s/R_m \approx \sqrt{3}/2 = 0.866$. Interestingly, our experiments show that once this condition is reached, a further increase in η_{in}/η_{out} or decrease in h/b induces the morphology transition to dense-branching growth. This suggests that the morphology transition occurs when the difference between the pressure gradient in the straight channels and the 30° direction becomes negligible, and therefore the role of anisotropy becomes negligible, such that the parabolic tips can no longer be stabilized allowing for tip-splitting to occur. Reaching a full understanding of this morphology transition can be topic of further research.

3.4 Conclusions

Our results reveal a rich morphology of patterns created by pairs of miscible fluids in anisotropic systems. They demonstrate the important role of the viscosity ratio between the two fluids, which, together with the degree of anisotropy, governs both the morphology transition from dense-branching to dendritic growth and the selected symmetry of the dendrites. Upon approaching the morphology boundary, the dendritic patterns systematically transition from six-fold towards twelve-fold symmetry in the parameter regime where interfacial flow is governed by an effective slip tensor, whose orthogonality imparts square symmetry to the original pattern.

This diversity of different dendritic patterns provides novel opportunities for tuning the growth of complex structures, not only in viscous fingering, but perhaps also in other cases of interfacial motion limited by gradient-driven transport processes, which lie in the same

universality class [120]. In general, we expect that dendritic growth following the preferred directions of an anisotropic environment will tend to acquire orthogonal symmetry for "weak anisotropy", whenever transport near the interface is governed by a local effective conductance tensor, which must be orthogonal like the effective slip tensor in a weakly textured Hele-Shaw cell [115]. For example, in template-assisted directional solidification [121, 122], a similar morphological transition may arise, controlled by the ratio of thermal diffusivities (analogous to the ratio of inverse viscosities here), whenever the pattern is controlled by the conduction of latent heat away from the interface in the liquid phase. Similarly, in template-assisted electrodeposition [123–126], it may be possible to tune the symmetry of dendritic patterns by varying the strength of diffusion anisotropy in the electrolyte domain. Active control of anisotropic dendritic growth may also be achieved, for example, by applying electric fields to control viscous fingering [79, 80] over patterned, charged surfaces [127] having anisotropic electro-osmotic slip tensors [128].

3.A Appendices

3.A.1 Negligible effects of diffusion in the numerical simulations

The numerical simulations are governed by the second-order advection-diffusion transport equation, and in accordance with the experiments the simulations are performed in the high Péclet number regime where advection dominates over diffusive effects. We confirm this by varying the diffusion coefficient by several orders of magnitude and showing that the pattern morphology is independent of the diffusion coefficient (or equivalently of a dimensionless Péclet number) over eight orders of magnitude, as shown in Fig. 3.6. At low enough Péclet number, diffusive effects dominate the pattern growth and stabilize the instability. All the simulations reported in the main part of Chapter 3 are performed far from this low Péclet number regime.

To provide a dimensionless point of reference, we define the Péclet number as $\mathrm{Pe} = UL/D$, where U is the characteristic velocity, L is a characteristic length scale and D is the diffusion coefficient [129]. For a radial flow, $\mathrm{Pe} = Q/D$ has been used [97, 130] with Q

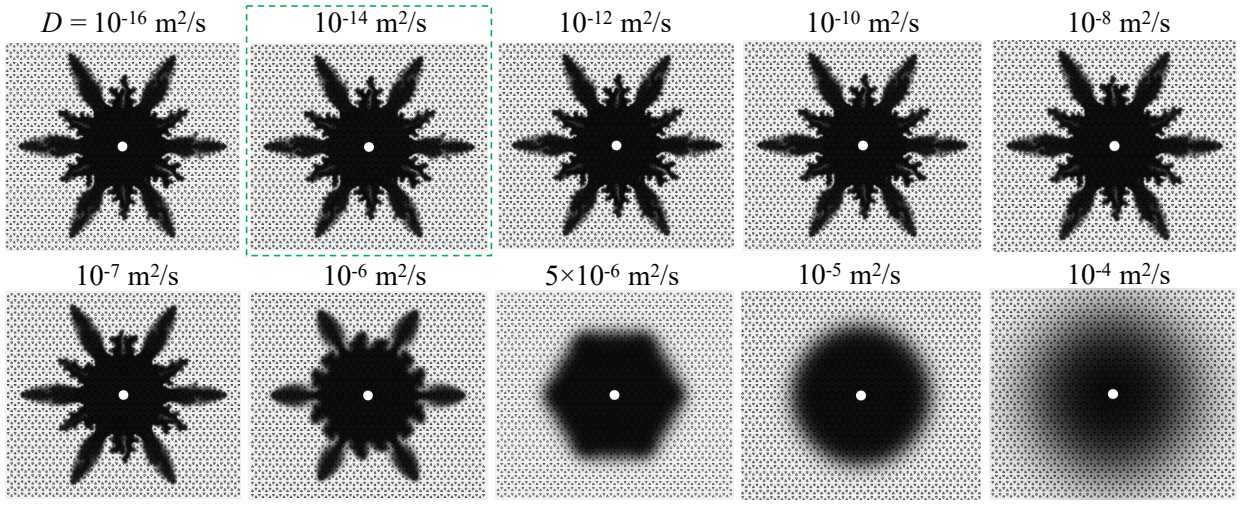

Figure 3.6: Simulated patterns ($\eta_{\text{in}}/\eta_{\text{out}} = 0.05$ and $h/b = 0.49$) obtained for different diffusion coefficients D. The dashed box denotes the conditions used in the main part of Chapter 3.

[m^2/s] the gap-averaged flow rate, i.e. the volumetric flow rate per unit depth. As discussed in [131], this implies that the characteristic velocity for radial source flows is $U = Q/L$, where L is the distance from the center of the cell. For a constant injection rate and a *stable* displacement, $U \propto 1/L$ and UL is equal to Q at any point. However, this equality and hence the applicability of the expression $\text{Pe} = Q/D$ holds only for a stable radial flow propagation. When instabilities are present, the velocity does not vary as $1/L$ and UL at a finger tip can be larger than Q. $\text{Pe} = Q/D$ therefore provides a lower bound for radial flows subject to viscous fingering instabilities. Keeping this in mind, we now use this definition of Pe.

The injection velocity is set to 0.14 m/s and imposed on an inner circle (inlet hole) of radius 1.4 mm. This gives a depth-averaged $Q \sim 0.0002$ m^2/s, comparable to the depth-averaged Q used in the experiments ranging from 0.00012 to 0.0033 m^2/s. We have confirmed that UL at any point beyond the injection source and sufficiently behind the unstable interface maintains this value, but it increases at a finger tip. Given a certain diffusion coefficient and Q, we can estimate a lower bound for the Péclet number. For instance, a Péclet number $\sim O(1)$ required to suppress the instability [130] in an *isotropic* system would imply a diffusion coefficient $\sim 10^{-4}$ m^2/s, in good agreement with our value of $\sim 10^{-5}$ m^2/s for an *anisotropic* system reported in Fig. 3.6. Exploring the stabilizing effect of diffusion on the transition between dendritic and dense-branching growth in anisotropic media is an exciting

line of future research.

3.A.2 Convergence of the numerical simulations

We have paid careful attention to the robustness and validity of the numerical modeling and have confirmed the numerical convergence, as demonstrated in Fig. 3.7. An optimal numerical mesh is chosen such that the fine features of the domain are well discretized, the simulations are computationally feasible, and a good degree of convergence is achieved in the flow dynamics and the pattern morphology. The optimal mesh that meets these criteria consists of 222,162 triangular elements that discretize an annular mesh area encompassing arrays of triangular objects. The average mesh element quality is above 0.9 with respect to various mesh quality measures including skewness, maximum angle, and growth rate of elements. The mesh element quality is a dimensionless quantity between 0 and 1, where 1 represents a perfectly regular element and 0 represents a degenerated element. A larger than 0.9 mesh quality represents a geometrically well-behaved and high-quality mesh that facilitates numerical convergence.

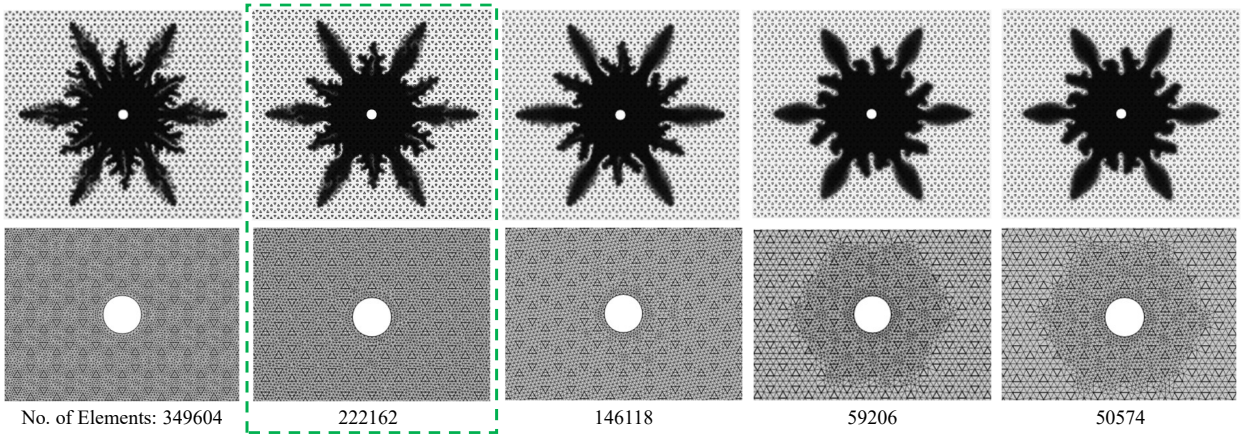

Figure 3.7: Simulated patterns ($\eta_{\text{in}}/\eta_{\text{out}} = 0.05$, $h/b = 0.49$) for different mesh resolutions. The mesh used for the results reported in the main part of Chapter 3 is denoted by the dashed box.

3.A.3 Simplified model to account for the effect of the degree of anisotropy and the viscosity ratio on the pattern growth

Our experiments and simulations reveal that the degree of anisotropy h/b and the viscosity ratio $\eta_{\text{in}}/\eta_{\text{out}}$ govern the growth of the sub and main dendrites in an anisotropic environment. We simplify our topology by considering flow in two directions with respect to the direction of parallel engraved channels, to capture the role of h/b and $\eta_{\text{in}}/\eta_{\text{out}}$ in governing the pattern growth: (a) the pressure gradient ∇p is parallel to the channels, corresponding to the growth of the main dendrites and (b) the pressure gradient ∇p is perpendicular to the channels, representing the growth of the sub dendrites, as shown in Figs. 3.8a and b. We note that such a texture, as well as that of our more complex six-fold symmetric lattice, is isotropic for a single-phase flow. For a two-phase flow, however, the presence of the interface leading to a gradient of viscosity in the flow direction can locally break the symmetry and lead to an anisotropic two-phase permeability of the interface region. To account for this, we use concepts derived for the hydrodynamics of slippage on textured surfaces for two-phase flows over hydrophobic surfaces [116, 117].

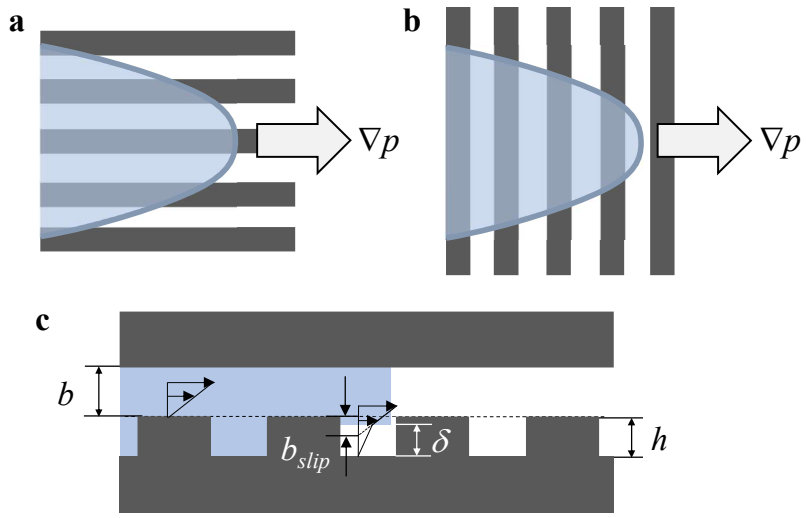

Figure 3.8: Schematic of the simplified channel texture. (a) The main dendrites grow along channels parallel to the flow direction. (b) The sub dendrites grow along channels perpendicular to the flow direction. (c) The effective slip length b_{slip} at the interface between the two fluids modifies the local permeability as the inner fluid flows above the channels. The light blue region represents the less-viscous inner fluid, the white region represents the more-viscous outer fluid within the channel.

In analogy to these concepts, and to account for the local asymmetry, we consider that the more-viscous outer fluid can get partially trapped in the channels as the less-viscous fluid flows above the texture following the path of least resistance, as schematically shown in Fig. 3.8c. This conceptualization allows us to introduce a local effective slip length to model the interface region [116, 118, 119, 132, 133].

We denote the height of the layer of trapped outer fluid as $\delta = \alpha h$, where α denotes a direction-dependent coefficient. The local effective slip length felt by the inner fluid over a valley of height h, measured from the no-slip boundary at the surface of the channel-free region (dashed line in Fig. 3.8c), scales as

$$b_{\text{slip}} = h - \delta\left(1 - \frac{\eta_{\text{in}}}{\eta_{\text{out}}}\right) = h - \alpha h\left(1 - \frac{\eta_{\text{in}}}{\eta_{\text{out}}}\right) \tag{3.5}$$

The enhancement of permeability due to b_{slip} scales as

$$\frac{b_{\text{slip}}}{b} = \frac{h}{b} - \frac{h}{b}\alpha\left(1 - \frac{\eta_{\text{in}}}{\eta_{\text{out}}}\right). \tag{3.6}$$

For single-phase flow, where $\eta_{\text{in}}/\eta_{\text{out}} = 1$, $b_{\text{slip}} = h$ and the permeability above the channel is proportional to $h + b$. For two-phase flow, however, b_{slip} decreases with decreasing viscosity ratio leading to a smaller enhancement of the permeability. The decrease of b_{slip} depends on the direction of the channels with respect to the flow, leading to a local symmetry breaking and the rich anisotropic pattern selection.

When $\text{Tr}(\mathbf{b}_{\text{slip}})/b \gg 1$, the effect of the channels dominates and an analysis in terms of an effective slip tensor is not applicable. The case of interest here is when $\text{Tr}(\mathbf{b}_{\text{slip}})/b \ll 1$, where the texture can be analyzed locally in terms of an effective slip tensor. This effective slip tensor is positive definite and 90° symmetric between the fast and slow directions [115, 132],

$$\mathbf{b}_{\text{slip}} = \mathbf{S}_\theta \begin{pmatrix} b_{\text{slip},\parallel} & 0 \\ 0 & b_{\text{slip},\perp} \end{pmatrix} \mathbf{S}_{-\theta} \tag{3.7}$$

where $\mathbf{S}_\theta = \begin{pmatrix} \cos\theta & \sin\theta \\ -\sin\theta & \cos\theta \end{pmatrix}$ and θ is the angle between the pressure gradient and the

texture. $b_{\text{slip},\parallel}$, $b_{\text{slip},\perp}$ are two eigenvalues of $\mathbf{b}_{\text{slip}}$. The subscripts $\parallel, \perp$ denote the fast direction and the slow direction, respectively. Note that here, the fast direction of the effective slip tensor corresponds to the direction of the main dendrites, the slow direction corresponds to the direction of the sub dendrites. The two corresponding eigenvectors have a 90° symmetry [115], corresponding to the formation of, respectively, the main dendrites at 0°, 60°, 120° and the sub dendrites at 30°, 90°, 150°.

From Eq. (3.5), we have

$$b_{\text{slip},\parallel} = h\left(1 - \alpha_{\parallel} + \alpha_{\parallel}\frac{\eta_{\text{in}}}{\eta_{\text{out}}}\right) \tag{3.8}$$

and

$$b_{\text{slip},\perp} = h\left(1 - \alpha_{\perp} + \alpha_{\perp}\frac{\eta_{\text{in}}}{\eta_{\text{out}}}\right) \tag{3.9}$$

where $\alpha_{\parallel,\perp}$ denotes the coefficient for the fast and slow direction, respectively, related to the effective slip tensor. As $b_{slip,\parallel} > b_{slip,\perp}$, we have $\alpha_{\perp} > \alpha_{\parallel}$.

The dimensionless effective permeability tensor, scaled to its value without slip, is expressed as

$$\mathbf{K} = \mathbf{I} + 3\mathbf{A_p} \tag{3.10}$$

where $\mathbf{A_p}$ is a dimensionless matrix describing a slip-driven plug flow in the $\mathbf{A_p}\nabla p$ direction [115]. We have

$$\mathbf{A_p} = \mathbf{S}_{\theta}\begin{pmatrix} A_s\left(b_{\parallel}\right) & 0 \\ 0 & A_s\left(b_{\perp}\right) \end{pmatrix}\mathbf{S}_{-\theta} \tag{3.11}$$

where $A_s\left(b_{\perp,\parallel}\right) = \frac{b_{\perp,\parallel}}{b+b_{\perp,\parallel}}$. For $\theta = 0°$, this gives

$$\mathbf{K} = \begin{pmatrix} K_{xx} & K_{xy} \\ K_{yx} & K_{yy} \end{pmatrix} = \begin{pmatrix} 1 + \frac{3}{\frac{b}{b_{\text{slip},\parallel}}+1} & 0 \\ 0 & 1 + \frac{3}{\frac{b}{b_{\text{slip},\perp}}+1} \end{pmatrix} \tag{3.12}$$

Substituting Eq. (3.8) and Eq. (3.9) into Eq. (3.12) yields

$$\mathbf{K} = \begin{pmatrix} 1 + \frac{3}{\frac{b}{h\left(1-\alpha_{\parallel}+\alpha_{\parallel}\frac{\eta_{\text{in}}}{\eta_{\text{out}}}\right)}+1} & 0 \\ 0 & 1 + \frac{3}{\frac{b}{h\left(1-\alpha_{\perp}+\alpha_{\perp}\frac{\eta_{\text{in}}}{\eta_{\text{out}}}\right)}+1} \end{pmatrix} \tag{3.13}$$

For our case where $b_{\text{slip}}/b \ll 1$, the effective permeability tensor can be expressed as

$$\kappa \approx \frac{b^2}{12\eta_{\text{in}}} \begin{pmatrix} 1 + \frac{3h\left(1-\alpha_{\parallel}+\alpha_{\parallel}\frac{\eta_{\text{in}}}{\eta_{\text{out}}}\right)}{b} & 0 \\ 0 & 1 + \frac{3h\left(1-\alpha_{\perp}+\alpha_{\perp}\frac{\eta_{\text{in}}}{\eta_{\text{out}}}\right)}{b} \end{pmatrix} \tag{3.14}$$

For the simplified topology in Fig. 3.8, the main dendrites form along the fast direction of the effective permeability and the sub dendrites form along the slow direction of the effective permeability:

$$\kappa_{\text{m}} = \frac{b^2}{12\eta_{\text{in}}} K_{xx} \approx \frac{b^2}{12\eta_{\text{in}}} \left(1 + \frac{3h}{b}\left(1 - \alpha_{\parallel} + \alpha_{\parallel}\frac{\eta_{\text{in}}}{\eta_{\text{out}}}\right)\right) \tag{3.15}$$

$$\kappa_{\text{s}} = \frac{b^2}{12\eta_{\text{in}}} K_{yy} \approx \frac{b^2}{12\eta_{\text{in}}} \left(1 + \frac{3h}{b}\left(1 - \alpha_{\perp} + \alpha_{\perp}\frac{\eta_{\text{in}}}{\eta_{\text{out}}}\right)\right) \tag{3.16}$$

This shows that as $\eta_{\text{in}}/\eta_{\text{out}}$ increases, the effective permeabilities in the main and sub channels, κ_{m} and κ_{s}, increase. Accordingly, the interface velocities in the main and sub channels, $\mathbf{u}_{\text{m}} = -\kappa_{\text{m}}\nabla p$ and $\mathbf{u}_{\text{s}} = -\kappa_{\text{s}}\nabla p$, increase. Let us now discuss the role of the viscosity ratio $\eta_{\text{in}}/\eta_{\text{out}}$ for the increase in permeability for both the main dendrites and the sub dendrites.

The ratio of the derivatives of the permeability for sub dendrites and main dendrites is

$$\frac{\partial\kappa_{\text{s}}/\partial\left(\eta_{\text{in}}/\eta_{\text{out}}\right)}{\partial\kappa_{\text{m}}/\partial\left(\eta_{\text{in}}/\eta_{\text{out}}\right)} \sim \frac{\alpha_{\perp}}{\alpha_{\parallel}} > 1 \tag{3.17}$$

Therefore, for increasing viscosity ratio, the increase in permeability along the sub dendrites (slow direction) is larger than the increase in permeability along the main dendrites (fast direction).

The ratio of the interface velocities between the sub dendrites and the main dendrites

scales as

$$\frac{u_{\mathrm{s}}}{u_{\mathrm{m}}} \simeq \frac{\kappa_{\mathrm{s}}}{\kappa_{\mathrm{m}}} \simeq 1 - \frac{3\left(1-\frac{\eta_{\mathrm{in}}}{\eta_{\mathrm{out}}}\right)\left(\alpha_{\perp}-\alpha_{\parallel}\right)}{\frac{b}{h}+3\left(1-\alpha_{\parallel}\left(1-\frac{\eta_{\mathrm{in}}}{\eta_{\mathrm{out}}}\right)\right)} \tag{3.18}$$

where $\alpha_{\perp} - \alpha_{\parallel} \geqslant 0$.

This analysis shows that for the case of $b_{\mathrm{slip}}/b \ll 1$, $u_{\mathrm{s}}/u_{\mathrm{m}}$ increases with an increase in the viscosity ratio $\eta_{\mathrm{in}}/\eta_{\mathrm{out}}$ or a decrease in the degree of anisotropy h/b. When the viscosity ratio $\eta_{\mathrm{in}}/\eta_{\mathrm{out}}$ approaches 1, $u_{\mathrm{s}}/u_{\mathrm{m}}$ will be close to 1. When h/b approaches zero, $u_{\mathrm{s}}/u_{\mathrm{m}}$ approaches 1. Clearly, this description is oversimplified but it does capture the essential features of how the viscosity ratio $\eta_{\mathrm{in}}/\eta_{\mathrm{out}}$ and the degree of anisotropy h/b affect the interface velocities of the main and sub dendrites, and therefore the growth of R_{m} and R_{s}.

3.A.4 Growth of sub dendrites

At early stage, two fingers grow between pairs of neighboring main dendrites on each side of the 30° direction to the straight channels, as shown in Fig. 3.9a. This is observed at any viscosity ratio. At low viscosity ratio and large h/b, these fingers soon merge with the main dendrites, which results in a six-fold symmetric pattern. With increasing $\eta_{\mathrm{in}}/\eta_{\mathrm{out}}$ and decreasing h/b, each of the two fingers will further split into two as they reach the next lattice

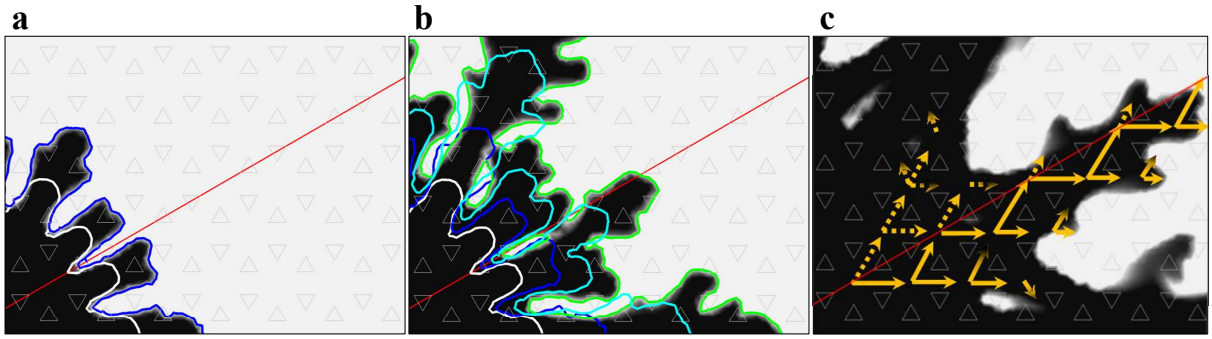

Figure 3.9: Formation and growth of sub dendrites. (a) At early stage, two fingers emerge between the neighboring main dendrites (white contour). They further split as they reach the center of a next lattice (blue contour). (b) One of the fingers outgrows the other one and becomes a sub dendrite (in this example, the one below the red 30° line). The colored contours represent the interface position at different times. (c) The sub dendrite further grows along the zig-zag path illustrated by the solid yellow arrows. A smaller amount of flow also goes towards the dashed yellow arrows, leading to the formation of side branches.

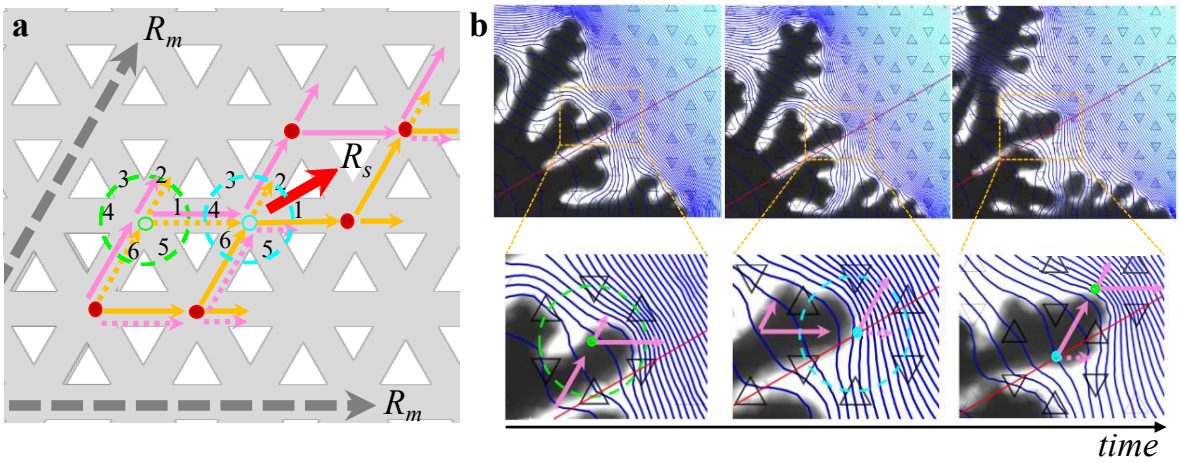

Figure 3.10: Path selection towards 30° direction governed by pressure profile. (a) As the tip of a sub dendrite reaches a junction that is *not* on the 30° line, indicated by a green dot, the pressure profile in the outer fluid imposed by the two neighboring main dendrites pushes the tip towards the 30° line through channel 1, as shown in the left inset of (b). As the tip reaches a junction *on* the 30° line, indicated by a cyan dot, through channel 4, it grows towards channel 2 because the local pressure gradient is highest in that direction, as shown in the middle inset of (b). The sub dendrite continues to grow on the same side of the 30° line where it first developed. The pink arrows denote the path of a sub dendrite formed above the 30° line, the yellow arrows denote the path of a sub dendrite formed below the 30° line. The solid arrows indicate the main direction of the flow, but a small amount of flow goes towards the dashed arrows and leads to the side-branch decoration of the dendrites.

junction. One branch advances parallel to the main dendrite and eventually merges with it. The other branch diverts towards the 30° direction and will merge with its counterpart on the other side of the 30° direction into a sub dendrite, as shown in Fig. 3.9b. Depending on which finger grew slightly faster, the sub dendrite will grow in a zig-zag path along the 30° direction either right below or above this direction, as illustrated by the arrows in Fig. 3.9c and Fig. 3.9a. The absence of interfacial tension implies that the flow is unaffected by pinning effects on corners that become important in immiscible fluids [107, 108]. As a result, when the tip of a sub dendrite reaches an entrance of a junction, as shown in the schematics of the zoomed-in region in Fig. 3.10, its path is governed by the combination of the global pressure distribution from the main dendrites and the local pressure distribution from the tip of the sub dendrites.

When the tip of a sub dendrite reaches a junction that is not on the 30° line, indicated

by a green dot in Fig. 3.10a, the pressure profile in the outer fluid imposed by the main dendrites pushes the tip predominantly towards the 30° line through channel 1. When the tip of a sub dendrite reaches a junction on the 30° line through channel 4, indicated by a cyan dot in Fig. 3.10a, it grows towards channel 2 as the local pressure field at the tip is biased towards its initial side of the 30° line, where it first started to grow. Note that in Fig. 3.10a, we differentiate between these two sides by the pink and yellow arrows; the sub dendrite follows either the yellow or the pink zig-zag path depending on the side it first appeared.

We note that a small amount of fluid also goes towards the direction that is not selected by the sub dendrite tip (channel 1 from the cyan dot for an incoming liquid through the horizontal channel 4, for example). This flow leads to the side-branch decoration along the sub dendrites.

Chapter 4

Dendritic patterns from shear-enhanced anisotropy in nematic liquid crystals

This chapter is based on Ref. [66].

Spontaneous pattern growth at an unstable interface between two fluids is a common phenomenon in many nonequilibrium systems [1, 8, 75, 76, 134, 135]. A famous example is the viscous-fingering instability, in which one fluid is displaced by another less viscous one in the quasi two-dimensional geometry of a Hele-Shaw cell [16]. In this instability, fingers of the displacing fluid grow into the displaced one and undergo successive tip-splitting, which leads to ramified patterns with many branches that belong to the class of dense-branching growth [2, 3, 12]. Remarkably, the ubiquitous tip-splitting can be prevented by introducing anisotropy in the interfacial dynamics, which stabilizes the fingertips into parabolic shapes; the resulting pattern transitions to dendritic growth [4–9, 63]. Dense-branching growth and dendritic growth are two essential morphologies that emerge in a diverse range of physical phenomena, including electrochemical deposition and the growth of bacteria colonies [75, 76, 83, 84, 136].

Given the important role of anisotropy in selecting the growth morphology, various experimental methods have been developed to introduce anisotropy in the viscous-fingering instability [18, 22–24, 26, 27, 137, 138]. The most well-established means is to geometrically

modify the growth environment by engraving ordered channels on one of the plates of the Hele-Shaw cell [18, 63]. Another strategy is to use nematic liquid crystals as one of the fluids, where the anisotropy is an intrinsic property of the medium itself [27]. Previous studies have exploited this strategy using thermotropic liquid crystals (TLCs) as the displaced fluid [27]. Most TLCs in the nematic phase are flow-aligned materials [61], for which the director maintains a stable angle in the shear plane set by the viscous torques acting on the director [28]. The flow-alignment gives rise to a smaller viscosity parallel to the flow direction compared to that perpendicular to the flow direction [28]. This difference in viscosities leads to a direction-dependent velocity of the interface and introduces anisotropy in the interfacial dynamics, causing the transition from dense-branching to dendritic growth [28]. The flow-alignment, and thus the growth morphology transition, occurs when the viscous torque from the shear flow becomes dominant over the Frank elastic torque produced by the gradient in the continuum director field. This condition is reached when the Ericksen number, which denotes the ratio between the viscous torque and the Frank elastic torque, is larger than unity [31].

Here, we demonstrate a different pathway to dendritic growth that occurs at much higher Ericksen numbers deep in the flow-dominated regime. We observe this pathway when a low viscosity silicone oil displaces a solution of nematic lyotropic chromonic liquid crystals (LCLCs). LCLCs are aqueous dispersions of organic disk-like molecules that self-assemble into cylindrical aggregates, which are responsible for the formation of liquid crystal phases [39, 43–47]. In contrast to most nematic TLCs that flow-align for Ericksen numbers $\mathrm{Er} > 1$, nematic LCLCs exhibit a flow-tumbling behavior where the material does not adopt a stable director field but experiences a non-zero viscous torque acting on the director. In this tumbling state, defects can form in the nematic LCLC solutions [61, 65]. Since LCLC aggregates are about 100 times longer than TLC molecules, their rotational relaxation is slow compared to the timescales of the flow and flows can reach the regime of Deborah numbers close to unity, a regime not accessible in TLCs [46, 61]. The Deborah number denotes the ratio of the rotational relaxation time of the aggregates to the characteristic time of the flow. We demonstrate how these unique characteristics lead to dendritic growth in the viscous-fingering instability by a different mechanism than that reported for nematic TLCs,

and over a large range of injection flow rates for different viscosities of the displacing fluid.

We reveal that the morphology transition from dense-branching to dendritic growth necessitates an enhancement of anisotropy of the tumbling nematic liquid crystal solution. In the tumbling state, the viscous-fingering instability adopts dense-branching growth. We find that the tumbling behavior can be suppressed by high enough shear leading to a flow-alignment of the material, which enhances the LCLC anisotropy and induces the transition to dendritic growth. This flow-alignment occurs deep in the flow-dominated regime for Er $>>$ 1. The shear-enhanced anisotropy is reached when the viscous torque induced by the shear flow becomes dominant over the elastic torque from the nematic potential. This provides a quantitative criterion for the growth morphology transition and establishes the relation between the orientation of the LCLC aggregates at the microscale and the growth morphology selection at the macroscale.

In a small range very close to the fingertip of the invading fluid, the LCLC aggregates experience a uniaxial extensional flow induced by the finger growth. We show how LCLC aggregates can break when the uniaxial extensional flow dominates over simple shear flow, and how this can locally induce a phase transition of the LCLC solution from the nematic phase to the isotropic phase. Such flow-induced phase transition, which is tunable and reversible, could be exploited in applications using LCLC solutions as flow field sensors.

4.1 Methods

Our experiments are performed in a radial Hele-Shaw cell consisting of two 19 mm thick circular glass plates of diameter 140 mm. The spacing between the two plates, b, is maintained by spacers placed around the plate perimeter and varies from 12 μm to 50 μm. We use silicone oils (Sigma Aldrich and Consolidated Chemical & Solvents LLC) with viscosities ranging from 0.83 mPa s to 48 mPa s as the displacing inner fluid, and aqueous solutions of the lyotropic chromonic liquid crystal disodium cromoglycate (DSCG) (TCI America, purity $>$ 98.0%) as the displaced outer fluid. We prepare nematic DSCG solutions with concentrations of 14 wt%, 16 wt%, and 18 wt% DSCG in water at room temperature $T = 23 \pm 0.5$°C; the three concentrations cover the regime of nematic phase [50]. The fluids are injected

through a 2 mm diameter hole in the center of one of the plates at a volumetric flow rate ranging from $q = 0.05 - 5.5$ ml/min controlled by a syringe pump (Harvard PHD 2000). We visualize the patterns through crossed polarizers and record their growth with a LUMIX GH5 camera at frame rates up to 60 fps.

To investigate the director field and the flow field in the region close to the fingertips, we use a smaller Hele-Shaw cell with plate spacing 25 μm, consisting of two 6 mm thick square glass plates of size 75 mm x 75 mm. The director field is observed through crossed polarizers in an optical microscope (OMAX M837T) with an objective of magnification M = 4$\times$ and numerical aperture NA = 0.1. The flow field is quantified by tracking polystyrene microspheres (Alpha Nanotech Inc.) of diameter 2 μm using the optical microscope. The microspheres are dispersed in the DSCG solutions at a concentration of 0.05 wt%. The director field and the flow field are captured using a high-speed camera (Chronos 1.4) at frame rates of 1069 fps. We determine the two-dimensional velocity field using a digital particle image velocimetry tool for MATLAB (PIVlab) [139, 140].

4.2 Results and Discussion

4.2.1 Growth morphology transition in nematic LCLC solutions

Two distinct pattern morphologies emerge as a nematic solution of the lyotropic liquid crystal disodium cromoglycate (DSCG) is displaced by a lower viscosity silicone oil in a radial Hele-Shaw cell. At low volumetric flow rates, fingers grow by repeated tip-splitting which results in the generic dense-branching growth. Above a certain volumetric flow rate, however, the fingertips are stabilized, and the morphology transitions to dendritic growth, as shown in Fig. 4.1(A and B). Such a morphology transition occurs for different viscosities of the displacing silicone oils ($\eta_{\text{in}} = 0.83$ mPa s in Fig. 4.1A and $\eta_{\text{in}} = 48$ mPa s in Fig. 4.1B). The global features of the patterns depend on the viscosity ratio between the displacing and displaced fluids. In particular, an inner circular region within which the outer fluid is completely displaced appears for larger viscosity ratios [29, 63, 141]. To classify the pattern morphologies, we consider the temporal evolution of the fingertip width, w, measured 300 μm

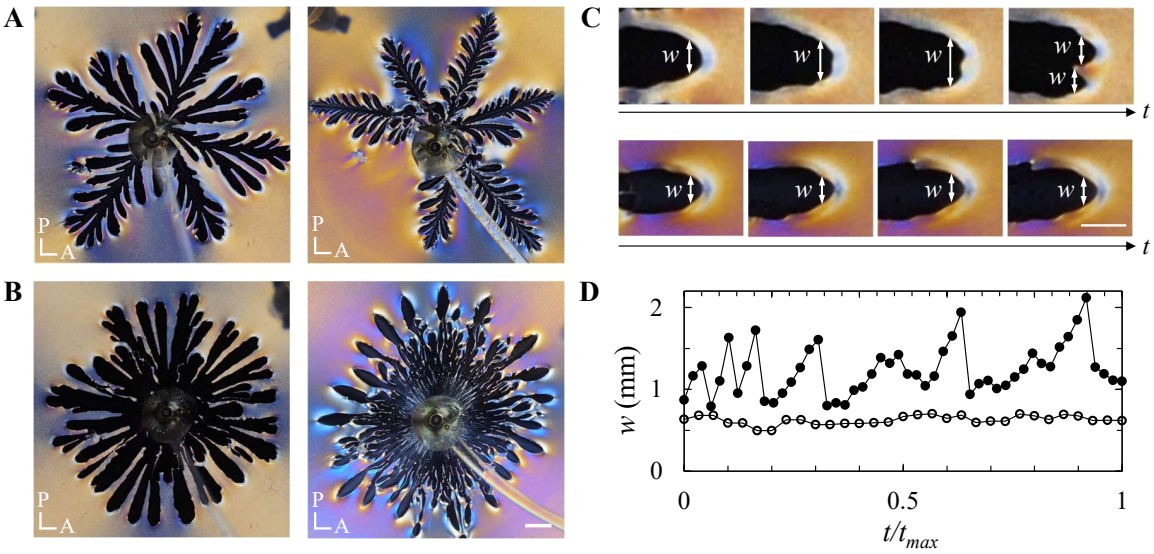

Figure 4.1: **Morphology transition from dense-branching to dendritic growth observed as silicone oil displaces aqueous solutions of disodium cromoglycate in the nematic phase.** (**A**, **B**) With increasing volumetric flow rate q, the pattern transitions from dense-branching growth (left) to dendritic growth (right). (**A**) Silicone oil viscosity $\eta_{\text{in}} = 0.83$ mPa, and $q = 0.1$ ml/min (left) and $q = 0.4$ ml/min (right). (**B**) Silicone oil viscosity $\eta_{\text{in}} = 48$ mPa s, and $q = 0.05$ ml/min (left) and $q = 1$ ml/min (right). The scale bar is 5 mm. The images are captured using a crossed polarizer, P, and analyzer, A. (**C**) The width of the fingertip w varies with time t for dense-branching growth characterized by repeated tip-splitting (upper panel). The width w remains constant for dendritic growth characterized by stable parabolic tips (lower panel). The scale bar is 2 mm. (**D**) Temporal evolution of w for dense-branching growth (●) and dendritic growth (○) for $\eta_{\text{in}} = 0.83$ mPa s. t_{max} denotes the time when the fingers reach a length of 30 mm.

behind the fingertip. For dense-branching growth, w increases until it reaches a width of twice the most unstable wavelength set by the competition between surface tension forces and viscous forces [16], whereupon the tip splits and w decreases. By contrast, w remains constant for the stabilized parabolic tips of dendritic patterns, as shown in Fig. 4.1(C and D).

4.2.2 Growth morphology transition induced by shear-enhanced anisotropy

To understand what governs the morphology transition from dense-branching to dendritic growth, we measure the optical retardance of the DSCG solutions that gives information

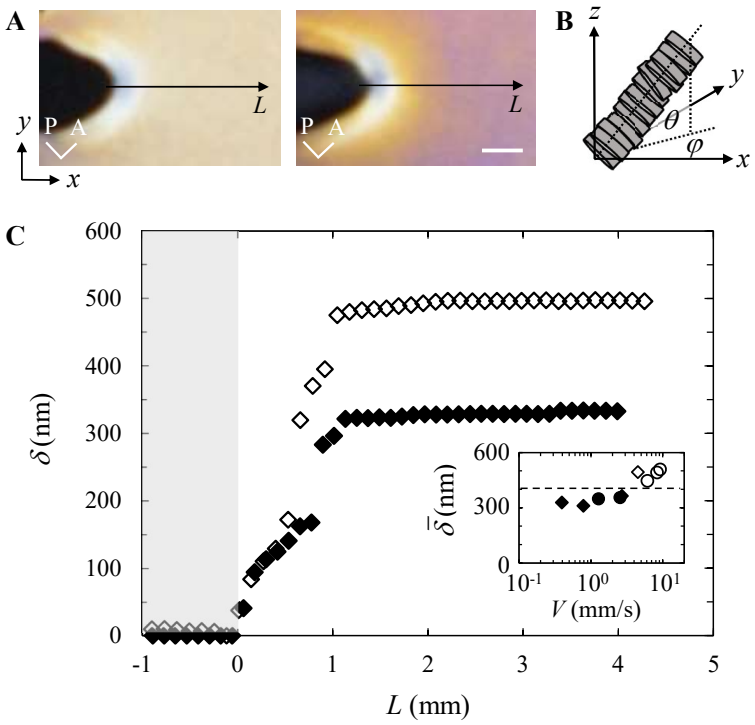

Figure 4.2: **Distinct director fields for dense-branching and dendritic growth.** (**A**) The difference in color observed in DSCG solutions far from the fingertip denotes distinct director fields for dense-branching growth at $q = 0.05$ ml/min (left) and for dendritic growth at $q = 1$ ml/min (right). We define a local coordinate system where the x-axis is in the direction of the fingertip growth, the y-axis is perpendicular to the growth direction, and the z-axis denotes the direction of the plate spacing. L is the distance from the fingertip along the x-direction. The scale bar is 1 mm. (**B**) Schematic of the director orientation. The in-plane azimuthal angle is denoted as φ and the out-of-plane polar angle as θ. (**C**) The optical retardance δ along the distance L for dense-branching growth (◆) and dendritic growth (◇). The data correspond to the images in **A**. The gray area at $L < 0$ denotes the isotropic oil phase, where the retardance is zero. Inset: Mean optical retardance far from the fingertip averaged over 1.5 mm $< L <$ 4 mm, $\overline{\delta}$, versus the fingertip velocity, V, for silicone oils with viscosities $\eta_{\text{in}} = 9.8$ mPa s (○) and $\eta_{\text{in}} = 48$ mPa s (◇). The dashed line marks the transition between dense-branching and dendritic growth.

about the director field. Imaged under crossed polarizers, the interference color is distinct for the two growth morphologies, as shown in Fig. 4.2A, indicating differences in the alignment of the director field. We determine the in-plane azimuthal angle, φ (Fig. 4.2B), by adding a static 560 nm full-wave-plate optical compensator with its slow axis oriented at 45° to the crossed polarizers and find that $\varphi \approx 0$; the directors are, on average, uniformly aligned in the radial flow direction for both dense-branching and dendritic growth (see Appendix 4.A.1).

The optical retardance, $\delta = \int_0^b |n_{\text{eff,local}}(\theta) - n_o| dz = b|n_{\text{eff}}(\bar{\theta}) - n_o|$, then provides information about the average out-of-plane polar angle, $\bar{\theta}$, where b is the plate spacing of the Hele-Shaw cell, and n_{eff} and n_o are the effective and ordinary refractive indices [142].

Comparing the interference color with a customized Michel-Lévy color chart, we determine the optical retardance δ along the center line in front of a fingertip, L (see Chapter 2.3 and Appendix 4.A.1). In the isotropic oil phase, the retardance is close to zero. Within a small region in front of the fingertip, δ is similar for both types of patterns, as shown in Fig. 4.2C. Away from the fingertip, however, the retardance is higher for the dendritic pattern than for the dense-branching pattern. These features are consistently observed for different silicone oil viscosities and different fingertip velocities, V, where V is measured at the fingertips as they grow from a radius of $R = 15$ mm to $R = 30$ mm: Dendritic growth occurs beyond a critical value of retardance, as shown in the inset of Fig. 4.2C.

A low value of retardance in flowing DSCG solutions reflects the tumbling character of the material that leads to a non-zero viscous torque for any orientation of the director with $\alpha_2\alpha_3 < 0$, where α_2 and α_3 are the Leslie viscosity coefficients [31]. As a result of the non-zero viscous torque, twist-type topological defects spontaneously occur in the material, which lead to a low retardance [61, 65]. That the viscous-fingering instability adopts dense-branching growth in this regime indicates that the tumbling state at the microscale makes the liquid behave isotropically at the macroscale, even for a material that exhibits global nematic ordering. A high value of retardance, by contrast, reflects a small average polar angle ($\bar{\theta} \lesssim 15^\circ$) indicative of a stable flow-aligned state. High shear can thus, remarkably, suppress the tumbling of DSCG solutions. Our results suggest that this transition from tumbling to the flow-aligned state introduces a large enough shear-enhanced anisotropy that allows for the growth morphology transition from dense-branching growth to dendritic growth.

To test this hypothesis, we consider that the morphology transition in DSCG solutions occurs in the regime of high Ericksen number $\text{Er} = \frac{\eta_2 \bar{\dot{\gamma}}_{xz} b^2}{K_2}$ ranging from 1.7×10^6 – 9.4×10^7 in our experiments, where η_2 is the twist viscosity, K_2 is the twist Frank elastic constant, and $\bar{\dot{\gamma}}_{xz} = V/b$ is the average shear rate in the xz-plane [31, 50]. In this regime, the material response is flow-dominated. Moreover, given the large size of DSCG aggregates [50], the Deborah number $\text{De} = \tau_r/\tau_f \approx 1$, where $\tau_r = 1/D_r$ is the rotational relaxation time of the

aggregates, $D_r = \frac{3k_BT(\ln(l/d)-0.8)}{\pi\eta_s l^3}$ is the rotational diffusion coefficient, l is the length and d is the diameter of the DSCG aggregate, η_s is the solvent viscosity, k_B is the Boltzmann constant, T is the temperature, and $\tau_f = 1/\bar{\dot{\gamma}}_{xz}$ is the characteristic time of the shear flow [62]. For Deborah numbers of order unity, the director field cannot be considered as a continuum field and the classical Ericksen-Leslie theory does not apply [62]. Instead, we need to consider the dynamics of individual molecular aggregates, which is set by the competition between the elastic torque from the nematic potential that induces collective tumbling of the directors and the viscous torque from shear flow that drives individual aggregates to reorient towards the stationary angle adopted in the flow-aligned state. We express the elastic torque acting on the aggregates as $M_{\mathrm{el}} = l\frac{dU_{\mathrm{nem}}}{dz} \approx l\frac{U_{\mathrm{nem}}}{b}$, where U_{nem} is the nematic potential that we express using the Onsager excluded-volume potential $U_{\mathrm{nem}} = 2dl^2Ck_BT$, $C = 4\phi/\pi d^2 l$ is the number of aggregates per unit volume, and ϕ is the volume fraction of DSCG in water [46, 143]. The viscous torque from the shear flow is $M_{\mathrm{visc}} \approx \eta_{\mathrm{eff}}\dot{\gamma}_{xz}(z)\, bl^2$, where $\eta_{\mathrm{eff}} \approx \frac{\phi}{dl^2}\xi$ is the effective viscosity that is related to the drag coefficient $\xi \approx \frac{\pi}{6}\eta_s l^3$ [143]. The competition between M_{visc} and M_{el} can be expressed by $\Pi = \frac{M_{\mathrm{visc}}}{M_{\mathrm{el}}} \approx \frac{\pi^2}{48}\frac{\eta_s lb^2\dot{\gamma}_{xz}(z)}{k_BT}$. A similar expression can be more rigorously obtained from the Smoluchowski equation (see Appendix 4.A.2). We consider almost all directors to be flow-aligned when the shear rate in the center region of the gap reaches $\dot{\gamma}_{xz,c} = \frac{12z_c}{b}\bar{\dot{\gamma}}_{xz,c}$, where $\bar{\dot{\gamma}}_{xz,c} = \frac{V^*}{b}$ is the average critical shear rate, V^* is the gap-averaged critical velocity denoting the transition from tumbling to flow-alignment, and $z_c \approx 10^{-4}\frac{b}{2}$ is a characteristic length scale denoting the center region chosen of the order of the radius of a DSCG aggregate ($\approx$ 1 nm). Setting $\Pi = 1$ then yields $V^* \approx \frac{8\times10^4}{\pi^2}\frac{k_BT}{\eta_s lb}$.

We can now probe whether V^* governs the transition from dense-branching to dendritic growth by varying the plate spacing, b, and the length of the aggregates, l. The length of the aggregates can be tuned by using different concentrations of DSCG in water [46, 50]. For a set of experiments at a given b and l, the growth morphology transition occurs at a critical fingertip velocity V_c, which is independent of the viscosity of the displacing silicone oil, η_{in}, as shown in Fig. 4.3(A and B). Both changing b and l systematically shifts V_c. We can indeed rescale all data by normalizing the fingertip velocity V with V^*, as shown in Fig. 4.3C. This corroborates that the microscopic transition from tumbling to flow alignment occurring at V^* governs the macroscopic growth morphology transition.

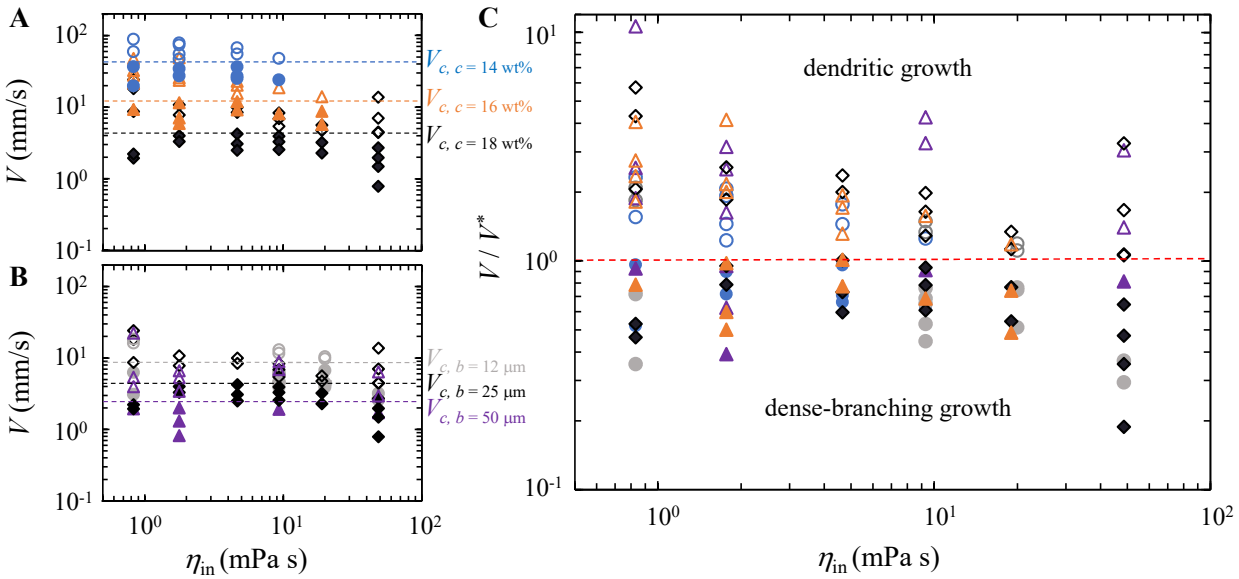

Figure 4.3: **Morphology diagrams denoting the transition from dense-branching to dendritic growth controlled by the fingertip velocity, V.** (**A**) Experiments performed at fixed plate spacing, $b = 25\mu$m, for three concentrations of DSCG in water: $c = 14$ wt% (○), $c = 16$ wt% (△), and $c = 18$ wt% (◇). Closed symbols denote dense-branching growth, open symbols denote dendritic growth. The dashed lines mark the transitions between dense-branching growth and dendritic growth occurring at critical fingertip velocities V_c. (**B**) Experiments performed at fixed concentration of DSCG in water, $c = 18$ wt%, for three plate spacings: $b = 12\mu$m (○), $b = 25\mu$m (◇), and $b = 50\mu$m (△). (**C**) Morphology diagram where V is normalized with V^*, the velocity denoting the balance of the elastic torques from the nematic ordering and the viscous torques from the shear flow.

It is interesting to note that for both nematic thermotropic liquid crystals (TLCs) and nematic lyotropic chromonic liquid crystals (LCLCs), the transition from dense-branching to dendritic growth occurs as the directors adopt a flow-aligned state. The mechanism that governs the flow alignment, however, is distinct for the two classes of liquid crystals. The flow alignment in nematic TLCs is described within the framework of the Ericksen-Leslie theory, where the dynamics of the director is set by the competition between the Frank elastic torque produced by the gradient of the continuum director field and the viscous torque from the shear flow expressed by the Ericksen number [31]. Flow alignment occurs for Er > 1. In a tumbling liquid crystal such as the nematic DSCG solution, by contrast, the flow alignment occurs at much higher Er $> 10^6$ and at high Deborah numbers De $\approx 10^{-2}$–10^1 compared to De $< 10^{-5}$ for TLCs. In this Deborah number regime, the Ericksen-Leslie theory is not

applicable and instead molecular theories considering the nematic potential resisting the shear flow deforming individual aggregates, as expressed by Π, describe the flow alignment. Our experiments show that dendritic growth can occur for De $\gtrsim 1$ in nematic tumbling LCLCs, and not only in the previously reported regime of De $<< 1$ in nematic flow-aligned TLCs, and that distinct mechanisms govern the morphology transition in the two regimes.

4.2.3 Extensional flow locally breaks DSCG aggregates at fingertips

. While the morphology selection is determined by the state of alignment of LCLC aggregates far from the fingertip, the invading oil finger modifies the state of the LCLC aggregates close to the oil-liquid crystal interface. In a small region directly in front of the fingertip, we observe a dark region that denotes a significant decrease in retardance compared to the region away from the tip, as shown in Fig. 4.4A. Such a low value of retardance could be due to three possible effects: i) a homeotropic alignment ($\theta = 90^\circ$) of the director field, ii) a twist deformation of the director in the gap direction, or iii) a decrease of the order parameter [61]. To test which of these effects is the cause of the lower retardance, we tilt the Hele-Shaw cell by 20°. We find that the dark area remains dark upon tilting the Hele-Shaw cell, as shown in Fig. 4.4A, which indicates that the lower retardance is due to a decrease of the order parameter as the two other possible effects would induce a change in retardance upon tilting the cell. The decrease in retardance occurs over a similar range L_c for different volumetric flow rates, as shown in Fig. 4.4B.

To understand why the order parameter is lower in the region in front of the fingertip, we measure the two-dimensional velocity field $\mathbf{v}(x, y, t)$ using tracer particles. The relative velocity of the DSCG solution in the frame of the moving fingertip reveals a combination of uniaxial extensional flow and simple shear flow, as shown by the black arrows in Fig. 4.4C. The color map of the strain rate calculated as $\dot{\gamma} = \sqrt{\dot{\gamma}_e^2 + \dot{\gamma}_s^2}$ shows that the maximum strain rate occurs in the fingertip region, where $\dot{\gamma}_e = \frac{1}{2}\left(\frac{\partial v_x}{\partial x} - \frac{\partial v_y}{\partial y}\right)$ is the extensional component of the strain rate and $\dot{\gamma}_s = \frac{1}{2}\left(\frac{\partial v_x}{\partial y} + \frac{\partial v_y}{\partial x}\right)$ is the shear component of the strain rate. We hypothesize that the order parameter decreases in the region of high strain rate as a result of the strong extensional flow. This might appear counter-intuitive, as extensional flows have been reported to increase the order parameter in rigid rods suspended in a fluid by promoting the

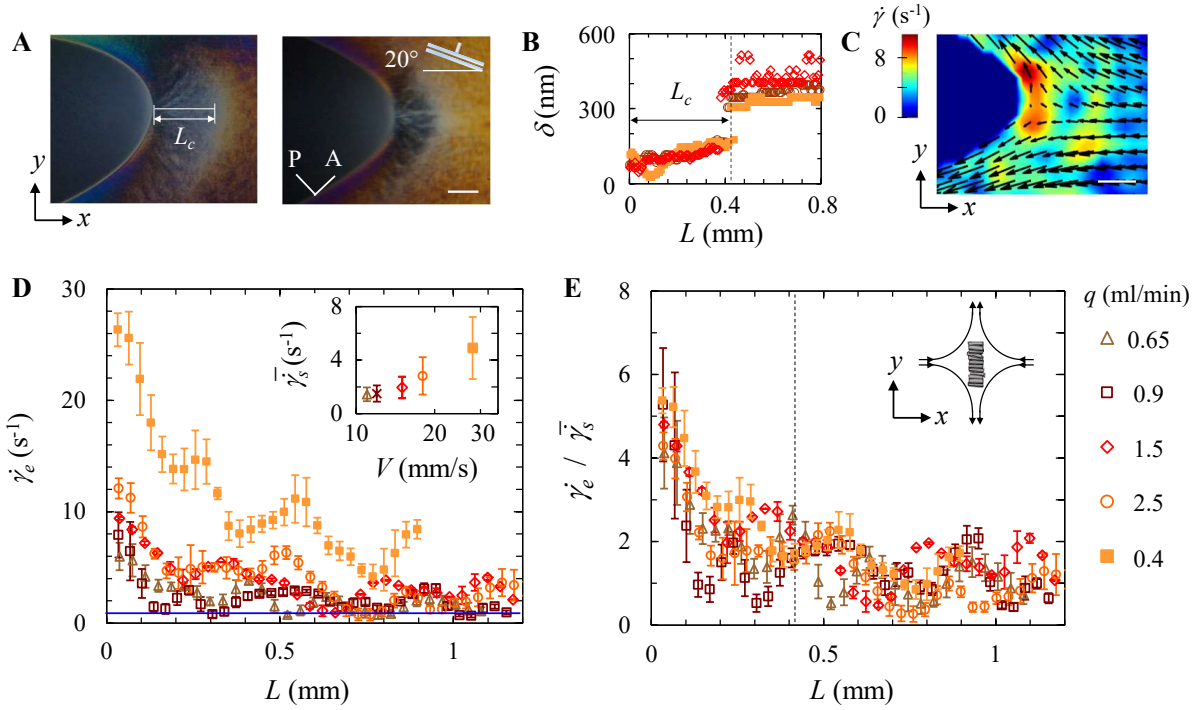

Figure 4.4: **Extensional shear at the fingertip induces isotropic liquid crystal phase.** (**A**) Zoomed image of the fingertip region for a volumetric flow rate $q = 1.5$ ml/min. A dark region of length L_c is seen in front of the fingertip (top image), which remains dark upon tilting the Hele-Shaw cell by 20° (bottom image). The scale bar is 200 μm. (**B**) Optical retardance, δ, measured at the center line of a finger for experiments at different volumetric flow rates q (see legend to the right). Closed symbols denote $\eta_{\text{in}} = 0.83$ mPa s, open symbols denote $\eta_{\text{in}} = 48$ mPa s. L_c, indicated by the dashed line, denotes the region characterized by a low δ. (**C**) Map of the relative velocity (arrows) in the frame of the moving fingertip and the strain rate $\dot{\gamma}$ (color map) for $q = 1.5$ ml/min. The scale bar is 200 μm. (**D**) Extensional component of the strain rate, $\dot{\gamma}_e$, measured at the center line of a finger versus the distance from the fingertip, L. The blue line denotes the critical extensional component of the strain rate above which an aggregate breaks, $\dot{\gamma}_{e,cr}$. Inset: The mean shear component of the strain rate, $\bar{\dot{\gamma}}_s$, increases with increasing fingertip velocity, V. (**E**) Scaled master curve of $\dot{\gamma}_e/\bar{\dot{\gamma}}_s$ versus L. The dashed line indicates L_c. Inset: A DSCG aggregate aligns parallel to the uniaxial extensional flow when $\dot{\gamma}_e > \bar{\dot{\gamma}}_s$. Strong shear can break the aggregate, which results in the isotropic liquid crystal phase.

rods to align [144, 145]. However, distinct from rigid rods, the DSCG aggregates can break and consequently form an isotropic phase [52], which would indeed significantly decrease the order parameter.

To test this hypothesis, we estimate the effect of the extensional flow on the DSCG aggregates by considering: i) The energy balance between the scission energy of aggregates,

E_{sci}, which describes the energy required to break an aggregate into two, and the energy input from extensional flow, E_{ext}. ii) The alignment of DSCG aggregates in the extensional flow, which determines whether the aggregates are in tension or in compression.

The scission energy is $E_{sci} \approx 10k_BT$ [50]. The energy from extensional flow is expressed as $E_{ext} = \sigma_e \Lambda \phi^{-1}$, where $\sigma_e = -(\alpha_2 + \alpha_3)\dot{\gamma}_e$ is the extensional stress, α_2 and α_3 are the Leslie viscosity coefficients, $\Lambda \approx dl^2$, and ϕ is the volume fraction of DSCG aggregates in water (see Appendix 4.A.3). Balancing the two energies, $E_{sci} = E_{ext}$, yields a critical extensional strain rate inducing breakage of the aggregates, $\dot{\gamma}_{e,cr} \approx 1\ \mathrm{s}^{-1}$, shown as a blue line in Fig. 4.4D. The measured extensional component of the strain rate $\dot{\gamma}_e$ intersects $\dot{\gamma}_{e,cr}$ at different distances L from the fingertip for experiments performed at different volumetric flow rates q. This is inconsistent with the independence of L_c on q (Fig. 4.4B). Indeed, $\dot{\gamma}_{e,cr}$ denotes the onset of aggregate breakage only for the condition where the aggregates are in tension, which is the case when the aggregates are oriented parallel to the uniaxial extensional direction (inset of Fig. 4.4E). Conversely, when the aggregates are oriented perpendicular to the uniaxial extensional direction, they are in compression, and $\dot{\gamma}_{e,cr}$ does not induce breakage. To determine the orientation of the aggregates in the fingertip region, we consider that the aggregates undergo a simple shear flow in the x-direction that favors alignment in the x-direction and an uniaxial extensional flow in the y-direction that favors alignment in the y-direction [61, 144, 145]. The competition between $\dot{\gamma}_e$ and $\dot{\gamma}_s$ governs the aggregate orientation. $\dot{\gamma}_s$ is almost constant in the fingertip region (see Appendix 4.A.4), and the mean shear component of the strain rate, $\overline{\dot{\gamma}}_s$, systematically increases with fingertip velocity, as shown in the inset of Fig. 4.4D. We thus normalize $\dot{\gamma}_e$ with $\overline{\dot{\gamma}}_s$, which indeed rescales all data and shows that $\dot{\gamma}_e/\overline{\dot{\gamma}}_s > 1$ for $L < L_c$, as displayed in Fig. 4.4E. The DSCG aggregates align in the y-direction close to the fingertip and break as $\dot{\gamma}_e > \dot{\gamma}_{e,cr}$, which induces the transition from the nematic to the isotropic phase reflected in the decrease in retardance.

4.3 Conclusions

We demonstrate how fast flows can suppress the tumbling behavior of nematic lyotropic chromonic liquid crystal solutions and induce a flow alignment of the director field. As a

result of such a shear-enhanced anisotropy of the liquid crystal, the pattern obtained in the viscous-fingering instability transitions from dense-branching growth to dendritic growth. We have established a quantitative criterion for this growth morphology transition in terms of the competition between the elastic torque from the nematic potential and the viscous torque from shear flow, which allows us to controllably tune the pattern growth occurring in interfacial fluid instabilities.

The self-assembled nature of LCLC solutions introduces the potential of aggregate breakage. We show that the high uniaxial extensional shear close to a fingertip during finger growth can break LCLC aggregates and induce a phase transition from the nematic to the isotropic phase. This might be exploited to design flow field sensors with reversible phase transitions that can easily be induced by tuning the flow rate [34, 146].

4.A Appendices

4.A.1 Far-field director orientation in DSCG solutions

To estimate the average in-plane azimuthal angle across the plate spacing, φ, of the director field of DSCG solutions, we add a static full-wave-plate optical compensator (560 nm) with the slow axis $\vec{\lambda}_{\mathrm{g}}$ oriented at 45° to the crossed polarizers and in the direction parallel to the flow. The optical birefringence of a 18 wt% DSCG solution at rest is $\Delta n = n_{\mathrm{e}} - n_{\mathrm{o}} = -0.02$ at a wavelength $\lambda_w = 633$ nm, where n_{e} and n_{o} are the extraordinary and ordinary refractive indices [72]. At $b = 25 \pm 1$ μm, the maximum optical retardance is $\delta = b|\,(n_{\mathrm{e}} - n_{\mathrm{o}})\,| = 500 \pm 20$ nm.

We compare the birefringence colors with the customized Michel-Lévy color chart to determine the optical retardance of DSCG solutions (see Chapter 2.3). In experiments performed without the full-wave-plate optical compensator, we find that the retardance of flowing DSCG solutions is approximately 330 nm (light yellow color) for dense-branching growth, Fig. 4.5(A), and 500 nm (purple color) for dendritic growth, Fig. 4.5(B). After the compensator is inserted, a change in color, representing a change in the retardance, gives information about the azimuthal angle of the director field: an increase of the retardance by 560 nm indicates that the director is perpendicular to $\vec{\lambda}_{\mathrm{g}}$; a decrease of the

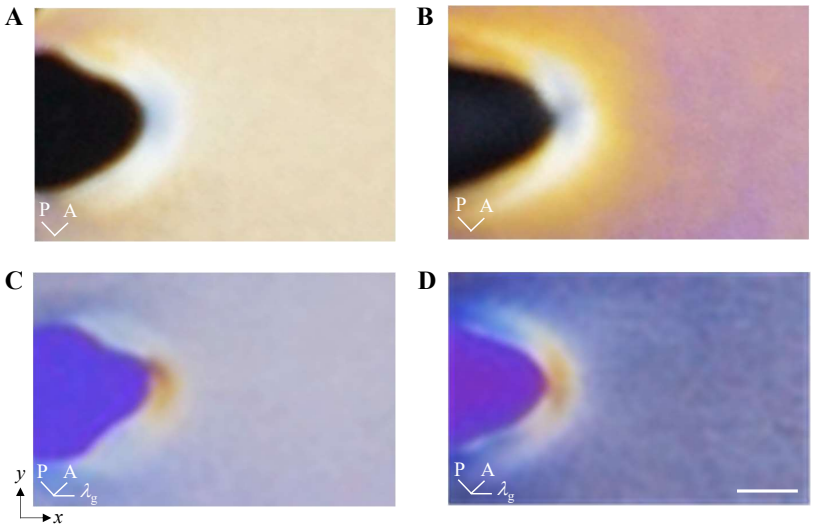

Figure 4.5: **Director orientation in DSCG solutions for dense-branching growth and dendritic growth.** Imaged under crossed polarizer and analyzer, regions away from the fingertip show distinct colors for dense-branching growth (**A**) and dendritic growth (**B**), denoting differences in the optical retardance. The shift in the optical retardance upon adding a static full-wave-plate optical compensator ($\lambda_g = 560$ nm) allows us to estimate the in-plane azimuthal angle for dense-branching growth (**C**) and dendritic growth (**D**). The viscosity of the displacing silicone oil is $\eta_{in} = 48$ mPa s. The flow rate is $q = 0.05$ ml/min for dense-branching growth and $q = 1$ ml/min for dendritic growth. The scale bar denotes 0.5 mm.

retardance by 560 nm indicates that the director is parallel to $\vec{\lambda}_g$. For dense-branching growth, the retardance of the flowing DSCG solution away from the fingertip is approximately 230 nm = $|330 - 560|$ nm (change in birefringence color from light yellow (330 nm) to light gray (230 nm), Fig. 4.5(A and C)). For dendritic growth, the retardance similarly decreases by 560 nm; 60 nm = $|500 - 560|$ nm (change in birefringence color from purple (500 nm) to deep gray (60 nm), Fig. 4.5(B and D)). The director field of DSCG solutions is thus parallel to $\vec{\lambda}_g$ and to the flow direction (x-direction) for both dense-branching and dendritic growth.

4.A.2 Flow behavior of DSCG solutions described by the Smoluchowski equation

We complement our scaling arguments describing the effect of flow on the orientation of DSCG aggregates outlined in the main part of Chapter 4 with a more rigorous description

using the Smoluchowski equation. We consider a DSCG aggregate at a position $\mathbf{x}$ with orientation $\mathbf{m}$, where $\mathbf{m} = (\cos\theta'\cos\varphi', \cos\theta'\sin\varphi', \sin\theta')$ with θ' the out-of-plane polar angle and φ' the in-plane azimuthal angle of an aggregate [147]:

$$\begin{aligned}\frac{Df}{Dt} = \nabla\cdot\left\{\left[D_{\parallel}\mathbf{mm} + D_{\perp}\left(\mathbf{I}-\mathbf{mm}\right)\right]\cdot\left(\nabla f + \frac{1}{k_BT}f\nabla U_{\mathrm{nem}}\right)\right\} \\ + D_r\,\mathrm{Re}\cdot\left(\mathrm{Re}\,f + \frac{1}{k_BT}f\,\mathrm{Re}\,U_{\mathrm{nem}}\right) - \mathrm{Re}\left(\mathbf{m}\times\left(\nabla\mathbf{v}\right)^{\mathrm{T}}\cdot\mathbf{m}f\right),\end{aligned} \tag{4.1}$$

where f is the orientation distribution of the DSCG aggregates, U_{nem} is the nematic potential, k_B is the Boltzmann constant, T is the temperature, $\mathbf{v}$ is the velocity, $\mathrm{Re} = \mathbf{m}\times(\partial/\partial\mathbf{m})$, η_s is the solvent viscosity, $D_r = \frac{3k_BT(\ln(l/d)-0.8)}{\pi\eta_s l^3}$ is the rotational diffusion coefficient for rod-like aggregates in dilute solution, l is the length and d is the diameter of the DSCG aggregate, $D_{\parallel}{=}\frac{1}{6}D_r l^2$ and $D_{\perp}{=}\frac{1}{12}D_r l^2$ are the translational diffusivities parallel and perpendicular to the aggregate orientation.

Eq. 4.1 can be expressed using the plate spacing b as the characteristic length scale, $t_0 = b/V_f$ as the characteristic time, where V_f is a characteristic velocity of the flow field that we set to be the fingertip velocity V, and $U_0 = k_BT$ as the characteristic potential: $\mathbf{x}^* = \frac{\mathbf{x}}{b}$, $\mathbf{v}^* = \frac{\mathbf{v}}{V}$, $t^* = \frac{t}{t_0}$, $U^* = \frac{U_{\mathrm{nem}}}{U_0}$. This yields the non-dimensional form:

$$\begin{aligned}\frac{\partial f}{\partial t^*} + \mathbf{v}^*\cdot\nabla^* f = \varepsilon^2\frac{D_r b}{V}\nabla^*\cdot\left\{\left[D_{\perp}^*\left(\mathbf{I}+\mathbf{mm}\right)\right]\cdot\left(\nabla^* f + f\nabla^* U^*\right)\right\} \\ + \frac{D_r b}{V}\,\mathrm{Re}\cdot\left(\frac{1}{\mathrm{Re}}f + f\,\mathrm{Re}\,U^*\right) - \mathrm{Re}\left(\mathbf{m}\times\left(\nabla^*\mathbf{v}^*\right)^{\mathrm{T}}\cdot\mathbf{m}f\right),\end{aligned} \tag{4.2}$$

where $\varepsilon = \frac{l}{b}$ and $D_{\perp}^* = \frac{1}{12}$. The term $\ln(l/d)$ ranges from 3.2–5; we here approximate it as a constant such that $D_r \propto \frac{k_BT}{\pi\eta_s l^3}$. The dimensionless term $\varepsilon^2\frac{D_r b}{V}$ in Eq. 4.2 can be expressed as

$$\Pi_1 = \frac{V}{\varepsilon^2 D_r b} \propto \frac{\eta_s l b V}{k_BT}. \tag{4.3}$$

Π_1 has a similar form as the dimensionless number we obtain from the scaling analysis described in Chapter 4, $\Pi = \frac{M_{\mathrm{visc}}}{M_{\mathrm{el}}} \approx \frac{\pi^2}{48}\frac{\eta_s l b^2\dot{\gamma}_{xz}(z)}{k_BT}$, where $\dot{\gamma}_{xz}(z) \propto \frac{V}{b}$.

4.A.3 Extensional viscosity of DSCG solutions and director characteristics under uniaxial extensional flow

Considering the average strain rate $\overline{\dot{\gamma}}$ in the xy-plane in front of a fingertip, where the x-axis is in the direction of the fingertip growth and the y-axis is perpendicular to the growth direction, we find the Deborah number in the xy-plane $\mathrm{De}_{xy} = \overline{\dot{\gamma}}/D_r \approx 10^{-3} << 1$. For $\mathrm{De}_{xy} << 1$, we use the Ericksen-Leslie theory to determine the extensional viscosity of DSCG solutions assuming that the DSCG aggregates are not broken by the flow. Given the velocity field $\mathbf{v}$ and the nematic liquid crystal director field $\mathbf{n} = (\cos\theta\cos\varphi, \cos\theta\sin\varphi, \sin\theta)$, where θ is the out-of-plane polar angle and φ is the in-plane azimuthal angle, the general form of the nematodynamic equation is [31]

$$\frac{dn_i}{dt} = \frac{1}{\gamma_1}\delta_{ij}^{\perp}h_j + W_{ik}n_k + \lambda\delta_{ij}^{\perp}A_{jk}n_k, \tag{4.4}$$

where γ_1 is the rotational viscosity, $A_{jk} = \frac{1}{2}\left(\frac{\partial v_j}{\partial x_k} + \frac{\partial v_k}{\partial x_j}\right)$ and $W_{ik} = \frac{1}{2}\left(\frac{\partial v_i}{\partial x_k} - \frac{\partial v_k}{\partial x_i}\right)$ are the symmetric and antisymmetric parts of the velocity gradients, $\delta_{ij}^{\perp}$ is the transverse Kronecker delta and $\lambda = \frac{\alpha_2+\alpha_3}{\alpha_2-\alpha_3}$ with α_2 and α_3 the Leslie viscosity coefficients. $h_i = -\frac{\partial f_{FO}}{\partial n_i} + \frac{\partial}{\partial x_j}\left(\frac{\partial f_{FO}}{\partial(\partial n_i/\partial x_j)}\right)$, where f_{FO} is the Frank–Oseen elastic energy density.

We consider the high Ericksen number regime ($\mathrm{Er} >> 1$) where the elastic term h_i is negligible, and assume steady state so that $\frac{dn_i}{dt} = 0$. Eq. 4.4 then simplifies to

$$W_{ik}n_k + \lambda\delta_{ij}^{\perp}A_{jk}n_k = 0. \tag{4.5}$$

Further assuming a negligible out-of-plane polar angle ($\theta \approx 0$) at high Er [65], the director field simplifies to $\mathbf{n} = (\cos\varphi, \sin\varphi, 0)$, which yields

$$(\alpha_2 - \alpha_3)\,\omega_{xy} + (\alpha_2 + \alpha_3)\sin 2\varphi\dot{\gamma}_e + (\alpha_2 + \alpha_3)\left(1 - 2\cos^2\varphi\right)\dot{\gamma}_s = 0, \tag{4.6}$$

where $\omega_{xy} = \frac{1}{2}\left(\frac{\partial v_x}{\partial y} - \frac{\partial v_y}{\partial x}\right)$ is the vorticity in the xy-plane, $\dot{\gamma}_s = \frac{1}{2}\left(\frac{\partial v_x}{\partial y} + \frac{\partial v_y}{\partial x}\right)$ is the shear component of the strain rate in the xy-plane, and $\dot{\gamma}_e = \frac{1}{2}\left(\frac{\partial v_x}{\partial x} - \frac{\partial v_y}{\partial y}\right)$ is the extensional component of the strain rate in the xy-plane. The term for the extensional component in Eq. 4.6 gives a viscosity coefficient characteristic of extensional flow, $-(\alpha_2 + \alpha_3)$.

We investigate the dynamics of a director that initially aligns along the x-direction ($\varphi(t=0)=0$) under a uniaxial extensional flow along the y-direction. For an uniaxial extensional flow, Eq. 4.4 yields

$$\frac{d\varphi}{dt} = \left(\frac{\alpha_2+\alpha_3}{\alpha_2-\alpha_3}\right)\cos\varphi\sin\varphi|\dot{\gamma}_e|. \tag{4.7}$$

We conduct a linear stability analysis by considering a small in-plane perturbation φ_1. Linearizing Eq. 4.7 yields:

$$\frac{d\varphi_1}{dt} = \left(\frac{\alpha_2+\alpha_3}{\alpha_2-\alpha_3}\right)\left(1-\frac{\varphi_1^2}{2}\right)\varphi_1|\dot{\gamma}_e|. \tag{4.8}$$

From Eq. 4.8, we obtain $\varphi = \varphi_1 = \pm\frac{\sqrt{2}e^{At}}{\sqrt{e^{2At}+C}}$, where $A = \left(\frac{\alpha_2+\alpha_3}{\alpha_2-\alpha_3}\right)|\dot{\gamma}_e|$ and C is a constant. For $t >> 1$, φ approaches $\pm\sqrt{2}$, which demonstrates that the director under a uniaxial extensional flow rotates towards the extensional direction.

4.A.4 Shear flow in the fingertip region

We measure the shear component of the strain rate $\dot{\gamma}_s$ in the fingertip region, as shown in the color map in Fig. 4.6(A). $\dot{\gamma}_s$ is zero at the center line of a finger due to the symmetry

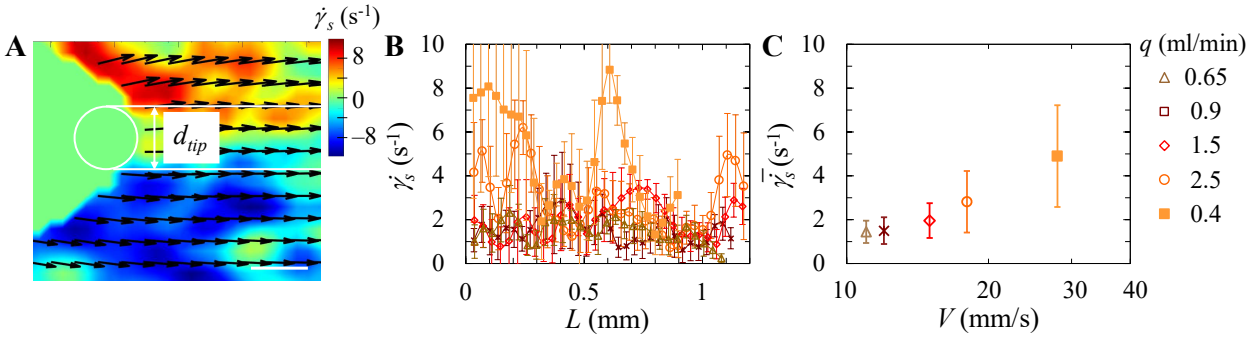

Figure 4.6: **Dependence of shear component of strain rate on fingertip velocity.** (**A**) Map of the relative velocity (arrows) and the shear component of the strain rate $\dot{\gamma}_s$ (color map) for $q = 1.5$ ml/min and $\eta_{\text{in}} = 48$ mPa s. d_{tip} is the diameter of fingertip curvature. The scale bar denotes 200 μm. (**B**) Average shear component of the strain rate, $\dot{\gamma}_s$, measured in the range d_{tip} versus the distance from the fingertip, L. Closed symbols denote $\eta_{\text{in}} = 0.83$ mPa s, open symbols denote $\eta_{\text{in}} = 48$ mPa s. (**C**) The mean shear component of the strain rate, $\bar{\dot{\gamma}}_s$, increases with increasing fingertip velocity, V.

of the flow field, which induces theoretically a singularity and generates experimentally a large noise in the ratio between the extensional component of the strain rate $\dot{\gamma}_e$ and $\dot{\gamma}_s$. To circumvent this issue, we consider the average of $\dot{\gamma}_s$ within a region of characteristic width d_{tip}, where d_{tip} is the diameter of fingertip curvature, as shown in Fig. 4.6(A). $\dot{\gamma}_s$ fluctuates around an approximately constant mean, $\overline{\dot{\gamma}}_s$, along the distance away from the fingertip, L, as displayed in Fig. 4.6(B). $\overline{\dot{\gamma}}_s$ increases with an increase in fingertip velocity, as shown in Fig. 4.6(C).

Chapter 5

Structures and topological defects in pressure-driven lyotropic chromonic liquid crystals

This chapter is based on Ref. [65].

Lyotropic chromonic liquid crystals (LCLCs) are aqueous dispersions of organic disk-like molecules that self-assemble into cylindrical aggregates, which form nematic or columnar liquid crystal phases under appropriate conditions of concentration and temperature [39, 43–47]. These materials have gained increasing attention in both fundamental and applied research over the past decade, due to their distinct structural properties and bio-compatiblility [34–42]. Used as a replacement for isotropic fluids in microfluidic devices, nematic LCLCs have been employed to control the behavior of bacteria and colloids [41, 148–153].

Nematic liquid crystals form topological defects under flow, which gives rise to complex dynamical structures that have been extensively studied in thermotropic liquid crystals (TLCs) and liquid crystal polymers (LCPs) [62, 154–161]. In contrast to lyotropic liquid crystals that are dispersed in a solvent and whose phase can be tuned by either concentration or temperature, TLCs do not need a solvent to possess a liquid-crystalline state and their phase depends only on temperature [31]. Most thermotropic liquid crystals are shear-aligned

nematics, in which the director evolves towards an equilibrium out-of-plane polar angle. Defects nucleate beyond a critical Ericksen number due to the irreconcilable alignment of the directors from surface anchoring and shear alignment in the bulk flow [157, 162–164]. With an increase in shear rate, the defect type can transition from π-walls (domain walls that separate regions whose director orientation differs by an angle of π) to ordered disclinations and to a disordered chaotic regime [165]. Recent efforts have aimed to tune and control the defect structures by understanding the relation between the selection of topological defect types and the flow field in flowing TLCs. Strategies to do so include tuning the geometry of microfluidic channels, inducing defect nucleation through the introduction of isotropic phases or designing inhomogeneities in the surface anchoring [166–170]. Liquid crystal polymers are typically tumbling nematics for which $\alpha_2\alpha_3 < 0$, where α_2 and α_3 are the Leslie viscosities. This leads to a non-zero viscous torque for any orientation of the director, which allows the director to rotate in the shear plane [31, 155, 161, 171]. The tumbling character of LCPs facilitates the nucleation of singular topological defects [155, 171]. Moreover, the molecular rotational relaxation times of LCPs are longer than those of TLCs, and they can exceed the time scales imposed by the shear rate. As a result, the rheological behavior of LCPs is governed not only by spatial gradients of the director field from the Frank elasticity, but also by changes in the molecular order parameter [62, 172–174]. With increasing shear rate, topological defects in LCPs have been shown to transition from disclinations to rolling cells and to worm-like patterns [62, 158, 174].

Topological defects occurring in the flow of nematic LCLCs have so far received much more limited attention [61, 175]. At rest, LCLCs exhibit unique properties distinct from those of TLCs and LCPs [39, 43, 44, 46, 47, 61]. In particular, LCLCs have significant elastic anisotropy compared to TLCs; the twist Frank elastic constant, K_2, is much smaller than the splay and bend Frank elastic constants, K_1 and K_3. The resulting relative ease with which twist deformations can occur can lead to a spontaneous symmetry breaking and the emergence of chiral structures in static LCLCs under spatial confinement, despite the achiral nature of the molecules [39, 49, 52–56]. When driven out of equilibrium by an imposed flow, the average director field of LCLCs has been reported to align predominantly along the shear direction under strong shear but to reorient to an alignment perpendicular

to the shear direction below a critical shear rate [57–59]. A recent study has revealed a variety of complex textures that emerge in simple shear flow in the nematic LCLC disodium cromoglycate (DSCG) [61]. The tumbling nature of this liquid crystal leads to enhanced sensitivity to shear rate. At shear rates $\dot{\gamma} < 1\ \mathrm{s}^{-1}$, the director realigns perpendicular to the flow direction adapting a so-called log-rolling state characteristic of tumbling nematics. For $1\ \mathrm{s}^{-1} < \dot{\gamma} < 10\ \mathrm{s}^{-1}$, polydomain textures form due to the nucleation of pure-twist disclination loops, for which the rotation vector is parallel to the loop normal, and mixed wedge-twist disclination loops, for which the rotation vector is perpendicular to the loop normal [60, 61]. Above $\dot{\gamma} > 10\ \mathrm{s}^{-1}$, the disclination loops gradually transform into periodic stripes in which the director aligns predominantly along the flow direction [61].

Here we report on the structure and dynamics of topological defects occurring in the pressure-driven flow of nematic disodium cromoglycate. A quantitative evaluation of such dynamics has so far remained challenging, in particular for fast flow velocities, due to the slow image acquisition rate of current quantitative polarization-resolved imaging techniques. Quantitative polarization imaging traditionally relies on three commonly used techniques: fluorescence confocal polarization microscopy, polarizing optical microscopy and LC-Polscope imaging. Fluorescence confocal polarization microscopy can provide accurate maps of birefringence and orientation angle, but the fluorescent labeling may perturb the flow properties [176]. Polarizing optical microscopy requires a mechanical rotation of the polarizers and multiple measurements, which severely limits the imaging speed. LC-Polscope, an extension of conventional polarization optical microscopy, utilizes liquid crystal universal compensators to replace the compensator used in conventional polarization microscopes [177]. This leads to an enhanced imaging speed and better compensation for polarization artifacts of the optical system. The need for multiple measurements to quantify retardance, however, still limits the acquisition rate of LC-Polscopes.

We overcome these challenges by using a novel single-shot quantitative polarization microscopy technique, termed polarized shearing interference microscopy (PSIM). PSIM combines circular polarization light excitation with off-axis shearing interferometry detection. Using a custom polarization retrieval algorithm, we achieve single-shot mapping of the retardance, which allows us to reach imaging speeds that are limited only by the camera frame

rate while preserving a large field-of-view and micrometer spatial resolution. We provide a brief discussion of the optical design of PSIM in the Methods section; further details of the measurement accuracy and imaging performance of PSIM are reported in [64].

Using a combination of experiments, numerical simulations and scaling analysis, we show that in the pressure-driven flow of nematic disodium cromoglycate solutions in a microfluidic channel, pure-twist disclination loops emerge for a certain range of shear rates. These loops are elongated in the flow with a fixed aspect ratio. We demonstrate that the disclination loops nucleate at the boundary between regions where the director aligns predominantly along the flow direction close to the channel walls and regions where the director aligns predominantly perpendicular to the flow direction in the center of the channel. The large elastic stresses of the director gradient at the boundary are then released by the formation of disclination loops. We show that both the characteristic size and the fluctuations of the pure-twist disclination loops can be tuned by controlling the flow rate.

5.1 Methods

5.1.1 Experimental methods

We dissolve disodium cromoglycate (DSCG) (TCI America, purity > 98.0%) at 13.0 wt% in deionized water. The sample is sealed in a glass tube and heated until it reaches the isotropic phase, indicated by a turbidity change from turbid to transparent. The sample is subsequently cooled to room temperature (22.5 ± 0.5 °C), where it is in the nematic phase [50, 178]. The rectangular microfluidic channel consists of two glass plates separated by 6.5 ± 1 μm spacers. To ensure a well-controlled initial condition of the liquid crystal, we use a protocol of surface rubbing which induces a planar alignment of DSCG along the direction of the flow, where both glass plates are rubbed along the cell length direction using diamond particles of diameter ≈ 50 nm [68].

An aqueous solution of 13 wt% disodium cromoglycate (DSCG) is injected into a rectangular microfluidic channel of length $l = 50$ mm, width $w = 15$ mm, and thickness $b = 6.5 \pm 1$ μm. At this concentration, DSCG is in the nematic phase at room temperature

$T = 22.5 \pm 0.5$ °C [50, 178]. The optical birefringence of 13 wt% DSCG at rest, $\Delta n = n_e - n_o$, is -0.015 at a wavelength $\lambda_w = 633$ nm, where n_e and n_o are the extraordinary and ordinary refractive indices [72]. The corresponding maximum retardance, $\Gamma_{max} = \frac{2\pi}{\lambda_w}\Delta n b$, is 0.98 ± 0.15 rad. The liquid crystal is initially planar aligned along the direction of the flow. The flow is induced by injecting DSCG solutions at a volumetric flow rate q, ranging from $q = 0.07$–25 μl/min, controlled by a syringe pump (Harvard PHD 2000). The corresponding Ericksen numbers $\mathrm{Er} = \frac{\eta_2 \bar{\dot{\gamma}} b^2}{K_2}$ vary from 306–109,267, where Er characterizes the relative importance of the viscous forces to the elastic forces. Here, η_2 is the twist viscosity, K_2 is the twist Frank elastic constant, and $\bar{\dot{\gamma}} = q/(wb^2)$ is the average shear rate [46, 50].

After injecting the sample in the microfluidic channel, we allow it to relax for 1 h, until it appears black when imaged through crossed polarizers, where one polarizer is placed parallel to the channel direction. The flow is controlled by a syringe pump (Harvard PHD 2000) set to a volumetric flow rate q ranging between $q = 0.07$–25 μl/min. Once the flow has reached steady state, we image the sample at the center line of the channel at a frame rate of 506 frames per second in a 250×250 μm^2 region far from the inlet (20–30 mm) to avoid artifacts due to the injection protocol. At the lowest flow rate (0.07 μl/min), we start the measurement 40–50 min after the onset of flow. At intermediate flow rates (0.1–0.5 μl/min), we start the measurement after 15–20 min. At higher flow rates (1–25 μl/min), we start the measurement after 5–10 min. These times are well within the steady-state regime, as determined in additional experiments.

5.1.2 Numerical methods

We adopt a hybrid lattice Boltzmann method to simulate the pressure-driven flow of nematic DSCG solutions. This method has been used in prior studies of passive and active lyotropic nematics [149, 168, 179–181]. The nematic is described by a symmetric and traceless tensorial order parameter, defined as [30]

$$\mathbf{Q} = S(\mathbf{nn} - \mathbf{I}/3), \tag{5.1}$$

where S is the scalar order parameter, $\mathbf{n}$ is the unit vector representing the local nematic orientation, and $\mathbf{I}$ is an identity tensor. The governing Beris-Edwards equation of the nematic

microstructure (5.2) reads [182]

$$(\partial_t + \mathbf{u}\cdot\nabla)\mathbf{Q} - \mathbf{S}(\mathbf{W},\mathbf{Q}) = \Gamma\mathbf{H} \tag{5.2}$$

where $\mathbf{u}$ is the velocity vector and Γ is related to the rotational viscosity of the nematic γ_1 via $\Gamma = 2S_0^2/\gamma_1$, with S_0 the equilibrium scalar order parameter. The generalized advection term $\mathbf{S}(\mathbf{W},\mathbf{Q})$ is defined as

$$\begin{aligned}\mathbf{S}(\mathbf{W},\mathbf{Q}) =&(\xi\mathbf{A}+\mathbf{\Omega})(\mathbf{Q}+\mathbf{I}/3) + (\mathbf{Q}+\mathbf{I}/3)(\xi\mathbf{A}-\mathbf{\Omega})\\ &- 2\xi(\mathbf{Q}+\mathbf{I}/3))\,\mathrm{tr}(\mathbf{Q}\mathbf{A}),\end{aligned} \tag{5.3}$$

where $\mathbf{A} = (\nabla\mathbf{u} + (\nabla\mathbf{u})^T)/2$ is the strain rate tensor, $\mathbf{\Omega} = (\nabla\mathbf{u} - (\nabla\mathbf{u})^T)/2$ the vorticity, and ξ a flow-alignment parameter. Here we choose $\xi < 3S_0/(2+S_0)$ to enter a flow-tumbling regime [183]. The molecular field $\mathbf{H}$ is a symmetric, traceless projection of the functional derivative of the free energy of the nematic. Its index form reads

$$H_{ij} = \frac{1}{2}\left(\frac{\delta F}{\delta Q_{ij}} + \frac{\delta F}{\delta Q_{ji}}\right) - \frac{\delta_{ij}}{3}\,\mathrm{tr}\left(\frac{\delta F}{\delta Q_{ij}}\right) \tag{5.4}$$

in which the free energy functional is $F = \int_V f dV$. The density f consists of a short-range Landau-de Gennes component and a long-range elastic component [184]:

$$\begin{aligned}f =& \frac{A_0}{2}\left(1-\frac{U}{3}\right)Q_{ij}Q_{ij} - \frac{A_0U}{3}Q_{ij}Q_{jk}Q_{ki} + \frac{A_0U}{4}(Q_{ij}Q_{ij})^2\\ &+ \frac{1}{2}L_1Q_{ij,k}Q_{ij,k} + \frac{1}{2}L_2Q_{jk,k}Q_{jl,l}\\ &+ \frac{1}{2}L_3Q_{ij}Q_{kl,i}Q_{kl,j} + \frac{1}{2}L_4Q_{jk,l}Q_{jl,k},\end{aligned} \tag{5.5}$$

where A_0 and U are material constants, $Q_{ij,k}$ denotes $\partial_k Q_{ij}$, and L_1 to L_4 are related to the Frank elastic constants through [181]

$$\begin{aligned}L_1 &= \frac{1}{2S_0^2}\left[K_2 + \frac{1}{3}(K_3 - K_1)\right],\\ L_2 &= \frac{1}{S_0^2}(K_1 - K_{24}),\\ L_3 &= \frac{1}{2S_0^3}(K_3 - K_1),\end{aligned} \tag{5.6}$$

$$L_4 = \frac{1}{S_0^2}(K_{24} - K_2),$$

where K_1, K_2, K_3, and K_{24} denote the splay, twist, bend and saddle-splay Frank elastic constants, respectively. Eq. 5.2 is solved using a finite difference method.

The hydrodynamic flow is governed by a momentum equation [183, 185, 186]:

$$\begin{aligned} &\rho(\partial_t + u_j\partial_j)u_i = \partial_j \Pi_{ij} \\ &+ \eta\partial_j \left[\partial_i u_j + \partial_j u_i + (1 - 3\partial_\rho P_0)\partial_\gamma u_\gamma \delta_{ij}\right], \end{aligned} \tag{5.7}$$

where ρ is the density, η is the isotropic viscosity, and $P_0 = \rho T - f$ is the hydrostatic pressure with T being the temperature. The additional stress accounting for the nematic anisotropy is defined as [183, 185, 186]

$$\begin{aligned} \Pi_{ij} = &- P_0\delta_{ij} - \xi H_{ik}\left(Q_{kj} + \frac{1}{3}\delta_{kj}\right) \\ &- \xi\left(Q_{ik} + \frac{1}{3}\delta_{ik}\right)H_{kj} \\ &+ 2\xi\left(Q_{ij} + \frac{1}{3}\delta_{ij}\right)Q_{kl}H_{kl} \\ &- \partial_j Q_{kl}\frac{\delta F}{\delta \partial_i Q_{kl}} + Q_{ik}H_{kj} - H_{ik}Q_{kj}. \end{aligned} \tag{5.8}$$

Eq. 5.7 is solved simultaneously via a lattice Boltzmann method over a D3Q15 grid [185]. The simulation is performed in a rectangular box $[X, Y, Z] = [150, 150, 50]$ in simulation units with periodic boundary conditions in the x- and y-direction, and no-slip and planar anchoring condition in the z-direction. A body force $g \in [2.5 \times 10^{-5} - 5 \times 10^{-5}]$ is applied to generate a pressure-driven flow. Additional details on this method can be found in [186]. Typical simulation parameters are $\Gamma = 0.1$, $\eta = 0.33$, $A = 0.01$, $U = 3.5$ corresponding to $S_0 \sim 0.62$, $\xi = 0.6$ giving rise to $\alpha_3/\alpha_2 = -0.08$, and $[L_1, L_2, L_3, L_4] = [0.01, 0, 0.03247, 0.01333]$ leading to $K_1 : K_2 : K_3 : K_{24} = 1 : 0.33 : 3 : 1$.

5.1.3 Polarized shearing interference microscopy

The optical design of polarized shearing interference microscopy (PSIM) is based on the combination of off-axis shearing interferometry and circular polarization microscopy, as shown in Fig. 5.1. A supercontinuum laser serves as the illumination source with center wavelength at 633 nm set by a bandpass filter with a 10 nm pass band. The excitation is transmitted through a quarter waveplate to produce circular polarization light before impinging on the birefringent sample. The scattered light is then collected by a microscope and transmitted through a second quarter wave plate to transform the electric field's polarization states back to linear polarization. The electric field component parallel and perpendicular to the slow axis of the quarter wave plate encode specimen birefringence information. To quantify the ratio of these two electric field components, the image is duplicated by a diffraction grating, each polarization component is selected by a linear polarizer at the Fourier plane, and they are recombined after a linear polarizer set at 45° to form an interferogram on the CMOS camera.

In the interferogram, interference fringes will only appear in the region that has birefrin-

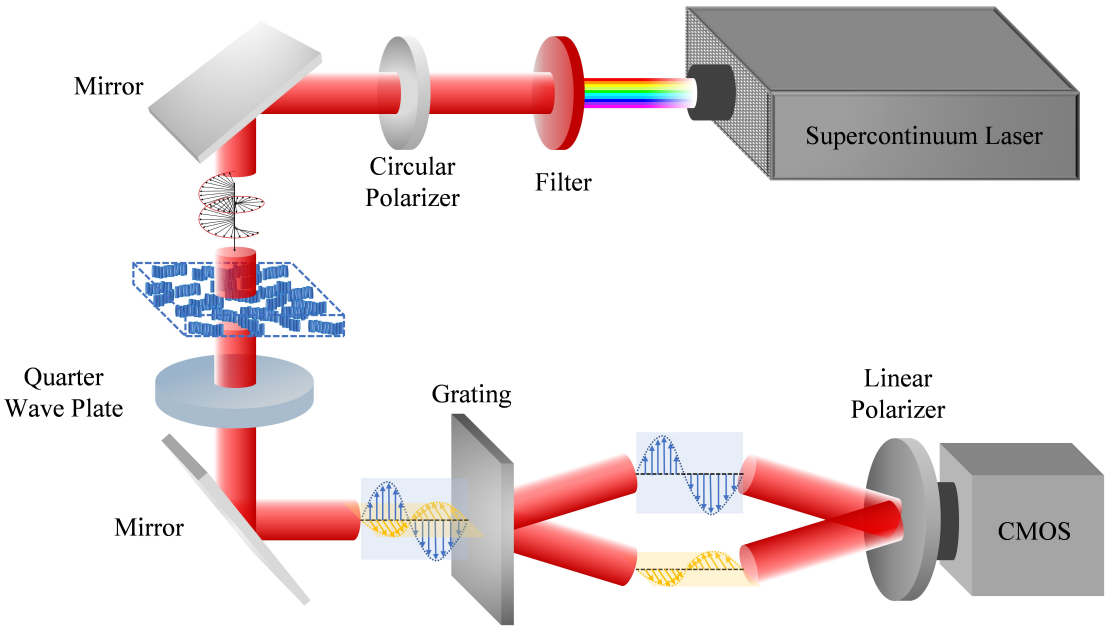

Figure 5.1: **Schematic diagram of polarized shearing interference microscopy (PSIM).** The filter is a band pass filter centered at wavelength 633 nm with bandwidth 10 nm.

gent signals. The retrieval of the optical retardance is thus related to the extraction of the interference fringe's amplitude. Similar to quantitative phase microscopy [187], we extract the amplitude of the retrieved +1 order E, along with the amplitude of the DC term A from the interferograms with a digital holography algorithm. The retardance Γ is extracted as

$$\Gamma = \sin^{-1}\left(\frac{2E}{A}\right). \tag{5.9}$$

This straightforward polarization parameter retrieval algorithm avoids the amplification of noise while quantitatively mapping the retardance from a single interferogram.

During image processing, we down-sample each frame by a factor of 10 (1200×1200 pixels to 120×120 pixels) to reduce the data size. This significantly increases the processing speed, but negligibly affects the information retrieved from the images as the down-sampled pixel size is still comparable to the diffraction limit (the diffraction limit is 1.54 μm, the down-sampled pixel size is 2.08×2.08 μm^2). The time interval between two consecutive frames is 1.97 ms.

5.2 Results and Discussion

5.2.1 Emerging structures in pressure-driven flow of nematic DSCG solutions

When we inject the nematic disodium cromoglycate (DSCG) solution at 13 wt% into the rectangular microfluidic channel, distinct structures emerge in the material upon the onset of the pressure-driven flow, as shown in the snapshots in Fig. 5.2A which are imaged in polarizing optical microscopy with a static full-wave-plate optical compensator (560 nm) with the slow axis oriented at 45° to the crossed polarizers and in the direction parallel to the flow. Orange colors indicate that the director is parallel to the flow direction (x-direction), blue colors indicate that the director is perpendicular to the flow direction [72]. At low flow rate, DSCG is preferentially aligned perpendicular to the flow, adopting a log-rolling state with in-plane orientation angle $\varphi = 90°$, even though before the onset of flow the director is parallel to the flow direction $\varphi = 0°$ (Fig. 5.2B). This realignment of the director

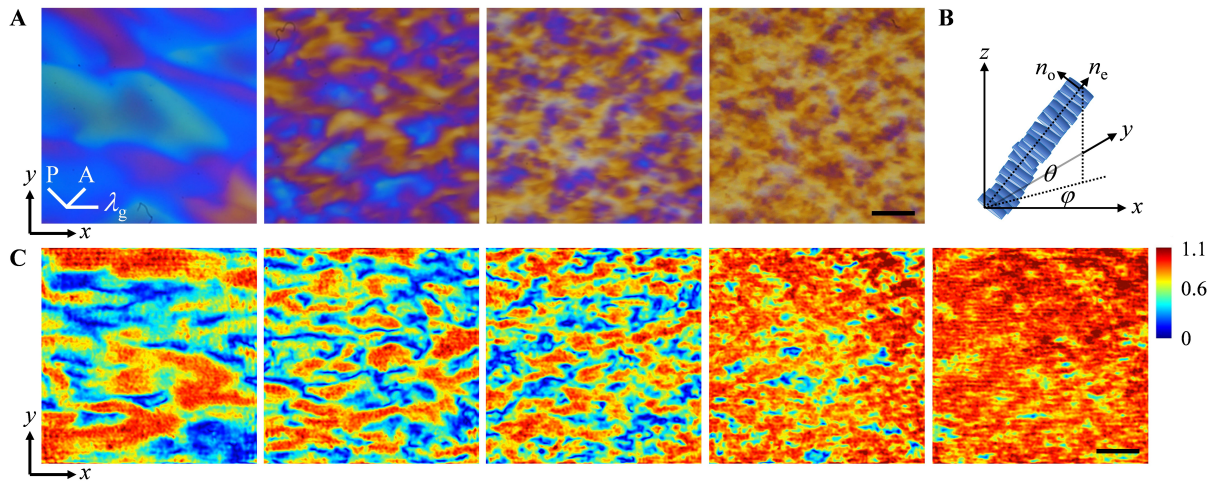

Figure 5.2: **Flow-induced structures in nematic DSCG solutions.** (A) Structures observed in polarizing optical microscopy for (from left to right): $q = 0.07$ μl/min, 0.2 μl/min, 0.5 μl/min, and 3 μl/min, using a full-wave-plate optical compensator with its slow axis, λ_g, aligned parallel to the flow direction. The flow is in the x-direction, the height of the microfluidic channel is in the z-direction. A denotes the analyzer and P denotes the polarizer. (B) Schematic of the director orientation. n_e is the extraordinary refractive index, n_o is the ordinary refractive index. The in-plane orientation angle (azimuthal angle) and out-of-plane orientation angle (polar angle) are φ and θ. (C) Retardance maps obtained from PSIM images for (from left to right): $q = 0.07$ μl/min, 0.2 μl/min, 0.5 μl/min, 3 μl/min and 25 μl/min. The color represents the optical retardance. The scale bars in (A) and (C) are 50 μm.

is a consequence of the tumbling character of DSCG and the significant anisotropy in the splay Frank elastic constant K_1 and twist Frank elastic constant K_2, where $K_1/K_2 \approx 10$; the director reorients by a twist deformation towards the y-axis, instead of deforming in the shear plane which would involve splay deformations [61, 188]. With an increase in flow rate, domains appear where the director increasingly aligns in the direction of the flow. The characteristic size of these domains becomes systematically smaller with increasing flow rate.

To quantify these structures, we use PSIM to obtain a map of the effective optical retardance, as shown in Fig. 5.2C where the colors represent the value of the optical retardance averaged over the thickness of the channel (z-direction). We determine the characteristic size of the domains of varying retardance by calculating the normalized 2D spatial autocovariance in the x- and y-directions, C_x and C_y, as shown in Fig. 5.3A (see Appendix 5.A.1 for details) [189]. The observed decrease in domain size with increasing flow rate is reflected in a decay of the autocovariance at increasingly smaller Δx and Δy, which denote the shift in the

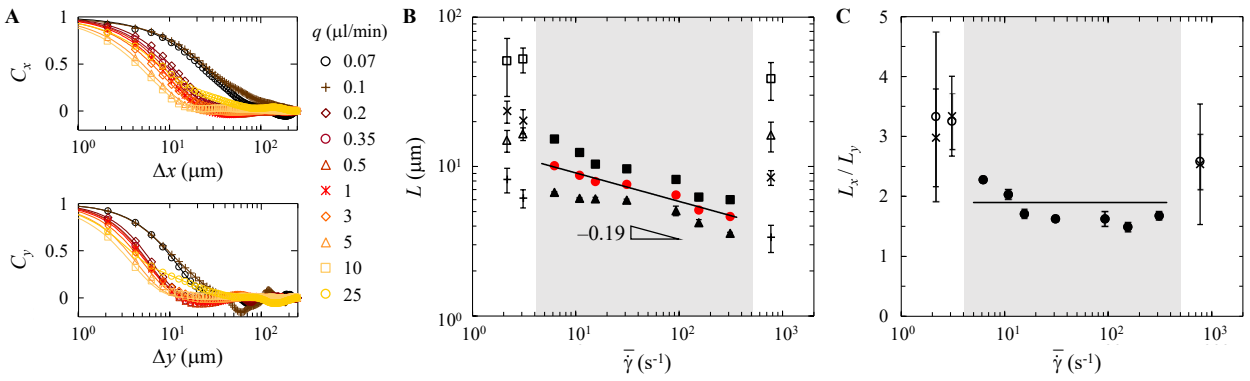

Figure 5.3: **Characteristic size of structures in flowing DSCG solutions controlled by average shear rate.** (A) Normalized 2D spatial autocovariance in the x-direction (top) and in the y-direction (bottom), for different flow rates q. The solid lines denote compressed single or double exponential fits. (B) Characteristic domain sizes versus average shear rate $\dot{\bar{\gamma}}$. Along the x-direction for intermediate average flow rates, L_x (■), and for low and high average flow rates, L_{x_1} (▫), L_{x_2} (×); along the y-direction for intermediate flow rates, L_y (▲), and for low and high flow rates, L_{y_1} (△), L_{y_2} (+); and the average characteristic size $L = \sqrt{L_x L_y}$ (●). The black line denotes $L \propto \dot{\bar{\gamma}}^{-0.19}$. (C) Aspect ratio L_x/L_y (●) for intermediate average flow rates, L_{x_1}/L_{y_1} (○) and L_{x_2}/L_{y_2} (×) for low and high average flow rates. The black line indicates $L_x/L_y \approx \sqrt{K_3/K_1} = 1.9$. In (B) and (C), some of the error bars are smaller than the symbols.

x- and y-direction, respectively. For the two lowest and the highest flow rates probed, C_x and C_y exhibit a two-step decay suggesting a coexistence of structures of two characteristic sizes. We use a double compressed exponential fit to access the characteristic length scales L_{x_1}, L_{x_2}, L_{y_1} and L_{y_2}, characterizing the average sizes of structures along the x- and y-direction. For the intermediate range of flow rates, we fit C_x and C_y with a single compressed exponential function, which yields L_x and L_y. Details on the fits and fit parameters are provided in the Appendix 5.A.1. Remarkably, L_x and L_y decrease monotonically with the average shear rate for $4\ \text{s}^{-1} < \dot{\bar{\gamma}} < 500\ \text{s}^{-1}$, as displayed in Fig. 5.3B. The average characteristic size, defined as $L = \sqrt{L_x L_y}$, exhibits a power-law dependence with the shear rate, $L \propto \dot{\bar{\gamma}}^{-0.19}$. The domains are elongated in the flow direction, with an approximately constant aspect ratio $L_x/L_y = 1.8 \pm 0.3$, as shown in Fig. 5.3C. A decrease or an increase in shear rate leads to different characteristics of the domain sizes and the aspect ratio. We focus our discussion on the intermediate range of shear rates.

5.2.2 Structures represent pure-twist disclination loops

To identify the nature of the structures, we need to understand the observed changes in the optical retardance, which could be attributed to three possible effects: (i) changes of the out-of-plane orientation angle θ, (ii) changes of the order parameter at topological defects or (iii) twist deformations along the z-direction [61]. To reveal the dominant effect leading to the observed retardance and the nature of the structures formed in DSCG solutions, we perform hydrodynamic simulations of tumbling nematic liquid crystals using a hybrid lattice Boltzmann method, which allows us to access the director field for Ericksen numbers $\mathrm{Er} = \frac{\eta_2 \bar{\dot{\gamma}} b^2}{K_2}$ varying from 579–8214, a range which overlaps with the lower flow rates probed in the experiments. At $\mathrm{Er} < 2480$, the directors are predominantly aligned perpendicular to the flow direction (see Appendix 5.A.2 for details). With increasing Er, the directors gradually reorient towards the flow direction. Disclination loops nucleate in the flow, shown as blue lines denoting isosurfaces of order parameter 0.35 in Fig. 5.4*A* for $\mathrm{Er} = 7438$, where the dark rods denote the director field in the plane of the loop. To link the simulations to the experiments, we calculate the effective optical retardance averaged over the channel thickness, as shown in Fig. 5.4*B* (see Appendix 5.A.3). This reveals that the low retardance regions correspond to disclination loops. The majority of the disclination loops are topologically neutral pure-twist disclination loops, where the rotation vector is parallel to the normal direction of the loop [60], as shown in Fig. 5.4*C*.

We can rationalize the formation of pure-twist disclination loops by considering the elastic powers of splay, twist and bend deformations, which can be expressed as $P_{\mathrm{splay}} = \int_\Lambda d\Lambda (\nabla \cdot \mathbf{n})^2$, $P_{\mathrm{twist}} = \int_\Lambda d\Lambda (\mathbf{n} \cdot \nabla \times \mathbf{n})^2$ and $P_{\mathrm{bend}} = \int_\Lambda d\Lambda (\mathbf{n} \times \nabla \times \mathbf{n})^2$, where Λ is a control volume. The simulations indeed show that P_{twist} is larger than the powers associated with splay and bend modes (see Appendix 5.A.4). Therefore, even though the tumbling property of DSCG allows for the formation of wedge disclinations [61], twist-type defects are dominant in pressure-driven flow. To further quantify the prevalence of pure-twist disclination loops, we determine the local winding of the director field along the loop, which is characterized by the twist angle β between the rotation vector $\mathbf{\Omega}$ and the local tangent vector $\mathbf{t}$ of a disclination loop (see inset of Fig. 5.4*D*). A value of $\beta = \pi/2$ denotes a local twist winding; a value of

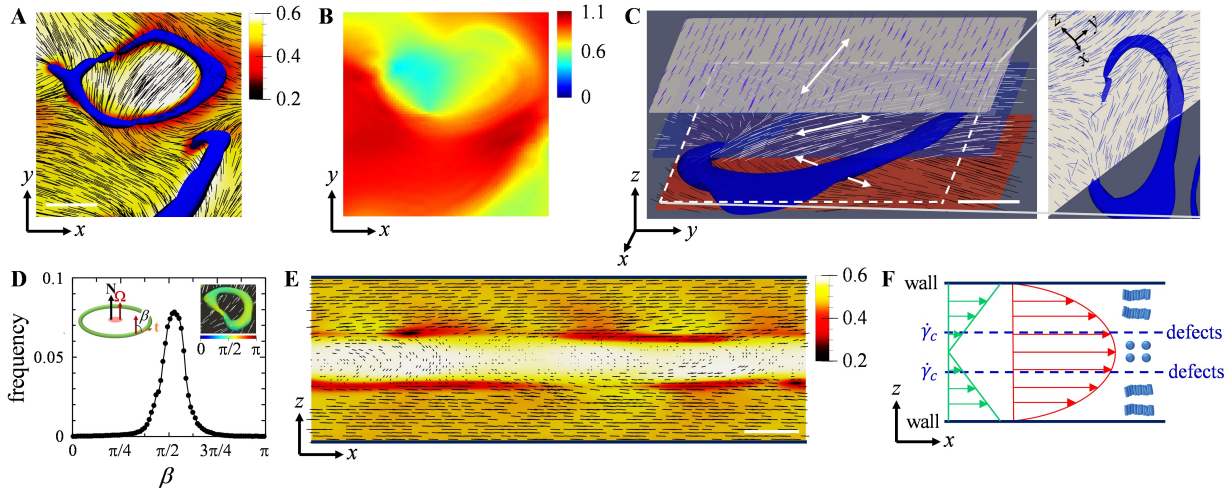

Figure 5.4: **Simulations of the director field in pressure-driven flow for Er = 7438.** (A) Top view of a disclination loop (blue isosurface of order parameter 0.35). The loop is located in the xy-plane. The dark rods denote the directors in the plane of the disclination loop. The color bar denotes the value of the scalar order parameter. The scale bar corresponds to 3 μm in the experiment. (B) Map of the optical retardance averaged along the z-axis and determined from the director field. (C) Structure of a pure-twist disclination loop (blue isosurface). The arrows indicate the local buildup of the twist distortion. The scale bar is 2 μm. (D) Probability distribution of the twist angle β extracted from approximately 100 loops in the simulations. β is the angle between the rotation vector $\mathbf{\Omega}$ and the local tangent vector $\mathbf{t}$ of a disclination loop (left inset). β is close to $\pi/2$, which reveals the prevalence of twist winding. Right inset: The coloring of the disclination loop indicates the twist angle β. (E) Cross-section along the flow direction. The directors align perpendicular to the flow direction in the center of the channel and parallel to the flow direction near the channel walls. The defects predominantly nucleate at the interface between these two regions. The color bar denotes the value of the scalar order parameter. The scale bar is 2 μm. (F) Schematics indicating the log-rolling layer ($\dot{\gamma} < \dot{\gamma}_c$), the layers aligned in the flow direction ($\dot{\gamma} > \dot{\gamma}_c$), and the location of defects. The red arrows schematically represent the velocity profile, the green arrows represent the shear rate profile $\dot{\gamma}$.

$\beta = 0$ or π denotes a local $\pm 1/2$ wedge winding [60]. For a pure-twist disclination loop, the distribution of β is a delta function with $\beta = \pi/2$ everywhere along the loop. A wedge-twist disclination loop, by contrast, is characterized by a β that continuously varies from 0 to π and back to 0 upon one full revolution around the loop (see Appendix 5.A.5 for details). The distribution of β measured for the disclination loops emerging in the flow of DSCG solutions exhibits a peak at $\beta = \pi/2$, as shown in Fig. 5.4D, which reveals that pure-twist disclination loops are indeed prevalent compared to wedge-twist disclination loops. This is

further evidenced by the finding that the rotation vector $\mathbf{\Omega}$ is almost uniformly parallel to the loop normal $\mathbf{N}$ (see Appendix 5.A.5). The emergence of pure-twist disclination loops is a consequence of the smallness of the twist Frank elastic constant, which favors the local buildup of twist distortions in the z-direction, from which the loops nucleate [30, 31, 61].

The pure-twist disclination loops form at the boundary between two regions of irreconcilable director alignments: close to the two channel walls, the directors are aligned in the shear plane, while in a region at the center of the channel the directors adopt a log-rolling state, as shown in Fig. 5.4*E*. Due to the high stored energy in the director gradient at the interface between these two frustrated regions, the elastic stress is released by forming topological defects. This complex director field within the channel gap results from the tumbling character of DSCG and the non-uniform shear rate across the gap; DSCG is in a log-rolling state below a critical shear rate $\dot{\gamma}_c$, but rotates towards the shear plane above $\dot{\gamma}_c$ [59, 61], as schematically shown in Fig. 5.4*F*.

To understand the transition to a different regime of flow structures at lower shear rates, we note that twist deformations can, a priori, lead to two types of topological defects: twist walls aligned parallel to the xy-plane, and pure-twist disclination loops [30, 60]. The energy required to form a twist wall is $E_{\text{twist wall}} \approx 0.4 L_w b\sqrt{-\alpha_2 K_2 \dot{\gamma}}$, where L_w is the length of the twist wall, $K_2 \approx 0.4$ pN is the twist Frank elastic constant and $\alpha_2 \approx -1.66$ Pa s is the Leslie viscosity coefficient for 13 wt% DSCG solutions [50] (see Appendix 5.A.6 for details). The energy required to form a pure-twist disclination loop is $E_{\text{pure-twist}} = \frac{\pi}{4} K_2 L_p \ln\left(\frac{L}{a}\right)$ [30], where L_p and L are the perimeter and the diameter of a pure-twist disclination loop, respectively, and a is the diameter of the defect core in the nematic phase which we estimate to be approximately 0.1 μm. Pure-twist disclination loops rather than twist walls form when $E_{\text{pure-twist}} < E_{\text{twist wall}}$; this condition is reached for a critical shear rate $\dot{\gamma}^* \approx 0.8\ \text{s}^{-1}$. Considering the nonuniform shear rates across the thickness of the channel, twist walls become negligible when the shear rate in the center region (within a nematic coherence length $\approx a$ [31]) reaches $0.8\ \text{s}^{-1}$, which corresponds to a critical average shear rate $\bar{\dot{\gamma}}^* = \frac{\dot{\gamma}^* b}{12a} \approx 4\ \text{s}^{-1}$. This value indeed denotes the onset of the intermediate shear rate regime in Fig. 5.3*B*.

5.2.3 Characteristic size and aspect ratio of pure-twist disclination loops

Having established the emergence of pure-twist disclination loops in the range of intermediate average shear rates now allows us to rationalize the observed power-law dependence of $L \propto \overline{\dot{\gamma}}^{-0.19}$. To do so, we consider the nucleation forces and annihilation forces acting on the loop. The non-uniform twist deformation across the gap favors the nucleation, the viscous force imposed by the flow acts to annihilate the nucleated defects. The energy input to nucleate N pure-twist disclination loops is $E_{\mathrm{n}} = NE_{\text{pure-twist}}$. Simulations have determined that the number of nucleated twist defects at a given time induced by shear flow scales as $N \propto (\mathrm{Er} - \mathrm{Er_c})^{0.5}$ [190], where $\mathrm{Er_c}$ is the critical Ericksen number above which defects nucleate and $\mathrm{Er} = \frac{\eta_2 \dot{\gamma} b^2}{K_2}$ is the Ericksen number that governs the nucleation of twist-type defects. We here set $(\mathrm{Er} - \mathrm{Er_c})^{0.5} \approx \mathrm{Er}^{0.5}$, as we focus on the range where $\mathrm{Er} >> \mathrm{Er_c}$. This then yields the nucleation energy per unit volume as $e_n = E_{\mathrm{n}}/\Lambda \propto \frac{1}{\Lambda}\left(\frac{\eta_2 \dot{\gamma} b^2}{K_2}\right)^{0.5} K_2 L_p \ln\left(\frac{L}{a}\right)$, where Λ is a control volume. The annihilation of pure-twist disclination loops is driven by the viscous force and resisted by the elasticity, and can be expressed as the sum of the viscous forces and the elastic forces in a control volume Λ: $f_a = \frac{1}{\Lambda}\left(\int \eta_2 \dot{\gamma} dS + K_2\right)$, where $\int dS \propto L^2$ is the area occupied by a twist loop of size L. For our range of intermediate average shear rates, $\mathrm{Er} >> 1$, indicating that viscous effects dominate, thus $f_a \propto \frac{\eta_2 \dot{\gamma} L^2}{\Lambda}$. Balancing the nucleation and annihilation forces, $\frac{de_n}{dL} + f_a = 0$, gives an expression for the average characteristic size of the disclination loops:

$$L \propto \left(\frac{K_2}{\eta_2}\right)^{0.25} b^{0.5} \overline{\dot{\gamma}}^{-0.25}. \tag{5.10}$$

This scaling argument indeed yields a power-law exponent for $\overline{\dot{\gamma}}$ fairly close to that observed in experiments, $L \propto \overline{\dot{\gamma}}^{-0.19}$. The characteristic loop size is thus governed by a balance between the nucleation force and the annihilation force acting on the loop.

We can likewise understand the aspect ratio of the pure-twist disclination loops, $L_x/L_y \approx 1.8 \pm 0.3$, as being due to the asymmetric elastic deformation that results from the non-negligible splay-bend anisotropy of DSCG. We consider the aspect ratio to be dominated by the elastic relaxation related to the deformation of the director field at the boundary of the disclination loop. This is a justified assumption given that the timescales related to the loop

fluctuations induced by the viscous torque are much shorter than those characterizing the elastic deformation. The director field within the plane of a pure-twist disclination loop is described by $\mathbf{n} = (\cos\theta\cos\varphi, \cos\theta\sin\varphi, \sin\theta)$, where $\theta = 0°$. The director field outside the loop is uniform and predominantly along the x-direction, so that φ is a small angle close to $0°$. Inside the loop, the director field is likewise uniform, but $\varphi > 0$. With these assumptions, and realizing that the deformation at the boundary of a pure-twist disclination loop along the x-direction involves bend deformations, while that along the y-direction involves splay deformations, the nematodynamic equation [30, 31] along the x-direction then reads (see Appendix 5.A.7 for details)

$$K_3\frac{\partial^2\varphi}{\partial x^2} + K_2\frac{\partial^2\varphi}{\partial z^2} = \gamma_1\frac{d\varphi}{dt}, \tag{5.11}$$

and along the y-direction

$$K_1\frac{\partial^2\varphi}{\partial y^2} + K_2\frac{\partial^2\varphi}{\partial z^2} = \gamma_1\frac{d\varphi}{dt}, \tag{5.12}$$

where γ_1 is the rotational viscosity, $\frac{\partial^2\varphi}{\partial x^2} \propto \frac{1}{{L_x}^2}$, $\frac{\partial^2\varphi}{\partial y^2} \propto \frac{1}{{L_y}^2}$, and $\frac{\partial^2\varphi}{\partial z^2} \propto \frac{1}{b^2}$. We interrogate the characteristic length scales in the x- and y-directions related to the spatial gradient of the director field within a certain time window. The time scales related to the elastic deformation in the x- and y-direction then scale as $\Delta t_x \propto \frac{\gamma_1}{\left(\frac{K_3}{{L_x}^2} + \frac{K_2}{b^2}\right)}$ and $\Delta t_y \propto \frac{\gamma_1}{\left(\frac{K_1}{{L_y}^2} + \frac{K_2}{b^2}\right)}$, respectively. With $K_1, K_3 >> K_2$ [46], this simplifies to $\Delta t_x \propto \frac{\gamma_1 {L_x}^2}{K_3}$ and $\Delta t_y \propto \frac{\gamma_1 {L_y}^2}{K_1}$. At steady state, $\Delta t_x = \Delta t_y$, which yields

$$\frac{L_x}{L_y} \approx \sqrt{\frac{K_3}{K_1}} = 1.9. \tag{5.13}$$

The value of 1.9 is in good agreement with the experimentally determined value of 1.8 ± 0.3.

5.2.4 Dynamics of pure-twist disclination loops

Our single-shot imaging technique PSIM allows us to resolve the dynamics of the pure-twist disclination loops. We calculate the normalized spatiotemporal autocovariance, C_t, which contains the coupled information of two contributions: the fluctuations of the disclination loops characterized by a fluctuation time τ_1 and the translation of the disclination loops imposed by the background flow characterized by a translation time τ_2. To remove the contribution from the background flow, we need to place ourselves in the frame of reference

of the disclination loop. In this Lagrangian framework, we move the region of interest by $\Delta x = V_f \Delta t$ at each time lag Δt, where V_f is the velocity of the frame of reference. Only if V_f is equal to the center of mass velocity of the disclination loop, V^*, we access the fluctuations. In our pressure-driven flow, the flow velocity varies across the thickness of the channel. As the location of the pure-twist disclination loops within the channel is unknown, V^* is unknown. We thus calculate C_t for different frame of reference velocities, as shown in Fig. 5.5*A* for V_f equal to the average velocity across the channel $\bar{V}$, and determine the characteristic time τ by fitting to a stretched exponential function (details on the fit and fit parameters are provided in the Appendix 5.A.1). The relation between the fluctuation time τ_1, the translation time τ_2 and the characteristic time τ can be expressed as (see Appendix 5.A.8 for details)

$$\frac{1}{\tau} = \frac{1}{\tau_1} + \frac{1}{\tau_2}, \tag{5.14}$$

where $\frac{1}{\tau_2} = \frac{|V^* - V_f|}{L_x}$ with L_x the characteristic length scale along the x-direction. This expression indeed well describes the dependence of τ^{-1} on $V_f/\bar{V}$, as shown in Fig. 5.5*B* for different flow rates.

The frame of reference velocity V_f at which τ^{-1} reaches a minimum denotes the center of mass velocity, V^*, which is between 1.1–1.4$\bar{V}$. This indicates that the disclination loops are located in the bulk flow rather than near the channel walls, in agreement with our simulations. Fitting τ^{-1} with Eq. 5.14 yields the fluctuation time τ_1 and the characteristic length scale along the x-direction, L_x, as shown in Fig. 5.5*C* and *D*. The agreement between L_x from this fit and L_x from the normalized spatial autocovariance validates our approach. The fluctuation time τ_1 scales as $1/\bar{\dot{\gamma}}$. To understand this dependence, we consider the nematodynamic equations for the director field $\mathbf{n} = (\cos\theta\cos\varphi, \cos\theta\sin\varphi, \sin\theta)$. Given the high Ericksen number regime of our experiments, we here neglect the elastic contributions [30, 31]:

$$\gamma_1 \cos\theta\dot{\varphi} = -\alpha_2 \sin\theta \sin\varphi\dot{\gamma}, \tag{5.15}$$

$$\gamma_1\dot{\theta} = (\alpha_2 \sin^2\theta - \alpha_3 \cos^2\theta)\cos\varphi\dot{\gamma}, \tag{5.16}$$

where α_2 and α_3 are the Leslie viscosity coefficients, and γ_1 is the rotational viscosity. We

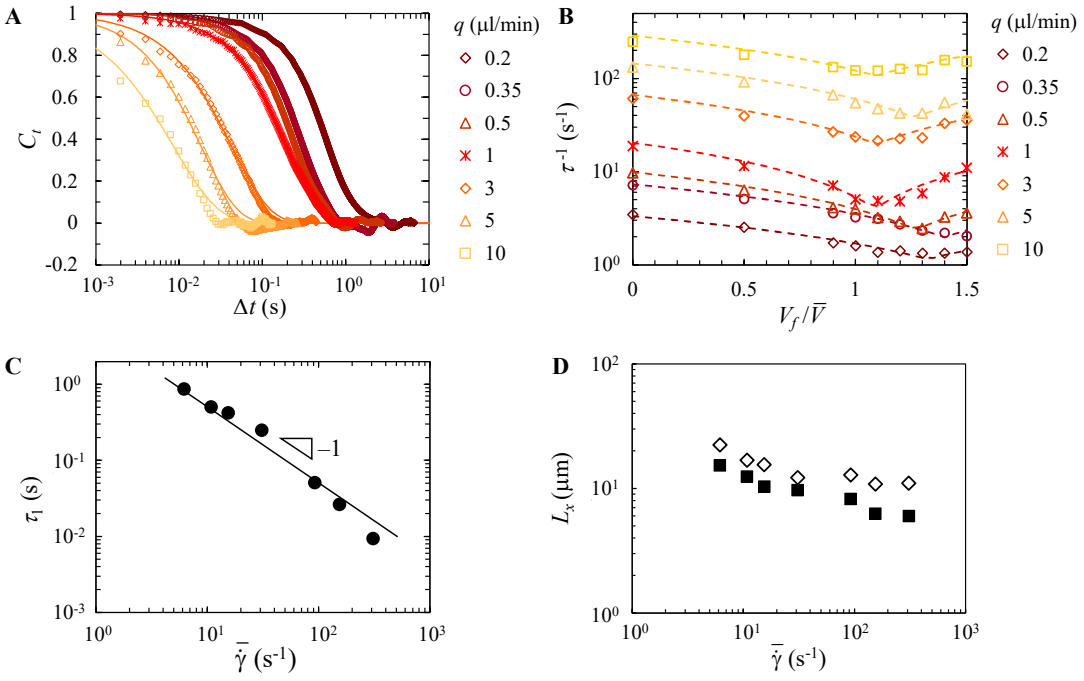

Figure 5.5: **Dynamics of pure-twist disclination loops.** (A) Normalized spatiotemporal autocovariance for different flow rates q, for a frame of reference velocity V_f equal to the average velocity $\bar{V}$. The lines denote stretched/compressed exponential fits. (B) Inverse characteristic time, τ^{-1}, versus $V_f/\bar{V}$ for different flow rates q. The dashed lines denote best-fits to Eq. 5.14. (C) The fluctuation time τ_1 decreases linearly with the average shear rate. The black line denotes $\tau_f \approx \frac{3}{4}\frac{\gamma_1}{\sqrt{-\alpha_2\alpha_3}}\frac{1}{\dot{\bar{\gamma}}}$. (D) Comparison between L_x from fitting τ^{-1} ($\diamond$) and L_x from fitting the normalized spatial autocovariance ($\blacksquare$).

account for the tumbling character of nematic DSCG solutions by considering small out-of-plane perturbations θ_1 and in-plane perturbations φ_1 for directors aligned perpendicular to the flow direction: $\theta = \theta_1$ and $\varphi = \frac{\pi}{2} + \varphi_1$. Linearizing Eq. 5.15 and Eq. 5.16 in terms of these perturbations yields a characteristic fluctuation time of the tumbling nematics: $\tau_f \approx \frac{3}{4}\frac{\gamma_1}{\sqrt{-\alpha_2\alpha_3}}\frac{1}{\dot{\bar{\gamma}}}$ (see Appendix 5.A.9 for details). Using $\alpha_2 \approx -1.66$ Pa s and $\alpha_3 \approx 0.03$ Pa s [50], we observe a good agreement with τ_1 from our experiments, as shown by the black line in Fig. 4*C*. This shows that the fluctuations of the pure-twist disclination loops are a direct reflection of the tumbling dynamics of the director.

5.3 Conclusions

Our studies reveal the emergence of pure-twist disclination loops in a range of intermediate shear rates in pressure-driven flow of nematic DSCG solutions. The disclination loops form at the boundary between two regions of irreconcilable director alignments. Their nucleation releases the high elastic stresses of the director gradient at the boundary, which induces twist-type defects because of the low elastic cost associated with the twist mode compared to bend and splay modes in DSCG solutions. By controlling the shear rate we can tune both the size and the dynamics of the pure-twist disclination loops, which could provide guidelines for using flowing LCLCs to guide the assembly of active matter or particles [151]. We demonstrate the power of polarized shearing interference microscopy in unraveling fluctuations of defects, which may also enable investigations of the dynamics of other non-equilibrium systems, including active nematics or turbulent elongated cells [60, 191, 192].

5.A Appendices

5.A.1 Normalized Autocovariance

We calculate the normalized 2D spatial autocovariance in the x- and y-direction as

$$C_{xy}(\Delta x, \Delta y) = \left\langle \frac{E\left[\left(\Gamma_{x,y,t} - \mu_{x,y}\right)\left(\Gamma_{x+\Delta x,y+\Delta y,t} - \mu_{x,y}\right)\right]}{\sigma^2_{x,y}} \right\rangle_t, \tag{5.17}$$

where $\Gamma_{x,y,t}$ denotes the retardance at a location (x, y) at time t. $\mu_{x,y}$ is the average spatial retardance and $\sigma^2_{x,y}$ is the spatial variance at time t. The bracket $\langle\rangle_t$ denotes the temporal average. Δx and Δy are shifts in the x- and y-direction, respectively. The normalized 2D spatial autocovariance in the x-direction, C_x, is defined as $C_{xy}(\Delta x, \Delta y = 0)$, and the normalized 2D spatial autocovariance in the y-direction, C_y, is defined as $C_{xy}(\Delta x = 0, \Delta y)$.

The normalized temporal autocovariance is calculated as

$$C_t(\Delta t) = \left\langle \frac{E\left[\left(\Gamma_{x,y,t} - \mu_t\right)\left(\Gamma_{x,y,t+\Delta t} - \mu_t\right)\right]}{\sigma^2_t} \right\rangle_{x,y}, \tag{5.18}$$

where μ_t is the average temporal retardance and σ^2_t is the temporal variance at a location

(x, y). The brackets $\langle\rangle_{x,y}$ denote the spatial average.

We use a Lagrangian framework where we move the region of interest by $\Delta x = V_f \Delta t$ at each time lag Δt, where V_f denotes the velocity of the frame of reference. The normalized temporal autocovariance in this moving framework then becomes a normalized spatiotemporal autocovariance:

$$C_t(\Delta t) = \left\langle \frac{E\left[\left(\Gamma_{x,y,t} - \tilde{\mu}_t\right)\left(\Gamma_{x+V_f\Delta t,y,t+\Delta t} - \tilde{\mu}_t\right)\right]}{\tilde{\sigma}_t^2} \right\rangle_{x,y}, \tag{5.19}$$

where $\tilde{\mu}_t$ is the average temporal retardance and $\tilde{\sigma}_t$ is the temporal variance at a fixed point in the moving framework.

Fitting method for the normalized autocovariance

In the range of shear rates $4\ \mathrm{s}^{-1} < \overline{\dot{\gamma}} < 500\ \mathrm{s}^{-1}$, we fit C_x and C_y with a single compressed/stretched exponential function:

$$\begin{aligned} C_x &= \exp\left(-\left(\frac{\Delta x}{L_x}\right)^{\alpha_x}\right), \\ C_y &= \exp\left(-\left(\frac{\Delta y}{L_y}\right)^{\alpha_y}\right), \end{aligned} \tag{5.20}$$

where α_x and α_y are the compressed exponents for C_x and C_y, and L_x and L_y are the characteristic length scales of the structures along each direction. The values of α_x and α_y are reported in Table 5.1.

For $\overline{\dot{\gamma}} < 4\ \mathrm{s}^{-1}$ and $\overline{\dot{\gamma}} > 500\ \mathrm{s}^{-1}$, we fit C_x and C_y with a double compressed/stretched exponential function:

$$\begin{aligned} C_x &= (1 - c_x)\exp\left(-\left(\frac{\Delta x}{L_{x,1}}\right)^{\alpha_{x_1}}\right) + c_x \exp\left(-\left(\frac{\Delta x}{L_{x,2}}\right)^{\alpha_{x_2}}\right), \\ C_y &= (1 - c_y)\exp\left(-\left(\frac{\Delta y}{L_{y,1}}\right)^{\alpha_{y_1}}\right) + c_y \exp\left(-\left(\frac{\Delta y}{L_{y,2}}\right)^{\alpha_{y_2}}\right), \end{aligned} \tag{5.21}$$

where c_x and c_y are weight coefficients of the second decay. We then obtain four characteristic length scales: L_{x_1} and L_{x_2} along the x-direction, and L_{y_1} and L_{y_2} along the y-direction, suggesting the coexistence of structures of two characteristic sizes. The values of α_{x_1}, α_{x_2},

Table 5.1: Exponents and weight coefficients of the decays along the x-direction and the y-direction

$\bar{\dot{\gamma}}$ (s^{-1})	α_x	α_{x_1}	α_{x_2}	c_x	α_y	α_{y_1}	α_{y_2}	c_y
2.16		0.98	1.26	0.45		1.83	1.40	0.47
3.09		0.93	1.78	0.32		1.45	1.76	0.25
6.17	0.97				1.65			
10.80	1.06				1.64			
15.43	1.36				1.65			
30.86	1.35				1.63			
92.59	1.23				1.48			
154.32	1.23				1.44			
308.64	1.16				1.34			
771.60		0.95	1.29	0.68		1.16	1.49	0.58

α_{y_1} and α_{y_2}, and the values for c_x and c_y, are reported in Table 5.1.

Finally, in the range of shear rates $4\ s^{-1} < \bar{\dot{\gamma}} < 500\ s^{-1}$, we fit the normalized spatiotemporal autocovariance, C_t, calculated for different frame of reference velocities, V_f, with a stretched/compressed exponential function:

$$C_t = \exp\left(-\left(\frac{\Delta t}{\tau}\right)^{\beta}\right), \tag{5.22}$$

where β is the exponent and τ the characteristic time. The values of β for different V_f are reported in Table 5.2.

Table 5.2: Fitting parameters for the normalized spatiotemporal autocovariance C_t

V_f/V_0	0	0.5	0.9	1	1.1	1.2	1.3	1.5
$\bar{\dot{\gamma}}$ (s^{-1})	β	β	β	β	β	β	β	β
6.17	1.49	1.40	1.23	1.28	1.16	1.29	1.20	1.10
10.8	1.46	1.36	1.29	1.32	1.36	1.25	1.08	0.97
15.43	1.53	1.40	1.26	1.24	0.97	1.05	1.01	0.97
30.86	1.50	1.32	1.10	1.04	0.86	0.83	0.90	1.07
92.59	1.42	1.22	1.06	0.93	0.90	0.68	0.70	0.84
154.32	1.44	1.28	1.06	0.99	0.94	0.74	0.68	0.72
308.64	1.53	1.30	1.09	0.74	0.64	0.64	0.59	0.87

5.A.2 Director field in the numerical simulations

With an increase in Ericksen number Er from 579 to 8214, the directors in the center of the channel transition from being aligned perpendicular to the flow direction to exhibiting undulations, as shown in the top panel of Fig. 5.6.

The director field across the thickness of the channel exhibits distinct features at different average shear rates. For lower shear rates (Er = 1147 and Er = 2480), most directors are aligned perpendicular to the flow direction (Fig. 5.6 *A* and *B*); at higher shear rates (Er = 5734 and Er = 7438), directors in the center of the channel remain perpendicular to the flow direction but those close to the two channel walls reorient parallel to the flow direction (Fig. 5.6 *C* and *D*). Disclinations nucleate at the boundary between these two frustrated regions. Calculating the retardance maps in simulations and evaluating the characteristic length scales L_x and L_y following the same procedure as in the experiments, we find an aspect ratio $L_x/L_y \approx 2.4 \pm 0.2$ for Er = 5734 and Er = 7438, fairly close to the value obtained in experiments at comparable Ericksen numbers, $L_x/L_y \approx 1.8 \pm 0.3$. The aspect ratio measured in simulations increases significantly (~ 9) at lower shear rates (Er = 2480), again in qualitative agreement with the experimental findings. In these low Ericksen number flows, twist walls are the dominant type of defect in pressure-driven DSCG solutions. The undulations

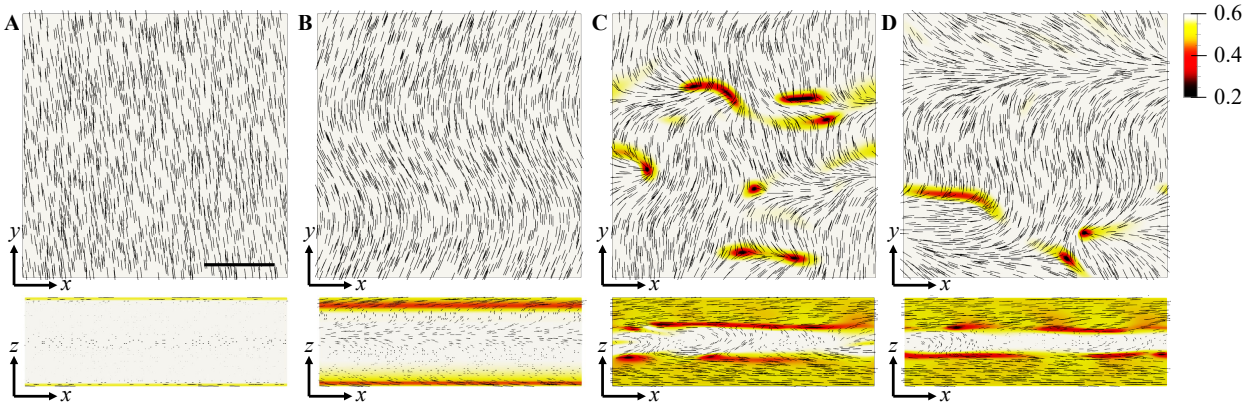

Figure 5.6: Simulation snapshots of the director field in pressure-driven flow for Ericksen numbers Er = 1147 (*A*), Er = 2480 (*B*), Er = 5734 (*C*), and Er = 7438 (*D*). The scale bar corresponds to 5 μm in the experiment. Top row: top view of the center plane of the channel. Bottom row: side view of the channel. The short black lines denote the director field, the color indicates the scalar order parameter.

observed in simulations (Fig. 5.6B) indicate the coexistence of left-twist and right-twist walls along the z-direction. Forming a boundary of these domains in the y-direction would involve a splay-mode elastic penalty, while forming a boundary in the x-direction would involve a bend-mode elastic penalty. As $K_3 > K_1$, the splay-mode elastic penalty is lower, and thus the domain walls align in the x-direction, which results in the large aspect ratio.

5.A.3 Forward model for the determination of the retardance map from simulation data

We develop a model to calculate the retardance map from the liquid crystal director field obtained in simulations. This allows us to qualitatively compare the retardance maps obtained experimentally in PSIM with those from simulations. The model is based on the Beam Propagation Method [193, 194], where the specimen volume is divided into multiple layers and the optical field is updated after accounting for the layer perturbation on the field. The relation between the optical field at axial position z, and the optical field at axial position $z + \delta z$, can be expressed as

$$a(x, y, z + \delta z) = e^{jk_0(\delta n(\mathbf{r}))\delta z} \times \mathrm{Im}^{-1}\left(\mathrm{Im}\{(a(\cdot, \cdot, z))\} \times e^{-j\left(\frac{\omega_x^2+\omega_y^2}{k_0 n_0+\sqrt{k_0^2 n_0^2-\omega_x^2-\omega_y^2}}\right)\delta z}\right), \quad (5.23)$$

where $a(\mathbf{r})$ is the complex envelope of the paraxial optical wave $u(\mathbf{r}) = a(\mathbf{r}) \exp\{(jk_0 n_0 z)\}$, and $\mathbf{r} = (x, y, z)$ denotes the position in three-dimensional (3D) space. k_0 is the wave number of the illumination light, n_0 is the refractive index of the medium, ω_x and ω_y denote the spatial frequencies along the x- and y-directions, Im represents a two-dimensional (2D) spatial Fourier transform, δz is the interval between layers, and $\delta n(\mathbf{r}) = n(\mathbf{r}) - n_0$ is the refractive index difference between the medium and the sample.

This equation though only describes the isotropic scattering of a scalar light field and must be generalized to account for the material birefringence on a vector field. Eq. 5.23 is rewritten

as

$$\mathbf{E}(x,y,z+\delta z) = J(x,y,z+\delta z) \times \mathrm{Im}^{-1}\left(\mathrm{Im}\{(\mathbf{E}(\cdot,\cdot,z))\} \times e^{-j\left(\frac{\omega_x^2+\omega_y^2}{k_0 n_0 + \sqrt{k_0^2 n_0^2 - \omega_x^2 - \omega_y^2}}\right)\delta z} \right), \quad (5.24)$$

where $\mathbf{E}(.,.,z)$ is the vectorial expression of the paraxial light wave field at axial position z. The three components of the electric field along the x-, y- and z-directions at a location denoted by a 3D position vector $\mathbf{r}$ are

$$\mathbf{E}(\mathbf{r}) = \begin{pmatrix} E_x(\mathbf{r}) \\ E_y(\mathbf{r}) \\ E_z(\mathbf{r}) \end{pmatrix}. \quad (5.25)$$

A Jones matrix formulation is used to describe the birefringent properties of the medium. $J(\mathbf{r})$ is the Jones matrix of the sample at position $\mathbf{r}$ and describes the anisotropic scattering property of the specimen. The expression of the Jones matrix can be expressed as

$$J(\mathbf{r}) = \begin{pmatrix} J_{xx} & J_{xy} & J_{xz} \\ J_{yx} & J_{yy} & J_{yz} \\ J_{zx} & J_{zy} & J_{zz} \end{pmatrix}(\mathbf{r}). \quad (5.26)$$

Each component of the Jones matrix can be related to the local director field of liquid crystals at a position $\mathbf{r}$:

$$\begin{aligned}
J_{xx} &= e^{j\phi_\mathrm{e}} \cos^2\varphi \sin^2\theta + e^{j\phi_\mathrm{o}}(\sin^2\varphi + \cos^2\varphi \sin^2\theta), \\
J_{xy} &= -\left(e^{j\phi_\mathrm{e}} - e^{j\phi_\mathrm{o}}\right) \sin\varphi \cos\varphi \cos^2\theta, \\
J_{xz} &= \left(e^{j\phi_\mathrm{e}} - e^{j\phi_\mathrm{o}}\right) \cos\varphi \sin\theta \cos\theta, \\
J_{yx} &= J_{xy}, \\
J_{yy} &= e^{j\phi_\mathrm{e}} \sin^2\varphi \cos^2\theta + e^{j\phi_\mathrm{o}}(\cos^2\varphi + \sin^2\varphi \sin^2\theta), \\
J_{yz} &= -\left(e^{j\phi_\mathrm{e}} - e^{j\phi_\mathrm{o}}\right) \sin\varphi \sin\theta \cos\theta, \\
J_{zx} &= J_{xz},
\end{aligned} \quad (5.27)$$

$$J_{zy} = J_{yz},$$
$$J_{zz} = e^{j\phi_{\mathrm{e}}} \sin^2\theta + e^{j\phi_{\mathrm{o}}} \cos^2\theta.$$

For notational simplicity, we have not explicitly expressed the position $\mathbf{r}$ of the Jones matrix components. φ and θ are the in-plane and out-of-plane orientation angles of the director field at position $\mathbf{r}$. ϕ_{e} and ϕ_{o} are the phase delays caused by the local refractive index of the sample along the extraordinary axis n_{e} and the ordinary axis n_{o}:

$$\begin{aligned} \phi_{\mathrm{e}} &= k_0 n_{\mathrm{e}} \delta z, \\ \phi_{\mathrm{o}} &= k_0 n_{\mathrm{o}} \delta z. \end{aligned} \tag{5.28}$$

In PSIM, right-hand circular polarization illumination is used; the electric field at layer 0 is thus expressed as

$$\mathbf{E}(\cdot, \cdot, z = 0) = \frac{1}{\sqrt{2}} \begin{pmatrix} 1 \\ i \end{pmatrix}. \tag{5.29}$$

We keep track of the components along the x- and y-directions since the camera can only detect the intensity distribution in the x-y plane. Eq. 5.24 is used recursively to calculate the light field scattered by the birefringent specimen layer by layer, and the light field exiting the specimen is denoted as $\mathbf{E}_{out}$. After exiting the specimen, the light field transmits through a quarter wave plate (QWP). Thereafter, the components of the light field along the x-direction and the y-direction are separated by a diffraction grating, and interfere at the image plane with a linear polarizer with a polarization direction that is 45° to the x-direction. The light field after transmitting the QWP is expressed as

$$\mathbf{E}_{out}^{(1)} = J_{\mathrm{QWP}} \mathbf{E}_{out} = \begin{pmatrix} 1 & 0 \\ 0 & i \end{pmatrix} \mathbf{E}_{out}. \tag{5.30}$$

The vectorial optical field after the grating is expressed as

$$\mathbf{E}_{out}^{(2)} = \frac{1}{\sqrt{2}} \begin{pmatrix} 1 & 1 \\ -1 & 1 \end{pmatrix} \mathbf{E}_{out}^{(1)}. \tag{5.31}$$

Finally, the retardance distribution is determined as

$$\Gamma = \sin^{-1}\left(|E^{(2)}_{out,x} \cdot E^{(2)}_{out,y}|\right), \tag{5.32}$$

where $E^{(2)}_{out,x}$ and $E^{(2)}_{out,y}$ are the components of $\mathbf{E}^{(2)}_{out}$ along the x- and y-directions. $|\cdot|$ denotes the operation of extracting the amplitude value from a complex number. This simulation is performed in a box of size $150 \times 150 \times 50$ pixels, and the pixel size in the x-y plane is ~ 0.2 μm same as in the experiment, while the interval along the z-direction is $\delta z = 0.12$ μm. The refractive index values along the extraordinary axis n_e and the ordinary axis n_o are 1.350 and 1.365, while the refractive index of the medium n_0 is 1.337.

5.A.4 Elastic powers of splay, twist and bend deformations

From the director field in the numerical simulations, we calculate the elastic powers of splay, twist and bend deformations, which are expressed as $P_{\text{splay}} = \int_\Lambda d\Lambda(\nabla \cdot \mathbf{n})^2$, $P_{\text{twist}} = \int_\Lambda d\Lambda(\mathbf{n} \cdot \nabla \times \mathbf{n})^2$ and $P_{\text{bend}} = \int_\Lambda d\Lambda(\mathbf{n} \times \nabla \times \mathbf{n})^2$, where Λ is a control volume. P_{twist} is larger than the powers associated with splay and bend deformations (Fig. 5.7).

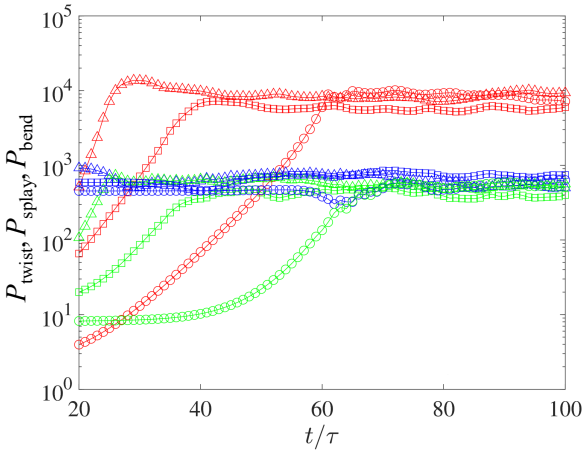

Figure 5.7: Elastic power analysis of different deformation modes in simulations. Temporal evolution upon the onset of flow of the power of twist, P_{twist} (red), the power of splay, P_{splay} (blue) and the power of bend, P_{bend} (green) for Ericksen numbers Er = 6509 (△), Er = 7438 (▫) and Er = 8214 (○). In steady state, the power of twist is significantly larger than the powers of the other two modes.

5.A.5 Topological structure of disclination loops in numerical simulations

We characterize the topological structure of the disclination loops by calculating the local winding of the director field along the loop [60, 168, 195]. We introduce the twist angle β, which denotes the angle between the rotation vector $\mathbf{\Omega}$ and the local tangent vector $\mathbf{t}$ of a disclination loop, as illustrated in Fig. 5.8A; $\cos\beta = \mathbf{t}\cdot\mathbf{\Omega}$. In a wedge-twist disclination loop, β varies continuously from 0 (denoting $+1/2$ wedge winding) to π (denoting $-1/2$ wedge winding) and back to 0 upon a full revolution along the loop. In a pure-twist disclination loop, $\beta = \pi/2$ at all points on the loop [60].

Validation of β and γ determination

By choosing an appropriate ansatz, we construct a wedge-twist disclination loop and a pure-twist disclination loop in simulation as shown in Fig. 5.8B and C, to validate our calculation

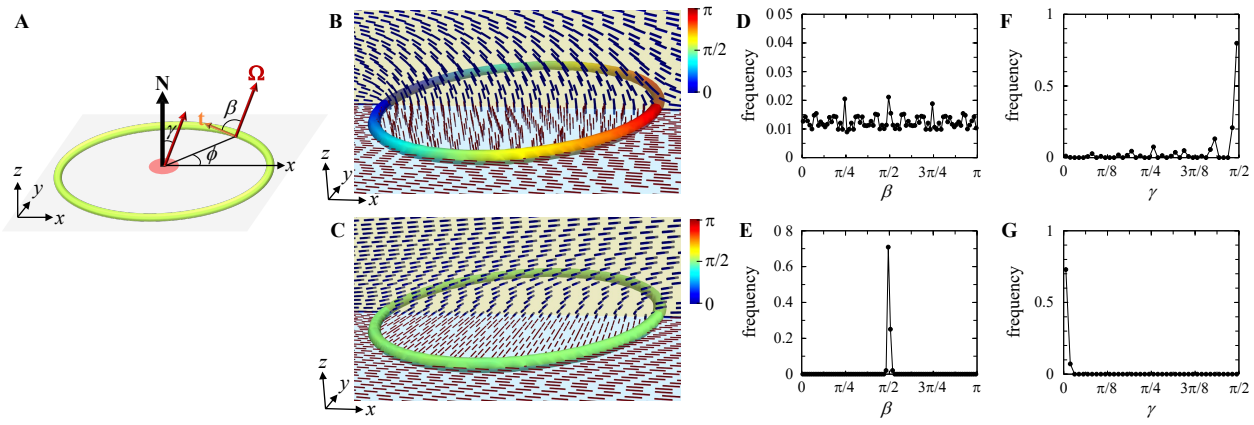

Figure 5.8: Local winding in wedge-twist and pure-twist disclination loops. (A) Schematics illustrating the tangent vector $\mathbf{t}$, the rotation vector Ω, the disclination loop normal $\mathbf{N}$, the azimuthal angle ϕ, the twist angle β, and the angle γ. (B) A designed wedge-twist disclination loop and (C) a designed pure-twist disclination loop. The color map indicates the twist angle β. In (B) and (C), the yellow background indicates the xz-plane across the center line of the loop; the blue background indicates the xy-plane across the center line of the loop. The blue rods denote directors in the xz-plane; the brown rods denote directors in the xy-plane. (D) Distribution of β for the wedge-twist disclination loop shown in (B). (E) Distribution of β for the pure-twist disclination loop shown in (C). (F) Distribution of γ inferred from the distribution of β for the wedge-twist disclination loop. (G) Distribution of γ inferred from the distribution of β for the pure-twist disclination loop.

of the distribution of the twist angle β. We define the angle ψ as the angle between the director and the x-axis. For a wedge-twist disclination loop, we set $\mathbf{n} = \mathbf{x}\cos(\psi) + \mathbf{z}\sin(\psi)$ inside and $\mathbf{n} = \mathbf{x}$ outside a cylindrical region, with ψ continuously changing from 0 at the bottom channel wall to π at the top channel wall. For a pure-twist disclination loop, we set $\mathbf{n} = \mathbf{x}\cos(\psi) + \mathbf{y}\sin(\psi)$ inside and $\mathbf{n} = \mathbf{x}$ outside a cylindrical region, with ψ again continuously varying from 0 to π along the z-direction. We equilibrate the system for 30,000 time steps and then evaluate β for all grid points within the disclination region characterized by a scalar order parameter $S \leqslant 0.37$ following a similar method as discussed in [60]. By calculating the tangent vector $\mathbf{t}$ and the rotation vector $\mathbf{\Omega}$, we find $\beta = \arccos \mathbf{t} \cdot \mathbf{\Omega}$. For the wedge-twist disclination loop, the distribution of β is approximately uniform from 0 to π, as shown in Fig. 5.8*D*. The distribution of β for the pure-twist disclination loop exhibits a peak at $\beta = \pi/2$, as shown in Fig. 5.8*E*. These findings are in agreement with the expected values for β.

Given that the rotation vector $\mathbf{\Omega}$ is spatially uniform for both types of disclination loops [60], we can define the angle γ as the angle between $\mathbf{\Omega}$ and the normal of the disclination loop $\mathbf{N}$, another measure used to infer the topological structure of disclination loops. In a wedge-twist disclination loop $\gamma = \pi/2$, in a pure-twist disclination loop $\gamma = 0$. We here show how we can estimate γ from the statistics of β.

We first derive the distribution of β for a disclination loop. We introduce the azimuthal angle ϕ to get the expressions $\mathbf{t} = (-\sin\phi)\mathbf{x} + (\cos\phi)\mathbf{y}$ and $\mathbf{\Omega} = (\sin\gamma)\mathbf{x} + (\cos\gamma)\mathbf{z}$, which yields the relation $\cos\beta = -\sin\phi\sin\gamma$. The symmetry of the problem allows us to focus on $-\pi/2 < \phi \leqslant \pi/2$. We denote the probability of having a value of β for a given γ as $P(\beta|\gamma)$, and the probability of having a value of ϕ for a given γ as $P(\phi|\gamma)$, such that $P(\beta|\gamma)d\beta = P(\phi|\gamma)d\phi$.

Because of the circular geometry of a disclination loop that implies that $P(\phi|\gamma) = 1/\pi$, we have $P(\beta|\gamma) = P(\phi|\gamma)\frac{d\phi}{d\beta} = \frac{1}{\pi}\frac{\sin\beta}{\sqrt{\sin^2\beta - \cos^2\gamma}}$. The non-negativity of probability requires $\pi/2 - \gamma \leqslant \beta \leqslant \pi/2 + \gamma$, or equivalently $|\pi/2 - \beta| \leqslant \gamma$. For wedge-twist disclination loops with $\gamma = \pi/2$, $P(\beta|\gamma) = 1/\pi$ corresponding to a uniform distribution for $0 \leqslant \beta \leqslant \pi$. For pure-twist disclination loops with $\gamma = 0$, $P(\beta|\gamma) = \delta(\beta - \pi/2)$ corresponding to a delta function distribution centered at $\beta = \pi/2$.

The unconditional probability distribution $P(\gamma)$ is the solution of $P(\beta)$, where $P(\beta) = \int_{|\frac{\pi}{2}-\beta|}^{\frac{\pi}{2}} P(\beta|\gamma)P(\gamma)d\gamma$ and $P(\beta|\gamma)$ are known. To numerically solve for $P(\gamma)$, we convert the integral into a linear algebra problem $P(\beta) = \sum_\gamma P(\beta|\gamma)P(\gamma)\Delta\gamma$, where $P(\beta)$ and $P(\gamma)$ are one-dimensional arrays, $P(\beta|\gamma)$ is a two-dimensional matrix, and $\Delta\gamma$ is the choice of integral step. The unknown distribution $P(\gamma)$ can then be calculated as $P(\gamma) = \Delta\gamma \sum_\beta P(\beta|\gamma)^{-1}P(\beta)$. We validate our numerical method by calculating the distribution of γ from the distribution of β for the two designed loops. For the wedge-twist disclination loop, the peak of the distribution of γ is approximately at $\pi/2$, as shown in Fig. 5.8*F*. For the pure-twist disclination loop, the distribution of γ exhibits a peak at ≈ 0, as shown in Fig. 5.8*G*.

Topological structure of disclination loops in pressure-driven DSCG solutions

In the main part of Chapter 5, we determine the structure of the disclination loops formed in pressure-driven DSCG solutions by evaluating the twist angle β for approximately 100 loops for an Ericksen number of Er = 7438. We here show this data again in Fig. 5.9*A*; the location of the peak at $\beta = \pi/2$ indicates that the disclination loops are of pure-twist type. The structure of the disclination loops is fairly complex; multiple loops can be entangled, which makes it difficult to directly determine γ of an individual loop. We therefore use the statistics of the twist angle β to infer the distribution of γ, as outlined in the previous section. We make the simplifying assumptions that (i) the disclination loops are circular

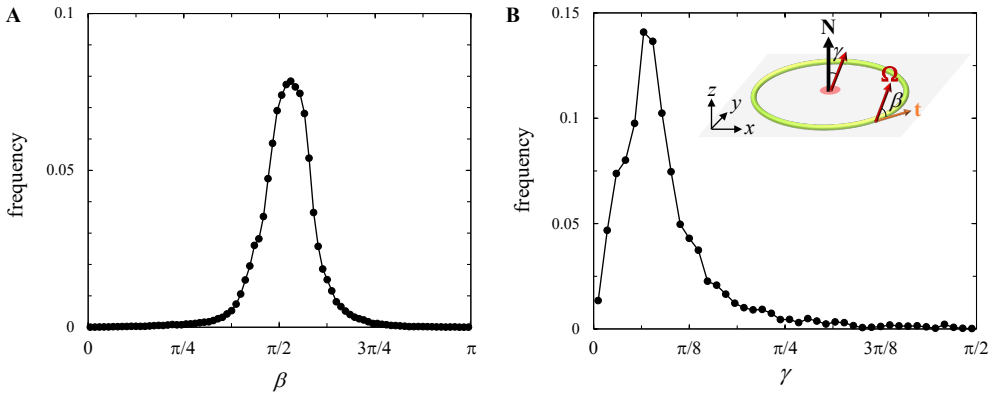

Figure 5.9: Local winding in disclination loops emerging in pressure-driven DSCG solutions. (*A*) Distribution of the twist angle β extracted from approximately 100 disclination loops forming in the simulations of pressure-driven DSCG solutions. (*B*) Distribution of the angle γ inferred from the distribution of β. Inset: Definition of β and γ.

and (ii) they are disconnected. We find that γ indeed exhibits a peak close to zero, as shown in Fig. 5.9*B*. This confirms that the disclination loops are composed predominantly of pure-twist structures.

5.A.6 Estimate of the energy of twist walls

The director field is described by $\mathbf{n} = (\cos\theta\cos\varphi, \cos\theta\sin\varphi, \sin\theta)$, where θ is the out-of-plane polar angle and φ the in-plane azimuthal angle ($\theta = 0^\circ$ for a director in the xy plane, $\varphi = 0^\circ$ for a director in the shear plane). As the spatial confinement in our channel suppresses the tumbling behavior significantly, θ remains close to $\theta = 0^\circ$ across the channel thickness, such that $\frac{\partial\theta}{\partial z} \approx 0$. The nematodynamic equation in the limit of high Ericksen numbers simplifies to [31]

$$\alpha_2 \sin\theta \sin\varphi\dot{\gamma} = \left(K_2\cos^2\theta + K_3\sin^2\theta\right)\cos\theta\frac{\partial^2\varphi}{\partial z^2}, \tag{5.33}$$

$$-\left(\alpha_2\sin^2\theta - \alpha_3\cos^2\theta\right)\cos\varphi\dot{\gamma} = \left(\sin^2\theta K_3 + \cos^2\theta K_1\right)\frac{\partial^2\theta}{\partial z^2} - \left(K_2\cos^2\theta + K_3\sin^2\theta\right)\sin\theta\cos\theta\left(\frac{\partial\varphi}{\partial z}\right)^2. \tag{5.34}$$

where α_2 and α_3 are the Leslie viscosity coefficients, and K_1, K_2 and K_3 are the splay, twist and bend Frank elastic constants [50]. For simplicity, we here consider a simple shear flow with a constant shear rate. As $\sin\theta << 1$, $K_2\cos^2\theta + K_3\sin^2\theta \approx K_2$. Eq. 5.33 then yields

$$\frac{d\varphi}{dz} = \sqrt{-2\frac{\alpha_2\dot{\gamma}\sin\theta}{K_2\cos\theta}\cos\varphi}, \tag{5.35}$$

where we use the average value of $\theta \approx 4^\circ$ obtained in our simulations. Substituting Eq. 5.35 into the expression of the energy of a twist wall yields

$$E_{\text{twist wall}} = \frac{1}{2}L_w K_2 b\int_{-\frac{b}{2}}^{\frac{b}{2}}\left(\frac{d\varphi}{dz}\right)^2 dz \approx 0.4 L_w b\sqrt{-\alpha_2 K_2\dot{\gamma}}, \tag{5.36}$$

where L_w is the length of twist-wall and b is the thickness of the channel.

5.A.7 Derivation of simplified nematodynamic equation to describe the aspect ratio of pure-twist disclination loops

Given the nematic liquid crystal's director field $\mathbf{n} = (\cos\theta\cos\varphi, \cos\theta\sin\varphi, \sin\theta)$, where θ is the out-of-plane polar angle and φ the in-plane azimuthal angle, and the velocity field $\mathbf{v}$, the general form of the nematodynamic equation is [30, 31]

$$\frac{dn_i}{dt} = \frac{1}{\gamma_1}\delta_{ij}^{\perp}h_j + W_{ik}n_k + \lambda\delta_{ij}^{\perp}A_{jk}n_k. \tag{5.37}$$

where γ_1 is the rotational viscosity, $A_{jk} = \frac{1}{2}\left(\frac{\partial v_j}{\partial x_k} + \frac{\partial v_k}{\partial x_j}\right)$ is the symmetric part of the velocity gradients, $W_{ik} = \frac{1}{2}\left(\frac{\partial v_i}{\partial x_k} - \frac{\partial v_k}{\partial x_i}\right)$ is the antisymmetric part of the velocity gradients, and $\delta_{ij}^{\perp}$ is the transverse Kronecker delta. $\lambda = \frac{\alpha_2+\alpha_3}{\alpha_2-\alpha_3}$, where α_2 and α_3 are the Leslie viscosity coefficients. $h_i = -\frac{\partial f_{FO}}{\partial n_i} + \frac{\partial}{\partial x_j}\left(\frac{\partial f_{FO}}{\partial(\partial n_i/\partial x_j)}\right)$, where $f_{FO} = \frac{1}{2}K_1(\nabla\cdot\mathbf{n})^2 + \frac{1}{2}K_2(\mathbf{n}\cdot(\nabla\times\mathbf{n}))^2 + \frac{1}{2}K_3(\mathbf{n}\times(\nabla\times\mathbf{n}))^2$ is the Frank–Oseen elastic energy density. K_1, K_2 and K_3 are the splay, twist, and bend Frank elastic constants, respectively.

Our assumption that the aspect ratio of the disclination loops is dominated by the elastic relaxation related to the deformation of the director field at the boundary of the loop simplifies Eq. 5.37 to

$$\frac{dn_i}{dt} = \frac{1}{\gamma_1}\delta_{ij}^{\perp}h_j. \tag{5.38}$$

We consider the director field within the plane of the pure-twist disclination loops, and assume that the out-of-plane polar angle $\theta = 0^\circ$, which simplifies the director field to $\mathbf{n} = (\cos\varphi, \sin\varphi, 0)$. Eq. 5.38 is then expressed as

$$\gamma_1\frac{d\varphi}{dt} = \cos\varphi h_y - \sin\varphi h_x. \tag{5.39}$$

Moreover, we find that the director field outside the loop is uniform and predominantly along the x-direction, such that $\varphi \approx 0$. Inside the loop, the director field is likewise uniform, with $\varphi > 0$. Considering the director deformation across the center planes of the loop, we note that $\frac{\partial\varphi}{\partial y} = 0$ in the x-direction and $\frac{\partial\varphi}{\partial x} = 0$ in the y-direction, given the uniformity of the director field both outside and inside the loop. Along the x-direction, Eq. 5.39 then simplifies

to

$$\gamma_1 \frac{d\varphi}{dt} = K_3 \frac{\partial^2 \varphi}{\partial x^2} + K_2 \frac{\partial^2 \varphi}{\partial z^2}, \tag{5.40}$$

and along the y-direction to

$$\gamma_1 \frac{d\varphi}{dt} = K_1 \frac{\partial^2 \varphi}{\partial y^2} + K_2 \frac{\partial^2 \varphi}{\partial z^2}. \tag{5.41}$$

5.A.8 Decoupling the contributions of fluctuations and translation to the dynamics of disclination loops

A disclination loop initially at a location $\vec{R}$ and at time t moves with a center of mass velocity $\vec{V}^*$ while simultaneously undergoing fluctuations. To remove the contribution of the center of mass velocity to the dynamics, we move the observation window with a velocity $\vec{V}_f$ for our calculation of the spatiotemporal autocovariance. In such a moving coordinate system, the normalized spatiotemporal autocovariance of the retardance, Γ, can be described by an exponential function:

$$\Big\langle \Delta\Gamma(\vec{R}, t)\Delta\Gamma(\vec{R} + \vec{V}\Delta t, t + \Delta t) \Big\rangle_{\vec{R}} = e^{-\frac{\Delta t}{\tau}}, \tag{5.42}$$

where $\vec{V} = \vec{V}_f - \vec{V}^*$, Δt denotes the lag time, and τ is the time characterizing the dynamics of the disclination loop, which can contain contributions of both the fluctuations and the translation. Linearizing both sides of Eq. 5.42 gives

$$1 + \left\langle \vec{V}\Delta t \Delta\Gamma(\vec{R}, t) \frac{\partial \Delta\Gamma}{\partial t} \right\rangle_{\vec{R}} + \left\langle \Delta t \Delta\Gamma(\vec{R}, t) \frac{\partial \Delta\Gamma}{\partial t} \right\rangle_{\vec{R}} + O(\Delta t^2) \approx 1 - \frac{\Delta t}{\tau}. \tag{5.43}$$

Likewise, the normalized spatial autocovariance of Γ can be described by an exponential function:

$$\Big\langle \Delta\Gamma(\vec{R}, t)\Delta\Gamma(\vec{R} + \vec{r}, t) \Big\rangle_{\vec{R}} = e^{-\left|\frac{\vec{r}}{L_x}\right|}, \tag{5.44}$$

where $\vec{r}$ is a shift in space and L_x is the characteristic length of the disclination loop along the x-direction. Linearizing both sides of Eq. 5.44 and reorganizing yields

$$\left\langle \Delta\Gamma(\vec{R}, t) \frac{\partial \Delta\Gamma}{\partial \vec{R}} \vec{i} \right\rangle_{\vec{R}} \approx -\frac{1}{L_x}. \tag{5.45}$$

When $\vec{V} = 0$, the dynamics of the disclination loop is only determined by the fluctuations, which are characterized by a fluctuation time τ_1. We then have the normalized temporal autocovariance:

$$\left\langle \Delta\Gamma(\vec{R},t)\Delta\Gamma(\vec{R},t+\Delta t)\right\rangle_{\vec{R}} = e^{-\frac{\Delta t}{\tau_1}}. \tag{5.46}$$

Linearizing both sides of Eq. 5.46 yields

$$1 + \left\langle \Delta t\Delta\Gamma(\vec{R},t)\frac{\partial\Delta\Gamma}{\partial t}\right\rangle_{\vec{R}} \approx 1 - \frac{\Delta t}{\tau_1}. \tag{5.47}$$

Substituting Eq. 5.45 and Eq. 5.47 into Eq. 5.43 gives the relation between the translation, the fluctuations and the combined dynamics:

$$\frac{\left|\vec{V}^* - \vec{V}_f\right|}{L_x} + \frac{1}{\tau_1} = \frac{1}{\tau}. \tag{5.48}$$

5.A.9 Fluctuation time determined by tumbling character of nematic DSCG

The dynamics can be described by the nematodynamic equations in the limit of high Ericksen numbers, where the director field is $\mathbf{n} = (\cos\theta\cos\varphi, \cos\theta\sin\varphi, \sin\theta)$ [30, 31]

$$\gamma_1\cos\theta\dot{\varphi} = -\alpha_2\sin\theta\sin\varphi\dot{\gamma}, \tag{5.49}$$

$$\gamma_1\dot{\theta} = \dot{\gamma}(-\alpha_2\sin^2\theta + \alpha_3\cos^2\theta)\cos\varphi. \tag{5.50}$$

where α_2 and α_3 are the Leslie viscosity coefficients and γ_1 is the rotational viscosity. We consider the directors to undergo small out-of-plane perturbations θ_1 and small in-plane perturbations φ_1. For directors aligned perpendicular to the flow direction, this gives $\theta = \theta_1$ and $\varphi = \frac{\pi}{2} + \varphi_1$. Linearizing Eq. 5.49 and Eq. 5.50 in terms of these angle deviations yields

$$\gamma_1\left(1 - \frac{{\theta_1}^2}{2}\right)\dot{\varphi}_1 = \alpha_2\theta_1\left(1 - \frac{{\varphi_1}^2}{2}\right)\dot{\gamma} \tag{5.51}$$

$$\gamma_1\dot{\theta}_1 = \dot{\gamma}\varphi_1\left(-\alpha_2{\theta_1}^2 + \alpha_3\left(1 - {\theta_1}^2\right)\right). \tag{5.52}$$

We neglect the higher order terms in Eq. 5.51 and Eq. 5.52, and take the second derivative of Eq. 5.52 to get

$$\dot{\varphi}_1 = \frac{\alpha_2 \theta_1}{\gamma_1} \dot{\gamma}, \tag{5.53}$$

and

$$\ddot{\theta}_1 = \frac{\alpha_3}{\gamma_1} \dot{\gamma} \dot{\varphi}_1. \tag{5.54}$$

Substituting Eq. 5.53 into Eq. 5.54 yields

$$\ddot{\theta}_1 = \frac{\alpha_3 \alpha_2}{{\gamma_1}^2} \dot{\gamma}^2 \theta_1. \tag{5.55}$$

From Eq. 5.55, we obtain a timescale characterizing the fluctuations of a tumbling director: $\tau_f \approx \frac{3}{4} \frac{\gamma_1}{\sqrt{-\alpha_2 \alpha_3}} \frac{1}{\dot{\gamma}}$. We find that τ_f corresponds well to our experimentally determined time τ_1 characterizing the fluctuations of the disclination loops, suggesting that the loop fluctuations are a reflection of the tumbling character of nematic DSCG.

Chapter 6

Flow-induced periodic chiral structures in an achiral nematic liquid crystal

This chapter is based on Ref. [67]

Chirality, or the absence of mirror symmetry, is ubiquitous in living systems, from DNA to the placement of organs in mammals [196, 197], and chiral objects in chemistry and material science have revolutionized chemical catalysis [198], optical sensors [199], and metamaterial design [200, 201]. There are two common ways how supramolecular chiral structures emerge. They can either be induced by a chiral input which in turn generates a chiral output, or they are composed of molecular building blocks that are themselves chiral [202]. By contrast, the emergence of chirality in centrosymmetric systems is much less common, and it requires a spontaneous mirror symmetry breaking [56]. Elucidating the routes to induce chirality in achiral molecular assemblies will help reveal the mechanism of mirror symmetry breaking [203–205].

Liquid crystals (LCs) are materials composed of anisotropic mesogens. Achiral LCs of specific molecular shapes can form chiral structures [206]. The molecular bow shape of bend-core liquid crystals in the smectic phase, for instance, can introduce chirality through an intralayer polar orientational ordering combined with a collective tilt of the smectic planes [207]. Mirror symmetry breaking has also been shown to emerge in rod-shaped liquid

crystals in the nematic phase when the material is confined to a specific spatial confinement that can be imposed by curved or inclined surfaces, or by hybrid anchoring boundary conditions [56, 208, 209]. The spontaneous mirror breaking induced by spatial confinement is particularly prevalent in nematic lyotropic chromonic liquid crystals (LCLCs) [49, 210, 211]. LCLCs are aqueous dispersions of disk-shaped molecules that self-assemble into cylindrical aggregates. Over a range of temperature and concentration, LCLCs exhibit a nematic phase. Due to the semi-flexibility of the aggregates, nematic LCLCs have a large elastic anisotropy; the twist Frank elastic constant, K_2, is an order of magnitude lower than the elastic constants of splay, K_1, and bend, K_3 [50, 51]. If nematic LCLCs are forced to adapt with bend and splay deformations to a curved surface, they will instead relieve these deformations through a twist deformation to minimize the elastic free energy as a consequence of the small K_2. Such a twist deformation is a pivotal element in forming chiral helices [49, 210]. In addition to these three elastic constants, the saddle-splay Frank elastic constant, K_{24}, also plays an essential role in triggering and stabilizing chiral structures through lowering the elastic energy in cylindrical and toroidal geometries [53, 54, 212]. Exploiting the ease with which twist deformations occur and the non-negligible saddle-splay elasticity that stabilizes chiral structures, programmed anchoring conditions have been developed to control chiral structures in achiral nematic LCLCs [55, 213]. To date, structural chirality in achiral nematic LCs induced by anisotropic elasticities and confined boundary conditions has been explored exclusively in the static state, where an imposed curvature or a pre-patterned surface are necessary for the emergence of chirality [56].

In this study, we report our discovery of shear-driven mirror symmetry breaking in nematic LCLCs in the absence of curved or pre-patterned surfaces. We reveal the emergence of an unexpected chiral structure when the material is flowing in a microfluidic channel. The chirality results from a periodic double-twist deformation of the liquid crystal and leads to striking stripe patterns perpendicular to the flow direction. We show that the stripe period is determined by a competition between the viscous torque and the bend elastic torque acting on directors, and can be easily tuned by varying the plate spacing of the microfluidic channel and the flow velocity.

We demonstrate that the mirror symmetry breaking of the director field is induced by

i) the tumbling property of nematic LCLCs and ii) an elastic instability of a specific configuration of the director field. The tumbling nature leads to non-zero viscous torque for any orientation of the director ($\alpha_2\alpha_3 < 0$, where α_2 and α_3 are the Leslie viscosities [61]), and destabilizes the director field in shear flow. This induces different configurations, including a biaxial-splay configuration characterized by opposite directions of the splay deformation in two orthogonal planes. We show that this biaxial-splay configuration, in which the stability solution is dictated by the saddle-splay elasticity, is unstable and evolves towards a lower energy state of the director field; the periodic double-twist configuration that is selected due to the small twist Frank elastic constant of LCLCs. This path to chirality is unique. The structural chirality is here triggered by a dynamic process when an achiral nematic system is driven away from equilibrium and adopts a chiral lower energy state.

6.1 Methods

6.1.1 Experimental methods

Nematic disodium cromoglycate (DSCG) (TCI America, purity > 98.0%) solutions are prepared by dissolving DSCG in deionized water at 13.0 wt% [50]. The sample is heated to $T \approx 90$ °C where it reaches the isotropic phase, which allows the DSCG to fully dissolve into water. The sample is then cooled to room temperature ($T = 23.2 \pm 0.5$°C) where it adopts the nematic phase [50, 178]

The microfluidic channel consists of two glass plates separated by 8 – 26 μm spacers (Specac, MY SPR RECT 0.006 mm OMNI, and PRECISION BRAND). The width of the channel is 40 mm, the length is 50 mm. A reservoir of 25 mm in height, 40 mm in width, and 2 – 3 mm in interior thickness is connected to one end of the channel to induce a uniform velocity profile at the inlet. Both channel walls are treated to introduce a uniform planar anchoring condition along the flow direction by following a protocol of surface rubbing, where the glass plates are rubbed along the cell length direction using a diamond particle paste with particle diameter of ≈ 50 nm (TechDiamondTools) [68].

To obtain the stripe patterns, the nematic DSCG solution is injected into the microfluidic

channel through a 1 mm diameter hole at the top of the reservoir at controlled volumetric flow rates, q, ranging between $q = 0.25$–0.375 μl/min. The volumetric flow rate is set by a syringe pump (Harvard PHD 2000).

The flow field is observed through crossed polarizers compensated with a retarder (560 nm), placed at 45° to the polarizer, using an optical microscope (OMAX M837T) with an objective of magnification M = 4× and numerical aperture NA = 0.1, and M = 10× and NA = 0.25. This setup allows to us identify the director field averaged in the channel thickness direction. We further quantify the director field averaged in the gap direction using a PolScope (OpenPolScope).

We employ fluorescence confocal polarizing microscopy (Leica SP5) with a water immersion objective of magnification of M = 25× and numerical aperture NA = 0.95 to determine the director field of the stripe patterns in the thickness direction. We add fluorescent particles (Acridine Orange, Biotium) at a concentration of 100 ppm to the DSCG solutions. In the nematic phase, the fluorescent molecules are aligned by the orientation of the disk-like DSCG molecules that is perpendicular to the direction of the directors. The polarized probing beam excites the fluorescent molecules and causes fluorescence. The efficiency of excitation depends on the angle between the transition dipole of the fluorescent molecules and the polarization of the probing beam [214]. A high fluorescence intensity indicates that the polarization of the probing beam is parallel to the fluorescent molecules and thus perpendicular to the aligned direction of the DSCG aggregates. A low fluorescence intensity indicates that the polarization of the probing beam is perpendicular to the fluorescent molecules and thus parallel to the aligned direction of the DSCG aggregates. In our experiments, the polarization of the probing beam is perpendicular to the flow direction. A high fluorescence intensity then indicates that the director is either aligned more parallel to the flow direction or homeotropically in the thickness direction; a low fluorescence intensity indicates that the director is more perpendicular to the flow direction pointing in the y-direction. When capturing the director field in the thickness direction, we scan eight layers from the top wall to the bottom wall of the microfluidic channel. During the scan, the stripe pattern moves with the flow. We therefore analyze the cross-section through the thickness of the channel in a Lagrangian framework in the frame of reference of the stripes. While taking fluorescence im-

ages, we simultaneously capture images through crossed polarizer and analyzer. This allows us to trace the displacement of stripes during the scanning process, and to correspondingly shift the region of interest for each layer accounting for the motion of the stripes.

6.1.2 Numerical methods

The numerical simulations employ the Leslie-Ericksen theory to account for the dynamics of directors on the domain wall that forms at divergent splay deformations in pressure-driven flow. The velocity field $\mathbf{u}$ and the director field $\mathbf{n}$ describe the nematodynamics of nematic liquid crystals. The polar angle θ and the azimuthal angle φ describe the director $\mathbf{n} = (\sin\theta\cos\varphi, \sin\theta\sin\varphi, \cos\theta)$. The director field $\mathbf{n}$ at steady state is governed by an angular momentum equation, the nematodynamic equation [31]:

$$\frac{1}{\gamma_1}\delta_{ij}^{\perp}h_j + W_{ik}n_k + \lambda\delta_{ij}^{\perp}A_{jk}n_k = 0, \tag{6.1}$$

where γ_1 is the rotational viscosity, $A_{jk} = \frac{1}{2}\left(\frac{\partial u_j}{\partial x_k} + \frac{\partial u_k}{\partial x_j}\right)$ and $W_{ik} = \frac{1}{2}\left(\frac{\partial u_i}{\partial x_k} - \frac{\partial u_k}{\partial x_i}\right)$ are the symmetric and antisymmetric parts of the velocity gradients, $\delta_{ij}^{\perp}$ is the transverse Kronecker delta and $\lambda = \frac{\alpha_2+\alpha_3}{\alpha_2-\alpha_3}$ with α_2 and α_3 the Leslie viscosity coefficients. $h_i = -\frac{\partial f_{FO}}{\partial n_i} + \frac{\partial}{\partial x_j}\left(\frac{\partial f_{FO}}{\partial(\partial n_i/\partial x_j)}\right)$, where f_{FO} is the Frank–Oseen elastic energy density. We focus on the configuration of the director field at the domain wall that forms at divergent splay deformations in the xz-plane, which allows us to simplify the nematodynamic equation to one-dimensional (1D) governing equations. We note that $\phi \approx 0^\circ$ and $\frac{\partial\varphi}{\partial z} \approx 0$ at the domain wall. We further approximate $K_1 \approx K_3 \approx \bar{K} \approx (K_1 + K_3)/2$ for simplification, which is justified as K_1 and K_3 are of the same order of magnitude. Eq. 6.1 can then be simplified to

$$\bar{K}\frac{\partial^2\theta}{\partial z^2} = \left(\alpha_2\cos^2\theta - \alpha_3\sin^2\theta\right)\dot{\gamma}, \tag{6.2}$$

where $\dot{\gamma} = \frac{\partial u_x}{\partial z}$ is the shear rate and u_x is the velocity in the x-direction.

To describe the velocity field $\mathbf{u}$ in the x-direction, we employ a linear momentum equation [215]:

$$\eta_{\text{eff}}\frac{\partial^2 u_x}{\partial z^2} = -G, \tag{6.3}$$

where $-G$ is the pressure gradient in the x-direction. η_{eff} is the effective viscosity, which is a function of the director field $\mathbf{n}$ and can be expressed as [31]

$$\eta_{\text{eff}} = \alpha_1 \sin^2\theta\cos^2\theta\sin\varphi + \eta^b \sin^2\theta\sin^2\varphi + \eta^c\cos^2\theta + \frac{1}{2}\alpha_4\sin^2\theta\cos^2\varphi, \tag{6.4}$$

where α_1 and α_4 are the Leslie viscosity coefficients. η^b and η^c are the Miesowicz viscosities.

We non-dimensionalize Eqs. 6.2, 6.3, and 6.4 using $z = bz^*$, $u_x = \frac{Gb^2}{\alpha_2}u_x^*$, $\eta_{\text{eff}}^* = \frac{\eta_{\text{eff}}}{\alpha_2}$ and $\dot{\gamma}^* = \frac{\partial u_x^*}{\partial z^*}$:

$$\frac{\partial^2\theta}{\partial z^{*2}} = \frac{Gb^3}{\bar{K}}\dot{\gamma}^*\left(\cos^2\theta - \frac{\alpha_3}{\alpha_2}\sin^2\theta\right), \tag{6.5}$$

$$\eta_{\text{eff}}^*\frac{\partial^2 u_x^*}{\partial z^{*2}} = -1, \tag{6.6}$$

$$\eta_{\text{eff}^*} = \frac{\alpha_1}{\alpha_2}\sin^2\theta\cos^2\theta + \frac{\eta^b}{\alpha_2}\sin^2\theta + \frac{\eta^c}{\alpha_2}\cos^2\theta. \tag{6.7}$$

We numerically solve Eqs. 6.5–6.6 using the finite difference method, applying no-slip boundary conditions and infinite anchoring conditions. In reality, however, the anchoring strength of LCLCs on rubbed glass is weak [216], corresponding to finite anchoring conditions in which the directors can deviate from the initial anchoring condition in shear flow. To mimic the finite anchoring conditions and to account for the tumbling characteristics of nematic LCLCs [61], we assign different polar angles at the top and bottom walls: $\theta_{b,top} = \theta_b$ and $\theta_{b,bottom} = 90^\circ - \theta_b$ ($90^\circ \geqslant \theta_b \geqslant 45^\circ$) [217] and validate it by comparing the anchoring strength at θ_b with the anchoring strength in reality (See Appendix 6.A.1 for details).

Eq. 6.5 gives an expression for the Ericksen number $\text{Er}_{\text{numerical}} = Gb^3/\bar{K}$. With $G \sim -\alpha_2\bar{\dot{\gamma}}/b$, we have $\text{Er}_{\text{numerical}} \sim -\alpha_2\bar{\dot{\gamma}}b^2/\bar{K} = \text{Er}_{\text{average}}$, where $\bar{\dot{\gamma}}$ is the average shear rate. We investigate the regime of $\text{Er}_{\text{numerical}} = 25 - 50$, which corresponds to the regime of $\text{Er}_{\text{average}}$ in which the stripe patterns form in the experiments. The Leslie viscosity coefficients are chosen to satisfy the tumbling character of flowing nematic LCLCs; $\alpha_1 = -0.0181$ Pa s, $\alpha_2 = -0.1104$ Pa s, $\alpha_3 = 0.0011$ Pa s, $\eta_b = 0.0251$ Pa s, $\eta_c = 0.1355$ Pa s.

To further access the azimuthal angles of the director field neighboring the domain wall that forms at divergent splay deformations, we employ the hybrid lattice Boltzmann

method (LBM) where the microstructure and hydrodynamic flow of the nematic LC are described by a tensorial order parameter $\mathbf{Q}$ and a velocity vector $\mathbf{u}$, respectively. For a uniaxial nematic LC, $\mathbf{Q} = S(\mathbf{nn} - \mathbf{I}/3)$, where the unit vector $\mathbf{n}$ represents the nematic director field, S is the scalar order parameter of the nematic LC and $\mathbf{I}$ is the identity tensor. By defining the strain rate $\mathbf{D} = (\nabla\mathbf{u} + (\nabla\mathbf{u})^T)/2$ and the vorticity $\mathbf{\Omega} = (\nabla\mathbf{u} - (\nabla\mathbf{u})^T)/2$, we introduce an advection term $\mathbf{S} = (\xi\mathbf{D} + \mathbf{\Omega}) \cdot (\mathbf{Q} + \frac{\mathbf{I}}{3}) + (\mathbf{Q} + \frac{\mathbf{I}}{3}) \cdot (\xi\mathbf{D} - \mathbf{\Omega}) - 2\xi(\mathbf{Q} + \frac{\mathbf{I}}{3})(\mathbf{Q} : \boldsymbol{\nabla}\mathbf{u})$, where ξ is the flow aligning parameter. We use $\xi = 0.6$ for the tumbling nematic LCLCs.

The governing equation of the $\mathbf{Q}$-tensor, the Beris–Edwards equation, reads [182]

$$\frac{\partial \mathbf{Q}}{\partial t} + \mathbf{u} \cdot \boldsymbol{\nabla}\mathbf{Q} - \mathbf{S} = \Gamma\mathbf{H}, \tag{6.8}$$

where Γ is related to the rotational viscosity of the nematic LC via $\gamma_1 = 2S_0^2/\Gamma$ [218], and $\mathbf{H}$ is the molecular field defined as $\mathbf{H} = -(\frac{\delta F}{\delta \mathbf{Q}} - \frac{\mathbf{I}}{3}\operatorname{tr}\left(\frac{\delta F}{\delta \mathbf{Q}}\right))$ that drives the system towards thermodynamic equilibrium with a free energy functional $F = \int_{bulk} f_{\mathrm{LdG}} dV + \int_{bulk} f_{\mathrm{elastic}} dV + \int_{surface} f_{\mathrm{surf}} dS$. The first term is the short-range Landau–de Gennes free energy density, which reads $f_{\mathrm{LdG}} = \frac{A_0}{2}(1 - \frac{U}{3})\operatorname{tr}(\mathbf{Q}^2) - \frac{A_0 U}{3}\operatorname{tr}(\mathbf{Q}^3) + \frac{AU_0}{4}(\operatorname{tr}(\mathbf{Q}^2))^2$ [30], where A_0 and U are material constants. The second term, the long-range elastic energy density, reads $f_{\mathrm{elastic}} = \frac{1}{2}L_1 Q_{ij,k}Q_{ij,k} + \frac{1}{2}L_2 Q_{jk,k}Q_{jl,l} + \frac{1}{2}L_3 Q_{ij}Q_{kl,i}Q_{kl,j} + \frac{1}{2}L_4 Q_{jk,l}Q_{jl,k}$ [219], where $Q_{ij,k}$ denotes $\partial_k Q_{ij}$, where we use the Einstein summation convention. The elastic constants L_1 to L_4 can be mapped onto the commonly used Frank elastic constants via [218]:

$$\begin{aligned}
L_1 &= \frac{1}{2S_0^2}\left[K_2 + \frac{1}{3}(K_3 - K_1)\right], \\
L_2 &= \frac{1}{S_0^2}(K_1 - K_{24}), \\
L_3 &= \frac{1}{2S_0^3}(K_3 - K_1), \\
L_4 &= \frac{1}{S_0^2}K_4.
\end{aligned} \tag{6.9}$$

where K_1, K_2, K_3 and K_{24} denote the splay, twist, bend and saddle-splay Frank elastic constants. The nematic coherence length is defined as $\xi_N = \sqrt{L_1/A_0}$ [219], and sets the unit of length in our simulations. The surface free energy density $f_{\mathrm{surf}} = \frac{1}{2}W(\mathbf{Q} - \mathbf{Q}_0)^2$ imposes

a boundary condition to the $\mathbf{Q}$-tensor by quadratically penalizing any deviation of $\mathbf{Q}$ at a surface from its preferred order parameter $\mathbf{Q}_0 \equiv S_0(\mathbf{n}_0\mathbf{n}_0 - \mathbf{I}/3)$ [220]. The parameter W is the anchoring strength. We consider planar anchoring, $\mathbf{n}_0 = \mathbf{x}$, with $\mathbf{x}$ the surface anchoring condition. The planar anchoring is weak with an anchoring strength $W = 0.02$ in simulation units.

The local fluid density ρ and the velocity $\mathbf{u}$ are governed by a linear momentum equation [149, 221]

$$\rho\left(\frac{\partial}{\partial t} + \mathbf{u}\cdot\nabla\right)\mathbf{u} = \nabla\cdot\mathbf{\Pi} + G\mathbf{x}, \tag{6.10}$$

The viscoelastic properties of the nematic LC are lumped in the passive stress, which is the sum of viscous and elastic terms. The stress, Π is written as [218, 220],

$$\mathbf{\Pi} = 2\eta\mathbf{D} - P_0\mathbf{I} + 2\xi(\mathbf{Q}+\frac{\mathbf{I}}{3})(\mathbf{Q}:\mathbf{H}) - \xi\mathbf{H}\cdot(\mathbf{Q}+\frac{\mathbf{I}}{3}) - \xi(\mathbf{Q}+\frac{\mathbf{I}}{3})\cdot\mathbf{H} - \boldsymbol{\nabla}\mathbf{Q} : \frac{\delta F}{\delta\boldsymbol{\nabla}\mathbf{Q}} + \mathbf{Q}\cdot\mathbf{H} - \mathbf{H}\cdot\mathbf{Q}, \tag{6.11}$$

where η is the isotropic viscosity and P_0 is the isotropic bulk pressure. We consider a pressure-driven flow along the x-direction.

We employ a hybrid lattice Boltzmann method to solve the coupled governing partial differential Eq. 6.8 and Eq.6.10 [149, 220, 221]. The simulation box size is $[L_x,\ L_y,\ L_z] = [5,\ 51,\ 5]$, with periodic boundary conditions in the x- and y-directions. We chose the following parameters: $\eta = 1/3$ and $\Gamma = 0.1$, $\xi = 0.6$, $U = 3.5$, which results in $S_0 \simeq 0.62$. We further use $A_0 = 0.1$, $L_1 = 0.1$, $L_2 = 0$, $L_3 = 0.3247$, and $L_4 = 0.133$, corresponding to $K_1 = 3K_2 = \frac{1}{3}K_3 = K_{24}$ in Eq. 6.9 for a tumbling nematic LC. A no-slip boundary condition is imposed at the two walls of a microfluidic channel.

6.1.3 Simulated director field

To reconstruct the 3D director field of the stripe patterns, we use continuum simulations to generate a nematic field that satisfies the experimentally observed director field, starting the simulation with an ansatz that satisfies the twisted structure found in the experiment. The chiral structure is then stabilized by minimizing the free energy representing a chiral nematic LC. The equilibrated director field is further processed to generate a crossed polarized im-

age, which agrees with the experimental image, supporting the validity of the reconstructed director field.

6.2 Results and Discussion

Flow-induced periodic double-twist structures in achiral nematic liquid crystals. An aqueous solution of 13 wt% disodium cromoglycate (DSCG) is placed in a rectangular microfluidic channel of length $l = 55$ mm, width $w = 40$ mm, and thickness $b = 26 \pm 1$ μm at room temperature $T = 23.2 \pm 0.5$ °C. At this concentration and the temperature, DSCG solutions form a nematic phase [50, 178]. The surface anchoring condition is controlled to be planar in the direction of the cell length, along the x-direction. We probe the alignment of the nematic liquid crystal using polarizing optical microscopy. In the static state, the optical birefringence of a 13 wt% DSCG solution, $\Delta n = n_{\mathrm{e}} - n_{\mathrm{o}}$, is -0.015, where n_{e} and n_{o} are the extraordinary and ordinary refractive indices [65, 72]. The maximum retardance, $\delta_{max} = \Delta n b$, is then 375 ± 15 nm. When imaged under crossed polarizer (placed along x-direction) and analyzer the material appears black; when imaged with an additional static full-wave-plate optical compensator (560 nm) with the slow axis oriented at 45° to the crossed polarizers and in the direction perpendicular to x-direction, the material appears green. This confirms that the director field is planar aligned in the x-direction, as shown in Fig. 6.1(A and B). Such uniform alignment governed by the surface anchoring conditions is the minimal energy state of static nematic liquid crystals in a rectangular channel [222].

Remarkably, under a weak flow at a volumetric flow rate of $q = 0.25$ μl/min, a stripe pattern perpendicular to the flow direction spontaneously emerges over large regions, as shown in Fig. 6.1(A). With the compensation of the retarder, the orange birefringence color in between two blue stripes indicates that the directors in that region are predominately perpendicular to the flow direction along the y-direction, adopting almost a log-rolling state (see Appendix 6.A.2). Using a PolScope (OpenPolScope) to quantify the retardance map, we find that the retardance is close to zero in certain regions of the stripes, indicating a homeotropic alignment where the directors are parallel to the cell thickness direction, as shown in Fig. 6.2(A). We denote this low-retardance region as region I in Fig. 6.2(A), and the

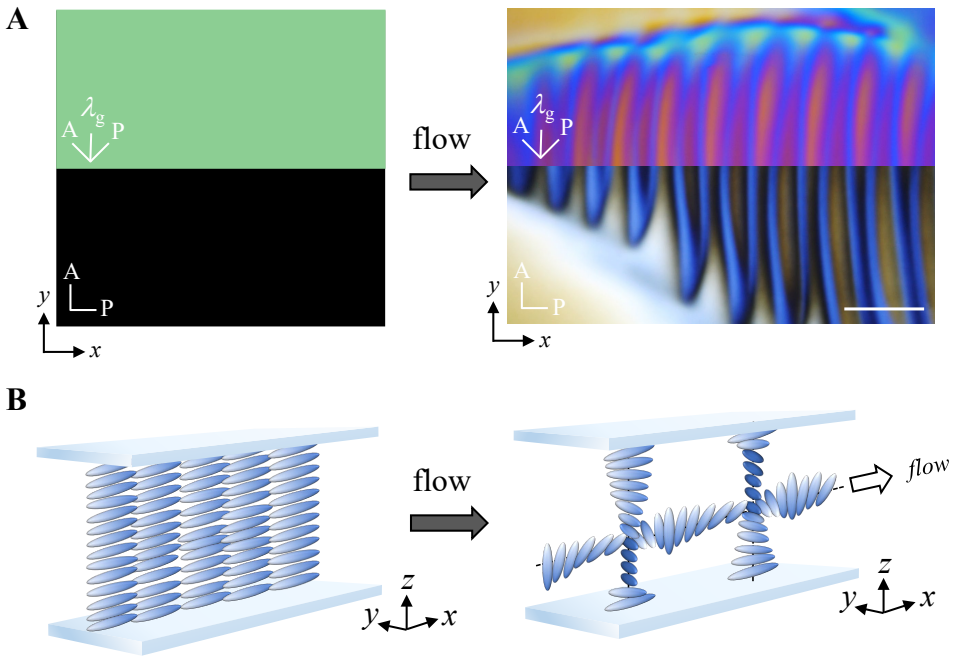

Figure 6.1: **Stripe patterns emerge from uniformly aligned nematic lyotropic chromonic liquid crystals in a weak flow.** (**A**) The flow is in the x-direction, the thickness of the microfluidic channel is in the z-direction. The images are captured using a crossed polarizer, P, an analyzer, A, and a full-wave-plate optical compensator with its slow axis, λ_g, oriented in the direction perpendicular to the flow direction. The scale bar is 200 μm. (**B**) Schematics of the transition from a uniform planar alignment of the director field in the static state to a periodic double-twist structure in weak flow.

region in between as region II. The directors rotate from being parallel to the z-direction (region I) with azimuthal angle $\varphi \approx 90^\circ$ (Fig. 6.2(B)), to being more parallel to the y-direction (region II) with polar angle $\theta \approx 0^\circ$. This indicates a periodic twist deformation in the flow direction, as schematically shown in Fig. 6.1(B). The selection of the twist deformation is a consequence of the small twist Frank elastic constant of nematic DSCG solutions [50].

To probe the alignment in the cell thickness direction, we use fluorescence confocal polarizing microscopy. A low fluorescence intensity I indicates an alignment of the director in the y-direction, a high fluorescence intensity indicates an alignment of the director in either the flow direction (x-direction) or the cell thickness direction (z-direction) [214]. In region II, the stripes have alternatively high and low fluorescence intensity when measured at the bottom layer of the microfluidic channel. As we scan across the cell thickness direction towards the top layer of the microfluidic channel, the fluorescence intensity switches; dark regions

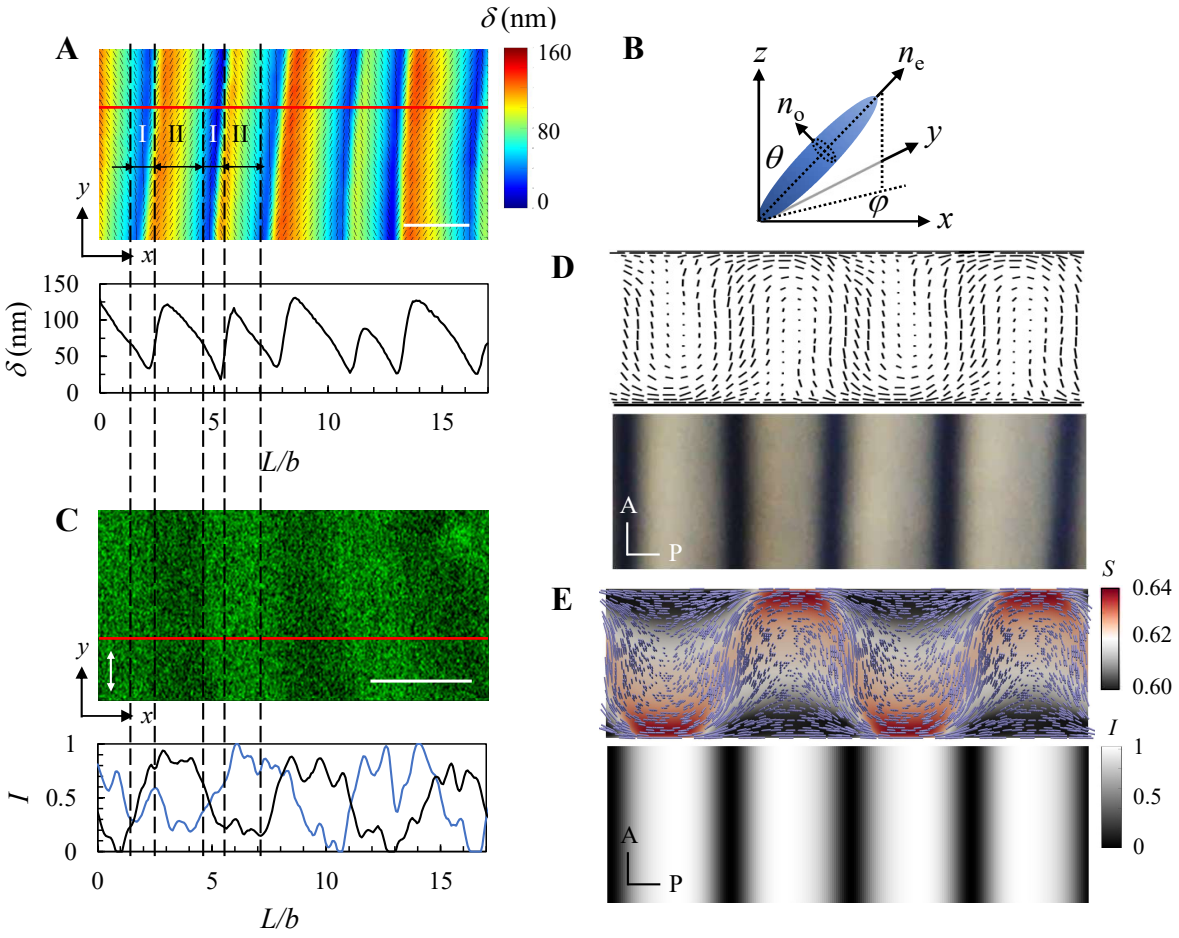

Figure 6.2: **Mirror symmetry breaking in weak flows of a nematic liquid crystal.** (**A**) Retardance map (upper panel), where the color represents the optical retardance averaged in the thickness direction δ, and the direction of the black rods denotes the orientation of directors averaged in the thickness direction projected in the xy-plane. The scale bar is 50 μm. Along the distance L indicated as a red line in the retardance map normalized by the plate spacing, b, the retardance varies periodically (lower panel). The low retardance region of stripes is denoted as region I, and the region in between low-retardance stripes is denoted as region II. (**B**) Schematic of the director orientation. φ is the azimuthal angle and θ is the polar angle. n_e is the extraordinary refractive index, n_o is the ordinary refractive index. (**C**) Fluorescence image of the stripe pattern in the xy-plane imaged at the bottom layer of the microfluidic channel (upper panel). The white arrow represents the polarization of the probing beam. The scale bar is 50 μm. Along the red line, L, the normalized fluorescence intensity at the top layer (black line) is out of phase with that at the bottom layer (blue line) in a xz-cross-section (lower panel). L is normalized by the plate spacing, b. (**D**) Schematics of the periodic double-twist deformation in the xz-plane (upper panel) and the corresponding stripe pattern (lower panel). (**E**) A map of the normalized light intensity, I, imaged through crossed polarizer and analyzer (lower panel) recovered from the simulated periodic double-twist director field (upper panel). S denotes the scalar order parameter.

become bright and bright regions become dark, indicating an alternating twist deformation for adjacent stripes in the cell thickness direction, as shown in Fig. 6.1(B) and Fig. 6.2(C).

The combination of the periodic twist deformation in the flow direction and the alternating twist deformation in the cell thickness direction results in a periodic double-twist structure, as schematically shown in Fig. 6.2(D). To further verify that the periodic double-twist structure corresponds to the stripe pattern, we calculate the effective optical retardance averaged over the channel thickness from a simulated director field; the retardance map is indeed in good agreement with the experimentally observed pattern (Fig. 6.2(E)). The periodic double-twist structure is remarkable in two aspects: i) It is a chiral structure built by an achiral nematic liquid crystal, which involves a spontaneous mirror symmetry breaking, and ii) the chiral structure possesses a well-defined characteristic period despite the absence of a pitch length in the achiral building blocks.

Mechanism of mirror symmetry breaking. To reveal the mechanism of the spontaneous mirror symmetry breaking, we analyze the dynamics of the director field associated with the different elastic deformation modes induced by the weak flow. Looking at a larger section of the cell through a crossed polarizer and analyzer shows that the stripe patterns are surrounded by regions of uniform director fields (Fig. 6.3(A)). Adding a full-wave-plate optical compensator with its slow axis, λ_g, oriented at 45 $^\circ$ to the polarizer, reveals that the regions surrounding the stripe patterns appear alternatively blue and yellow, which demonstrates that the directors tilt in opposite directions in the different domains (Fig. 6.3(B)). We further quantify the director field in these domains using a PolScope, which confirms the opposite tilt of the directors, as shown in Fig. 6.3(C). This tilted director field is induced by the competition between the shear flow and the elastic deformation as the directors resist the deviation from the initial anchoring condition induced by the flow. At low shear rate, the tumbling DSCG solutions would prefer to align perpendicular to the flow direction along the y-direction, adopting a log-rolling state [61, 65], as the log-rolling state avoids the more costly deformations of splay and bend that the director would experience if oriented in the shear plane [61, 65]. The log-rolling state, however, is inconsistent with the initial anchoring condition, which causes the director to tilt in the xy-plane adopting azimuthal angles of $\varphi \approx 65^\circ$ and $\varphi \approx 115^\circ$, as shown in Fig. 6.3(D) (see Appendix 6.A.3). Given that the

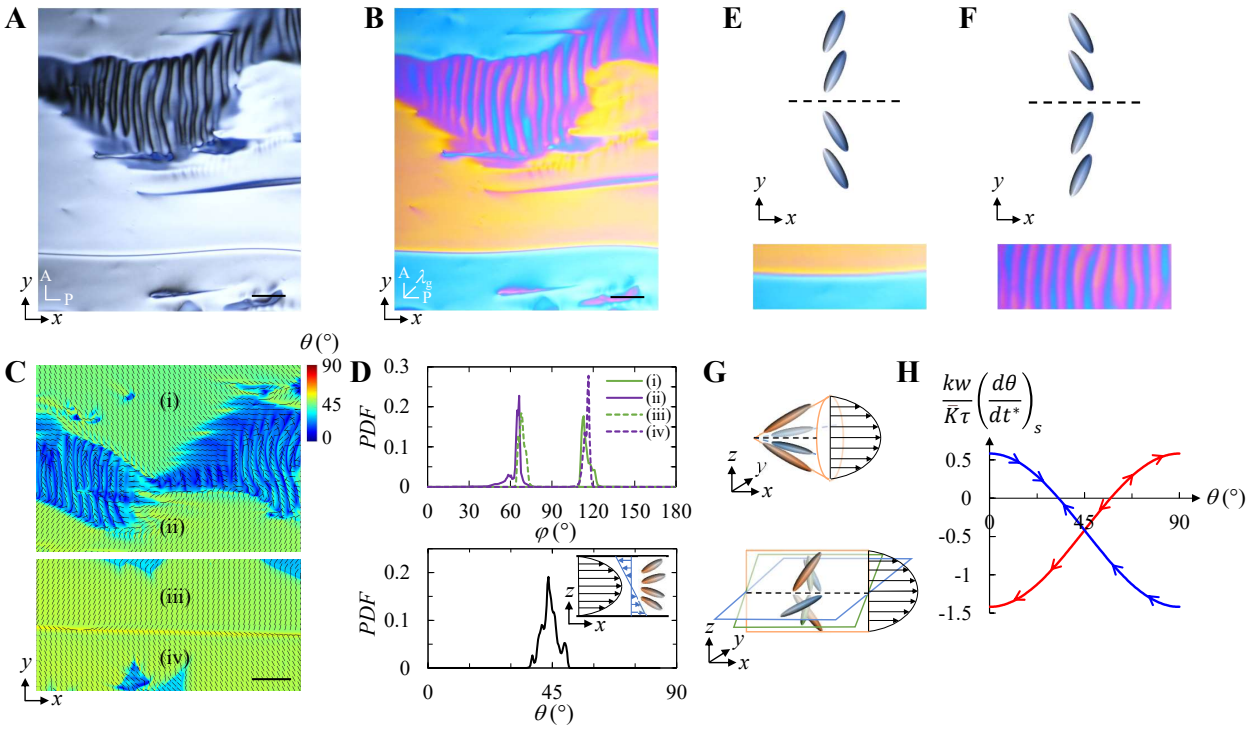

Figure 6.3: **Three-dimensional director field inducing periodic double-twist structures.** (**A**) The stripe patterns are surrounded by regions of uniform director fields, imaged through a crossed polarizer, P, and analyzer, A. The scale bar is 200 μm. (**B**) The director fields surrounding the stripe patterns appear alternatively blue and yellow when imaged using a full-wave-plate optical compensator. The blue color indicates that the director is more perpendicular to λ_g; the yellow color indicates that the director is more parallel to λ_g. The scale bar is 200 μm. (**C**) Map of the polar and azimuthial angles. The black rods represent the azimuthal angle of directors, φ, averaged in the cell thickness direction. The color bar denotes the value of the polar angle, θ, averaged in the cell thickness direction. The regions neighboring the stripe patterns are denoted as regions (i) and (ii); the regions neighboring the domain walls are denoted as regions (iii) and (iv). The scale bar is 500 μm. (**D**) Probability density function (PDF) of the azimuthal angle φ in regions (i)-(iv) (upper panel). PDF of the polar angle θ in regions neighboring the stripe patterns and the domain walls (lower panel). Inset: schematics indicating a divergent splay deformation in the xz-plane induced by the Poiseuille flow in the microfluidic channel. The black arrows represent the velocity profile, the blue arrows represent the shear rate profile. (**E**) A domain wall forms at divergent splay deformations. (**F**) Stripe patterns occur at convergent splay deformations. (**G**) Schematics of the biaxial splay configuration (upper panel) and the double-splay configuration (lower panel). (**H**) Evolution of θ on the channel walls at Ericksen number $\mathrm{Er}_{\mathrm{average}} = 30$ for double-splay (blue line) and biaxial-splay (red line) configurations. $\mathrm{Er}_{\mathrm{average}} = -\alpha_2 \bar{\dot{\gamma}} b^2 / \bar{K}$, where α_2 is a Leslie viscosity coefficient and $\bar{K}$ is the average Frank elastic constant.

cylindrical DSCG aggregates are symmetric, left- and right-handed twists are stochastically equal, and opposite twist deformations leads to the domains tilting in opposite directions.

The boundary of domains creates a splay deformation that can be either open to the flow direction, denoted as divergent splay deformation (Fig. 6.3(E)), or closed to the flow direction, denoted as convergent splay deformation (Fig. 6.3(F)). Remarkably, the stripe patterns only form at the boundary with the convergent splay; by contrast, the divergent splay leads to a domain wall with splay deformations appearing as a sharp line (Fig. 6.3(A–C)) [30].

Divergent splay deformations and convergent splay deformations cost the same amount of energy; why is the divergent splay deformation stable at a splay domain wall but the convergent splay deformation unstable evolving into stripe patterns? The answer lies in the three-dimensional director field at the boundary of the domains. Indeed, in addition to the splay deformation in the xy-plane, the shear torques induced by the Poiseuille flow in the gap of the microfluidic channel lead to a divergent splay deformation across the cell thickness, as shown in the inset of Fig. 6.3(F). This deformation of the director field is reflected in the value of the gap-averaged out-of-plane polar angle $\theta = 45^\circ$, compared to the initial planar alignment where $\theta = 90^\circ$ (Fig. 6.3(F)). The combination of the divergent splay deformation in the xy-plane and the divergent splay deformation in the xz-plane gives rise to a double-splay deformation, as schematically shown in Fig. 6.3(G). Conversely, the convergent splay deformation in the xy-plane and the divergent splay deformation in the xz-plane induces a biaxial-splay deformation.

The observation that periodic double-twist structures are triggered at regions with biaxial-splay configuration, but not at regions with double-splay configuration, suggests different dynamics of the director field for the two configurations. Analyzing the nematodynamic equations describing the dynamics of the directors near the channel walls, we find that the two configurations have different stable solutions, dictated by the saddle-splay elasticity. In the Oseen-Frank elastic energy density $f = 1/2[K_1(\nabla \cdot \mathbf{n})^2 + K_2(\mathbf{n} \cdot \nabla \times \mathbf{n})^2 + K_3(\mathbf{n} \times \nabla \times \mathbf{n})^2 - K_{24}\nabla \cdot (\mathbf{n} \cdot \nabla \times \mathbf{n} + \mathbf{n} \times \nabla \times \mathbf{n})]$, where $\mathbf{n}$ is the director and K_1, K_2, K_3 and K_{24} are the splay, twist, bend and saddle-splay Frank elastic constants, respectively, the saddle-splay term enters the free energy only through the boundary conditions given that it is a pure divergence. On a flat surface and when the anchoring condition or the bulk energy become dominant, this saddle-splay term is usually neglected [53]. The planar anchoring strength of DSCG solutions, however, has been reported to be weak, on the order

of $10^{-6} - 10^{-7}$ J/m^2 [69]. When the flow induces either a biaxial-splay or a double-splay deformation, the directors on the walls can thus deviate from the anchored state. This leads to spatial gradients of the director field in the orthogonal directions near the walls. As a consequence, the saddle-splay term plays here an important role. This deformation at the walls will ultimately affect the director field in the bulk.

To understand the stability of the biaxial-splay and double-splay deformations under perturbations, we consider the director field, $\mathbf{n} = (\sin\theta\cos\varphi, \sin\theta\sin\varphi, \cos\theta)$ in the vicinity of the symmetry axis in the xy-plane of the biaxial-splay and double-splay regions. In steady state, the change of the polar angle θ and the azimuthal angle φ in the x-direction is negligible. Assuming that $\varphi \sim 0^\circ$, $d\varphi/dx = 0$ and $d\theta/dx = 0$, the nondimensionalized nematodynamic equation at the top wall of the microfluidic channel reads (see Appendix 6.A.1 for details):

$$\frac{kw}{\bar{K}\tau}\left(\frac{d\theta}{dt^*}\right)_s = -\frac{w}{b}\left(\frac{\partial\theta}{\partial z^*}\right)_s + \frac{1}{2}\frac{K_{24}}{\bar{K}}\left(\cos^2\theta - \sin^2\theta\right)\frac{\partial\varphi}{\partial y^*}, \tag{6.12}$$

where $t^* = t/\tau$, $y^* = y/w$, and $z^* = z/b$, with τ the characteristic time, w the characteristic width of double-splay and biaxial-splay configurations. k is related to the rotational viscosity of the LCLC, the subscript s denotes the evolution of the director at the channel walls, and $\bar{K} = (K_1 + K_3)/2$ is an average elastic constant. The surface gradient of θ in the z-direction, $\partial\theta/\partial z \approx 0.836$, is solved numerically from the bulk nematodynamic equation (see Appendix 6.A.1). In the stationary state, for directors on the walls where the flow velocity is zero, $(d\theta/dt)_s = 0$, Eq. (1) yields a stationary solution of the polar angle at the top wall $\theta_s \approx 57^\circ$ for biaxial-splay configurations and $\theta_s \approx 33^\circ$ for double-splay configurations. We now probe whether this is a stable angle for double-splay and biaxial-splay configurations. For the double-splay configuration, the gradient of φ in the y-direction, $\partial\varphi/\partial y$ is positive. When θ is perturbed to an angle smaller than θ_s, $d\theta/dt > 0$ and θ increases back to θ_s. Inversely, when θ is perturbed to an angle larger than θ_s, $d\theta/dt < 0$ and θ decreases back to θ_s (Fig. 6.3(H)). The director thus always returns to the stationary polar angle, and it is stabilized by a splay domain wall. In contrast, for the biaxial-splay configuration, $\partial\varphi/\partial y < 0$. When the director is perturbed from θ_s, it thus will not return to θ_s but is unstable. Due to the weak anchoring strength, θ on the walls is larger than θ_s and goes

to 90° (see Appendix 6.A.1). The unstable biaxial-splay configuration evolves to a lower energy state, which is the double-twist configuration. To show this, we consider that in principle, there are three possible configurations out of biaxial-splay configuration: double-twist and double-splay configurations. By analyzing the Oseen-Frank elastic energy density for each configuration, we find that the double-twist configuration costs the least elastic free energy (see Appendix 6.A.4), and is therefore selected.

Period of periodic double-twist structures. In addition to the spontaneous mirror symmetry breaking, the second remarkable characteristics of the stripe patterns is their periodicity. Periodic structures frequently appear in cholesteric liquid crystals induced by the intrinsic pitch length of the material, but are rarely observed in achiral nematic liquid crystals [208].

The period of the stripes, corresponding to the period of the double-twist structure, p, can experimentally be tuned by varying the plate spacing, b, and the local velocity of stripes, V (Fig. 6.4(A and B)). For a given plate spacing, p decreases with a power law with exponent ≈ -0.5 with increasing velocity; for a constant velocity, p increases with b.

The elastic deformation modes in the periodic double-twist configuration are mainly bend and twist deformations. Both compete with the viscous torque from the flow and this

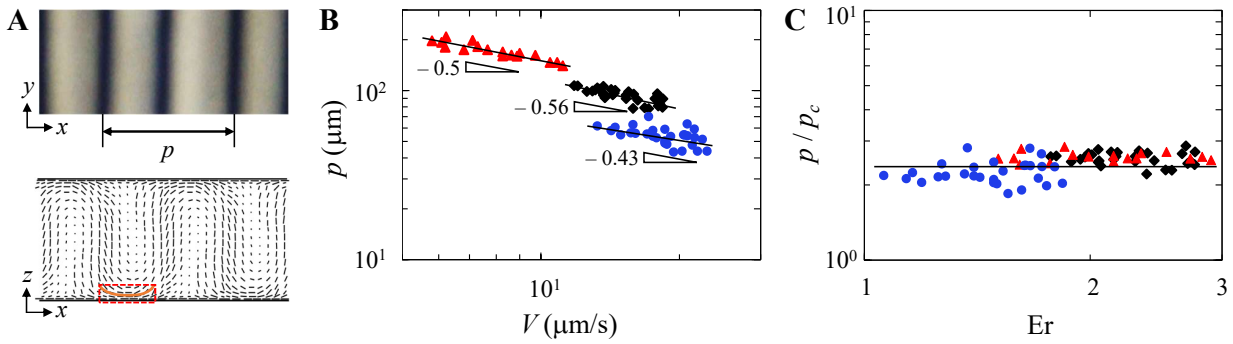

Figure 6.4: **Period of periodic double-twist structures controlled by velocity of stripes and plate spacing.** (**A**) Definition of the period of the double-twist structure, p (upper panel). Bend deformations occur in the periodic double-twist structure, as highlighted by the orange line. The region of bend deformation is indicated by the red dashed box (lower panel). (**B**) Period of the periodic double-twist structure, p, versus the velocity of the stripes, V, for plate spacings $b = 8$ μm (●), $b = 15$ μm (◆), and $b = 26$ μm (▲). (**C**) p normalized with p_c, the critical period denoting the competition between the bend elastic torque and the viscous torque from the flow.

competition sets the period of the structures. The bend mode dominates over the twist most in this competition as a consequence of the smallness of the twist Frank elastic constant. The relative importance between the viscous torque and the bend elastic torque is expressed by the Ericksen number $\mathrm{Er} = \eta_{eff} V b / K_3$, where $\eta_{eff} \approx 0.1$ Pas is the effective viscosity and $K_3 \approx 10$ pN is the bend Frank elastic constant [46, 61]. An increase in Er, which corresponds to an increase in V or b in the experiments, represents an increased viscous torque compared to the elastic torque. This induces a stronger bend deformation of the director field and a decrease of the period. To express the selection of the period in terms of the competition between the bend elastic torque and the viscous torque, we consider the director field in the region of bend deformation, as indicated in Fig. 6.4(A), $\mathbf{n} = (\sin\theta, 0, \cos\theta)$. With the assumption that $\theta \sim 90^\circ$, the nematodynamic equation then reads (see Appendix 6.A.5 for details) [31]:

$$\alpha_3 \dot{\gamma}_{xz} = -K_3 \frac{\partial^2 \theta}{\partial x^2}, \tag{6.13}$$

where α_3 is a Leslie viscosity coefficient and $\dot{\gamma}_{xz}$ is the shear rate. A scaling analysis gives $\partial^2\theta/\partial x^2 \propto -1/(p_c/2)^2$ and $\dot{\gamma}_{xz} \propto V/b$ (see Appendix 6.A.5 for details), with the characteristic period,

$$p_c \propto 2\sqrt{\frac{K_3 b}{\alpha_3 V}}. \tag{6.14}$$

This scaling argument gives a power-law exponent for V that is in good agreement with that observed in the experiments, $p \propto V^{-0.5}$. Indeed, we can rescale all the data at different V and b onto a master curve by normalizing p with p_c, as shown in Fig. 6.4(C). This corroborates that the period of the periodic double-twist structure is set by the competition between the bend elastic torque and the viscous torque from shear flow. We further non-dimensionalize the abscissa using the Ericksen number. The stripes emerge at Er of order one, confirming that both the viscous and the elastic torque are important for the formation of stripe patterns.

The configuration of the periodic double-twist structures is reminiscent of the periodic chiral structures that result from the Helfrich-Hurault elastic instability in cholesteric liquid crystals, where the period is set by the competition between the bend deformation and the pitch length-induced twist deformations [223]. Our achiral liquid crystal, however, does not have an intrinsic pitch length; instead, it is here the viscous torque that resists the bend

elastic deformation.

Conclusions

We discover the spontaneous emergence of a chiral structure in the weak flow of an achiral lyotropic chromonic liquid crystal. The mirror symmetry breaking is facilitated by the tumbling character of the LCLC that triggers the three-dimensional director field to form a biaxial-splay configuration. This biaxial-splay configuration is unstable, as dictated by the saddle-splay elasticity, and evolves into a lower energy state, a chiral double-twist structure, as a consequence of the small twist Frank elastic constant of LCLCs. The flow-induced mirror symmetry breaking provides a novel pathway to chiral structures in achiral molecular assemblies. Similar emergence of chirality might occur in other nematic materials that share the characteristics of tumbling and a small twist Frank elastic constant, for example in liquid crystal polymers. The flow-induced mirror symmetry breaking might also serve as a controllable and tunable platform with which to investigate chiral symmetry breaking of supramolecular assemblies that has been conjectured to be a key for understanding the prebiotic processes [224, 225].

6.A Appendices

6.A.1 Evolution of directors on walls of the microfluidic channel

The nematodynamic equation describing the evolution of directors on the walls of the microfluidic channel is

$$k\left(\frac{d\mathbf{n}}{dt}\right)_s = \hat{v}\cdot\frac{\partial f_b}{\partial\nabla\mathbf{n}} + \frac{\partial f_s}{\partial\mathbf{n}}, \tag{6.15}$$

where $\hat{v}$ is the surface normal, $\mathbf{n} = (\sin\theta\cos\varphi, \sin\theta\sin\varphi, \cos\theta)$ is the director field, θ is the polar angle, φ is the azimuthal angle, and k is a resistant coefficient. $f_b = \frac{1}{2}K_1(\nabla\cdot\mathbf{n})^2 + \frac{1}{2}K_2(\mathbf{n}\cdot\nabla\times\mathbf{n})^2 + \frac{1}{2}K_3(\mathbf{n}\times(\nabla\times\mathbf{n}))^2$ is the bulk term in the Oseen-Frank elastic free energy density, and $f_s = \frac{1}{2}K_{24}\nabla\cdot((\mathbf{n}(\nabla\cdot\mathbf{n})) + \mathbf{n}\times(\nabla\times\mathbf{n}))$ is the surface term.

For the flow of nematic disodium cromoglycate (DSCG) solutions in the rectangular microfluidic channel, we have $\hat{v} = (0, 0, 1)$ for the top wall. In steady state, $d\varphi/dx = 0$ and

$d\theta/dx = 0$. We consider the vicinity of the symmetry axis in the xy-plane of the biaxial-splay and double-splay regions, where the directors are predominantly aligned in the shear plane, so that $\varphi \sim 0^\circ$. The contribution of the bulk term to the evolution of directors on the walls simplifies to

$$\hat{v} \cdot \frac{\partial f_b}{\partial \nabla \mathbf{n}} \approx -\bar{K} \left(\frac{\partial \theta}{\partial z} \right)_s . \tag{6.16}$$

Likewise, the effect of the surface term on the evolution of directors on the walls simplifies to

$$\frac{\partial f_s}{\partial \mathbf{n}} \approx \frac{1}{2} K_{24} \left(\cos^2\theta - \sin^2\theta \right) \frac{\partial \varphi}{\partial y}. \tag{6.17}$$

Substituting Eq. 6.16 and Eq. 6.17 into Eq. 6.15 yields

$$k \left(\frac{d\theta}{dt} \right)_s = -\bar{K} \left(\frac{\partial \theta}{\partial z} \right)_s + \frac{1}{2} K_{24} \left(\cos^2\theta - \sin^2\theta \right) \frac{\partial \varphi}{\partial y}. \tag{6.18}$$

We nondimensionalize Eq. 6.18 using $y^* = y/w$, $z^* = z/b$, and $t^* = t/\tau$, where b is the plate spacing, $w \approx b/2$ is the characteristic width of double-splay or biaxial-splay configurations, and τ is the characteristic time:

$$\frac{kw}{\bar{K}\tau} \left(\frac{d\theta}{dt^*} \right)_s = -\frac{w}{b} \left(\frac{\partial \theta}{\partial z^*} \right)_s + \frac{1}{2} \frac{K_{24}}{\bar{K}} \left(\cos^2\theta - \sin^2\theta \right) \frac{\partial \varphi}{\partial y^*}. \tag{6.19}$$

For a double-splay configuration, the gradient of φ in the y-direction is positive and scales as $\frac{\partial \varphi}{\partial y^*} \sim 1$, whereas for a biaxial-splay configuration, $\frac{\partial \varphi}{\partial y^*} \sim -1$.

To solve Eq. 6.19 at stationary state, we need to know the distribution of θ in the z-direction, which can be obtained by solving the one-dimensional nematodynamic equation in the bulk [31]:

$$\gamma_1 \left(\frac{d\theta}{dt} \right)_b = \bar{K} \frac{\partial^2 \theta}{\partial z^2} - \dot{\gamma} \left(\alpha_2 \cos^2\theta - \alpha_3 \sin^2\theta \right), \tag{6.20}$$

where γ_1 is the rotational viscosity and α_2 and α_3 are the Leslie viscosity coefficients. In steady state, Eq 6.20 simplifies to

$$\bar{K} \frac{\partial^2 \theta}{\partial z^2} - \dot{\gamma} \left(\alpha_2 \cos^2\theta - \alpha_3 \sin^2\theta \right) = 0, \tag{6.21}$$

To solve Eq. 6.21, we need to determine the polar angle θ on the walls, denoted as θ_b (see

numerical methods). As the anchoring strength of nematic lyotropic chromonic liquid crystal solutions on rubbed glass is weak [216], the directors on the walls can deviate from the initial planar anchoring condition in shear flow; correspondingly, θ_b can deviate from the initial angle $\theta_{b,initial} = 90°$.

To determine θ_b in the flowing nematic LCLC solutions, we assume a sequence of θ_b ranging from 45° to 90°. Using Eq. 6.21, each presumed θ_b yields a distribution of θ in the z-direction (Fig. 6.5(A)), which further gives the gradient of θ on the walls, $\left(\frac{\partial\theta}{\partial z*}\right)_s$. By substituting the values of $\left(\frac{\partial\theta}{\partial z*}\right)_s$ into Eq. 6.19, we obtain the evolution of θ on the walls for a biaxial-splay configuration, as shown in Fig. 6.5(B). In stationary state where

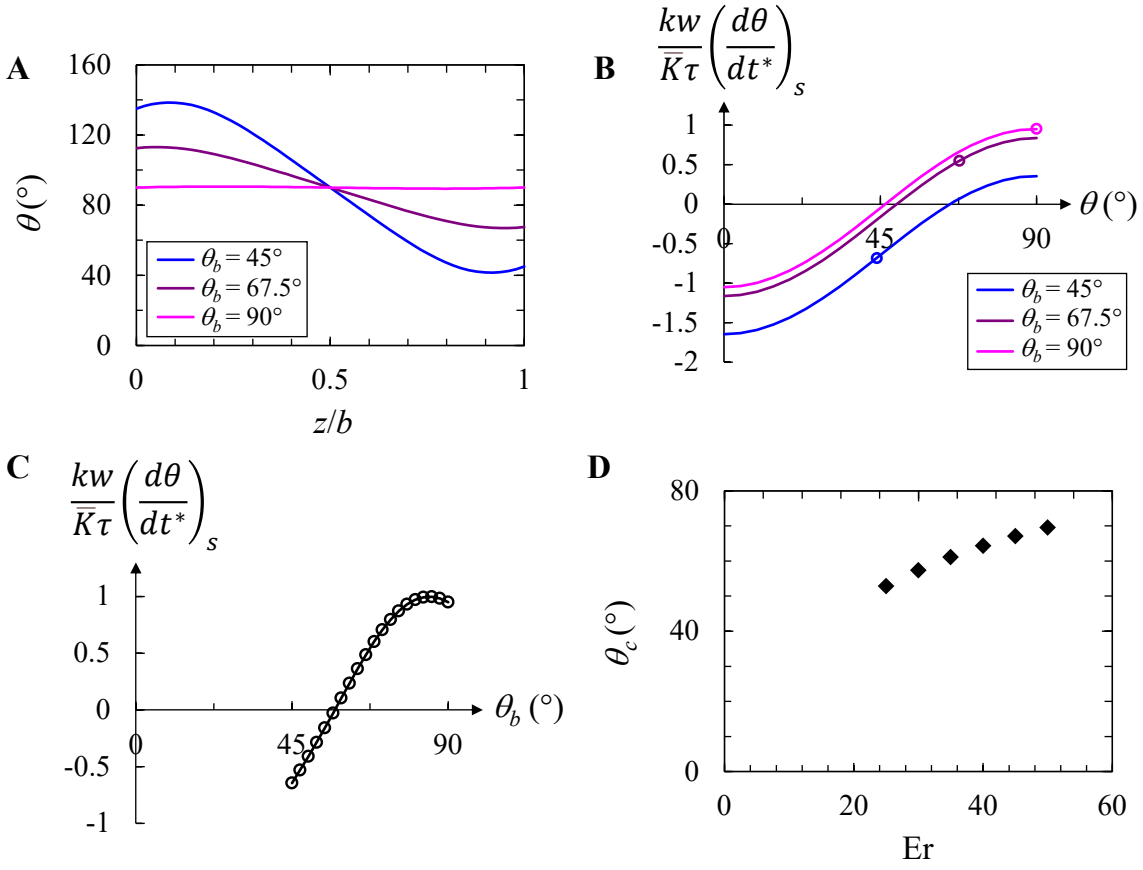

Figure 6.5: **Polar angle on the channel walls** (**A**) Distribution of polar angle, θ, in the z-direction for different presumed polar angles on the walls, θ_b, in steady state. (**B**) $\frac{kw}{\bar{K}\tau}\left(\frac{d\theta}{dt*}\right)_s$ versus θ, demonstrating the evolution of the polar angle on the walls. The open circles denote θ_b. (**C**) $\frac{kw}{\bar{K}\tau}\left(\frac{d\theta}{dt*}\right)_s$ versus θ_b. At $\frac{kw}{\bar{K}\tau}\left(\frac{d\theta}{dt*}\right)_s = 0$, this curve gives rise to a critical polar angle, θ_c. (**D**) θ_c versa $\mathrm{Er}_{\mathrm{average}}$.

$\frac{kw}{\bar{K}\tau}\left(\frac{d\theta}{dt*}\right)_s = 0$, we get the stationary angle denoted as θ_s. If $\theta_b > \theta_s$, $\frac{kw}{\bar{K}\tau}\left(\frac{d\theta}{dt*}\right)_s > 0$, which indicates that θ increases with time to reach 90°, corresponding to a planar alignment. By contrast, for $\theta_b < \theta_s$, a negative $\frac{kw}{\bar{K}\tau}\left(\frac{d\theta}{dt*}\right)_s$ indicates a decrease of θ to 0°, corresponding to a homeotropic alignment. We indicate the presumed θ_b on its corresponding curve of $\frac{kw}{\bar{K}\tau}\left(\frac{d\theta}{dt*}\right)_s$ versus θ in Fig. 6.5(B and C). Fig. 6.5(C) elucidates whether the directors at different θ_b in a biaxial-splay configuration eventually reach homeotropic or planar alignments. The condition $\frac{kw}{\bar{K}\tau}\left(\frac{d\theta}{dt*}\right)_s = 0$ denotes a critical angle, θ_c, that governs the evolution of directors on the walls. If $\theta_b < \theta_c$, the director adopts a homeotropic alignment rather than a planar alignment. In the regime of Ericksen number $\mathrm{Er}_{\mathrm{average}} = -\alpha_2\bar{\dot{\gamma}}b^2/\bar{K} = 25 - 50$, where the stripe patterns form in the experiments, the critical angle θ_c increases with an increase in $\mathrm{Er}_{\mathrm{average}}$, as shown in Fig. 6.5(D).

Given the importance of θ_c in setting the evolution of directors on the walls, we check whether $\theta_b = \theta_c$ can be a proper boundary condition by estimating the anchoring strength, W, for different θ_c. W can be evaluated by considering an extrapolation length, L_0 (Fig. 6.6(A)), as the ratio between the surface and bulk distortion energy is the ratio between L_0 and the

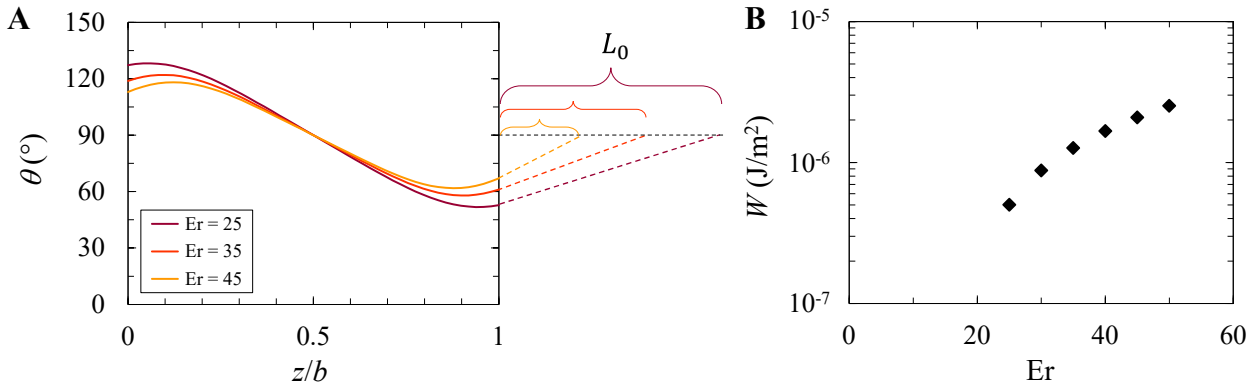

Figure 6.6: **Surface anchoring strength for assigned critical polar angles on the channel walls, θ_c.** (**A**) Distribution of polar angle, θ, in the z-direction, corresponding to different θ_c at different $\mathrm{Er}_{\mathrm{average}}$ in steady state. The extrapolation length, L_0, is obtained by extrapolating the curve from the walls to the location where θ reaches 90°. (**B**) The anchoring strength, W, for different θ_c in the regime of $\mathrm{Er}_{\mathrm{average}} = 25 - 50$, is on the order of $10^{-6} - 10^{-7}$ J/m^2.

plate spacing b [30]:

$$\frac{F_{surface}}{F_{bulk}} = \frac{L_0}{b}, \tag{6.22}$$

where $F_{surface} = \frac{1}{2}W\theta_b^2$ and $F_{bulk} = \frac{1}{2}\int_0^b \bar{K}\left(\frac{\partial\theta}{\partial y}\right)^2 dy$. The anchoring strength is expressed as

$$W = \frac{L_0}{b\theta_b^2}\int_0^b \bar{K}\left(\frac{\partial\theta}{\partial y}\right)^2 dy \approx \frac{L_0\bar{K}}{b^2}. \tag{6.23}$$

From θ_c obtained in the regime of $\mathrm{Er}_{\mathrm{average}} = 25 - 50$, we find that W is on the order of $10^{-6} - 10^{-7}$ J/m^2, as shown in Fig. 6.6(B). These values are in good agreement with experiment results that report anchoring strengths of nematic DSCG solutions on rubbed glass on the order of $10^{-6} - 10^{-7}$ J/m^2 [216].

6.A.2 Director field of stripe patterns

Using an optical microscope with crossed polarizer and analyzer, we identify the director field at the dark stripes by rotating the crossed polarizer and analyzer by 45°. The dark stripes remain dark, which indicates that the directors are homeotropically aligned in these regions (Fig. 6.7(A)). The dark stripes correspond to region I of the stripes, as indicated in Fig. 1(C).

We then determine the director field between two dark stripes, denoted as region II, by adding a full-wave-plate optical compensator (560 nm) with the slow axis oriented at 45° to the polarizer and in the direction perpendicular to the flow. In experiments performed without the full-wave-plate optical compensator, we find that the retardance in between two dark stripes is approximately 150 nm (light grey color) by comparing with a commercial Michel-Lévy color chart (issued by Zeiss Microscopy) (Fig. 6.7(A)). After the compensator is inserted, we can distinguish the directors in the direction more perpendicular or more parallel to the flow by considering the change in color, which represents a change in the retardance: an increase of the retardance by 560 nm, appearing as light blue, indicates that the director is aligned parallel to the flow direction; a decrease of the retardance by 560 nm, appearing as orange, indicates that the director is aligned perpendicular to the flow direction. We observe an orange color, indicating that the director is aligned more perpendicular to the flow

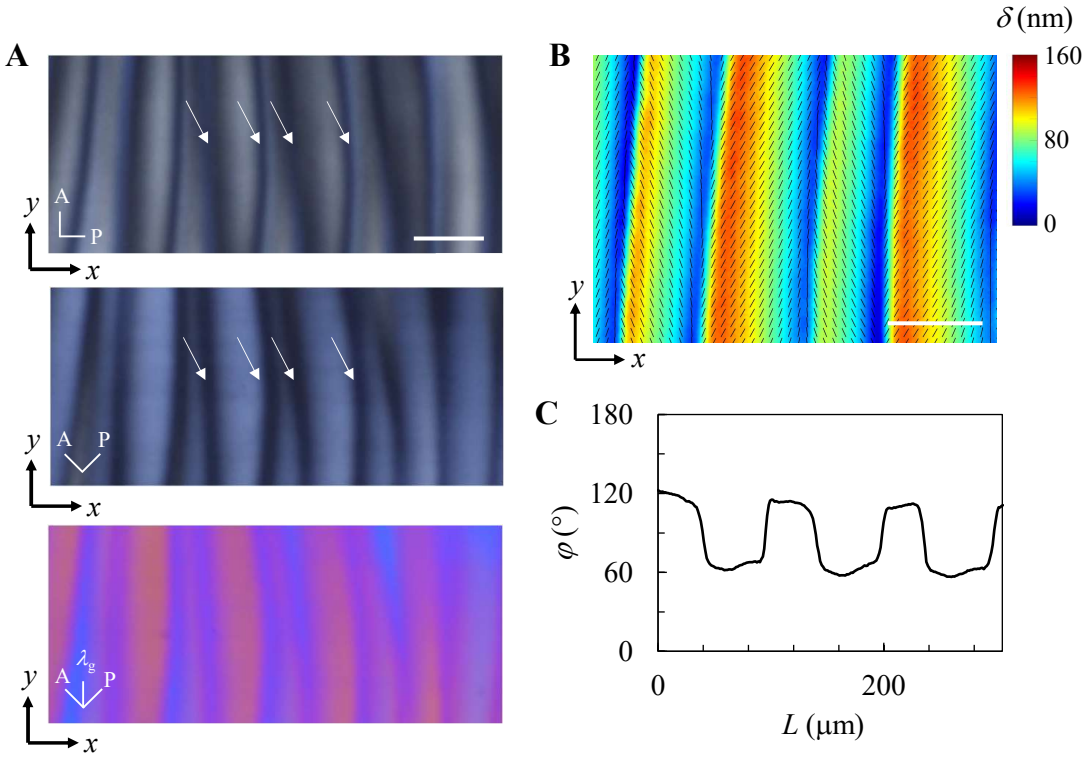

Figure 6.7: **Director field of stripe patterns.** (**A**) Stripe patterns are observed through crossed polarizer, P, and analyzer, A, where the polarizer is either parallel to flow direction along x-axis (upper panel) or is oriented at 45° to the flow direction (middle panel). Dark stripes remain dark as indicated by the white arrows. With crossed polarizer and analyzer oriented in the direction at 45° to the flow direction and compensated with full-wave-plate optical compensator with its slow axis, $\lambda_g = 560$ nm, perpendicular to the flow direction, regions in between stripe lines appear orange (lower panel). The scale bar is 100 μm. (**B**) Retardance map of the stripe patterns. The color represents the optical retardance, δ. The scale bar is 50 μm. (**C**) Along the line in x-direction across stripes, the azimuthal angle shows alternatively $\approx 62°$ and $\approx 115°$.

direction (Fig.S1(A)). The director rotates from being perpendicular to the flow direction pointing in the y-direction to being parallel to the thickness direction, which indicates a periodic twist deformation along the flow direction.

We quantify the director field averaged in the thickness direction by using PolScope. The azimuthal angle in between the low retardance regions (region I) is alternatively $\approx 62°$ and $\approx 115°$ (Fig. 6.7(B, C)). The angles closer to 90° rather than 0° and 180° demonstrate that the director field averaged in the thickness direction is more perpendicular to the flow, which is consistent with the observation using polarized microscopy in Fig. 6.7(A).

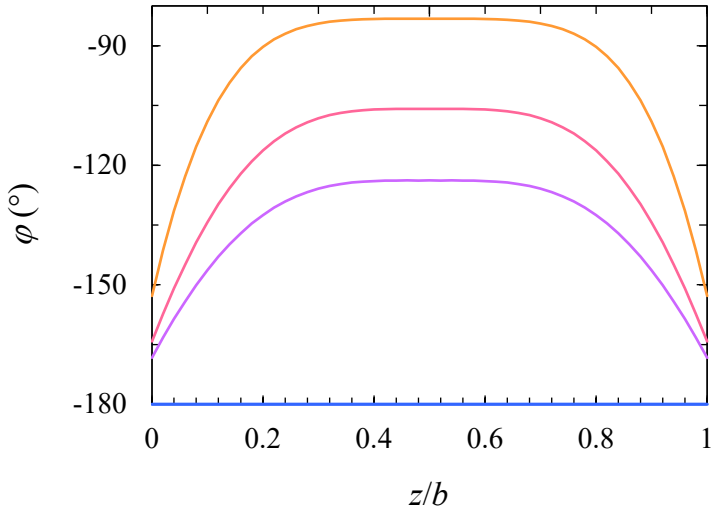

Figure 6.8: **Azimuthal angle of directors in weak flows.** With increasing pressure gradient ($G = 5 \times 10^{-6}$ (blue), 8×10^{-6} (purple), 1×10^{-5} (red), and 2×10^{-5} (orange) (in simulation units)), the azimuthal angle, φ, in the center region of the channel increases from -180 ° (initial anchored direction) to -90 ° (log-rolling state); φ on the walls also deviates from -180 °.

6.A.3 Azimuthal angles of nematic LCLC solutions in weak flows

To investigate the azimuthal angles of the directors of nematic LCLC solutions in weak flows, we simulate the director field based on the two-dimensional nematodynamic equation (see numerical methods). As the pressure gradient, G, increases from 5×10^{-6} to 2×10^{-5}, the azimuthal angle of the directors in the center of the channel increases from being parallel to the flow direction maintaining the initial anchoring condition to being tilted and to gradually approaching 90° corresponding to the log-rolling state, as shown in Fig. 6.8. The tilted director field in weak flows is in agreement with the experimental observations.

6.A.4 Frank elastic free energy for different configurations of the director field

Three configurations can possibly emerge in the weak flow of nematic disodium cromoglycate solutions: biaxial-splay, double-splay and double-twist configurations. We describe these configurations in a cylindrical coordinate system, where the longitudinal axis is in the z-direction. For a biaxial-splay configuration, the director field is $\mathbf{n} = (\sin\theta\cos\alpha, \sin\theta\sin\alpha, \cos\theta)$, where

$\theta = \theta(\rho)$ is the polar angle between the director and the z-axis, ρ the radial distance from the z-axis to the center point of the director, $\alpha = -2\phi$ is the azimuthal angle between the director and the ρ-axis, and ϕ is the angle between the reference direction on the chosen plane perpendicular to the longitudinal axis and the line from the origin to the projection of the director on the plane. Substituting the director field of the biaxial-splay configuration into the general form of the Oseen-Frank elastic free energy density,

$$f = 1/2[K_1(\nabla \cdot \mathbf{n})^2 + K_2(\mathbf{n} \cdot \nabla \times \mathbf{n})^2 + K_3(\mathbf{n} \times \nabla \times \mathbf{n})^2 - K_{24}\nabla \cdot (\mathbf{n} \cdot \nabla \times \mathbf{n} + \mathbf{n} \times \nabla \times \mathbf{n})], \tag{6.24}$$

yields

$$f_{\mathrm{biaxial-splay}} = \frac{1}{2}K_1\cos^2\alpha\left(\cos\theta\frac{\partial\theta}{\partial\rho} - \frac{\sin\theta}{\rho}\right)^2 + \frac{1}{2}K_2\sin^2\alpha\left(\frac{\partial\theta}{\partial\rho} - \frac{\sin\theta\cos\theta}{\rho}\right)^2 + \frac{1}{2}K_3\sin^2\theta\left(\frac{\sin^2\theta\sin^2\alpha}{\rho^2} + \cos^2\alpha\left(\frac{\partial\theta}{\partial\rho}\right)^2\right) + K_{24}\left(\frac{\sin\theta\cos\theta}{\rho}\frac{\partial\theta}{\partial\rho}\right). \tag{6.25}$$

For the double-splay configuration, the director field is $\mathbf{n} = (\sin\theta, 0, \cos\theta)$, and the Oseen-Frank elastic free energy density can be expressed as

$$f_{\mathrm{double-splay}} = \frac{1}{2}K_1\left(\cos\theta\left(\frac{\partial\theta}{\partial\rho}\right) + \frac{\sin\theta}{\rho}\right)^2 + \frac{1}{2}K_3\sin^2\theta\left(\frac{\partial\theta}{\partial\rho}\right)^2 - K_{24}\left(\frac{\sin\theta\cos\theta}{\rho}\frac{\partial\theta}{\partial\rho}\right). \tag{6.26}$$

The director field for the double-twist configuration can be expressed as $\mathbf{n} = (0, \sin\theta, \cos\theta)$, and the corresponding Oseen-Frank elastic free energy density is

$$f_{\mathrm{double-twist}} = \frac{1}{2}K_2\left(\frac{\sin\theta\cos\theta}{\rho} + \left(\frac{\partial\theta}{\partial\rho}\right)\right)^2 + \frac{1}{2}K_3\left(\frac{\sin^4\theta}{\rho^2}\right) - K_{24}\left(\frac{\sin\theta\cos\theta}{\rho}\frac{\partial\theta}{\partial\rho}\right). \tag{6.27}$$

The comparison of Eq. 6.25, Eq. 6.26, and Eq. 6.27 reveals that the saddle-splay elasticity term, $K_{24}\left(\frac{\sin\theta\cos\theta}{\rho}\frac{\partial\theta}{\partial\rho}\right)$, is negative for both double-twist and double-splay configurations, but positive for the biaxial-splay configuration. This indicates that the saddle-splay elasticity lowers the energy for double-splay and double-twist configurations, but increases the energy for the biaxial-splay configuration. Given that $K_{24} \approx K_3 \approx 3K_1 \approx 30K_2$ [222], $f_{\mathrm{biaxial-splay}}$ is

larger than $f_{\text{double-splay}}$ and $f_{\text{double-twist}}$. This indicates that the biaxal-splay configuration is much more costly and less preferred than the double-twist and double-splay configurations.

We further compare the Frank elastic free energy for the double-twist and double-splay configurations by integrating $f_{\text{double-splay}}$ and $f_{\text{double-twist}}$ in a cylinder with a radius of R and a unit length:

$$\Delta F_{\text{elastic}} = F_{\text{double-splay}} - F_{\text{double-twist}} = \int\int (f_{\text{double-splay}} - f_{\text{double-twist}})\rho d\rho d\theta. \quad (6.28)$$

We assume that the distribution θ in the radial direction, ρ, is linear and follows $\theta = 2\pi\rho/R$. Eq. 6.28 then yields $\Delta F_{\text{elastic}} \approx 3.69K_1 - 5.32K_2 - 0.21K_3$. Because the twist Frank elastic constant, K_2, is small compared to K_1 and K_3, $\Delta F_{\text{elastic}} = 25.28K_2 > 0$. This reveals that $F_{\text{double-splay}} > F_{\text{double-twist}}$. Therefore, the double-twist configuration costs the least elastic energy among these three configurations and is therefore selected.

6.A.5 Derivation of the period of stripes

Given that the twist Frank elastic constant is much smaller than the splay and bend Frank elastic constants, $K_2 << K_{1,3}$, we neglect the contribution of twist deformation to the total elastic energy of the periodic double-twist structure and consider the regions close to the walls of the microfluidic channel that are dominated by bend and splay deformations (Fig 6.4). The director field is described as $\mathbf{n} = (\sin\theta, 0, \cos\theta)$, where θ is the polar angle that is a function of x. The nematodynamic equation in steady state is [31]

$$(K_1 - K_3)\cos\theta\sin\theta\left(\frac{\partial\theta}{\partial x}\right)^2 + \left(K_3\sin^2\theta + K_1\cos^2\theta\right)\frac{\partial^2\theta}{\partial x^2} = \left(\alpha_2\cos^2\theta - \alpha_3\sin^2\theta\right)\dot{\gamma}_{xz}. \quad (6.29)$$

For simplicity, we assume a small θ in the region close to the channel walls, so that $\alpha_2\cos^2\theta - \alpha_3\sin^2\theta \approx -\alpha_3$, $(K_1 - K_3)\cos\theta\sin\theta \approx 0$, and $K_3\sin^2\theta + K_1\cos^2\theta \approx K_3$. Eq. 6.29 then yields:

$$\alpha_3\dot{\gamma}_{xz} = -K_3\frac{\partial^2\theta}{\partial x^2}. \quad (6.30)$$

We conduct a scaling analysis based on Eq. 6.30. The characteristic length scale of bend deformation in the x-direction scales as half of the period of stripes, $p_c/2$, and the shear rate is scaled by $\dot{\gamma}_{xz} \propto V/b$. The elastic term and the viscous term can then be expressed as $K_3/(p_c/2)^2$ and $\alpha_3 V/b$, respectively. The balance between the elastic torque and the viscous torque, $K_3/(p_c/2)^2 \propto \alpha_3 V/b$, yields an expression for the characteristic period of stripes: $p_c \propto 2\sqrt{K_3 b/\alpha_3 V}$.

Chapter 7

Conclusions

7.1 Summary

In this thesis, we establish strategies to control the non-equilibrium growth processes in anisotropic systems, in which the anisotropy either allows for a preferred growth direction of the interfacial motion of fluids or induces specific configurations of molecular aggregates. We investigate two anisotropic systems: a system that exhibits external anisotropy in the growth environment, and a system that possesses intrinsic anisotropy imposed by the orientation of nematic lyotropic chromonic liquid crystals (LCLCs). By analyzing the nonlinear dynamics and the competition among driving forces, we demonstrate the principles governing the selection of patterns in the interfacial viscous-fingering instability at the macroscale and the flow-induced structures created by supramolecular assemblies at the microscale. The key conclusions are summarized as follows.

1. In the viscous-fingering instability with two miscible fluids in an externally anisotropic system, where the anisotropy is introduced by engraving an ordered lattice on one of the plates of a Hele-Shaw cell, the morphology transition from dense-branching to dendritic growth and the selected symmetry of the dendrites are governed by the viscosity ratio between the two fluids and the degree of anisotropy. Upon approaching the morphology boundary, the dendritic patterns systematically transition from six-fold towards twelve-fold symmetry.

2. In the viscous-fingering instability with intrinsic anisotropy introduced by nematic lyotropic chromonic liquid crystal (LCLCs) solutions, the morphology transition to dendritic growth is induced by the suppression of the intrinsic tumbling behavior of nematic LCLC solutions, which leads to flow-alignment of the material that provides a shear-enhanced anisotropy. By relating the microscopic alignment to the macroscopic growth morphology selection, we develop a quantitative criterion for controlling the growth of interfacial fluid instabilities in terms of the competition between the elastic torque from the nematic potential and the viscous torque from shear flow.

3. When nematic LCLC solutions are pushed out-of-equilibrium by a pressure-driven flow, pure-twist disclination loops emerge in a certain range of shear rates. The disclination loops form at the boundary between two regions of irreconcilable director alignments, where the director aligns predominantly along the flow direction close to the channel walls but perpendicular to the flow direction in the center of the channel. The nucleation of the defects releases the high elastic stresses of the director gradient at the boundary. Pure-twist disclination loops emerge because of the significant elastic anisotropy characteristic of LCLCs, where twist deformations are energetically cheaper than bend or splay deformations.

4. The mirror symmetry of the assemblies of achiral LCLC aggregates can be broken by weak flow. We show that the mirror symmetry breaking is triggered at regions of biaxial-splay deformations, which are unstable and evolve into a lower energy-cost configuration of the director field, a periodic double-twist structure. This structure exhibits a characteristic period that is set by the competition between the elastic torque and the viscous torque acting on the director field, and that can be tuned by controlling the flow velocity.

7.2 Future work

7.2.1 Instability-mediated fabrication methods

The diversity of structures resulting from fluid instabilities opens the potential for using instabilities to impart shape and function to materials in manufacturing processes. Indeed, instability-mediated fabrication methods are in development [1, 226], as, distinct from current manufacturing techniques including 3D printing, instability-mediated methods do not require a layer-by-layer approach [227, 228] but rely on spontaneous self-amplified growth. Given the limited need for external assistance, these methods could significantly simplify manufacturing processes and minimize the environmental footprint. Recent approaches exploit instabilities to impart desired shapes [10, 11]. For example, thousands of uniform microscale droplets have been created from the Plateau-Rayleigh instability [10]. Harnessing instabilities to fabricate structures at multiscales, *e.g.*, organizing structures of molecular assemblies at the microscale to mediate the properties of metamaterials at the macroscale, however, is barely explored [200].

Flowing nematic lyotropic chromonic liquid crystal (LCLC) solutions provide an ideal platform to explore instability-mediated configurations of supramolecular assemblies for fabricating functional materials. We have demonstrated a rich variety of flow-induced structures resulting from the configurations of the director field in nematic LCLC solutions, as discussed in Chapters 5 and 6. As nematic LCLC directors can serve as a host to align monomers [229], monomers can potentially be assembled by the flow-induced structures. At the same time, we could 'freeze' the configuration of monomers through polymerization. For example, the periodic double-twist structures forming in weak flows of LCLC solutions discussed in Chapter 6, could be expected to impart helical structures to the polymerized material. Helical structures are known to strengthen materials with respect to deformations in multiple directions [230], and are useful elements in metamaterials [231].

To realize instability-mediated multiscale fabrication methods, a generic framework for triggering instabilities that provide the desired function to materials needs to be established. Such a framework is currently lacking, because of two main challenges: i) finding generalized analytic solutions describing the dynamics of flow-induced structures; ii) predicting the final

material properties of instability-mediated microstructures. Moreover, freezing the flow-induced structures will affect the non-linear growth dynamics during solidification [1]; the instability and the freezing process are interlinked. Experimental, numerical and theoretical efforts are required to reveal these intricate dynamic processes.

7.2.2 Pattern formation in drying droplets

Drying droplets of aqueous solutions of macromolecules such as polymers or microfibers are an intriguing model system that couples flow and phase transition to form complex patterns [232–236]. The morphologies of final dried patterns are affected by the interplay between capillary flows in the droplet and the phase transition of the macromolecular solutions [232, 237].

We find that aqueous solutions containing mixtures of the protein peptone (Sigma-Aldrich) and the salt sodium chloride (Sigma-Aldrich) form dendritic patterns during drying for salt concentrations ranging from 2 wt% to 20 wt% at a fixed peptone concentration of 9 wt%. How the nonlinear growth selects characteristic length scales and growth rates of the dendrites, and how the resulting pattern is affected by the growth environment that may be altered by the concentrations of peptone and salt, the humidity and the contact angle, is currently unknown. Remarkably, the characteristics of the dendrites and the location where nucleation occurs depend sensitively on the concentration of salt, as shown in Fig. 7.1(A).

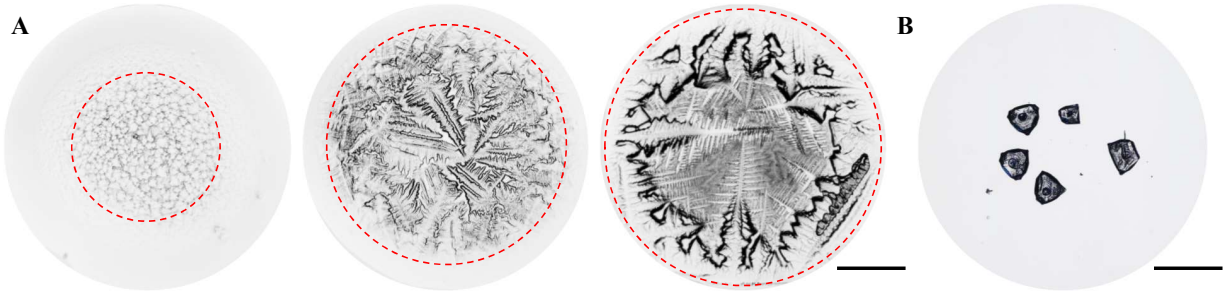

Figure 7.1: **Dendrite formation in drying drops.** (**A**) Quasi-two-dimensional dendritic patterns form during the drying of sessile drops composed of aqueous solutions of peptone and salt. From left to right, the salt concentrations are 2 wt%, 4.5 wt% and 18 wt%. The peptone concentration is 9 wt%. The red circles indicate the nucleation locations. The scale bar is 500 μm. (**B**) Three dimensional crystals grow in drying drops of aqueous salt solutions (9 wt%) that do not contain peptone . The scale bar is 500 μm.

At lower salt concentration, the nucleation occurs closer to the center of the drop, and the width of the dendritic fingers decreases. In the absence of peptone, only three-dimensional crystals, rather than quasi-two dimensional dendrites, emerge, as shown in Fig. 7.1(B). This suggests that peptone is necessary for the formation of dendritic patterns. Previous studies provide hints that suggest that the macromolecules pin the contact line of the drop, which can alter the capillary flows and might modify the growth environment and lead to the emergence of complex patterns [237]. An understanding of the role of peptone for the formation of dendritic patterns, and the mechanisms governing their growth, is currently lacking.

7.2.3 Extension of the principles of pattern formation in physical systems to biological systems

The patterns induced by interfacial instabilities in physical systems exhibit remarkable similarities to structures growing in biological systems. Examples range from bacteria colonies to neural networks and human lungs, which all exhibit ramified branching structures similar to those resulting from dense-branching growth [1]. Indeed, the collective motion of cells in living systems involves unstable processes, and the resulting patterns have recently been shown to share analogies with instabilities in physical systems [238–240]. For example, the folding brain orgnoids (Fig. 7.2(A)) and the fingering-like structures of epithelial cells (Fig. 7.2(B)) are results of instabilities arising during the growth process [238–240]. In the spreading of epithelial cells, a fingering instability arises from initial small perturbations and the boundary of the cells becomes unstable and evolves into finger-like structures [241, 242]. Similar to the viscous-fingering instability in immiscible fluids that results from two competing effects, the pressure gradient and the surface tension, the instability in the cells results from a competition between two forces, the active cellular traction force imposing a velocity gradient that induces an unstable accelerated front and the contractile intercellular stresses that stabilize the perturbation [242, 243].

Compared to physical systems, however, biological systems exhibit more complex dynamics induced by their activity sustained by a continuous energy consumption and interaction forces between cells [244]. For example, when the fingering instability arises in the spreading

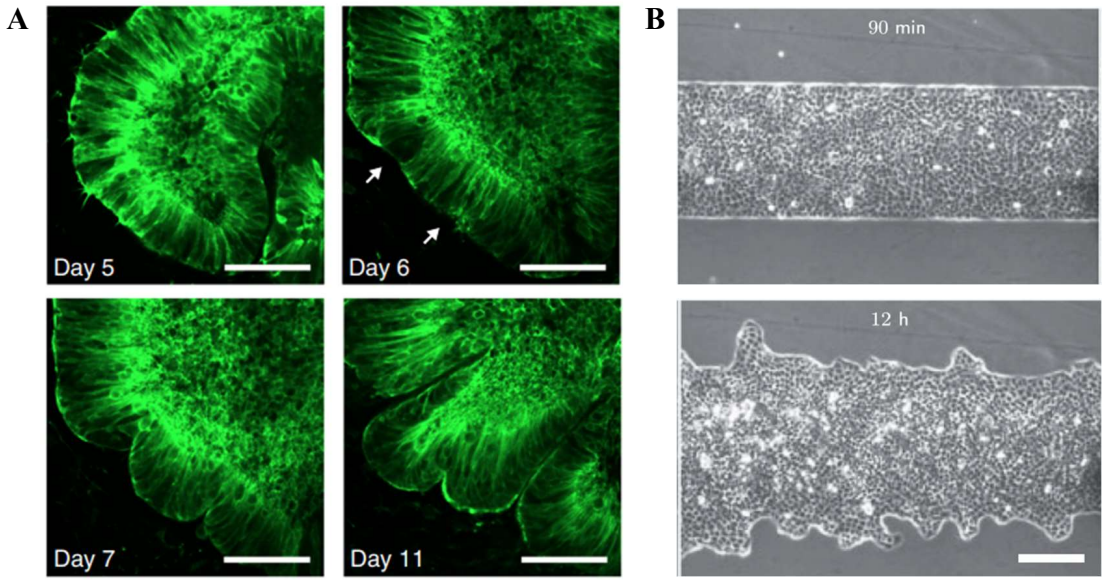

Figure 7.2: **Pattern formation in biological systems.** (**A**) An instability occurs at the free surface of organoids during the development of the organoids (the initial instability is indicated by the white arrows) and leads to finger-like structures and wrinkles. The scale bar is 50 μm. Adapted from [238]. Copyright 2018 Nature Publishing Group. (**B**) A fingering instability emerges during the spreading of epithelial cells. The scale bar is 200 μm. Adapted from [239]. Copyright 2019 APS.

of epithelial cells, due to the distinct velocity fields at different locations of the finger-like structures, the fastest moving cells at the fingertip tend to transition from non-epithelial to fibroblast appearance and behavior [241]. This transition creates an intercellular mechanical tension between the leader and follower cells that prevents the splitting of the fingertip [241]. The unstable processes in biological systems are thus more complex than instabilities controlled only by gradient-driven transport. To which extent we can adapt principles of pattern growth in physical systems to growth in biological systems requires extensive explorations.

A recent study [243], in an attempt to model the spreading of cells on substrates, has modified Darcy's law that describes flow in a porous medium

$$\mathbf{v} = -\frac{k}{\eta}\nabla P, \tag{7.1}$$

where $\mathbf{v}$ is the flow velocity, P is the pressure, k is the permeability, and η is the viscosity of the fluid, by adding a term accounting for the interaction between cells when the friction

with the substrate is large

$$\mathbf{v} = -\frac{1}{\xi}\nabla P + \frac{1}{\xi}\nabla \cdot \sigma, \tag{7.2}$$

where σ is the intercellular stress and ξ is the friction coefficient. Based on Eq. 7.2, a linear stability analysis has been performed to describe the velocity and pressure fields in the initial unstable state [243]. The later nonlinear growth stages, however, are not yet understood.

The collective motion of cells has been considered within the framework of active nematics with preferred orientations [192]. Indeed, the polar field of cells can be expressed in analogy to the director field of nematic liquid crystals. Epithelia cells in the fingers are oriented along the growth direction of the fingers [242]. This is reminiscent of the patterns formed in nematic liquid crystals, where we have shown that the growth morphology depends on the alignment of the director field: a shear-aligned director field can prevent the fingertip from splitting, as discussed in Chapter 4. Would the oriented cells in the fingers also suppress the instability and prevent the fingertips from splitting? The interplay between the alignment of cells and the selected growth morphology involves rich dynamics with fascinating open questions.

Revealing general mechanisms for pattern growth in biological systems is at the crossroad of several fields including biology, physics and chemistry. It might give insight into the development of organs and could be exploited in practical applications related to synthetic tissues.

7.2.4 Role of anchoring conditions for tuning flow-induced structures in nematic lyotropic chromonic liquid crystals

The surface anchoring conditions can sensitively affect the configuration of nematic liquid crystals (LCs) in the static state [31]. Under flow, it has so far been thought that the role of the surface anchoring condition for the dynamics of the director field is negligible if the viscous torque from the flow dominates over the elastic torque imposed as the directors resist the deviation from the initial anchoring condition induced by the flow [31]. The relative importance of the viscous torque compared to the elastic torque is evaluated by the Ericksen number $\mathrm{Er} = \eta\dot{\gamma}{l_c}^2/K$, where $\dot{\gamma}$ is the shear rate, l_c is a characteristic length

scale, η is the characteristic viscosity, and K is the characteristic Frank elastic constant [31]. In nematic lyotropic chromonic liquid crystal (LCLC) solutions, the value of the Ericksen number strongly depends on which deformation mode is considered, *i.e.*, twist, bend, or splay deformations, as nematic LCLC solutions have significant anisotropy in viscosity and elasticity [50]. For example, the twist viscosity can be hundreds of times larger than the bend viscosity, and the twist Frank elastic constant can be tens of times smaller than the bend Frank elastic constant [50]. Given that the dynamics of nematic LCLCs have been shown to be distinct from thermotropic liquid crystals and the current understanding of flowing nematic LCLC solutions is at a very early stage [61, 65], it is often unclear which the dominant deformation modes are in flowing nematic LCLC solutions, and the importance of the surface anchoring condition for the director alignment, particularly for the stability of the director field, under flow is currently unknown.

We have investigated flowing nematic lyotropic chromonic liquid crystal (LCLC) solutions with planar anchoring condition where the directors are in the direction parallel to the flow in Chapters 5 and 6. For this anchoring condition, pure-twist disclination loops and chiral periodic double-twist structures emerge in different regimes of shear rates. Would the flow-induced structures also form for different anchoring conditions, such as planar anchoring perpendicular to the flow direction or homeotropic anchoring? Indeed, when we tune the planar anchoring condition to be perpendicular to the flow direction, we discover entirely different structures, even though the Ericksen number based on the twist deformation mode can reach high values of $\approx 10^4$. Remarkable band textures perpendicular to flow direction, which coexist with small domains, emerge across the entire flow field at steady state, as shown in Fig. 7.3(A). The band textures become blurred and appear darker as we rotate the crossed polarizer and analyzer by 45 °, as shown in Fig. 7.3(B), which indicates that the directors are tilted in the directions close to either 45 ° or 135 °. Adding a full-wave-plate optical compensator with its slow axis, λ_g, oriented at 45 ° to the polarizer reveals that the directors in neighboring bands tilt in opposite directions, *i.e.*, alternatively adopt azimuthal angles of 45 ° and 135 °, as shown in Fig. 7.3(C).

Exploring the flow-induced structures in nematic LCLCs for different surface anchoring conditions can provide guidance to programming the director field under flow by patterning

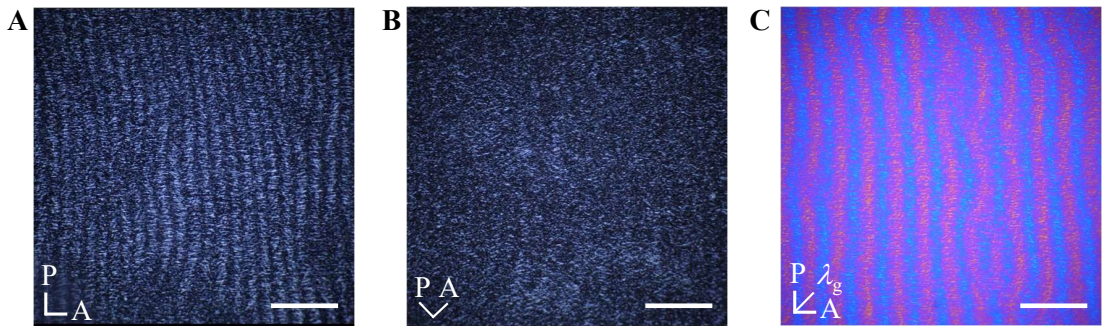

Figure 7.3: **Flow-induced band textures in nematic lyotropic chromonic liquid crystals.** An aqueous solution of 13 wt% disodium cromoglycate (DSCG) in the nematic phase at room temperature $T = 23.2 \pm 0.5$ °C is injected into a microfluidic cell with plate spacing of 15 μm at a volumetric flow rate of $q = 25$ μl/min. Band textures emerge in the flow of DSCG solutions, imaged through a crossed polarizer, P, and an analyzer, A, for the polarizer (**A**) parallel to the flow direction and (**B**) oriented at 45 ° to the flow direction. (**C**) The band textures appear alternatively blue and magenta when imaged using a full-wave-plate optical compensator. The blue color indicates that the director is more perpendicular to λ_g; the magenta color indicates that the director is more parallel to λ_g. The scale bars are 500 μm.

the anchoring on surfaces. Such control over the director field under flow may open new routes for using LCLCs to control assembly and flow of biological systems or particles in microfluidic devices [48, 245, 246].

Bibliography

[1] F. Gallaire and P.-T. Brun, "Fluid dynamic instabilities: theory and application to pattern forming in complex media," Phil. Trans. Math. Phys. Eng. Sci. **375**, 20160155 (2017).

[2] L. Paterson, "Radial fingering in a Hele-Shaw cell," J. Fluid Mech. **113**, 513–529 (1981).

[3] E. Ben-Jacob, G. Deutscher, P. Garik, N. D. Goldenfeld, and Y. Lareah, "Formation of a dense branching morphology in interfacial growth," Phys. Rev. Lett. **57**, 1903 (1986).

[4] J. S. Langer, "Instabilities and pattern formation in crystal growth," Rev. Mod. Phys. **52**, 1 (1980).

[5] J. S. Langer, "Dendrites, viscous fingers, and the theory of pattern formation," Science **243**, 1150–1156 (1989).

[6] Y. Couder, F. Argoul, A. Arnéodo, J. Maurer, and M. Rabaud, "Statistical properties of fractal dendrites and anisotropic diffusion-limited aggregates," Phys. Rev. A **42**, 3499 (1990).

[7] E. Ben-Jacob, N. Goldenfeld, J. S. Langer, and G. Schön, "Dynamics of interfacial pattern formation," Phys. Rev. Lett. **51**, 1930 (1983).

[8] E. Ben-Jacob and P. Garik, "The formation of patterns in non-equilibrium growth," Nature **343**, 523–530 (1990).

[9] H. Yasuda, K. Morishita, N. Nakatsuka, T. Nishimura, M. Yoshiya, A. Sugiyama, K. Uesugi, and A. Takeuchi, "Dendrite fragmentation induced by massive-like δ–γ transformation in Fe–C alloys," Nat. Commun. **10**, 1–8 (2019).

[10] J. J. Kaufman, G. Tao, S. Shabahang, E.-H. Banaei, D. S. Deng, X. Liang, S. G. Johnson, Y. Fink, and A. F. Abouraddy, "Structured spheres generated by an in-fibre fluid instability," Nature **487**, 463–467 (2012).

[11] E. Jambon-Puillet, M. R. Piéchaud, and P.-T. Brun, "Elastic amplification of the rayleigh–taylor instability in solidifying melts," Proc. Natl. Acad. Sci. U.S.A. **118**, e2020701118 (2021).

[12] F. M. Orr and J. J. Taber, "Use of carbon dioxide in enhanced oil recovery," Science **224**, 563–569 (1984).

[13] G. M. Homsy, "Viscous fingering in porous media," Ann. Rev. Fluid Mech. **19**, 271–311 (1987).

[14] M. B. Amar and D. Bonn, "Fingering instabilities in adhesive failure," Physica D **209**, 1–16 (2005).

[15] Y. Cinar, A. Riaz, and H. A. Tchelepi, "Experimental study of CO_2 injection into saline formations," Soc. Petrol. Eng. J. **14**, 588–594 (2009).

[16] P. G. Saffman and G. I. Taylor, "The penetration of a fluid into a porous medium or Hele-Shaw cell containing a more viscous liquid," Proc. R. Soc. Lond. A **245**, 312–329 (1958).

[17] H. S. Hele-Shaw, "The flow of water," Nature **58**, 34–36 (1898).

[18] E. Ben-Jacob, R. Godbey, N. D. Goldenfeld, J. Koplik, H. Levine, T. Mueller, and L. Sander, "Experimental demonstration of the role of anisotropy in interfacial pattern formation," Phys. Rev. Lett. **55**, 1315 (1985).

[19] E. Ben-Jacob, P. Garik, T. Mueller, and D. Grier, "Characterization of morphology transitions in diffusion-controlled systems," Phys. Rev. A **38**, 1370–1380 (1988).

[20] V. Horváth, T. Vicsek, and J. Kertész, "Viscous fingering with imposed uniaxial anisotropy," Phys. Rev. A **35**, 2353–2356 (1987).

[21] M. Rabaud, Y. Couder, and N. Gerard, "Dynamics and stability of anomalous Saffman-Taylor fingers," Phys. Rev. A **37**, 935–947 (1988).

[22] Y. Couder, O. Cardoso, D. Dupuy, P. Tavernier, and W. Thom, "Dendritic growth in the Saffman-Taylor experiment," EPL **2**, 437–443 (1986).

[23] G. Zocchi, B. E. Shaw, A. Libchaber, and L. P. Kadanoff, "Finger narrowing under local perturbations in the Saffman-Taylor problem," Phys. Rev. A **36**, 1894–1900 (1987).

[24] L. Ducloué, A. L. Hazel, D. Pihler-Puzović, and A. Juel, "Viscous fingering and dendritic growth under an elastic membrane," J. Fluid Mech. **826**, R2 (2017).

[25] S. W. McCue, "Short, flat-tipped, viscous fingers: novel interfacial patterns in a Hele-Shaw channel with an elastic boundary," J. Fluid Mech. **834**, 1–4 (2018).

[26] A. Juel, D. Pihler-Puzović, and M. Heil, "Instabilities in blistering," Annu. Rev. Fluid Mech. **50**, 691–714 (2018).

[27] A. Buka, J. Kertész, and T. Vicsek, "Transitions of viscous fingering patterns in nematic liquid crystals," Nature **323**, 424–425 (1986).

[28] A. Buka, P. Palffy-Muhoray, and Z. Racz, "Viscous fingering in liquid crystals," Phys. Rev. A **36**, 3984 (1987).

[29] I. Bischofberger, R. Ramachandran, and S. R. Nagel, "Fingering versus stability in the limit of zero interfacial tension," Nat. Commun. **5**, 1–6 (2014).

[30] P.-G. De Gennes and J. Prost, *The physics of liquid crystals* (Oxford University Press, 1993).

[31] M. Kleman and O. D. Lavrentovich, *Soft matter physics: an introduction* (Springer Science & Business Media, 2007).

[32] S. J. Woltman, G. D. Jay, and G. P. Crawford, "Liquid-crystal materials find a new order in biomedical applications," Nat. Mater. **6**, 929–938 (2007).

[33] S. W. Ula, N. A. Traugutt, R. H. Volpe, R. R. Patel, K. Yu, and C. M. Yakacki, "Liquid crystal elastomers: an introduction and review of emerging technologies," Liq. Cryst. Rev. **6**, 78–107 (2018).

[34] S. Shiyanovskii, O. Lavrentovich, T. Schneider, T. Ishikawa, I. Smalyukh, C. Woolverton, G. Niehaus, and K. Doane, "Lyotropic chromonic liquid crystals for biological sensing applications," Mol. Cryst. Liq. **434**, 259–587 (2005).

[35] T. Sergan, T. Schneider, J. Kelly, and O. D. Lavrentovich, "Polarizing-alignment layers for twisted nematic cells," Liq. Cryst. **27**, 567–572 (2000).

[36] S.-W. Tam-Chang, W. Seo, K. Rove, and S. M. Casey, "Molecularly designed chromonic liquid crystals for the fabrication of broad spectrum polarizing materials," Chem. Mater. **16**, 1832–1834 (2004).

[37] V. G. Nazarenko, O. P. Boiko, M. I. Anisimov, A. K. Kadashchuk, Y. A. Nastishin, A. B. Golovin, and O. D. Lavrentovich, "Lyotropic chromonic liquid crystal semiconductors for water-solution processable organic electronics," Appl. Phys. Lett. **97**, 284 (2010).

[38] F. Guo, A. Mukhopadhyay, B. W. Sheldon, and R. H. Hurt, "Vertically aligned graphene layer arrays from chromonic liquid crystal precursors," Adv. Mater. **23**, 508–513 (2011).

[39] S. Zhou, Y. A. Nastishin, M. M. Omelchenko, L. Tortora, V. G. Nazarenko, O. P. Boiko, T. Ostapenko, T. Hu, C. C. Almasan, S. N. Sprunt, *et al.*, "Elasticity of lyotropic chromonic liquid crystals probed by director reorientation in a magnetic field," Phys. Rev. Lett. **109**, 037801 (2012).

[40] H. S. Park and O. D. Lavrentovich, *Liquid crystals beyond displays: chemistry, physics, and applications* (John Wiley & Sons, 2012).

[41] S. Zhou, A. Sokolov, O. D. Lavrentovich, and I. S. Aranson, "Living liquid crystals," Proc. Natl. Acad. Sci. U. S. A. **111**, 1265–1270 (2014).

[42] A. Masters, "Chromonic liquid crystals: more questions than answers," Liq. Cryst. Today **25**, 30–37 (2016).

[43] H.-S. Park, S.-W. Kang, L. Tortora, Y. Nastishin, D. Finotello, S. Kumar, and O. D. Lavrentovich, "Self-assembly of lyotropic chromonic liquid crystal Sunset Yellow and effects of ionic additives," J. Phys. Chem. B **112**, 16307–16319 (2008).

[44] M. P. Renshaw and I. J. Day, "NMR characterization of the aggregation state of the azo dye Sunset Yellow in the isotropic phase," J. Phys. Chem. B **114**, 10032–10038 (2010).

[45] J. Lydon, "Chromonic liquid crystalline phases," Liq. Cryst. **38**, 1663–1681 (2011).

[46] S. Zhou, K. Neupane, Y. A. Nastishin, A. R. Baldwin, S. V. Shiyanovskii, O. D. Lavrentovich, and S. Sprunt, "Elasticity, viscosity, and orientational fluctuations of a lyotropic chromonic nematic liquid crystal disodium cromoglycate," Soft Matter **10**, 6571–6581 (2014).

[47] P. J. Collings, J. N. Goldstein, E. J. Hamilton, B. R. Mercado, K. J. Nieser, and M. H. Regan, "The nature of the assembly process in chromonic liquid crystals," Liq. Cryst. Rev. **3**, 1–27 (2015).

[48] H.-S. Park and O. D. Lavrentovich, "Lyotropic chromonic liquid crystals: Emerging applications," in *Liquid crystals beyond displays: chemistry, physics, and applications* (John Wiley & Sons: Hoboken, NJ, 2012) pp. 449–484.

[49] L. Tortora and O. D. Lavrentovich, "Chiral symmetry breaking by spatial confinement in tactoidal droplets of lyotropic chromonic liquid crystals," Proc. Natl. Acad. Sci. U. S. A. **108**, 5163–5168 (2011).

[50] S. Zhou, "Elasticity, viscosity, and orientational fluctuations of a lyotropic chromonic nematic liquid crystal disodium cromoglycate," in *Lyotropic chromonic liquid crystals: from viscoelastic properties to living liquid crystals* (Springer, 2017) pp. 51–75.

[51] C. F. Dietrich, P. J. Collings, T. Sottmann, P. Rudquist, and F. Giesselmann, "Extremely small twist elastic constants in lyotropic nematic liquid crystals," Proc. Natl. Acad. Sci. U.S.A. **117**, 27238–27244 (2020).

[52] S. Zhou, S. V. Shiyanovskii, H.-S. Park, and O. D. Lavrentovich, "Fine structure of the topological defect cores studied for disclinations in lyotropic chromonic liquid crystals," Nat. Commun. **8**, 1–7 (2017).

[53] K. Nayani, R. Chang, J. Fu, P. W. Ellis, A. Fernandez-Nieves, J. O. Park, and M. Srinivasarao, "Spontaneous emergence of chirality in achiral lyotropic chromonic liquid crystals confined to cylinders," Nat. Commun. **6**, 1–7 (2015).

[54] Z. S. Davidson, L. Kang, J. Jeong, T. Still, P. J. Collings, T. C. Lubensky, and A. G. Yodh, "Chiral structures and defects of lyotropic chromonic liquid crystals induced by saddle-splay elasticity," Phys. Rev. E **91**, 050501 (2015).

[55] G. Park, S. Čopar, A. Suh, M. Yang, U. Tkalec, and D. K. Yoon, "Periodic arrays of chiral domains generated from the self-assembly of micropatterned achiral lyotropic chromonic liquid crystal," ACS Cent. Sci. **6**, 1964–1970 (2020).

[56] O. D. Lavrentovich, "Design of chiral domains by surface confinement of liquid crystals," ACS Cent. Sci. **6**, 1858–1861 (2020).

[57] K. V. Kaznatcheev, P. Dudin, O. D. Lavrentovich, and A. P. Hitchcock, "X-ray microscopy study of chromonic liquid crystal dry film texture," Phys. Rev. E **76**, 061703 (2007).

[58] T. Suzuki and Y. Kojima, "Direct structural observation of the alignment and elongation in lyotropic chromonic liquid crystals under shear flow," Mol. Cryst. Liq. Cryst. **648**, 162–167 (2017).

[59] Y. J. Cha, M.-J. Gim, H. Ahn, T. J. Shin, J. Jeong, and D. K. Yoon, "Orthogonal liquid crystal alignment layer: templating speed-dependent orientation of chromonic liquid crystals," ACS Appl. Mater. Interfaces **9**, 18355–18361 (2017).

[60] G. Duclos, R. Adkins, D. Banerjee, M. S. Peterson, M. Varghese, I. Kolvin, A. Baskaran, R. A. Pelcovits, T. R. Powers, A. Baskaran, *et al.*, "Topological structure and dynamics of three-dimensional active nematics," Science **367**, 1120–1124 (2020).

[61] H. Baza, T. Turiv, B.-X. Li, R. Li, B. M. Yavitt, M. Fukuto, and O. D. Lavrentovich, "Shear-induced polydomain structures of nematic lyotropic chromonic liquid crystal disodium cromoglycate," Soft Matter **16**, 8565–8576 (2020).

[62] R. G. Larson, *The structure and rheology of complex fluids* (Oxford University Press, 1999).

[63] Q. Zhang, A. Amooie, M. Z. Bazant, and I. Bischofberger, "Growth morphology and symmetry selection of interfacial instabilities in anisotropic environments," Soft Matter **17**, 1202–1209 (2021).

[64] B. Ge, Q. Zhang, R. Zhang, J.-T. Lin, P.-H. Tseng, C.-W. Chang, C.-Y. Dong, R. Zhou, Z. Yaqoob, I. Bischofberger, *et al.*, "Single-shot quantitative polarization imaging of complex birefringent structure dynamics," ACS Photonics **8**, 3440–3447 (2021).

[65] Q. Zhang, R. Zhang, B. Ge, Z. Yaqoob, P. T. So, and I. Bischofberger, "Structures and topological defects in pressure-driven lyotropic chromonic liquid crystals," Proc. Natl. Acad. Sci. U. S. A. **118** (2021).

[66] Q. Zhang, S. Zhou, R. Zhang, and I. Bischofberger, "Dendritic patterns from shear-enhanced anisotropy in nematic liquid crystals," In review (2022).

[67] Q. Zhang, W. Wang, S. Zhou, R. Zhang, and I. Bischofberger, "Flow-induced periodic chiral structures in an achiral nematic liquid crystal," In preparation (2022).

[68] L. Parry-Jones, "Alignment properties of liquid crystals," in *Handbook of visual display technology* (Springer, 2016) pp. 2003–2020.

[69] C. K. McGinn, L. I. Laderman, N. Zimmermann, H.-S. Kitzerow, and P. J. Collings, "Planar anchoring strength and pitch measurements in achiral and chiral chromonic liquid crystals using 90-degree twist cells," Phys. Rev. E **88**, 062513 (2013).

[70] B. D. Guenther, *Modern optics* (OUP Oxford, 2015).

[71] A. Jákli, *One-and two-dimensional fluids: properties of smectic, lamellar and columnar liquid crystals* (CRC Press, 2006).

[72] Y. A. Nastishin, H. Liu, T. Schneider, V. Nazarenko, R. Vasyuta, S. Shiyanovskii, and O. Lavrentovich, "Optical characterization of the nematic lyotropic chromonic liquid crystals: light absorption, birefringence, and scalar order parameter," Phys. Rev. E **72**, 041711 (2005).

[73] B. E. Sørensen, "A revised Michel-Lévy interference colour chart based on first-principles calculations," Eur. J. Mineral. **25**, 5–10 (2013).

[74] B. Ge, R. Zhou, Y. Takiguchi, Z. Yaqoob, and P. T. So, "Single-shot optical anisotropy imaging with quantitative polarization interference microscopy," Laser Photonics Rev. **12**, 1800070 (2018).

[75] X. Cheng, L. Xu, A. Patterson, H. M. Jaeger, and S. R. Nagel, "Towards the zero-surface-tension limit in granular fingering instability," Nat. Phys. **4**, 234–237 (2008).

[76] R. Zenit, "Some fluid mechanical aspects of artistic painting," Phys. Rev. Fluids **4**, 110507 (2019).

[77] T. T. Al-Housseiny, P. A. Tsai, and H. A. Stone, "Control of interfacial instabilities using flow geometry," Nat. Phys. **8**, 747–750 (2012).

[78] T. T. Al-Housseiny and H. A. Stone, "Controlling viscous fingering in tapered Hele-Shaw cells," Phys. Fluids **25**, 092102 (2013).

[79] M. Mirzadeh and M. Z. Bazant, "Electrokinetic control of viscous fingering," Phys. Rev. Lett. **119**, 174501 (2017).

[80] T. Gao, M. Mirzadeh, P. Bai, K. M. Conforti, and M. Z. Bazant, "Active control of viscous fingering using electric fields," Nat. Commun. **10**, 1–8 (2019).

[81] T. E. Videbæk and S. R. Nagel, "Diffusion-driven transition between two regimes of viscous fingering," Phys. Rev. Fluids **4**, 033902 (2019).

[82] S. Suo, M. Liu, and Y. Gan, "Fingering patterns in hierarchical porous media," Phys. Rev. Fluids **5**, 034301 (2020).

[83] S. Parsa, E. Santanach-Carreras, L. Xiao, and D. A. Weitz, "Origin of anomalous polymer-induced fluid displacement in porous media," Phys. Rev. Fluids **5**, 022001 (2020).

[84] M. E. Rosti, S. Pramanik, L. Brandt, and D. Mitra, "The breakdown of Darcy's law in a soft porous material," Soft Matter **16**, 939–944 (2020).

[85] L. C. Morrow, T. J. Moroney, and S. W. McCue, "Numerical investigation of controlling interfacial instabilities in non-standard Hele-Shaw configurations," J. Fluid Mech. **877**, 1063–1097 (2019).

[86] D. Lu, F. Municchi, and I. C. Christov, "Computational analysis of interfacial dynamics in angled Hele-Shaw cells: Instability regimes," Transport Porous Med **131**, 907–934 (2020).

[87] I. Bischofberger and S. R. Nagel, "Fluid instabilities that mimic animal growth," Phys. Today **69**, 70–71 (2016).

[88] S. A. Setu, I. Zacharoudiou, G. J. Davies, D. Bartolo, S. Moulinet, A. A. Louis, J. M. Yeomans, and D. G. Aarts, "Viscous fingering at ultralow interfacial tension," Soft Matter **9**, 10599–10605 (2013).

[89] R. Almgren, W.-S. Dai, and V. Hakim, "Scaling behavior in anisotropic Hele-Shaw flow," Phys. Rev. Lett. **71**, 3461–3464 (1993).

[90] J. Ignés-Mullol and J. V. Maher, "Experiments on anisotropic radial viscous fingering," Phys. Rev. E **53**, 3788–3793 (1996).

[91] P. Meakin, "Universality, nonuniversality, and the effects of anisotropy on diffusion-limited aggregation," Phys. Rev. A **33**, 3371 (1986).

[92] J. Kertész and T. Vicsek, "Diffusion-limited aggregation and regular patterns: fluctuations versus anisotropy," J. Phys. A **19**, L257 (1986).

[93] M. Stepanov and L. Levitov, "Laplacian growth with separately controlled noise and anisotropy," Phys. Rev. E **63**, 061102 (2001).

[94] E. L. Decker, J. Ignés-Mullol, A. Baratt, and J. V. Maher, "Effect of lattice defects on Hele-Shaw flow over an etched lattice," Phys. Rev. E **60**, 1767–1774 (1999).

[95] C. Rana and M. Mishra, "Interaction between shock layer and viscous fingering in a Langmuir adsorbed solute," Phys. Fluids **29**, 032108 (2017).

[96] C. Rana, S. Pramanik, M. Martin, A. De Wit, and M. Mishra, "Influence of Langmuir adsorption and viscous fingering on transport of finite size samples in porous media," Phys. Rev. Fluids **4**, 104001 (2019).

[97] V. Sharma, S. Nand, S. Pramanik, C.-Y. Chen, and M. Mishra, "Control of radial miscible viscous fingering," J. Fluid Mech. **884**, A16 (2020).

[98] T. E. Videbæk, "Delayed onset and the transition to late time growth in viscous fingering," Phys. Rev. Fluids **5**, 123901 (2020).

[99] I. Bischofberger, R. Ramachandran, and S. R. Nagel, "An island of stability in a sea of fingers: emergent global features of the viscous-flow instability," Soft Matter **11**, 7428–7432 (2015).

[100] S. J. Jackson, D. Stevens, H. Power, and D. Giddings, "A boundary element method for the solution of finite mobility ratio immiscible displacement in a Hele-Shaw cell," Int. J. Numer. Meth. Fl. **78**, 521–551 (2015).

[101] P. H. A. Anjos, E. O. Dias, and J. A. Miranda, "Radial fingering under arbitrary viscosity and density ratios," Phys. Rev. Fluids **2**, 084004 (2017).

[102] B. Jha, L. Cueto-Felgueroso, and R. Juanes, "Quantifying mixing in viscously unstable porous media flows," Phys. Rev. E **84**, 066312 (2011).

[103] M. Islam and J. Azaiez, "Fully implicit finite difference pseudo-spectral method for simulating high mobility-ratio miscible displacements," Int. J. Numer. Methods Fluids **47**, 161–183 (2005).

[104] J. Chung and G. M. Hulbert, "A time integration algorithm for structural dynamics with improved numerical dissipation: the deneralized-α method," J. Appl. Mech. **60**, 371–375 (1993).

[105] K. E. Jansen, C. H. Whiting, and G. M. Hulbert, "A generalized-α method for integrating the filtered Navier–Stokes equations with a stabilized finite element method," Comput. Methods Appl. Mech. Eng. **190**, 305–319 (2000).

[106] J. D. Chen, "Radial viscous fingering patterns in Hele-Shaw cells," Exp. Fluids **5**, 363–371 (1987).

[107] A. G. Banpurkar, A. S. Ogale, A. V. Limaye, and S. B. Ogale, "Viscous fingering of miscible fluids in an anisotropic radial Hele-Shaw cell: coexistence of kinetic and surface-tension dendrite morphology types and an exploration of small-scale influences," Phys. Rev. E **59**, 2188–2191 (1999).

[108] A. G. Banpurkar, A. V. Limaye, and S. B. Ogale, "Occurrence of coexisting dendrite morphologies: immiscible fluid displacement in an anisotropic radial Hele-Shaw cell under a high flow rate regime," Phys. Rev. E **61**, 5507–5511 (2000).

[109] G. K. Batchlor, *An introduction to fluid dynamics*, Vol. 543 (London: Cambridge University Press, 1967).

[110] P. G. Saffman, "Viscous fingering in Hele-Shaw cells," J. Fluid Mech. **173**, 73–94 (1986).

[111] P. Gondret, N. Rakotomalala, M. Rabaud, D. Salin, and P. Watzky, "Viscous parallel flows in finite aspect ratio Hele-Shaw cell: Analytical and numerical results," Phys. Fluids **9**, 1841–1843 (1997).

[112] E. Lajeunesse, J. Martin, N. Rakotomalala, and D. Salin, "3D instability of miscible displacements in a Hele-Shaw cell," Phys. Rev. Lett. **79**, 5254 (1997).

[113] E. Lajeunesse, J. Martin, N. Rakotomalala, D. Salin, and Y. Yortsos, "Miscible displacement in a Hele-Shaw cell at high rates," J. Fluid Mech. **398**, 299–319 (1999).

[114] S. Torquato, *Random Heterogeneous Materials: Microstructure and Macroscopic Properties*, Vol. 16 (Springer Science & Business Media, 2013).

[115] M. Z. Bazant and O. I. Vinogradova, "Tensorial hydrodynamic slip," J. Fluid Mech. **613**, 125–134 (2008).

[116] O. I. Vinogradova, "Slippage of water over hydrophobic surfaces," Int. J. Miner. Process. **56**, 31–60 (1999).

[117] F. Feuillebois, M. Z. Bazant, and O. I. Vinogradova, "Effective slip over superhydrophobic surfaces in thin channels," Phys. Rev. Lett. **102**, 026001 (2009).

[118] A. D. Stroock, S. K. Dertinger, G. M. Whitesides, and A. Ajdari, "Patterning flows using grooved surfaces," Anal. Chem. **74**, 5306–5312 (2002).

[119] H. A. Stone, A. D. Stroock, and A. Ajdari, "Engineering flows in small devices: microfluidics toward a lab-on-a-chip," Annu. Rev. Fluid Mech. **36**, 381–411 (2004).

[120] M. Z. Bazant, J. Choi, and B. Davidovitch, "Dynamics of conformal maps for a class of non-laplacian growth phenomena," Phys. Rev. Lett. **91**, 045503 (2003).

[121] C. De Rosa, C. Park, E. L. Thomas, and B. Lotz, "Microdomain patterns from directional eutectic solidification and epitaxy," Nature **405**, 433–437 (2000).

[122] Y. Liu, J. Goebl, and Y. Yin, "Templated synthesis of nanostructured materials," Chem. Soc. Rev. **42**, 2610–2653 (2013).

[123] D. Bera, S. C. Kuiry, and S. Seal, "Synthesis of nanostructured materials using template-assisted electrodeposition," JOM **56**, 49–53 (2004).

[124] H. Liu, X. Zhao, Y. Yang, Q. Li, and J. Lv, "Fabrication of infrared left-handed metamaterials via double template-assisted electrochemical deposition," Adv. Mater. **20**, 2050–2054 (2008).

[125] J.-H. Han, E. Khoo, P. Bai, and M. Z. Bazant, "Over-limiting current and control of dendritic growth by surface conduction in nanopores," Sci. Rep. **4**, 7056 (2014).

[126] J.-H. Han, M. Wang, P. Bai, F. R. Brushett, and M. Z. Bazant, "Dendrite suppression by shock electrodeposition in charged porous media," Sci. Rep. **6**, 28054 (2016).

[127] A. Ajdari, "Transverse electrokinetic and microfluidic effects in micropatterned channels: lubrication analysis for slab geometries," Phys. Rev. E **65**, 016301 (2001).

[128] S. S. Bahga, O. I. Vinogradova, and M. Z. Bazant, "Anisotropic electro-osmotic flow over super-hydrophobic surfaces," J. Fluid Mech. **644**, 245–255 (2010).

[129] G. M. Homsy, "Viscous fingering in porous media," Annu. Rev. Fluid Mech **19**, 271–311 (1987).

[130] C. T. Tan and G. M. Homsy, "Stability of miscible displacements in porous media: radial source flow," Phys. Fluids **30**, 1239–1245 (1987).

[131] A. Riaz and E. Meiburg, "Radial source flows in porous media: Linear stability analysis of axial and helical perturbations in miscible displacements," Phys. Fluids **15**, 938–946 (2003).

[132] S. Schmieschek, A. V. Belyaev, J. Harting, and O. I. Vinogradova, "Tensorial slip of superhydrophobic channels," Phys. Rev. E **85**, 016324 (2012).

[133] K. Kamrin, M. Z. Bazant, and H. A. Stone, "Effective slip boundary conditions for arbitrary periodic surfaces: the surface mobility tensor," J. Fluid Mech. **658**, 409–437 (2010).

[134] S. Wei, Z. Cheng, P. Nath, M. D. Tikekar, G. Li, and L. A. Archer, "Stabilizing electrochemical interfaces in viscoelastic liquid electrolytes," Sci. Adv. **4**, eaao6243 (2018).

[135] S. Alqatari, T. E. Videbæk, S. R. Nagel, A. E. Hosoi, and I. Bischofberger, "Confinement-induced stabilization of the rayleigh-taylor instability and transition to the unconfined limit," Sci. Adv. **6**, eabd6605 (2020).

[136] Z. Ahmad, Z. Hong, and V. Viswanathan, "Design rules for liquid crystalline electrolytes for enabling dendrite-free lithium metal batteries," Proc. Natl. Acad. Sci. U.S.A. **117**, 26672–26680 (2020).

[137] A. Sonin and R. Bartolino, "Air viscous fingers in isotropic fluid and liquid crystals obtained in lifting hele-shaw cell geometry," Il Nuovo Cimento D **15**, 1–8 (1993).

[138] T. Tóth-Katona and A. Buka, "Nematic-liquid-crystal–air interface in a radial hele-shaw cell: Electric field effects," Phys. Rev. E **67**, 041717 (2003).

[139] W. Thielicke and E. Stamhuis, "Pivlab–towards user-friendly, affordable and accurate digital particle image velocimetry in matlab," J. Open Res. Softw. **2** (2014).

[140] W. Thielicke and R. Sonntag, "Particle image velocimetry for matlab: Accuracy and enhanced algorithms in pivlab," J. Open Res. Softw. **9** (2021).

[141] I. Bischofberger, R. Ramachandran, and S. R. Nagel, "An island of stability in a sea of fingers: emergent global features of the viscous-flow instability," Soft Matter **11**, 7428–7432 (2015).

[142] P. Yeh and C. Gu, *Optics of liquid crystal displays*, Vol. 67 (John Wiley & Sons, 2009).

[143] R. Larson, "Arrested tumbling in shearing flows of liquid-crystal polymers," Macromolecules **23**, 3983–3992 (1990).

[144] V. Calabrese, S. J. Haward, and A. Q. Shen, "Effects of shearing and extensional flows on the alignment of colloidal rods," Macromolecules **54**, 4176–4185 (2021).

[145] M. Trebbin, D. Steinhauser, J. Perlich, A. Buffet, S. V. Roth, W. Zimmermann, J. Thiele, and S. Förster, "Anisotropic particles align perpendicular to the flow direction in narrow microchannels," Proc. Natl. Acad. Sci. U.S.A. **110**, 6706–6711 (2013).

[146] P. Popov, L. W. Honaker, E. E. Kooijman, E. K. Mann, and A. I. Jákli, "A liquid crystal biosensor for specific detection of antigens," Sens. Bio-Sens. **8**, 31–35 (2016).

[147] H. Yu and P. Zhang, "A kinetic–hydrodynamic simulation of microstructure of liquid crystal polymers in plane shear flow," J. Non-Newton. Fluid Mech. **141**, 116–127 (2007).

[148] M. M. Genkin, A. Sokolov, O. D. Lavrentovich, and I. S. Aranson, "Topological defects in a living nematic ensnare swimming bacteria," Phys. Rev. X **7**, 011029 (2017).

[149] A. Sokolov, A. Mozaffari, R. Zhang, J. J. De Pablo, and A. Snezhko, "Emergence of radial tree of bend stripes in active nematics," Phys. Rev. X **9**, 031014 (2019).

[150] P. C. Mushenheim, R. R. Trivedi, S. S. Roy, M. S. Arnold, D. B. Weibel, and N. L. Abbott, "Effects of confinement, surface-induced orientations and strain on dynamical behaviors of bacteria in thin liquid crystalline films," Soft Matter **11**, 6821–6831 (2015).

[151] C. Peng, T. Turiv, Y. Guo, Q.-H. Wei, and O. D. Lavrentovich, "Command of active matter by topological defects and patterns," Science **354**, 882–885 (2016).

[152] S. Zhou, O. Tovkach, D. Golovaty, A. Sokolov, I. S. Aranson, and O. D. Lavrentovich, "Dynamic states of swimming bacteria in a nematic liquid crystal cell with homeotropic alignment," New J. Phys. **19**, 055006 (2017).

[153] C. Peng, T. Turiv, Y. Guo, S. V. Shiyanovskii, Q.-H. Wei, and O. D. Lavrentovich, "Control of colloidal placement by modulated molecular orientation in nematic cells," Sci. Adv. **2**, e1600932 (2016).

[154] I. Janossy, P. Pieranski, and E. Guyon, "Poiseuille flow in nematics: experimental study of the instabilities," J. Phys. **37**, 1105–1113 (1976).

[155] D. J. Graziano and M. R. Mackley, "Shear induced optical textures and their relaxation behaviour in thermotropic liquid crystalline polymers," Mol. Cryst. Liq. Cryst. **106**, 73–93 (1984).

[156] J. Vermant, P. Moldenaers, S. J. Picken, and J. Mewis, "A comparison between texture and rheological behaviour of lyotropic liquid crystalline polymers during flow," J. Non-Newton. Fluid **53**, 1–23 (1994).

[157] P. T. Mather, D. S. Pearson, and R. G. Larson, "Flow patterns and disclination-density measurements in sheared nematic liquid crystals I: Flow-aligning 5CB," Liq. Cryst. **20**, 527–538 (1996).

[158] J. A. Müller, R. S. Stein, and H. H. Winter, "Rotation of liquid crystalline macromolecules in shear flow and shear-induced periodic orientation patterns," Rheol. Acta **35**, 160–167 (1996).

[159] A. Sengupta, U. Tkalec, M. Ravnik, J. M. Yeomans, C. Bahr, and S. Herminghaus, "Liquid crystal microfluidics for tunable flow shaping," Phys. Rev. Lett. **110**, 048303 (2013).

[160] A. D. Rey and M. M. Denn, "Dynamical phenomena in liquid-crystalline materials," Annu. Rev. Fluid Mech. **34**, 233–266 (2002).

[161] D. H. Klein, L. G. Leal, C. J. García-Cervera, and H. D. Ceniceros, "Three-dimensional shear-driven dynamics of polydomain textures and disclination loops in liquid crystalline polymers," J. Rheol. **52**, 837–863 (2008).

[162] D. J. Graziano and M. R. Mackley, "Disclinations observed during the shear of MBBA," Mol. Cryst. Liq. Cryst. **106**, 103–119 (1984).

[163] A. Sengupta, B. Schulz, E. Ouskova, and C. Bahr, "Functionalization of microfluidic devices for investigation of liquid crystal flows," Microfluid Nanofluidics **13**, 941–955 (2012).

[164] Z. Liu, D. Luo, and K.-L. Yang, "Flow-driven disclination lines of nematic liquid crystals inside a rectangular microchannel," Soft Matter **15**, 5638–5643 (2019).

[165] A. Sengupta, U. Tkalec, and C. Bahr, "Nematic textures in microfluidic environment," Soft Matter **7**, 6542–6549 (2011).

[166] H. Agha and C. Bahr, "Connecting and disconnecting nematic disclination lines in microfluidic channels," Soft Matter **12**, 4266–4273 (2016).

[167] L. Giomi, Ž. Kos, M. Ravnik, and A. Sengupta, "Cross-talk between topological defects in different fields revealed by nematic microfluidics," Proc. Natl. Acad. Sci. U. S. A. **114**, E5771–E5777 (2017).

[168] T. Emeršič, R. Zhang, Ž. Kos, S. Čopar, N. Osterman, J. J. De Pablo, and U. Tkalec, "Sculpting stable structures in pure liquids," Sci. Adv. **5**, eaav4283 (2019).

[169] S. Čopar, Ž. Kos, T. Emeršič, and U. Tkalec, "Microfluidic control over topological states in channel-confined nematic flows," Nat. Commun. **11**, 1–10 (2020).

[170] T. Ouchi, K. Imamura, K. Sunami, H. Yoshida, M. Ozaki, *et al.*, "Topologically protected generation of stable wall loops in nematic liquid crystals," Phys. Rev. Lett. **123**, 097801 (2019).

[171] T. De'Nève, P. Navard, and M. Kleman, "Nature of the flow-induced worm texture of thermotropic polymers," Macromolecules **28**, 1541–1546 (1995).

[172] M. Doi and S. F. Edwards, *The theory of polymer dynamics* (Oxford University Press, 1988).

[173] G. Marrucci and F. Greco, "Flow behavior of liquid crystalline polymers," Adv. Chem. Phys. **86**, 331–404 (1993).

[174] G. Sgalari, G. L. Leal, and J. J. Feng, "The shear flow behavior of LCPs based on a generalized Doi model with distortional elasticity," J. Non-Newton. Fluid **102**, 361–382 (2002).

[175] A. Sharma, I. L. H. Ong, and A. Sengupta, "Time dependent lyotropic chromonic textures in microfluidic confinements," Crystals **11**, 35 (2021).

[176] I. I. Smalyukh, S. V. Shiyanovskii, and O. D. Lavrentovich, "Three-dimensional imaging of orientational order by fluorescence confocal polarizing microscopy," Chem. Phys. Lett. **336**, 88–96 (2001).

[177] M. Shribak and R. Oldenbourg, "Techniques for fast and sensitive measurements of two-dimensional birefringence distributions," Appl. Opt. **42**, 3009–3017 (2003).

[178] N. Zimmermann, G. Jünnemann-Held, P. J. Collings, and H.-S. Kitzerow, "Self-organized assemblies of colloidal particles obtained from an aligned chromonic liquid crystal dispersion," Soft Matter **11**, 1547–1553 (2015).

[179] R. Zhang, Y. Zhou, M. Rahimi, and J. J. de Pablo, "Dynamic structure of active nematic shells," Nat. Commun. **7**, 13483 (2016).

[180] R. Zhang, N. Kumar, J. L. Ross, M. L. Gardel, and J. J. de Pablo, "Interplay of structure, elasticity, and dynamics in actin-based nematic materials," Proc. Natl. Acad. Sci. U. S. A. **115**, E124–E133 (2018).

[181] N. Kumar, R. Zhang, J. J. de Pablo, and M. L. Gardel, "Tunable structure and dynamics of active liquid crystals," Sci. Adv. **4**, eaat7779 (2018).

[182] A. N. Beris and B. J. Edwards, *Thermodynamics of flowing systems with internal microstructure* (Oxford University Press, 1994).

[183] C. Denniston, E. Orlandini, and J. M. Yeomans, "Lattice Boltzmann simulations of liquid crystal hydrodynamics," Phys. Rev. E **63**, 056702 (2001).

[184] M. Ravnik and S. Žumer, "Landau-de Gennes modelling of nematic liquid crystal colloids," Liq. Crys. **36**, 1201–1214 (2009).

[185] C. Denniston, D. Marenduzzo, E. Orlandini, and J. M. Yeomans, "Lattice Boltzmann algorithm for three-dimensional liquid-crystal hydrodynamics," Phil. Trans. R. Soc. Lond. A **362**, 1745–1754 (2004).

[186] R. Zhang, T. Roberts, I. Aranson, and J. J. de Pablo, "Lattice Boltzmann simulation of asymmetric flow in nematic liquid crystals with finite anchoring," J. Chem. Phys. **14**, 084905 (2016).

[187] Y. Park, C. Depeursinge, and G. Popescu, "Quantitative phase imaging in biomedicine," Nat. Photonics **12**, 578–589 (2018).

[188] P. Manneville, "Non-linearities and fluctuations at the threshold of a hydrodynamic instability in nematic liquid crystals," J. Phys. **39**, 911–925 (1978).

[189] Q. Ouyang and H. L. Swinney, "Transition to chemical turbulence," Chaos **1**, 411–420 (1991).

[190] D. Grecov and A. D. Rey, "Shear-induced textural transitions in flow-aligning liquid crystal polymers," Phys. Rev. E **68**, 061704 (2003).

[191] C. Blanch-Mercader, V. Yashunsky, S. Garcia, G. Duclos, L. Giomi, and P. Silberzan, "Turbulent dynamics of epithelial cell cultures," Phys. Rev. Lett. **120**, 208101 (2018).

[192] A. Doostmohammadi, J. Ignés-Mullol, J. M. Yeomans, and F. Sagués, "Active nematics," Nat. Commun. **9**, 1–13 (2018).

[193] U. S. Kamilov, I. N. Papadopoulos, M. H. Shoreh, A. Goy, C. Vonesch, M. Unser, and D. Psaltis, "Learning approach to optical tomography," Optica **2**, 517–522 (2015).

[194] U. S. Kamilov, I. N. Papadopoulos, M. H. Shoreh, A. Goy, C. Vonesch, M. Unser, and D. Psaltis, "Optical tomographic image reconstruction based on beam propagation and sparse regularization," IEEE Trans. Comput. Imaging **2**, 59–70 (2016).

[195] E. Terentjev, "Disclination loops, standing alone and around solid particles, in nematic liquid crystals," Phys. Rev. E **51**, 1330 (1995).

[196] G. Joyce, G. Visser, C. Van Boeckel, J. Van Boom, L. Orgel, and J. Van Westrenen, "Chiral selection in poly (c)-directed synthesis of oligo (g)," Nature **310**, 602–604 (1984).

[197] M. Inaki, J. Liu, and K. Matsuno, "Cell chirality: its origin and roles in left–right asymmetric development," Philos. Trans. R. Soc. B: Biol. Sci. **371**, 20150403 (2016).

[198] R. Noyori, "Asymmetric catalysis: Science and opportunities (nobel lecture)," Angew. Chem. Int. Ed. **41**, 2008–2022 (2002).

[199] J. R. Brandt, F. Salerno, and M. J. Fuchter, "The added value of small-molecule chirality in technological applications," Nat. Rev. Chem. **1**, 1–12 (2017).

[200] B. Pokroy, S. H. Kang, L. Mahadevan, and J. Aizenberg, "Self-organization of a mesoscale bristle into ordered, hierarchical helical assemblies," Science **323**, 237–240 (2009).

[201] W. Wu, W. Hu, G. Qian, H. Liao, X. Xu, and F. Berto, "Mechanical design and multifunctional applications of chiral mechanical metamaterials: A review," Mater. Des. **180**, 107950 (2019).

[202] W. Xiao, K.-H. Ernst, K. Palotas, Y. Zhang, E. Bruyer, L. Peng, T. Greber, W. A. Hofer, L. T. Scott, and R. Fasel, "Microscopic origin of chiral shape induction in achiral crystals," Nat. Chem. **8**, 326–330 (2016).

[203] Y. Snir and R. D. Kamien, "Entropically driven helix formation," Science **307**, 1067–1067 (2005).

[204] S. M. Morrow, A. J. Bissette, and S. P. Fletcher, "Transmission of chirality through space and across length scales," Nat. Nanotechnol. **12**, 410–419 (2017).

[205] X. Ma, M. Pu, X. Li, Y. Guo, P. Gao, and X. Luo, "Meta-chirality: Fundamentals, construction and applications," J. Nanomater. **7**, 116 (2017).

[206] A. Jákli, O. D. Lavrentovich, and J. V. Selinger, "Physics of liquid crystals of bent-shaped molecules," Rev. Mod. Phys. **90**, 045004 (2018).

[207] D. Link, G. Natale, R. Shao, J. Maclennan, N. Clark, E. Körblova, and D. Walba, "Spontaneous formation of polar chiral layers from achiral molecules in a novel antiferroelectric liquid crystal phase," Science **278**, 1924 (1997).

[208] O. Lavrentovich and V. Pergamenshchik, "Periodic domain structures in thin hybrid nematic layers," Mol. Cryst. Liq. Cryst. **179**, 125–132 (1990).

[209] R. Ondris-Crawford, G. Crawford, S. Zumer, and J. Doane, "Curvature-induced configuration transition in confined nematic liquid crystals," Phys. Rev. Lett. **70**, 194 (1993).

[210] J. Jeong, Z. S. Davidson, P. J. Collings, T. C. Lubensky, and A. Yodh, "Chiral symmetry breaking and surface faceting in chromonic liquid crystal droplets with giant elastic anisotropy," Proc. Natl. Acad. Sci. U.S.A. **111**, 1742–1747 (2014).

[211] J. Jeong, L. Kang, Z. S. Davidson, P. J. Collings, T. C. Lubensky, and A. Yodh, "Chiral structures from achiral liquid crystals in cylindrical capillaries," Proc. Natl. Acad. Sci. U.S.A. **112**, E1837–E1844 (2015).

[212] P. W. Ellis, K. Nayani, J. P. McInerney, D. Z. Rocklin, J. O. Park, M. Srinivasarao, E. A. Matsumoto, and A. Fernandez-Nieves, "Curvature-induced twist in homeotropic nematic tori," Phys. Rev. Lett. **121**, 247803 (2018).

[213] Y. Xia, A. A. DeBenedictis, D. S. Kim, S. Chen, S.-U. Kim, D. J. Cleaver, T. J. Atherton, and S. Yang, "Programming emergent symmetries with saddle-splay elasticity," Nat. Commun. **10**, 1–9 (2019).

[214] O. Lavrentovich, "Fluorescence confocal polarizing microscopy: Three-dimensional imaging of the director," Pramana **61**, 373–384 (2003).

[215] P. K. Kundu, I. M. Cohen, and D. R. Dowling, *Fluid mechanics* (Academic press, 2015).

[216] P. J. Collings, P. van der Asdonk, A. Martinez, L. Tortora, and P. H. Kouwer, "Anchoring strength measurements of a lyotropic chromonic liquid crystal on rubbed polyimide surfaces," Liq. Cryst. **44**, 1165–1172 (2017).

[217] W. Wang, "Interplay of active stress and driven flow in self-assembled, tumbling active nematics," Crystals **11**, 1071 (2021).

[218] C. Denniston, E. Orlandini, and J. M. Yeomans, "Lattice boltzmann simulations of liquid crystal hydrodynamics," Phys. Rev. E **63**, 056702 (2001).

[219] M. Ravnik and S. Žumer, "Landau–de gennes modelling of nematic liquid crystal colloids," Liquid Crystals **36**, 1201–1214 (2009).

[220] R. Zhang, T. Roberts, I. S. Aranson, and J. J. De Pablo, "Lattice boltzmann simulation of asymmetric flow in nematic liquid crystals with finite anchoring," J. Chem. Phys. **144**, 084905 (2016).

[221] C. Denniston, D. Marenduzzo, E. Orlandini, and J. Yeomans, "Lattice boltzmann algorithm for three–dimensional liquid–crystal hydrodynamics," Philos. Trans. Royal Soc. A . **362**, 1745–1754 (2004).

[222] R. Chang, *Chiral configurations from achiral lyotropic chromonic liquid crystals under confinements*, Ph.D. thesis, Georgia Institute of Technology (2018).

[223] W. Helfrich, "Deformation of cholesteric liquid crystals with low threshold voltage," Appl. Phys. Lett. **17**, 531–532 (1970).

[224] I. Weissbuch, L. Leiserowitz, and M. Lahav, "Stochastic "mirror symmetry breaking" via self-assembly, reactivity and amplification of chirality: Relevance to abiotic conditions," in *Prebiotic Chemistry* (Springer Berlin Heidelberg, 2005) pp. 123–165.

[225] W. D. Piñeros and T. Tlusty, "Spontaneous chiral symmetry breaking in a random driven chemical system," Nat. Commun. **13**, 1–8 (2022).

[226] P. M. Reis, "A perspective on the revival of structural (in) stability with novel opportunities for function: from buckliphobia to buckliphilia," J. Appl. Mech. **82**, 111001 (2015).

[227] C.-W. Park, K.-S. Kwon, W.-B. Kim, B.-K. Min, S.-J. Park, I.-H. Sung, Y. S. Yoon, K.-S. Lee, J.-H. Lee, and J. Seok, "Energy consumption reduction technology in manufacturing—a selective review of policies, standards, and research," Int. J. Precis. Eng. Manuf. **10**, 151–173 (2009).

[228] M. D. Bambach, M. Bambach, A. Sviridov, and S. Weiss, "New process chains involving additive manufacturing and metal forming–a chance for saving energy?" Procedia Eng. **207**, 1176–1181 (2017).

[229] S. Wang, D. P. Maruri, J. M. Boothby, X. Lu, L. K. Rivera-Tarazona, V. D. Varner, and T. H. Ware, "Anisotropic, porous hydrogels templated by lyotropic chromonic liquid crystals," J. Mater. Chem. B **8**, 6988–6998 (2020).

[230] S. E. Naleway, M. M. Porter, J. McKittrick, and M. A. Meyers, "Structural design elements in biological materials: application to bioinspiration," Adv. Mater. **27**, 5455–5476 (2015).

[231] J. Kaschke and M. Wegener, "Optical and infrared helical metamaterials," Nanophotonics **5**, 510–523 (2016).

[232] I. I. Smalyukh, O. V. Zribi, J. C. Butler, O. D. Lavrentovich, and G. C. Wong, "Structure and dynamics of liquid crystalline pattern formation in drying droplets of dna," Phys. Rev. Lett. **96**, 177801 (2006).

[233] J. M. Gómez Gómez, J. Medina, D. Hochberg, E. Mateo-Martí, J. Martínez-Frías, and F. Rull, "Drying bacterial biosaline patterns capable of vital reanimation upon rehydration: novel hibernating biomineralogical life formations," Astrobiology **14**, 589–602 (2014).

[234] Z. S. Davidson, Y. Huang, A. Gross, A. Martinez, T. Still, C. Zhou, P. J. Collings, R. D. Kamien, and A. Yodh, "Deposition and drying dynamics of liquid crystal droplets," Nat. Commun. **8**, 1–7 (2017).

[235] M. Parsa, S. Harmand, and K. Sefiane, "Mechanisms of pattern formation from dried sessile drops," Adv. Colloid Interface Sci. **254**, 22–47 (2018).

[236] B. Pathak, J. Christy, K. Sefiane, and D. Gozuacik, "Complex pattern formation in solutions of protein and mixed salts using dehydrating sessile droplets," Langmuir **36**, 9728–9737 (2020).

[237] D. Kaya, V. Belyi, and M. Muthukumar, "Pattern formation in drying droplets of polyelectrolyte and salt," J. Chem. Phys. **133**, 114905 (2010).

[238] E. Karzbrun, A. Kshirsagar, S. R. Cohen, J. H. Hanna, and O. Reiner, "Human brain organoids on a chip reveal the physics of folding," Nat. phys. **14**, 515–522 (2018).

[239] R. Alert, C. Blanch-Mercader, and J. Casademunt, "Active fingering instability in tissue spreading," Phys. rev. lett. **122**, 088104 (2019).

[240] T. Büscher, A. L. Diez, G. Gompper, and J. Elgeti, "Instability and fingering of interfaces in growing tissue," New J. Phys. **22**, 083005 (2020).

[241] M. Poujade, E. Grasland-Mongrain, A. Hertzog, J. Jouanneau, P. Chavrier, B. Ladoux, A. Buguin, and P. Silberzan, "Collective migration of an epithelial monolayer in response to a model wound," Proc. Natl. Acad. Sci. U.S.A. **104**, 15988–15993 (2007).

[242] L. Petitjean, M. Reffay, E. Grasland-Mongrain, M. Poujade, B. Ladoux, A. Buguin, and P. Silberzan, "Velocity fields in a collectively migrating epithelium," Biophys. J. **98**, 1790–1800 (2010).

[243] A. Callan-Jones, J.-F. Joanny, and J. Prost, "Viscous-fingering-like instability of cell fragments," Phys. rev. lett. **100**, 258106 (2008).

[244] G. Gompper, R. G. Winkler, T. Speck, A. Solon, C. Nardini, F. Peruani, H. Löwen, R. Golestanian, U. B. Kaupp, L. Alvarez, *et al.*, "The 2020 motile active matter roadmap," J. Condens. Matter Phys. **32**, 193001 (2020).

[245] O. D. Lavrentovich, "Active colloids in liquid crystals," Curr. Opin. Colloid Interface Sci. **21**, 97–109 (2016).

[246] T. Turiv, I. Lazo, A. Brodin, B. I. Lev, V. Reiffenrath, V. G. Nazarenko, and O. D. Lavrentovich, "Effect of collective molecular reorientations on brownian motion of colloids in nematic liquid crystal," Science **342**, 1351–1354 (2013).